UNIVERSITY OF ILLINOIS
URBANA

AERONOMY REPORT

NO. 62

DESIGN AND CALIBRATION OF A
ROCKET-BORNE ELECTRON SPECTROMETER
FOR INVESTIGATION OF
PARTICLE IONIZATION IN THE NIGHTTIME
MIDLATITUDE E REGION

by
H. D. Voss
L. G. Smith

October 1, 1974

CITATION POLICY

A E R O N O M Y   R E P O R T

N O.   62

DESIGN AND CALIBRATION OF A ROCKET-BORNE ELECTRON SPECTROMETER
FOR INVESTIGATION OF PARTICLE IONIZATION IN THE
NIGHTTIME MIDLATITUDE E REGION

By

H. D. Voss
L. G. Smith

October 1, 1974

Aeronomy Laboratory
Department of Electrical Engineering
University of Illinois
Urbana, Illinois

ABSTRACT

An explanation is developed for the formation, near midnight at midlatitudes, of a broad electron-density layer extending approximately from 120 to 180 km and usually referred to as the intermediate E layer. The responsible mechanism is believed to be converging vertical ion drifts resulting from winds of the (2, 4) - mode of the solar semidiurnal tide. Numerical solutions of the continuity equation appropriate to the intermediate layer is described for particular models of ion drift, diffusion coefficients and ionization production. Analysis of rocket observations of the layers show that the ionization rate is highly correlated with the planetary geomagnetic index, K_p. Particle flux measurements support the idea that energetic electrons are the principal source of this ionization. A semiconductor spectrometer experiment for investigation of the particle flux, spectrum, and angular properties was designed and successfully flown on a Nike Apache rocket. A detailed description is made of the theory, design and calibration of this experiment and some preliminary results presented.

TABLE OF CONTENTS

LIST OF FIGURES

Figure   Page

Figure   Page

Figure   Page

1. INTRODUCTION

This report describes in detail the development of rocket-borne
instrumentation for investigation of the flux, spectrum, and relative
directional properties of energetic electrons in the ionosphere. The
need for these measurements derives from the lack of particle informa-
tion at midlatitudes under various ionospheric conditions. The signifi-
cance of particle precipitation as a source of ionization in the E
region, particularly the altitude range 120 to 180 km, is explored in
Chapter 2.

Present theories generally associate the observed ionization to be
a consequence of ultraviolet radiation (principally Lyman α, 1216 Å and
Lyman β, 1026 Å) scattered from the geocorona and to a minor degree of
galactic origin. The emphasis here is that energetic electrons may
play an important role in determining the nighttime E-region iono-
sphere, particularly at midnight during disturbed conditions.

In Chapter 3, an explanation is developed for the formation near
midnight of a broad electron-density layer extending approximately
from 120 to 180 kilometers. This layer is referred to as the inter-
mediate layer; it is above the region of sporadic-E layers and below
the F region. In the period from midnight to sunrise the layer is
observed to gradually narrow and descend at a rate of about 1.5 km min^{-1}
until it merges into the sporadic-E layers. The associated mechanism
responsible for this behavior is believed to be converging ion winds
(from horizontal wind shears) acted upon by the tidal winds of the
(2, 4) - mode of the solar semidiurnal tides. The layer is also more
noticeable during quiet geomagnetic conditions than disturbed.

The main part of this report concerns the development of a rocket-borne solid-state particle spectrometer. The design was developed for use on a Nike Apache rocket using IRIG telemetry. More elaborate procedures for data manipulation and reduction are available options to the system as familiarity, feasibility, and scientific objectives dictate. Chapter 4 is devoted to an explanation of semiconductor detector operation, sensitivity to internal and external conditions, and comparison with other particle detection schemes. Chapter 5 describes the design and fabrication of the spectrometer.

Discussion is given to optimal design techniques and methods and models to be used for interpretation of results. The calibration procedure, invoking various experimental procedures, is explained in Chapter 6.

2. ENERGETIC ELECTRONS AS AN IONIZATION SOURCE IN THE

NIGHTTIME E REGION

2.1 *Ionization Rates Calculated from Intermediate Layer Electron-Density Profiles*

The intermediate layer is observed near midnight in the altitude region from 120 to 180 km with peak near 150 km. It is formed as a result of the neutral winds, as developed in the next chapter. Applying the continuity equation described in Section ... 3 and integrating between the altitude limits z_1 and z_2 gives

$$\int_{z_1}^{z_2} (q - \alpha N^2) dz - \left[N\omega \right]_{z_1}^{z_2} + \left[D \frac{dN}{dz} \right]_{z_1}^{z_2} = 0 \qquad (2.1)$$

where q is the production rate, α is the recombination coefficient, D is the ambipolar diffusion coefficient and ω is the ion wind velocity function.

Now, if z_1 and z_2 are taken to be the nodes of the electron-density profile, then dN/dz and $\omega = 0$ at z_1 and z_2 requiring the square brackets in equation (2.1) to be zero. Therefore

$$\int_{z_1}^{z_2} q \; dz = \int_{z_1}^{z_2} \alpha N^2 \; dz \qquad (2.2)$$

Thus, the height-integrated ionization rate in the layer may be obtained without assuming any model for the vertical ion drift velocity. The proper choice of limits of integration has enabled the vertical ion drift (whether caused by neutral winds and/or electric fields) and diffusion to be averaged out; they have not been neglected.

An average ionization rate, $\bar{q}$, is immediately obtained as

$$\bar{q} = \frac{1}{(z_2 - z_1)} \int_{z_1}^{z_2} (\alpha N^2) dz \qquad (2.3)$$

The integration limits are met at both lower and upper valleys and at the peak of the layer. Thus the average ionization rate may be computed for (1) the layer below the peak, (2) the layer above the peak, and (3) the whole layer.

The choice of the recombination coefficient, α, is dealt with in Section 3.2.2. The formulation obtained (equation 3.1) is a function of altitude and magnetic index.

There are now five observations, shown in Figure 2.1, of the intermediate layer at Wallops Island near midnight: April 12, 1963 [*Cartwright*, 1964]; June 22, 1965 and February 22, 1968 [*Smith*, 1970]; and September 11, 1969 and November 1, 1972 [*Smith et al.*, 1974].

Applying the above procedure, the average ionization rate, $\bar{q}$, is obtained for each of the five cases: for the lower and upper parts of the layer, and for the whole layer. These values are given in Table 2.1 which also includes the altitudes of the valleys and the peaks used as limits in the integration of the continuity equation, and the associated values of K_p. The similarity of the ionization rates over the upper and lower portions of the layer suggest that the production is nearly uniform over this region.

The ionization rates are also strongly correlated with magnetic index, K_p, as shown in Figure 2.2. A least-squares fit to the data gives the experimental relationship as follows:
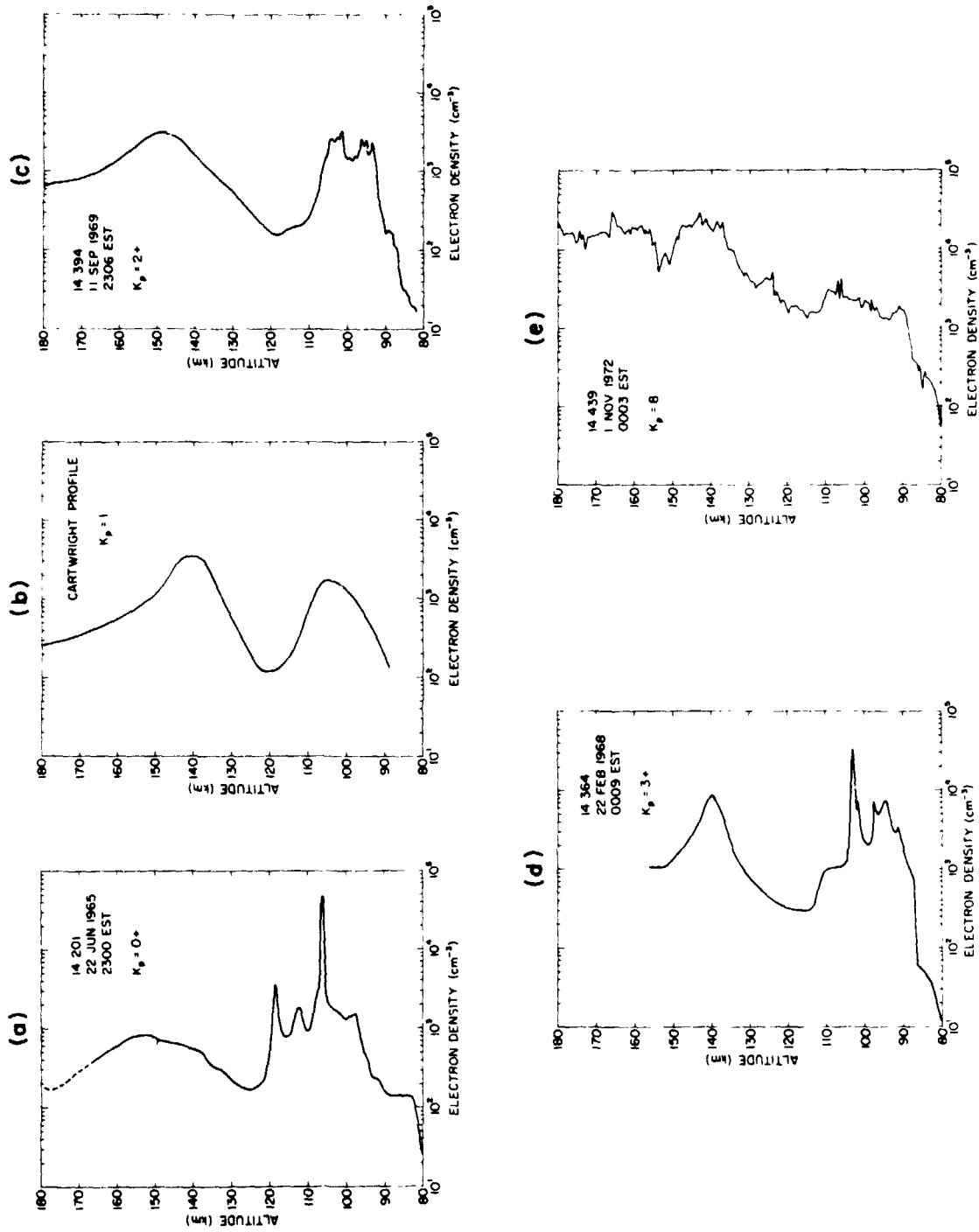
Figure 2.1 Compilation of electron-density profile measurements taken near midnight at Wallops Island, Virginia, under various geomagnetic conditions.

Table 2.1

Ionization Rate in the Upper E Region near Midnight.

Date	Altitude (km)			Ionization Rate (cm^{-3} sec^{-1})			K_p
	Valley	Peak	Valley	Lower	Upper	Whole	
12 Apr. 1963	120	140.5	182	0.90	0.48	0.62	1
22 Jun. 1965	125	153	177	0.090	0.071	0.081	0+
22 Feb. 1968	116	140	154	2.0	3.3	2.5	3+
11 Sep. 1969	118	148.5	180	0.60	0.59	0.59	2+
1 Nov. 1972	115	143	175	26	43	35	8
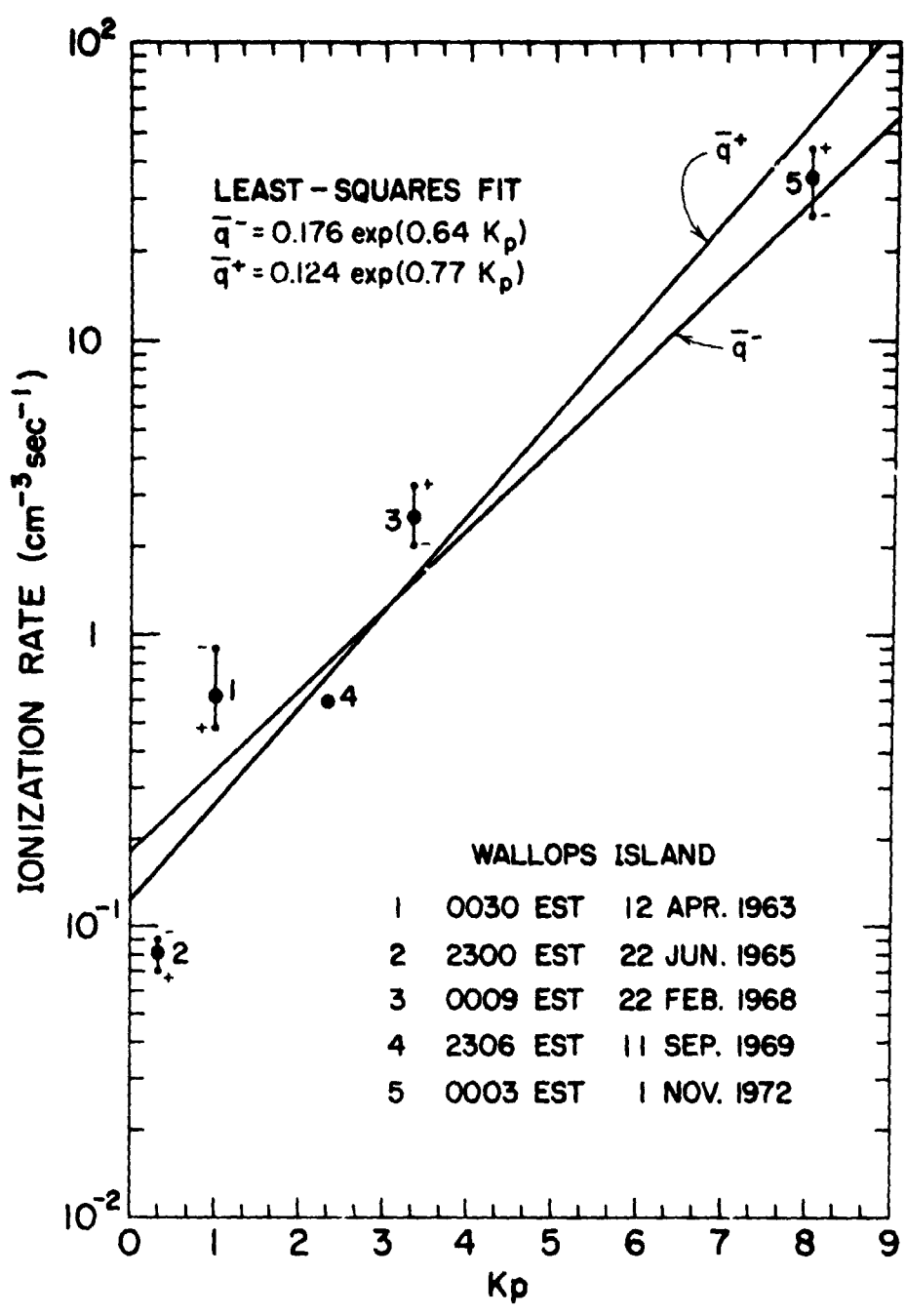
Figure 2.2 Values of $\bar{q}^-$ and $\bar{q}^+$, electron production rates in the lower and upper parts of the intermediate layer, respectively, as inferred by applying equation 2.3 to electron-density profiles 2.1a-2.1e, as a function of K_p. Smaller dots with "-" indicate $\bar{q}^-$, smaller dots with "+" indicate $\bar{q}^+$, and larger dots indicate q over the entire layer.

$$\overline{q} = 0.14 \exp(0.71 \ K_p) \text{cm}^{-3} \text{ sec}^{-1} \qquad (2.4)$$

The correlation coefficient for the five observations is 0.96. Interestingly, the data indicate that the lower profile ionization rate, Q_L, is always larger for K_p values less than 3 while the upper is always greater for K_p greater than 3. The least-squares fit corresponding to Q_L, and Q_U are

$$Q_L = 0.176 \exp(0.64 \ K_p)$$

$$\qquad (2.5)$$

$$Q_U = 0.124 \exp(0.766 \ K_p)$$

This reversal suggests that the particle spectrum and pitch angle distribution is such as to ionize more of the upper portion of the layer as K_p increases. The greater ionization rate observed at low K_p for the lower profile is expected since Ly β ionizes to a greater extent the lower E region. Similar results have been obtained by *Gough and Collin* [1973] in which they measured the flux of electrons (> 40 keV) at South Uist on thirteen rocket flights. Their correlation with magnetic activity by a least-squares fit gives an exponent of 0.98 K_p and a correlation coefficient of 0.79.

Applying the ionization rate calculation again to five nighttime launches on February 22, 1968, a time evolution of the intermediate layer production can be investigated. These results are shown in Figure 2.3 for the electron-density profiles of Figure 3.1. From midnight to at least 0130 the upper and lower ionization rates are similar and quite
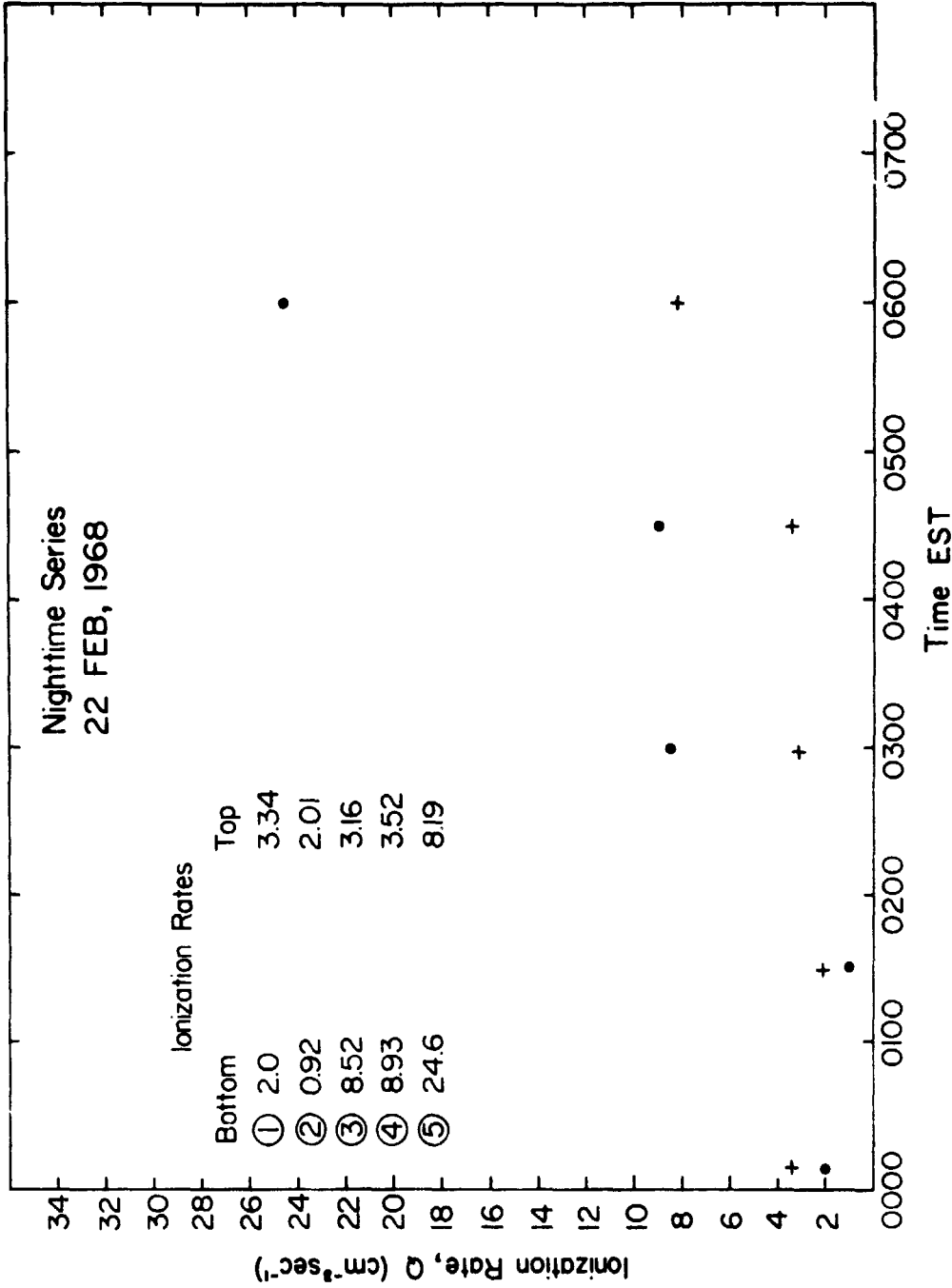
Figure 2.5 Average ionization rates calculated from the intermediate layer according to equation 2.3 for the nighttime series of profiles shown in Figure 3.1. The solid dots indicate the bottom profile production rate and the plus sign for the upper.

small. At 0300 and thereafter there is a substantial increase in upper

ionization rate presumably from the increasing Ly β flux from the geo-

corona and the descending of the layer to lower altitudes. At sunrise

the ionization quite naturally responds rapidly.

2.2 *Observation of Particle Precipitation in Midlatitudes*

Experimental observations are essential if energetic particles are

to be recognized as a possible midlatitude ionization source. To

ascertain the existence of particles, various direct or indirect methods

can be applied. Particle detectors onboard satellites or rockets pro-

vide the best direct access to particle information. However, they are

limited to mappings over a small time scale and require extensive faci-

lities if simultaneous geographic measurements are desired. Ground-based

observations rely on measurement of particle aftereffects invoking such

candidates as light emission, radio noise, magnetic field fluctuations,

and related ionospheric interactions.

2.2.1 *Rocket-borne particle observations.* The most direct measure-

ments of energetic particles can be made utilizing a rocket-borne

experiment. This type of experiment is capable of providing excellent

height resolution, spectrum, and pitch angle information. Although many

rocket measurements have been made at high latitudes relatively few

have been concerned with lower latitude observations. In fact, much of

the present low latitude data is derivable from the results of rocket-

borne X-ray experiments which are additionally sensitive to energetic

electrons.

Two particle detector experiments of the Aeronomy Laboratory were

launched from Wallops Island (38°N, 75°W; geomagnetic latitude 49°N) at

0003 EST on November 1, 1972, and at 2330 EST on April 18, 1974. The first payload was equipped with a Geiger counter sensitive to electrons greater than 70 keV while the second was equipped with the solid-state detector experiment described in Chapters 4, 5, and 6. Both payloads included tip mounted Langmuir probes [*Smith*, 1969] and a propagation experiment [*Mechtly and Smith*, 1970] for electron-density measurements.

The Geiger counter operation is discussed in Section 4.2.4. The particular Geiger counter employed used a beryllium window of area 0.203 cm^2 and thickness 5.1 x 10^{-3} cm. The geometrical factor is 0.303 cm^2 ster. The window of the counter is oriented perpendicular to the spin axis of the rocket and is covered, during the launch phase, by a door carrying a weak radioactive source. The door and source are ejected 41 sec after launch (43 km altitude).

The count rate measured during the flight is shown in Figure 2.4. Each data point is the average for a five-second interval. The uncertainty in count rate is indicated by error bars at representative points. The data below 60 km on the descending trajectory are of poor quality and are not included in the figure.

The count rate of the detector at sea-level (before launch) is 3.3 sec^{-1}, of which the source on the door contributes 3.0 sec^{-1} and the cosmic-ray background 0.3 sec^{-1}. The dashed line in Figure 2.4 connects points which have been corrected for the radioactive source carried in the early part of the flight. The resulting variation with altitude up to about 80 km, including the Pfotzer-Regener maximum near 20 km, is consistent with previous observations of cosmic-ray fluxes at mid-latitudes [*Van Allen*, 1952]. In other (daytime) flights with identical
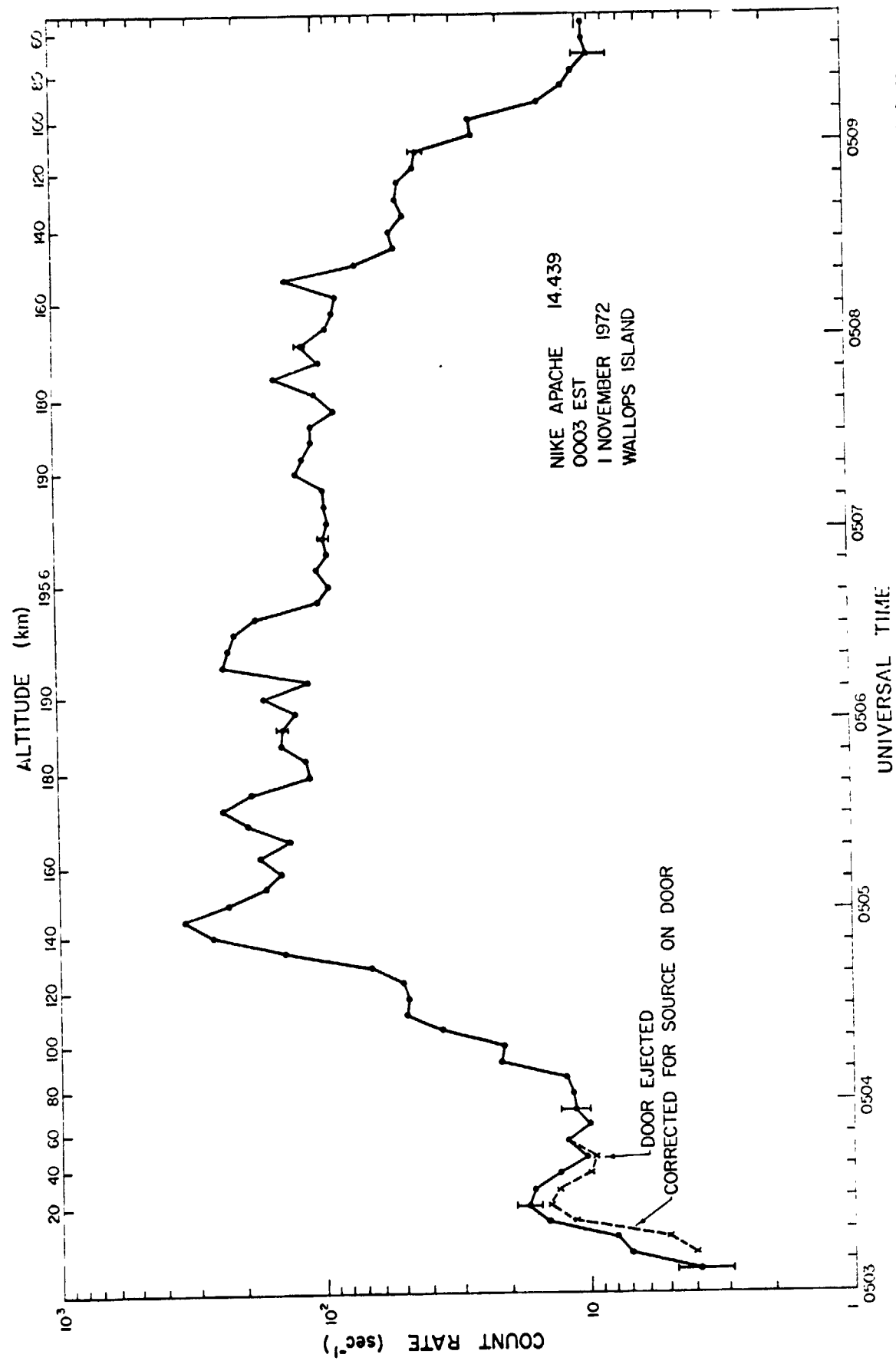
Figure 2.4 Geiger counter measurement of energetic electrons with energies greater than 70 keV.

counters the background count rate, due to cosmic rays, has been found to be about 10 sec^{-1} at altitudes greater than 40 km.

The excess counts on this flight are attributed to electrons with energies greater than 70 keV. The flux increases with increasing altitude in the range 80 to 140 km both on ascent and descent. The count rate reaches a maximum value of 339 ± 8 sec^{-1}, which, when corrected for cosmic rays, gives an average flux (> 70 keV) of 1086 ± 26$cm^{-2}sec^{-1}ster^{-1}$.

Two important considerations relative to the count rate profiles are (1) the detector is predominately looking at particles with pitch angles near 90 degrees, but, is modulated because of the rocket spin (7.3 rps) and processional (20 sec) periods, (2) the launch was made on a very disturbed night, with K_p = 8. The first consideration explains, to a large degree, the apparent count rate fluctuation since it is observed that the number of particles per incremental pitch angle (angular probability) varies appreciably near 90 degrees. The second consideration predominately governs the absolute magnitude of the count rate curve.

The launch on April 18, 1974, was made during a moderately disturbed night of K_p = 5+. Five channels were used for spectrum analysis corresponding to energies of 12, 25, 40, 60, and 80 keV. A preliminary study indicates that the spectrum near 160 km is related by a power law of exponent γ = 2 and that the pitch angle distribution varies markedly near pitch angles of 90 degrees. Figure 2.5 shows a portion of the flight chart record illustrating the typical experiment behavior. The spectrum is shown as the staircase waveforms (16 counts per pulse) with the high count channel (top one) associated with the lowest energy. The pitch
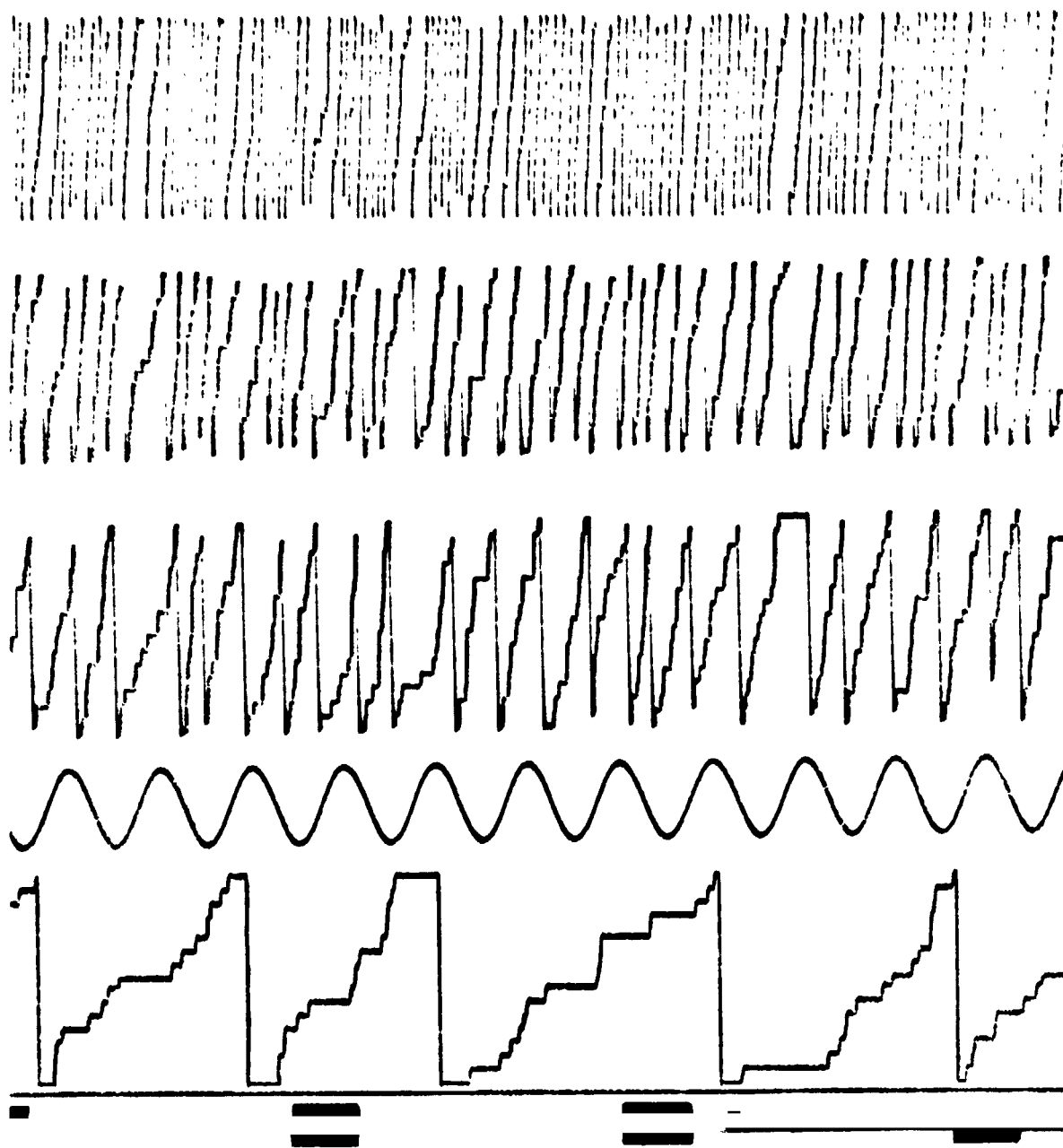
Figure 2.5   Four-inch-per-second chart record of particle data received from
             the five channel energetic electron spectrometer (staircase wave-
             forms). Also shown are the magnetometer signal (each period
             represents one rocket revolution), Langmuir probe and time code.
             The lowest channel (No. 1) is not shown because of the higher count
             rate. The particle modulation is evident in channel two at the
             top of the chart.

angle dependence can be verified in the second channel as a modulation
with the spin period. The sinusoidal signal is from the magnetometer and
indicates the relative position of the rocket with respect to the magnetic
field.

The particle count rate for the first channel (E > 12 keV) is dis-
played in Figure 2.6. The results clearly illustrate (1) particle flux
not changing with time; (2) processional modulation corresponding to
changing pitch angles; and (3) a nearly linear dependence or count
rate with altitude.

These data are amplified by three rocket-borne experiments designed
primarily to look at galactic X-rays, but also sensitive to energetic
electrons with energies greater than 4 keV.

Hill et al. [1970] used proportional counters aimed at right angles
to the spin axis. The collimation pattern was 5° (vertical) and 30°
(horizontal) FWHM using the standard egg-crate geometry. The counter
windows were approximately 60 μg/cm^2 Formvar. Two rockets were
launched from Kauai, Hawaii. The first on May 15, 1968, at 6:41:20 UT
(at apogee) and the second on May 17, 1969, at 6:56:15 UT (at apogee).
The L at apogee (158 km) was 1.16. The rocket spin axis was orientated
in the vertical causing the counters to scan a band of sky centered on
the horizon. The resultant count rate verses the azimuth angle for
both flights is shown in Figure 2.7. The maximum rate of change of
particle intensity occurs at pitch angles of 90° (corresponding to
azimuth angles of 270° and 90°) supporting the results obtained from the
Wallops experiments. Further agreement is made with the linear increase
in count rate verses altitude and is illustrated in Figure 2.8 for the

Ch I Count Rate J>12 keV

Nike Apache 14.520

Wallops Island

2330 EST

COUNT RATE (sec⁻¹)

7000 6000 5000 4000 3000 2000 1000

2332 2333 2334 2335 2336

EASTERN STANDARD TIME
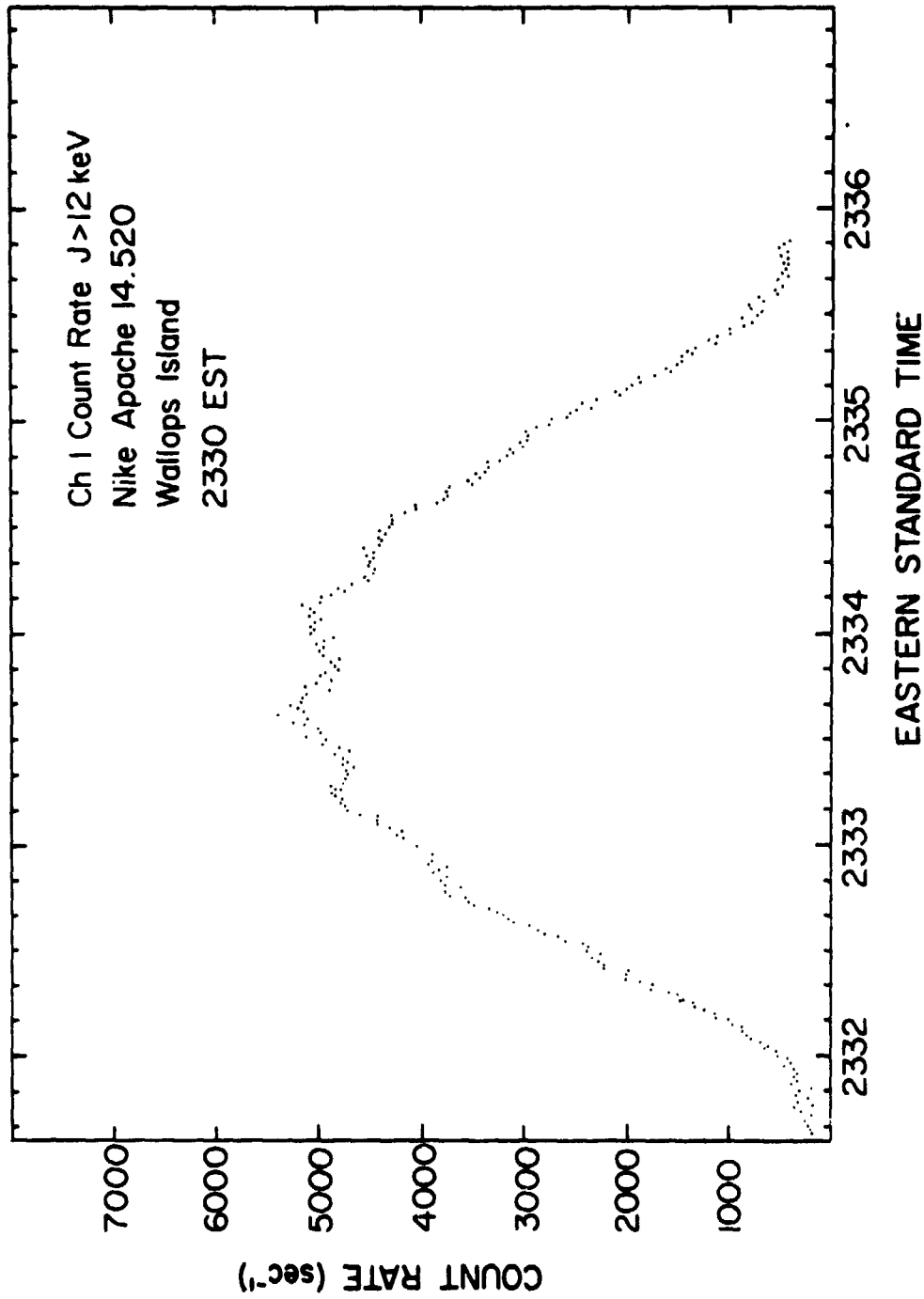
Figure 2.6 Energetic electron spectrometer low energy (12 keV) channel count rate. The data clearly show the 1) temporal smoothness, 2) linear count rate versus altitude and 3) precessional peaks due to pitch angle variation. Data were sampled every second.
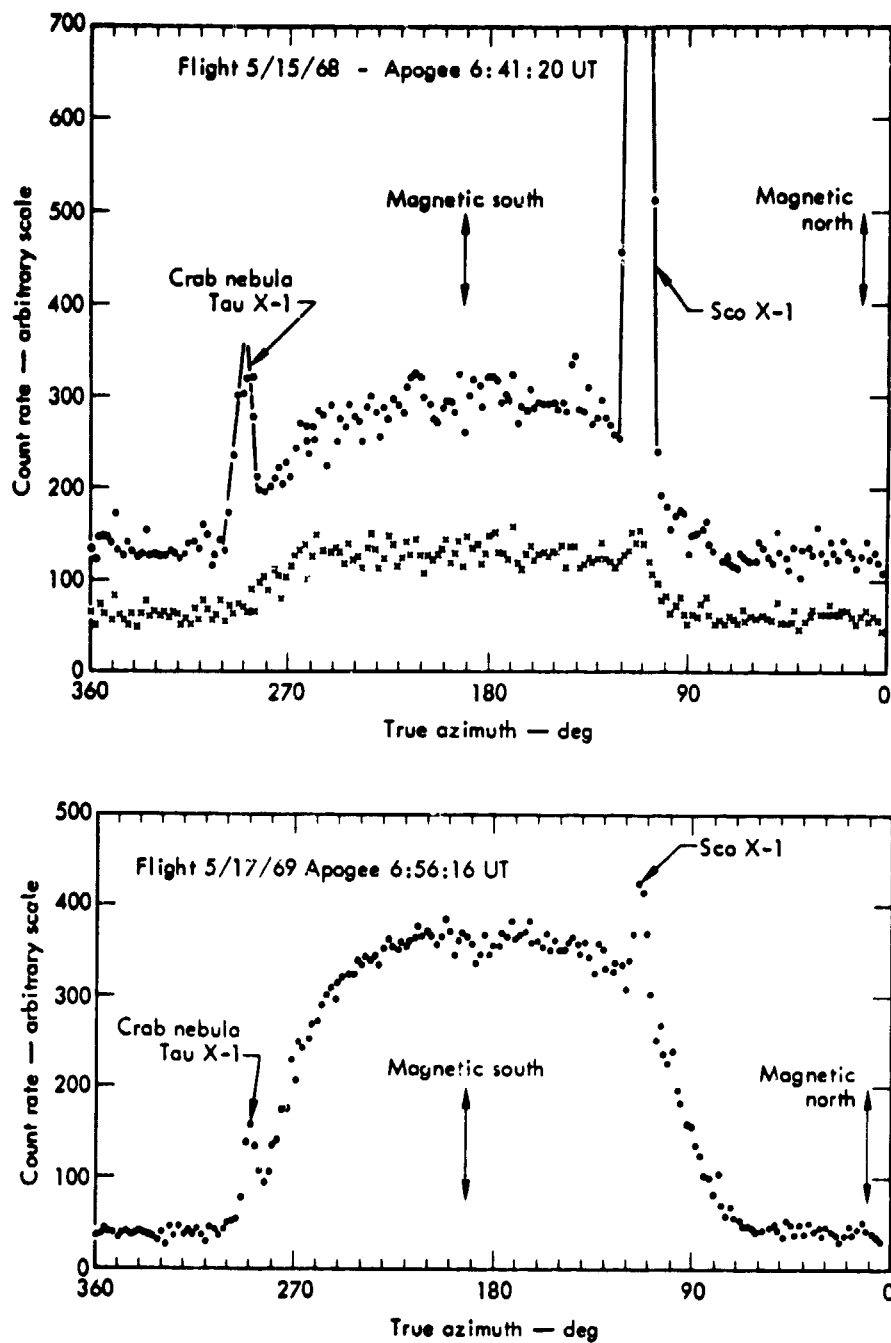
Figure 2.7 Count rate verses azimuth from an experiment by *Hill t al.* [1970] for two rocket flights made on 15 May 1968 and 17 May 1969. Solid circles show counts corresponding to 1-10 keV energy deposited into counter and crosses correspond to energy deposited greater than 10 keV.
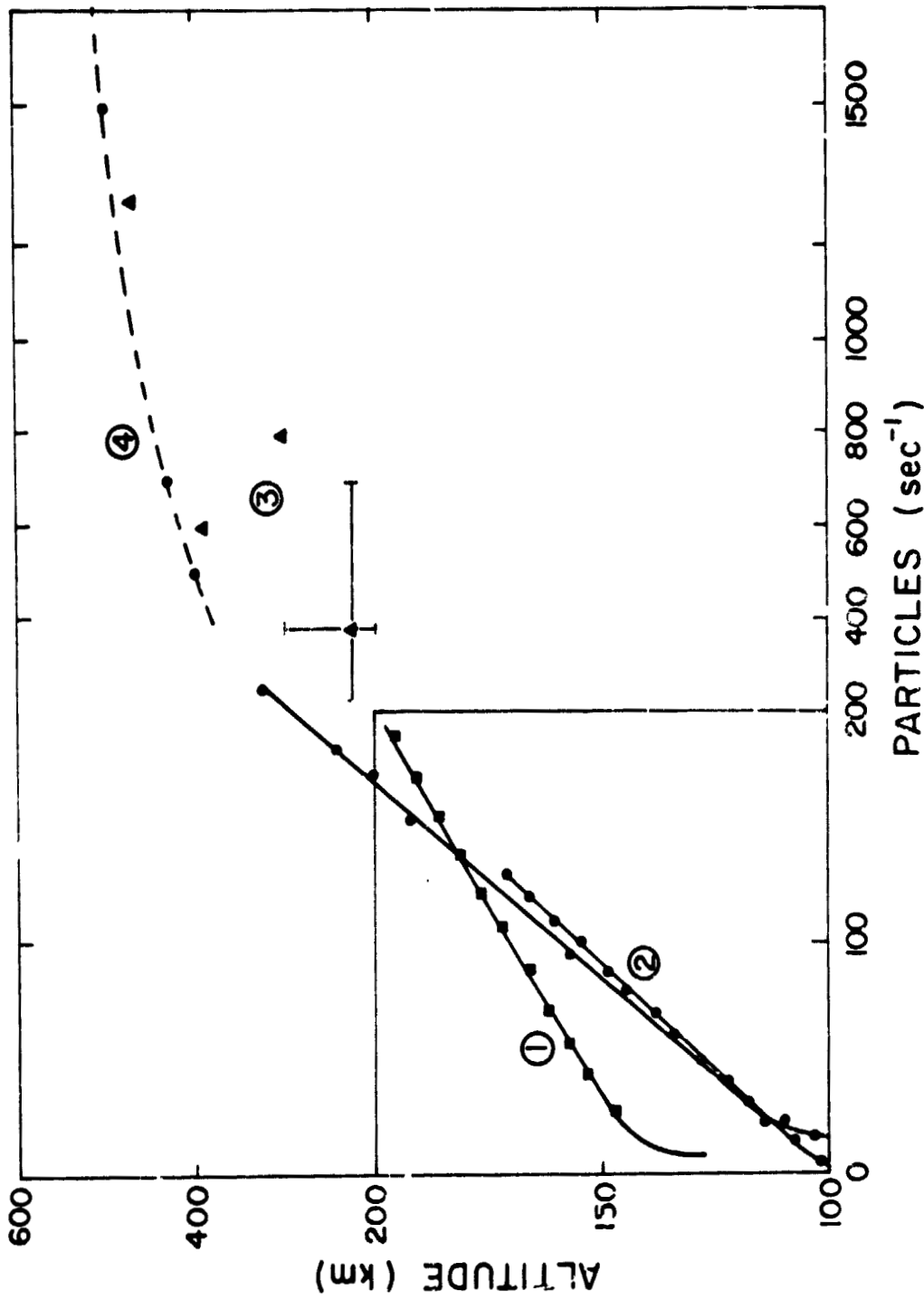
Figure 2.8 Particle count rate versus altitude showing the linear increase with altitude. Curve 1 is the 18 April 1974 launch by Smith for electrons with energies between 12 to 18 keV. Curves 2 are from *Hill et al.* [1970] for May 15, 1968 and May 17, 1969. Points in region 3 are from *Hayakawa et al.* [1973]. The dashed line, 4, is the deduced altitude dependance by *Maeda* [1965].

May 17, 1969, and for a previous flight on November 6, 1968. All flights were made with values of K_p less than 1.

Hayakawa et al. [1973] employed two proportional counters equipped with polypropylene windows of 100 and 50 μg cm^{-2} in thickness and effective areas of 32 and 26 cm^2, respectively. The 100 μg cm^{-2} counter was perpendicular to the role axis and the 50 μg cm^{-2} counter was angled 20° upward. Each X-ray event in the energy range 0.1 to 3 keV was pulse height analyzed. The equivalent electron energy range was deduced to extend from 5 to 10 keV.

The launch was made at 2100 Japanese Standard Time on September 3, 1971, from Kagoshima Space Center, 20°N geomagnetic latitude. The L value ranged from 1.17 to 1.25 over the rocket altitude range from 200 to 800 km. The magnetic dip angle was 42°. The count rate verses altitude and the azimuthal dependence is reproduced in Figure 2.8. The count rate, when multiplied by the appropriate angular sensitive factor of the detector, gives the count rate in units of cm^{-2} sec^{-1} ster. This count rate is comparable to the count rate of Hill for the overlapped altitude range. The dashed line above 400 km represents the altitude dependence estimated from the trapping lifetime for the ionization loss deduced by *Maeda*, [1965]. The curve is normalized to the highest altitude experimental data point. The lowest energy data differs significantly and is suggested to be the consequence of atmospheric backscatter. The pitch angle data reveal a very different type of distribution than that observed by Smith or Hill at lower altitudes. This anisotropy, however, is in agreement with the theoretical distribution (solid curve) of $(\sin^n\alpha)\, d(\cos\alpha)$ with $n = 8$.

Physically, the electrons are centered around 90 degree pitch angle suggesting that the radiation is trapped and is near the mirroring point. The smaller the pitch angle the lower the mirroring point and the greater the susceptibility to atmospheric interaction. The 200 to 500 km pitch angle distributions indicates a nearly isotropic dependence since the higher altitude particles with pitch angles near 90 degrees have been filtered out reducing the overall count rate. Continuing below 200 km the distributions by Smith and Hill show a gradual increase and narrowing of the distribution for particles with pitch angles less than 90 degrees. This is attributed to the increased absorption of particles as their pitch angle becomes 90 degrees. The time expended per unit height interval is increased as the particle approaches the 90 degree pitch angle in its downward trajectory, thereby, increasing the likelihood of an ionization event and particle absorption.

The third X-ray flight which additionally revealed the presence of energetic electrons is reported by *Tuohy and Harries* [1973], for their experiment launched from Woomera, South Australia, (L = 1.75), at 0030 hours UT on July 10, 1970. The K_p magnetic index was 7-. The detector was sensitive to 25 keV electrons and recorded a flux of 5 electrons cm^{-2} sec^{-1} keV^{-1} $ster^{-1}$ when at 90 degree pitch angle. The pitch angle distribution is peaked at 90 degrees with a FWHM spread of 30 degrees.

The data from the above experiments intuitively agree with expected behavior. Sufficient information exists to deduce ionization rates

given the pitch &. e distribution, energy spectrum and particle flux.
These results suggest that the observed midlatitude flux of energetic
electrons are a primary source of nighttime ionization and will be ex-
plored in more detail in Section 2.5.

2.2.2 *Satellite particle observations*. Satellite data compiled
by *Potemra and Zmuda* [1970] are shown in Figure 2.9. The average inten-
sities of electrons were made for energies greater than 40 keV and
during or near a solar-minimum epoch. Although the maximum intensities
occur at auroral latitudes it is apparent that there is significant
midlatitude (35° to 55°) flux and overall flux variability for all
latitudes.

2.2.3 *Indirect measurements of energetic electron precipitation*.
The indirect measurements of precipitating electrons are of unquestion-
able importance since they not only support the existence of particles
but verify the degree of interaction with the atmosphere. This inter-
action results in such processes as ionization, heating, chemical reac-
tions, and photon excitations.

Ionization processes culminate in enhanced electron densities.
Therefore, by monitoring the electron density by either rocket-borne or
ground-based techniques, it is possible to ascertain the source magni-
tude and altitude dependence. For example, if particle ionization is
observed predominately at altitudes of 120 kilometers, then conclusions
can be made about the energy spectrum as consisting of 1 to 10 keV
particles and/or the particle pitch angle distribution is maximized
around 90 degrees.
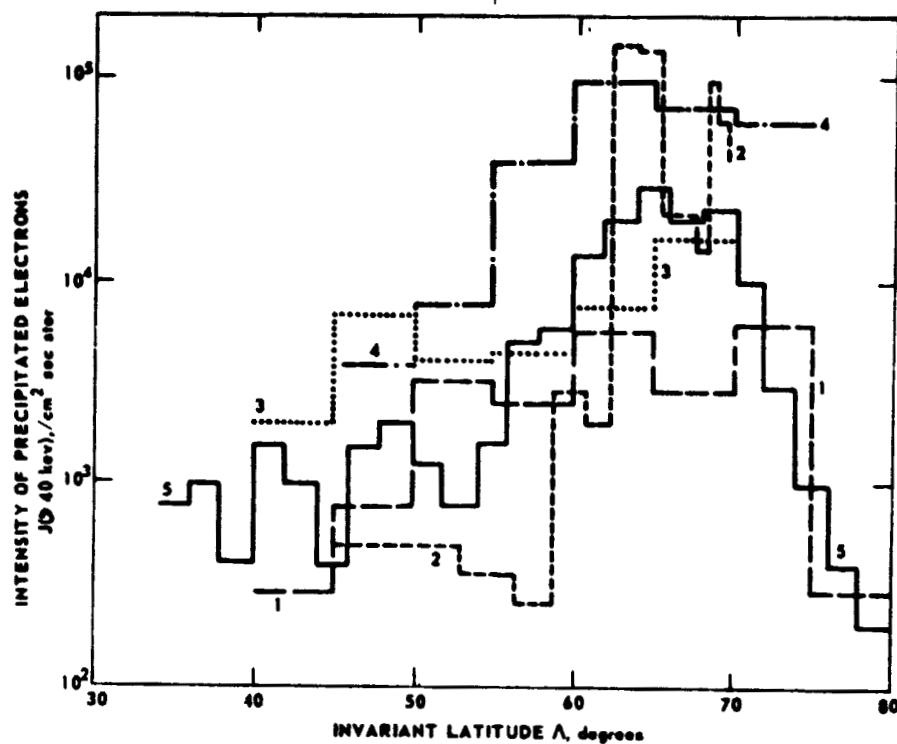
Figure 2.9 Averaged intensities at ≤1100 km altitude of precipitated electrons ≥40 keV assimilated by *Potemra and Zmuda* [1970], satellite observations are as follows: (1) Injun 1 during June-September 1961 [*O'Brien*, 1962]. (2) Injun 3, January 1963 [*O'Brien*, 1964]. (3) Injun 3, February-October 1963 [*Fritz*, 1967, 1968, and personal communication]. (4) Explorer 12, August-September 1961 [*O'Brien and Laughlin*, 1963]. (5) Alouette, October 1962 to January 1963 [*McDiarmid et al.*, 1963].

One particularly interesting observation is the relationship of the average ionization produced in the upper E region (120 to 180 km) for different values of magnetic index, K_p. This index is a logarithmic scale (from 0 thru 9) of the averaged magnetic field fluctuations. Furthermore, this K_p variation is directly correlated with particle precipitation since the particle trajectory is perturbed by the changing magnetic field. Consequently, Figure 2.2 illustrates the high correlation (0.91) of E-region ionization and particle precipitation.

Another technique which has been correlated with electron precipitation is VLF (3 to 30 kHz) electromagnetic wave reflection off the D region [*Potemra and Rosenberg*, 1973]. This method is based on measuring the phase change of a VLF electromagnetic wave as it is transmitted, reflected off the E region, and received at a distant point. The effective altitude of reflection and thus, the phase is directly related to the D-region ionization. The correlation is then made of reflection altitude verses magnetograms showing that enhanced particle precipitation ($E > 40$ keV), causing a magnetogram fluctuation, ionized a greater portion of the D region thereby changing the reflection height.

Airglow measurements in midlatitudes have been strongly correlated with magnetic activity [*Hirao et al.*, 1965] and hence provide an excellent particle flux indicator. The particles predominately excite the first negative system of N_2^+ releasing photons of 3914 Å over the altitude range 130 to 300 km. *Dalgarno* [1964] has found the upper limit of the particle flux to be 3×10^{-2} ergs cm^{-2} sec^{-1} assuming that the upper bound of the N_2^+ intensity is 60 Rayleighs. An excellent take-off to this experiment which would provide substantial ionization

information is to measure the airglow intensity over an extended period of time and to relate it with direct particle data from a simultaneous rocket-borne experiment.

The use of balloons to measure X-ray fluxes is another way to obtain an indirect particle measurement. Energetic particles colliding with neutral constituents create bremsstrahlung X-rays which are able to penetrate to low balloon altitudes (30 to 50 km).

2.3 *Charged Particle Dynamics in a Magnetic Field*

In order to properly understand tne defining relations and role of charged particles as an ionization source, attention must be given to the governing equations of motion of a particle in a nonuniform electromagnetic field. Conclusions may then be reached about particle fluxes and the energy spectrum; the variation of both with altitude and finally the ionization that is produced. A summary will be given of charged particle motion in a uniform and variable static magnetic field. The study of the variable magnetic field will lead to the fundamental adiabatic invariant with particular emphasis on the magnetic dipole field approximation to the earth's field and the associated implications.

2.3.1 *Charged particle motion in a uniform magnetic field.* The general equation of motion for a particle of charge Ze, according to Newton's laws, may be stated as the sum of forces due to $\vec{B}$, $\vec{E}$, and non-electromagnetic forces $\vec{F}_{ex}$. These forces acting on the particle must equal the time derivative of momentum $\vec{P}$

$$\frac{d\vec{P}}{dt} = Ze \ (\vec{V} \times \vec{B} + \vec{E}) + \vec{F}_{ex} \qquad (2.6)$$

For the case of a uniform static magnetic field with zero E and F_{ex}, the energy of the particle must be constant. Hence

$$\frac{d\vec{v}}{dt} = \vec{V} \times \vec{\omega}_B \qquad (2.7)$$

where

$$\omega_B = \frac{Ze\vec{B}}{\gamma_m} \qquad (2.8)$$

and γ_m is the relativistic mass and ω_B is the angular particle velocity. By choosing the reference frame such that the unit vector $\hat{\epsilon}_3$ points in the direction of the B field the first order matrix equation (2.7) may be simply solved, giving

$$\vec{V} = (v_1 \, \hat{\epsilon}_1 + v_2 \hat{\epsilon}_2) \, e^{-i\omega_B t} + v_{11} \, \hat{\epsilon}_3$$

where v_1, v_2, and v_{11} (parallel velocity) are the integration constants. v_1 and v_2 can be calculated by specifying a circular motion in the $\hat{\epsilon}_1$ and $\hat{\epsilon}_2$ plane. Hence

$$v(t) = \omega_B a \, (\hat{\epsilon}_1 - i\hat{\epsilon}_2) e^{-i\omega_B t} + v_{11} \, \hat{\epsilon}_3 \qquad (2.9)$$

where a is the orbit radius. $v(t)$ may be verified to be a solution of 2.7. For physical meaning the real part of $v(t)$ is chosen.

Integration of equation (2.9) yields the trajectory information

$$\vec{x}(t) = \vec{X}_O + v_{11} \, t\hat{\epsilon}_3 + ia(\hat{\epsilon}_1 - i\hat{\epsilon}_2)e^{-iw_B t} \tag{2.10}$$

where X_O is the position vector of the particle at time zero. The path mapped by $\vec{x}(t)$ is a helix of radius a and with pitch angle α, defined to be the angle between the field line and the velocity vector of the particle. Hence

$$\tan \alpha = \frac{v_{11}}{w_B a} \tag{2.11}$$

A useful relation is further obtained from equation (2.8) by substitution for $\gamma_m \vec{w}_B = \vec{P} \times \vec{r} = P_\perp a \, \epsilon_3$.

$$\frac{P_\perp}{eZ} = aB \equiv R \tag{2.12}$$

where R is called the magnetic rigidity.

2.3.2 *Charged particle motion in a uniform magnetic and external force field.* The next case of interest is charged particle motion in a combined static external and magnetic force. Equation (2.6) applies with $\vec{F}$ set equal to $Ze\vec{E} + \vec{F}_{ex}$, yielding two component parts:

$$\frac{d\vec{p}_{11}}{dt} = \vec{F}_{11}$$

$$\tag{2.13}$$

$$\frac{d\vec{p}_\perp}{dt} = \vec{F}_\perp + Ze\vec{V} \times \vec{B}$$

where $\vec{B}$ is in the reference direction.

The first equation is the conventional acceleration of the charged particle in the $\vec{F}_{11}$ direction. The second equation can further be decomposed into two component parts giving

$$P_x = Ze\,B_z y$$

$$P_y = F_\perp t - ZeB_z x \tag{2.14}$$

The motion executed by the particles in equation (2.14) is a cycloid in the plane perpendicular to $\vec{B}$. The motion is further illustrated in Figure 2.10 showing a uniform drift, V_F, perpendicular to $\vec{F}$ and $\vec{B}$ (sometimes called an $\vec{E}x\vec{B}$ drift). The velocity V_F may be obtained by taking an average of equation (2.9) resulting in $P_y = 0$ and

$$\vec{V}_F = \frac{\vec{F}_\perp}{ZeB_z} = \frac{\vec{E}_\perp}{B_z} + \frac{F_{ext}}{eZB_z} \tag{2.15}$$

Positive and negative particles drift in opposite directions for $F_{ext} = 0$ and in the same direction for $\vec{E}_\perp$ finite. For the case in which $F_\perp > ZeB_z$ the $\vec{B}$ field is not able to compensate the strong $F_\perp$ field and the particle is accelerated in the $F_\perp$ direction.

If the external force is a function of spatial coordinates, equation (2.6) still applies. The drift velocity in this case follows the equipotential line since $\vec{F} = -\nabla U$ where U is the potential energy. This is further illustrated in Figure 2.10 for a particle with 90° pitch angle in a uniform $\vec{B}$ field. The underlying approximation assumed here in the averaging is that the radius of curvature of the equipotential line is much larger than the particles gyroradius.
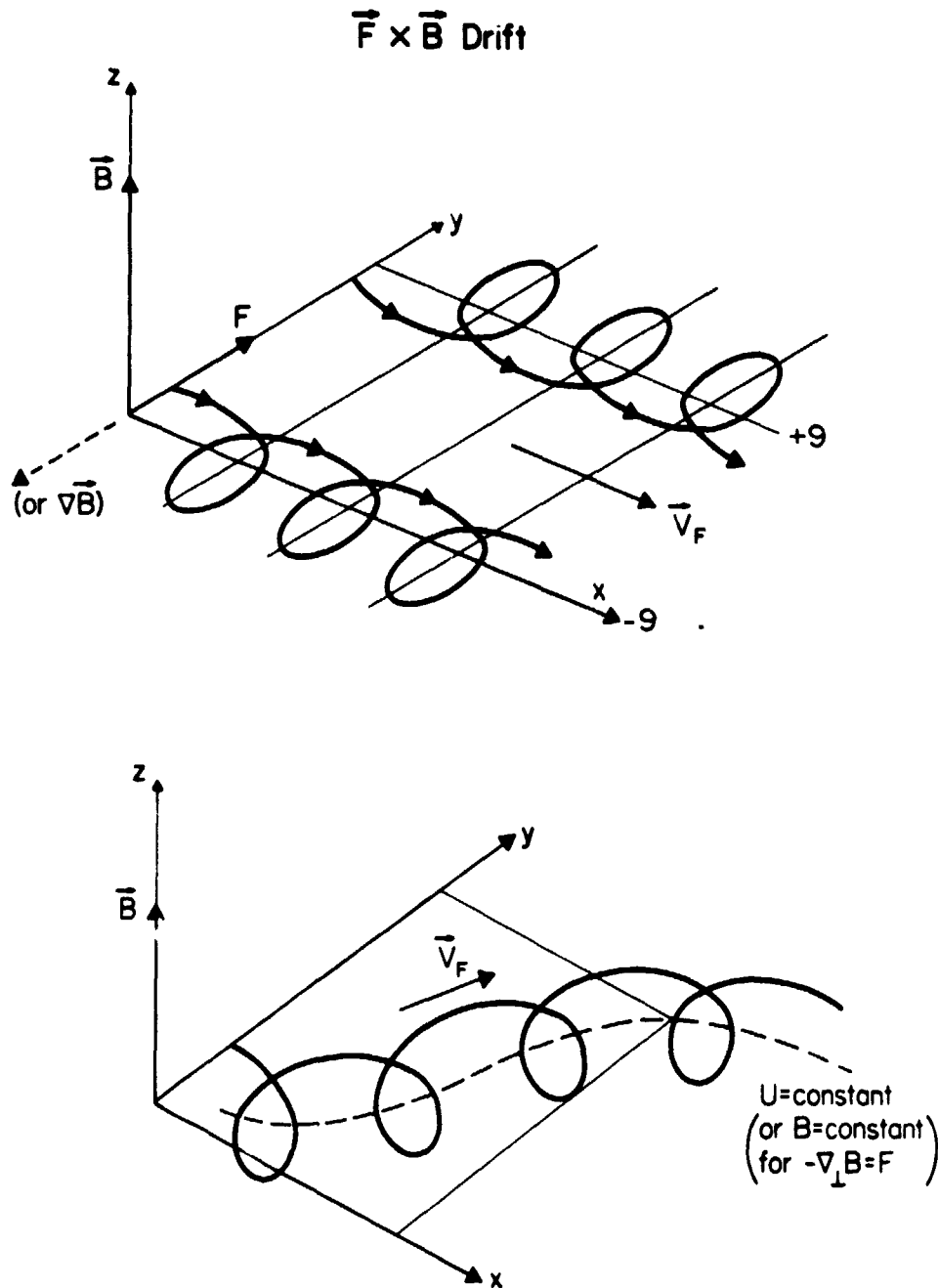
Figure 2.10 Perpendicular motion of a charged particle in a uniform
static magnetic field with an applied force field $\vec{F}$. The
upper figure shows that the averaged particle motion is
perpendicular to $\vec{B}$ and $\vec{F}$. The lower figure illustrates the
motion in a nonuniform potential force field.

2.3.3 *Charged particle motion in a nonuniform magnetic field.* The spatial gradients in a magnetic field can be divided into component form as $\nabla B = \nabla_{11} B + \nabla_{\perp} B$ relative to the magnetic field $\vec{B}$. From Maxwell's equations, $\vec{\nabla} \circ \vec{B} = 0$ and $\vec{\nabla} \times \vec{B} = 0$, it follows that if $\nabla_{\perp} B \neq 0$ then $\nabla_{11} \vec{B}$ is also nonzero. The $\nabla_{\perp}$ contribution will be examined first. Since the B field is constant in time, no energy is transferred to the particle so that $v_{\perp}$ remains constant. The gyroradius, $a = (mv_{\perp})/(qB)$ where B is the average field enclosed by an orbit, remains constant. The force experienced by the particle in the y direction does not average out over one revolution because of the field inhomogeneity and contributes to a y directed force as previously discussed. $F_{\perp}$ is directed opposite to $\nabla_{\perp} B$ and is given by the instantaneous y component as

$$f_y(\theta) = f \cos\theta = qv_{\perp}(B + \nabla_{\perp} Ba \cos\theta) \cos\theta \qquad (2.16)$$

where θ is the angle of orbit curvature related to the positive y direction. To obtain the average y directed force over one cycle, the integral is performed over θ from 0 to 2π.

$$F_{\perp} = \frac{1}{2\pi} \int_0^{2\pi} f_y \, d\theta = \frac{1}{2} qv_{\perp} \nabla_{\perp} Ba \qquad (2.17)$$

The associated gradient drift velocity, V_G, is computed from equation (2.15) giving

$$V_G = \frac{mv_{\perp}^2}{2eZB^2} \nabla_{\perp} B \qquad (2.18)$$

The motion executed is the same as shown in Figure 2.10. Again the implicit assumption made is that $\nabla_{\perp} Ba \ll B$ or the orbit curvature must be smaller than the field line curvature, $\frac{B}{\nabla_{\perp} B} = R_c$.

Additionally, if the parallel velocity, v_{11}, is nonzero (pitch angle not 90°) the parallel curvature of the field line contributes to a curvature drift where the centrifugal force is directed perpendicular to the $\mathcal{B}$ field line.

$$F_c = \frac{mv_{11}^2}{R_c}$$

and the curvature drift is given by equation (2.15) as

$$\vec{V}_c = \frac{mv_{11}^2}{eZR_cB} = -\frac{mv_{11}^2}{eZ}\frac{1}{B^2}\frac{\vec{B}}{B} \times \nabla_{\perp} B \qquad (2.19)$$

The vector combination of these drifts $\vec{V}_c + \vec{V}_g = \vec{V}_{cg}$ is

$$\vec{V}_{cg} = \frac{m}{2eZ\,B^2}\,(v^2 + 2v_{11}^2)\,\frac{\vec{B}}{B} \times \nabla_{\perp} B$$

$$= \frac{mv^2}{2eZ\,B^2}\,(1 + \cos^2\alpha)\,\frac{\vec{B}}{B} \times \nabla_{\perp} B \qquad (2.20)$$

$$= \frac{-mv^2}{2eZ\,R_cB}\,(2 - \sin^2\alpha)\,\frac{\vec{B}}{B} \times \vec{n}$$

where n is a unit vector in the opposite direction of the center of curvature. Reference to the upper diagram in Figure 2.11 depicts the curved B behavior.
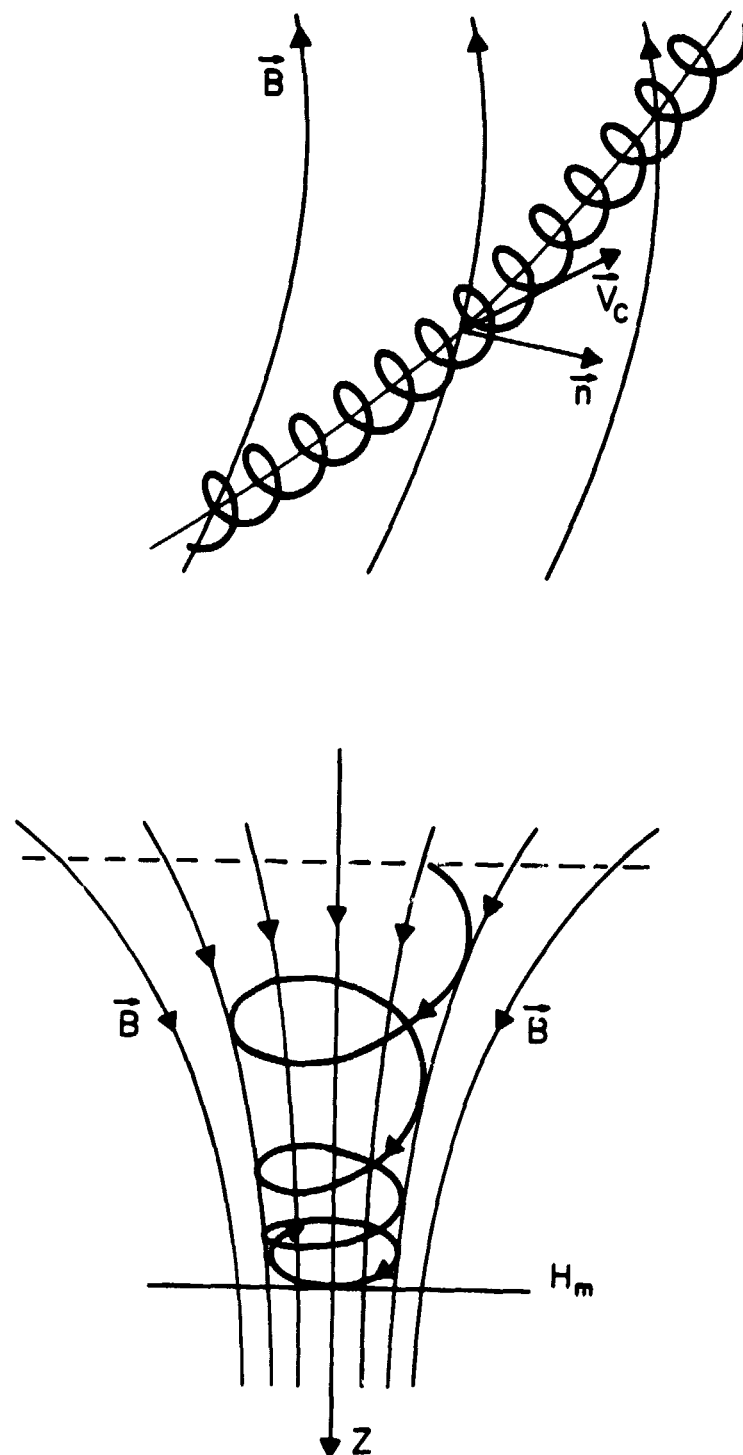
Figure 2.11 The upper figure shows the outward drift of a charged particle
as it traverses in a curved magnetic field. The drift velocity
is denoted by V_c. The lower figure illustrates the principle
of reflection of a charged particle in a converging magnetic
field. This is the reason for why charge particles can be
trapped in the earth's magnetic dipole field.

2.3.4 *Adiabatic invariance in a nonuniform magnetic field.* The magnetic moment, μ, is defined to be the product of a current $(\frac{ev}{2\pi r})$ enclosing an area πr^2 and hence

$$\mu \equiv IA = \frac{1}{2} e \, v \, r$$

where r is given by equation (2.8) so that μ becomes

$$\mu = \frac{mv_\perp^2}{2\,B_o} = \frac{W_\perp}{B_o} \qquad (2.21)$$

where $W_\perp$ is the kinetic energy of the circular particle motion.

Now in a nonuniform magnetic field the force exerted due to the nonuniformity is $\vec{F} = \mu\nabla B$. This force tends to slow down an energetic electron as it moves downward in the earth's converging magnetic field. If the magnetic field gradient is sufficient, the field line force is capable of completely stopping the particle longitudinal motion and return the particle back up the field line as shown in Figure 2.11. Since the earth's magnetic field lines are convergent on both sides of the dipole the particles are trapped in the geomagnetic field by continually being reflected back and forth. More precisely, this reflection point or mirror point occurs at an altitude Z, where $B = B_1$ so that the total change in longitudinal energy is

$$\frac{1}{2} m v_{11}^2 = \int_0^{Z_1} F dZ = \int_0^{Z_1} \mu\frac{2B}{2Z} = \mu(B_1 - B_o)$$

and from equation (2.21)

$$\left(\frac{v_{11}}{v}\right)^2 = \frac{B_1 - B_O}{B_O} \tag{2.22}$$

the pitch angle α is given by equation (2.11) requiring

$$\left(\frac{1}{\tan\alpha}\right)^2 = \frac{B_1 - B_O}{B_O} \tag{2.23}$$

If the pitch angle has a magnitude α_O at $Z = 0$, where $B = B_O$, the mirror point will occur when

$$B_1 = \frac{B_O}{\sin^2\alpha_O} \tag{2.24}$$

The adiabatic invariant can be derived in the following way. Invoking Faraday's Law, the E.M.F. generated in one orbit of a particle is

$$E.M.F. = \frac{\Delta W}{e} = \pi r^2 \left[\frac{\partial B}{\partial t}\right]$$

The time for one revolution is $2\pi r/v$ and if ΔB is the associated change in B as the particle proceeds downward in this time the time derivative is

$$\frac{\partial B}{\partial t} = \frac{v\,\Delta B}{2\pi r}$$

requiring

$$\Delta W = \frac{1}{2}mv^2\frac{\Delta B}{B} = W\left[\frac{\Delta B}{B}\right] \tag{2.25}$$

Differentiating equation (2.21) gives

$$\Delta\mu = \Delta\left(\frac{W}{B}\right) = \frac{\Delta W}{B} - \frac{W}{B^2}\Delta B = 0 \qquad (2.26)$$

and is zero by (2.25).

The adiabatic invariant are obtained by use of equation (2.21)

$$\mu = constant$$

$$P^2/B = constant \qquad (2.27)$$

$$Br^2 = constant$$

2.4 *Particle Spectrum and Pitch Angle Distribution*

The altitude region in which energetic particles ionize the most neutrals is determined by the energy spectrum and by the pitch angle distributions. Figure 2.12 illustrates the sensitivity of the exponent in the exponential spectrum. Also shown is the attenuation profiles for mono-energetic beams of electrons.

The power law and exponential spectrums are plotted in Figure 2.12 for energies from 1 to 10 keV. The energies from 1 to 10 keV are the predominant energies for upper E-region ionization and dramatically show the sensitivity of the exponent factors E_o and X. The spectrums, J, are based on the number of particles with energies greater than the energy E. The power law spectrum is given by

$$J_p(> E) = J_1 E^{-x} \qquad (2.28)$$
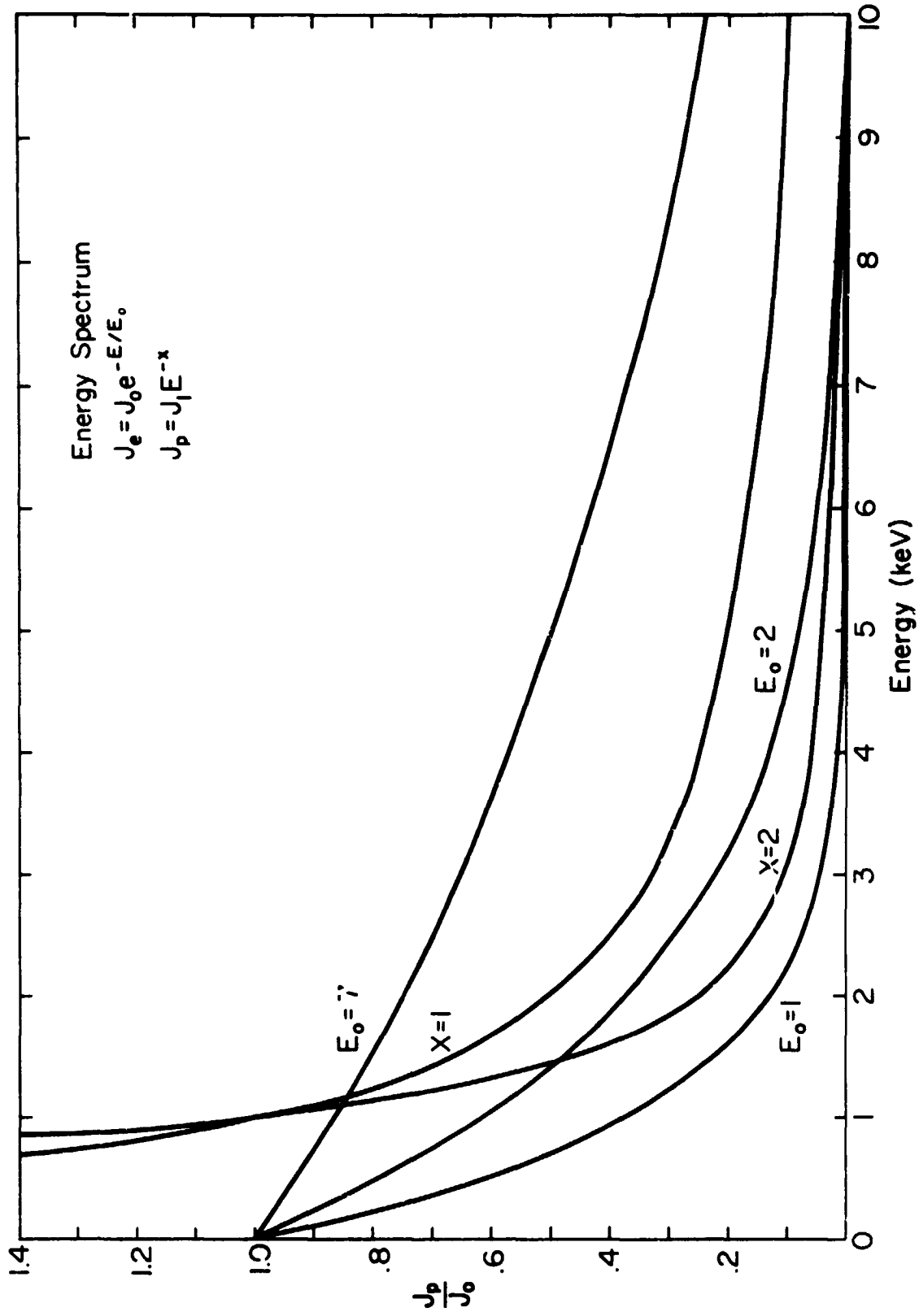
Figure 2.12 Exponential and power law spectrums are dramatically different for energies less than 6 keV. These energies are primary for E-region ionization. The spectrums, c_i, are given for all particles with energies greater than i.

and the exponential spectrum by

$$J_e(> E) = J_o \exp(-E/E_o) \tag{2.29}$$

The E-region particle data have shown power-law spectrums with X usually between 1.5 and 2.5. This supports the fact that particle ionization is nearly the same in the upper portion of the E region (150 to 180 km) as it is in the lower (120 to 150). This is a consequence of the ionization of the upper E region by predominately 1 to 4 keV electrons and the large increase in 1 to 4 keV particles associated with the power law spectrum.

Consideration must also be given to the fact that the particle spectrum can vary with pitch angle and consequently with the altitude. The process of obtaining a spectrum by averaging over a wide pitch angle spread must be justified. The incentive for the exponential spectrum is that it is Maxwellian in nature suggesting internal equilibrium. A plot of the differential number flux divided by the associated energy and plotted against energy will give a straight line for a Maxwellian spectrum.

The particle data show the flux to continually increase with altitude in a linear fashion at midlatitudes for particles with energies of at least 10 to 80 keV. The only viable explanation is that equal energy particles are being reflected at differing altitudes because of the mirroring point variation (equation 2.24). In other words, the pitch angle distribution is such as to cause particles of a particular energy to have a linear variation in mirroring altitude. Since the parallel velocity is zero at the mirror point, equation (2.22) becomes

$$v_o^2 = v_o^2 \frac{B(r,\theta)}{B_o} \qquad (2.30)$$

and since the pitch angle is related to the velocities as $\sin\alpha_o = \frac{v_{\perp o}}{v_o}$ the previous equation is expressed as

$$B(r,\theta) = \frac{B_o}{\sin^2\alpha_o} \qquad (2.31)$$

Now since an equal number of particles are reflected in each height interval over the concerned region, the solution of equation (2.31) for α_o will yield the predicted pitch angle distribution for any trajectory point invoking the earth's magnetic field variation.

2.5 *Ionization Rates Calculated from Flux and Spectrum Information*

The particle ionization rates may be calculated from knowledge of energetic particle flux, spectrum, and pitch angle together with information on the quantum efficiency of neutral constituent interaction. *Rees* [1963], *Berger et al.* [1970], and *Wulff* [1973] have investigated this problem for cases particularly associated with the higher latitude ionosphere. Important differences in particle pitch angle and ionosphere composition at night warrant further investigations.

The techniques developed are modifications of the methods employed by the above. The computer program developed for this calculation is given in Appendix I. Utilizing the method of Wulff, the ionization curves shown in Figure 2.13 were obtained for an isotropic pitch angle distribution. The results illustrate the sharp attenuation of particles with altitude. The curves are significantly altered by different pitch
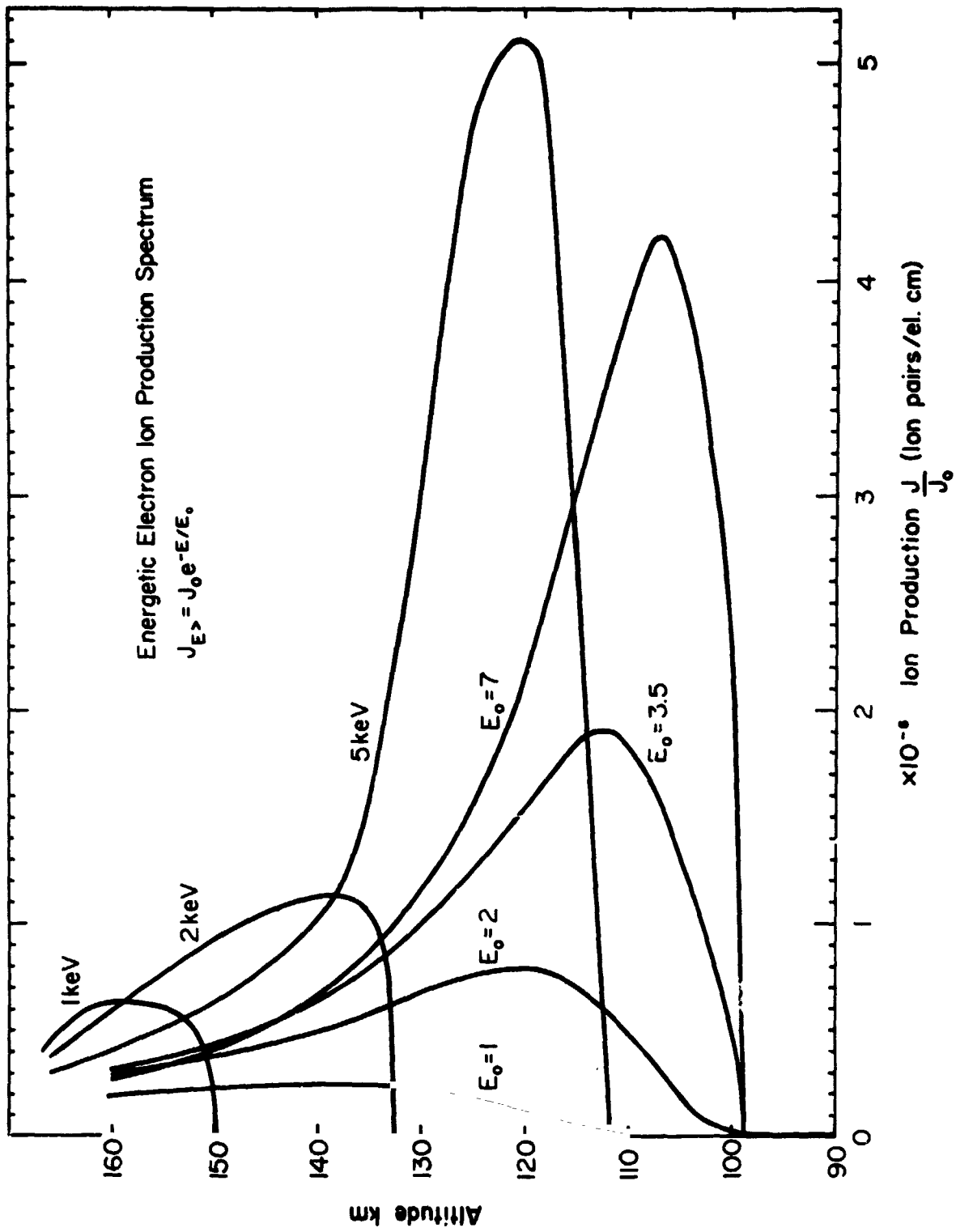
Figure 2.13 Altitude ionization production calculated (Appendix I) for various monoenergetic and exponential spectrums. The pitch angle was assumed to be isothropic.

angle distributions with greater dependence as the energy is decreased. This is exanplified by calculations from *Prasad and Singh* [1972] in which they deduced pitch angle dependence (Figure 2.14) of energetic particles attenuated in the earth's atmosphere.
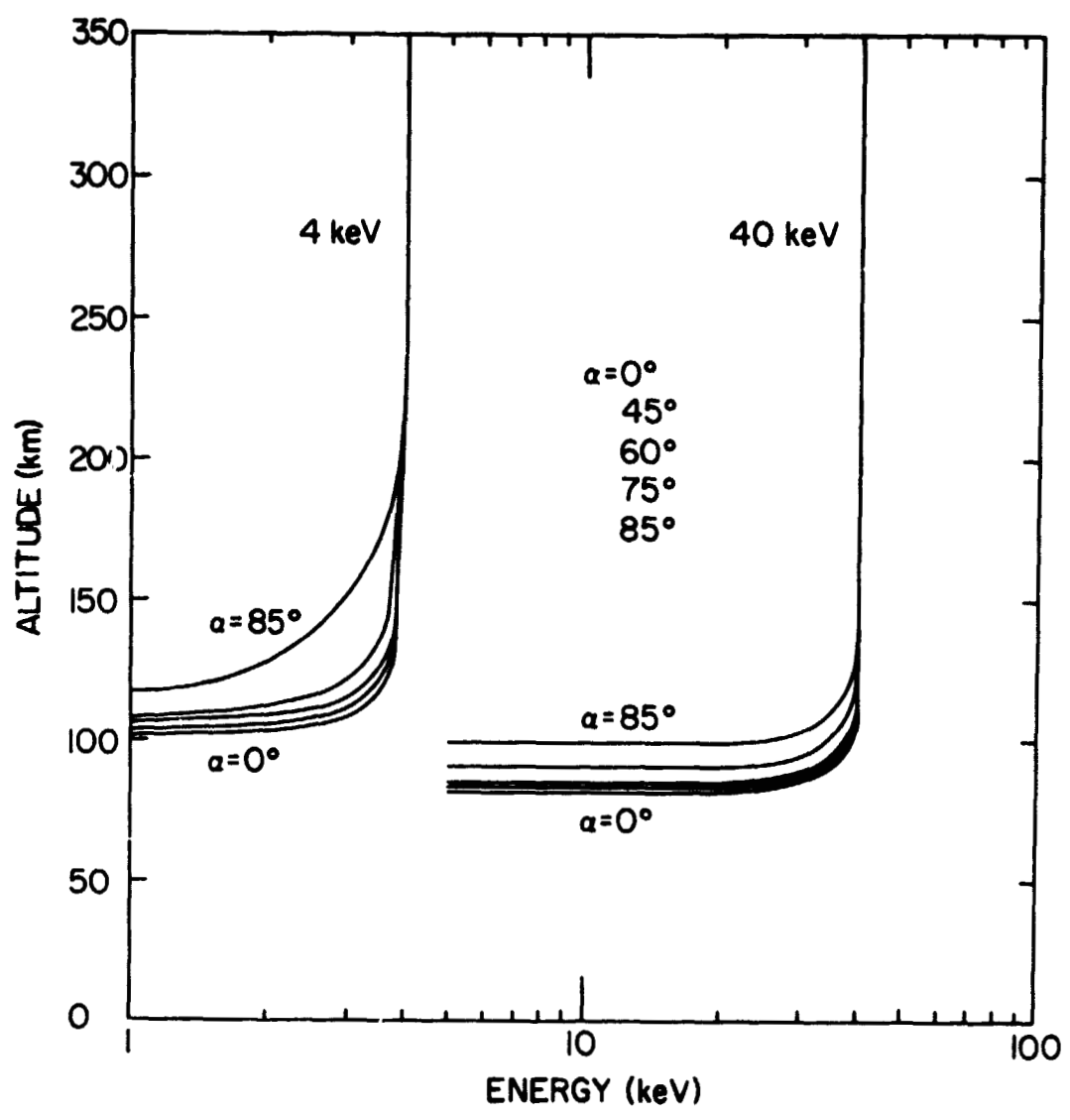
Figure 2.14 Pitch angle variation in ionization curves for monoenergetic electrons of 4 and 40 keV. Data replotted from *Prasad and Singh* [1972].

3. DYNAMICS INVOLVED IN THE FORMATION OF THE
E REGION INTERMEDIATE LAYER

3.1 *Morphology of the Intermediate Layer*

Experimental measurements of electron densities indicate the pre-
sence of a layer in the upper E region near midnight. The layer usually
extends from 120 to 180 km and has a peak near 150 km. The time evolu-
tion of the layer is observed to narrow and descend at approximately
1.5 km min^{-1} until it eventually appears as a morning sporadic-E layer.
Figure 3.1 presents five rocket observation [*Smith*, 1970] made from
Wallops Island (38°N, 75°W; geomagnetic latitude 49°N) which detail this
descent.

Five rocket observations made at midnight (Figure 2.1) of the
intermediate layer, suggest a strong relationship with K_p. The layer,
at low values of K_p, is quite sharply peaked as compared to the almost
uniform profiles at high K_p values.

Geographically, the intermediate layer is observed at middle lati-
tudes. Extensive studies concerning the global characteristics of the
intermediate layer are investigated by *Wakai and Sawada* [1964].

The critical frequency of the intermediate layer increases pole-
wards from latitudes 0° to 50° and decreases thereafter. Additionally,
the critical frequency of the layer has a positive correlation with K_p
[*Berkner and Seaton*, 1949]; [*Watts and Brown*, 1954].

3.2 *Continuity Equation as Applied to Vertical Ion Transports*

3.2.1 *Wind shear theory as utilized to explain the intermediate
layer.* Explanation for the ionization bunching in the vicinity of
150 km must reside in some dynamical forcing function since nighttime
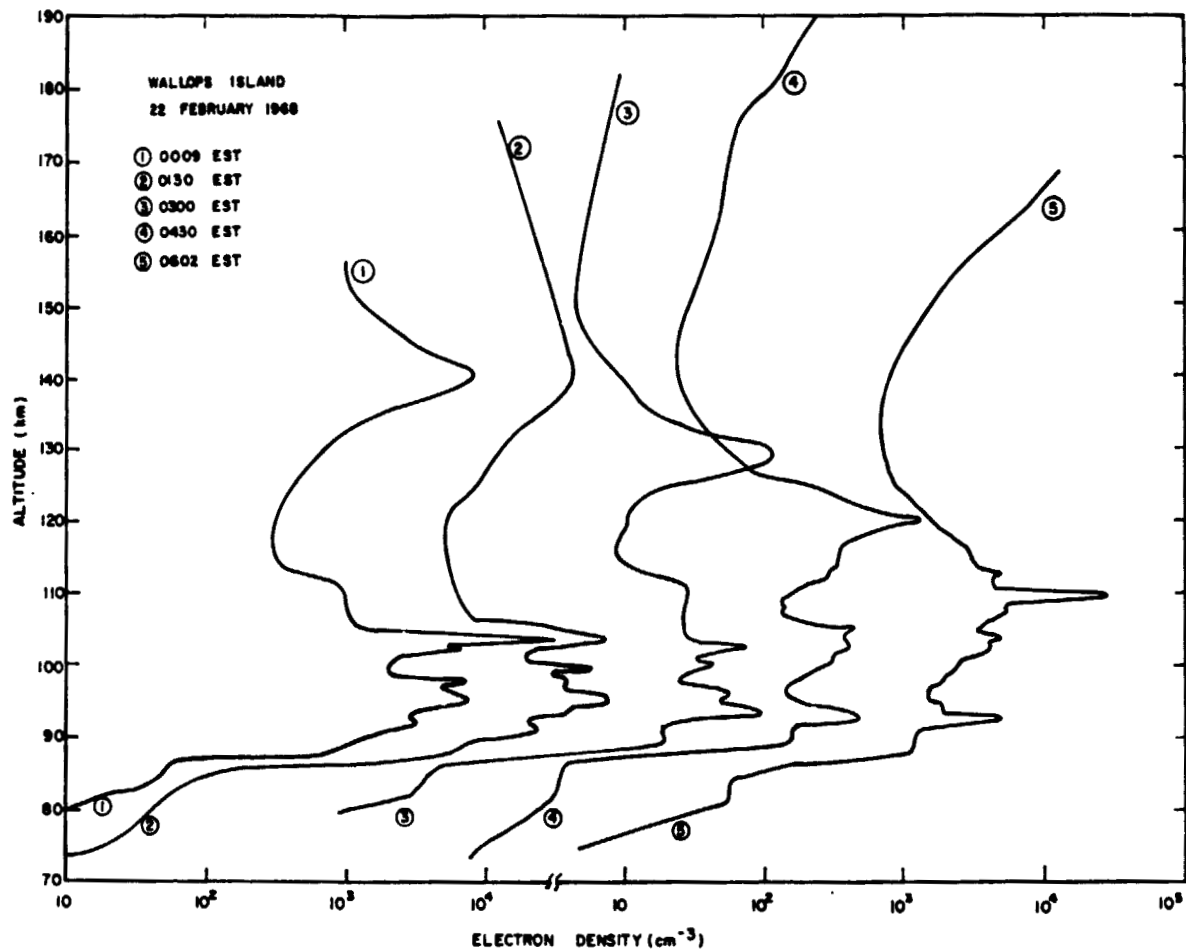
Figure 3.1 Electron-density profiles from the probes on rockets launched
from Wallops Island on 2₂ February 1968, [*Smith*, 1970]. The
profiles are each displaced by one decade. The electron-density
scales for the first and last profiles are given. The part of
the profiles below 90 km should be regarded as indicating the
structure, rather than as absolute values.

production and recombination are believed uniform. Previous investigations suggest that the vertical redistribution of ionization is a consequence of the neutral winds [*Constantinides and Bedinger*, 1971; *Fujitaka et al.*, 1971]. Basically, the predominant horizontal winds flow in opposite directions, one above the other, causing a shear in the vicinity of 150 km. Now, the motion of ionization is subject not only to the force of the wind but also to the magnetic field. The $\vec{V}x\vec{B}$ product gives a net upward flux and downward flux component dependent on the wind direction. For midlatitudes the wind system is such as to cause ionization to migrate towards the neutral wind shear region. Ionization is therefore transported to the peak from a lower and higher region surrounding the peak. An extensive analysis of vertical ion drift velocity from neutral winds is formulated by *MacLeod* [1966]. Electric fields may also contribute to the vertical ion drift velocity; the following analysis is independent of the mechanism producing the vertical ion drift, however.

3.2.2 *Production and recombination.* The source of ionization has been presumed to be solar UV radiation resonantly scattered by the geocorona, principally Lyman-α (1216A), which ionizes nitric oxide [*Swider*, 1965] and Lyman-β (1026Å), which ionizes molecular oxygen [*Ogawa and Tohmatsu*, 1966]. These UV sources are believed to be of secondary importance as compared to that of energetic electrons for the reasons enunciated in Chapter 2. Also, it has been found [*Meier*, 1974] that radiation is at a minimum near midnight.

The altitude variation of production for input into the continuity equation was initially taken to be constant. This was based on the

material presented in Section 2.4. Here ionization rates were deduced for the peak to upper node and for the peak to lower node from the intermediate layer electron-density profile and appropriate recombination coefficient. The justification for using a constant production rate over the concerned altitude is the result of the close agreement between upper and lower ionization rates. Further refinements will take into account variable production as data becomes available. The developed program for solving the continuity equation is compatible for such variations.

The recombination coefficient is calculated based on the particular ions present and their temperature. At night, in the altitude range of interest, the principal ion is NO^+ [*Holmes et al.*, 1965]. The loss process is presumed to be dissociative recombination of NO^+; the coefficient (α) being given by *Biondi* [1969] to be

$$\alpha = 4.5 \times 10^{-7} \ (300/T_e) \ cm^3 \ sec^{-1} \qquad (3.1)$$

The electron temperature (T_e) above 120 km, however, varies with geomagnetic activity. For purposes of calculation the data from *Evans* [1973] at Millstone Hill are employed such that the nighttime (2100-0300 EST) electron temperature at 200 km can be well represented by $(112K_p + 588)°K$ for eight occasions in 1966 and 1967 with a range of values of K_p of 1- to 5-. The correlation coefficient is 0.90. Following Evans the electron temperature at 120 km is assumed to be $T_e = 355°K$. A linear interpolation for altitudes between 120 and 200 kilometers gives

$$T_e(z) = (z-120) \times (1.40 \ K_p + 2.91) + 355°K \qquad (3.2)$$

Using Biondi's formula for α and allowing the extrapolation of electron temperature to $K_p = 8$ the recombination rate is obtained as a function of altitude and geomagnetic index.

3.2.3 *Solution to the continuity equation and sensitivity analysis.* The continuity equation for electron density is fundamental to an understanding of ionospheric variations. The basic conservation principle gives the temporal change in electron density at each height as

$$\frac{\partial N_e}{\partial t} = Q - L - \text{div}(v_e N_e) \qquad (3.3)$$

where the three right-hand terms represent the ionization production rate, the ionization loss rate, and the effect of transport, respectively. The transport term is made up of movements such as diffusion, electromagnetic drifts, and thermal expansions.

For the steady-state case with no transport *Ratcliffe* [1956] has formulated the loss term to be

$$L = LN_e^2 = \frac{[X]}{N_e + (\frac{\lambda}{\alpha}) \ [X]} N_e^2 \qquad (3.4)$$

where α and λ are, respectively, the rate coefficients of dissociative recombination and ion-atom interchange reactions. The brackets denote the number density of species X. The associated $[X]$, α, λ, and N_e for the E region is such that $N_e \ll \lambda[X]$ for the involved reactions. The recombination term is consequently of the form αN^2.

The divergence term is responsive to the flux motion. Of particular interest is the flux motion due to a forcing function giving the electrons a velocity $\vec{V}$ and the motion resultant of the gradient concentration, (diffusion). The diffusion flux term from elementary deduction is given as

$$\Phi = \vec{V}N = D\vec{\nabla}N \tag{3.5}$$

The general time dependent continuity equation for electrons in the E region, therefore, is given by

$$\frac{\partial N}{\partial t} + \vec{\nabla} \cdot (\vec{V}N) = q - \alpha N^2 + \vec{\nabla} \cdot D\vec{\nabla}N \tag{3.6}$$

This equation is simplified by omitting the term $\frac{dN}{dt}$ (since observations suggest the time variance to be small) along with the terms arising from the horizontal part of the gradient operator. Permitting w to be the vertical ion drift velocity, and z the altitude, equation (3.6) reduces to

$$\frac{\partial}{\partial z}(wN) = q - \alpha N^2 + \frac{\partial}{\partial z}\left(D\frac{\partial N}{\partial z}\right) \tag{3.7}$$

For the case of interest, the ion wind system as presented in Section 3.2.1 is convergent towards the intermediate layer peak. To ascertain the behavior of equation (3.7) a sinusoidal wind approximation is made. The actual winds measured, in fact, are in quite good agreement with this approximation. Of course, many such sinewave

solutions could be solved for and added in a Fourier series for general behavior. The wind system, therefore, representative of the intermediate E layer is taken to be

$$w = 20 \sin[\pi(150-z)/30] \text{ m s}^{-1} \qquad (3.8)$$

Here, the amplitude is taken as 20 m sec^{-1} with the layer peak at 150 km and upper and lower valleys at 120 and 180 kilometers, respectively.

Appendix II describes the solution of this equation for the case $D = 0$ with the assumed sinusoidal vertical ion drift. Due to the numerical sensitivity of this equation towards instability a precision predictor-corrector Euler-Romberg method was used for analysis. Additionally, a complicated analytic series solution was derived for the $D = 0$ case. The no-diffusion continuity equation may be transformed as the Riccati equation. Using various substitutions, a second order linear differential equation is obtained. Transformation again results in a form applicable to the WKB method of solution.

To solve the variable diffusion continuity equation (Appendix III) a Runge-Kutta method was applied with 0.2 km steps. Further, since the initial conditions cannot be specified at one point, as required by this iterative scheme, a convergence procedure is required. The two known boundary conditions of the second order equation are zero slope (zero flux) at the peak and valleys of the profile. Thus, by starting at the peak of the profile and assuming a typical electron density (i.e. a value between the $D = 0$ value and the photoequilibrium value) a

convergence towards the actual point will occur, if one monitors the final slope of the valley and corrects accordingly.

Solutions with and without diffusion are shown in Figure 3.2 for five values of Q. The thick profiles represent a diffusion coefficient, D, of 1 x 10^8 and the dotted profiles for D = 0, the results clearly indicate that diffusion is significant for low production rates. Results illustrate that the modeled nighttime intermediate layer is in close agreement with observation (Figure 2.1) and is therefore a plausible explanation.

Profile 1 (Q = 0.4 cm^{-3} s^{-1}) gives results looking quite similar to the intermediate layer at midnight under quiet conditions. As the ionization rate increases (eg. K_p increases according to Figure 2.2) the peak broadens and becomes less pronounced. Figure 3.3 illustrates the intermediate layer dependence on K_p using the relation developed in equation (2.4). The peak of the layer is similarly related to K_p as illustrated in Figure 3.4 for diffusion coefficient. of 0, 0.5 x 10^{-7} and 10^{-7} cm^2 sec.

The sensitivity of equation (3.7) to vertical ion wind variations in amplitude is illustrated in Figure 3.5. The computations are carried out for values of amplitude, A, of 0, 10, 20, and 50 m sec^{-1}. Much ionization redistribution is seen to occur at relative low values of the ionization drift velocity. However, this redistribution does not affect the electron-density profile in a proportional manner. For example, doubling A from 10 to 20 is seen to increase the peak value of electron density from about 5.1 x 10^3 cm^{-3} to 7.5 x 10^3 cm^3, an increase of about 50%, while increasing A from 20 to 50 gives an increase of only 20%.
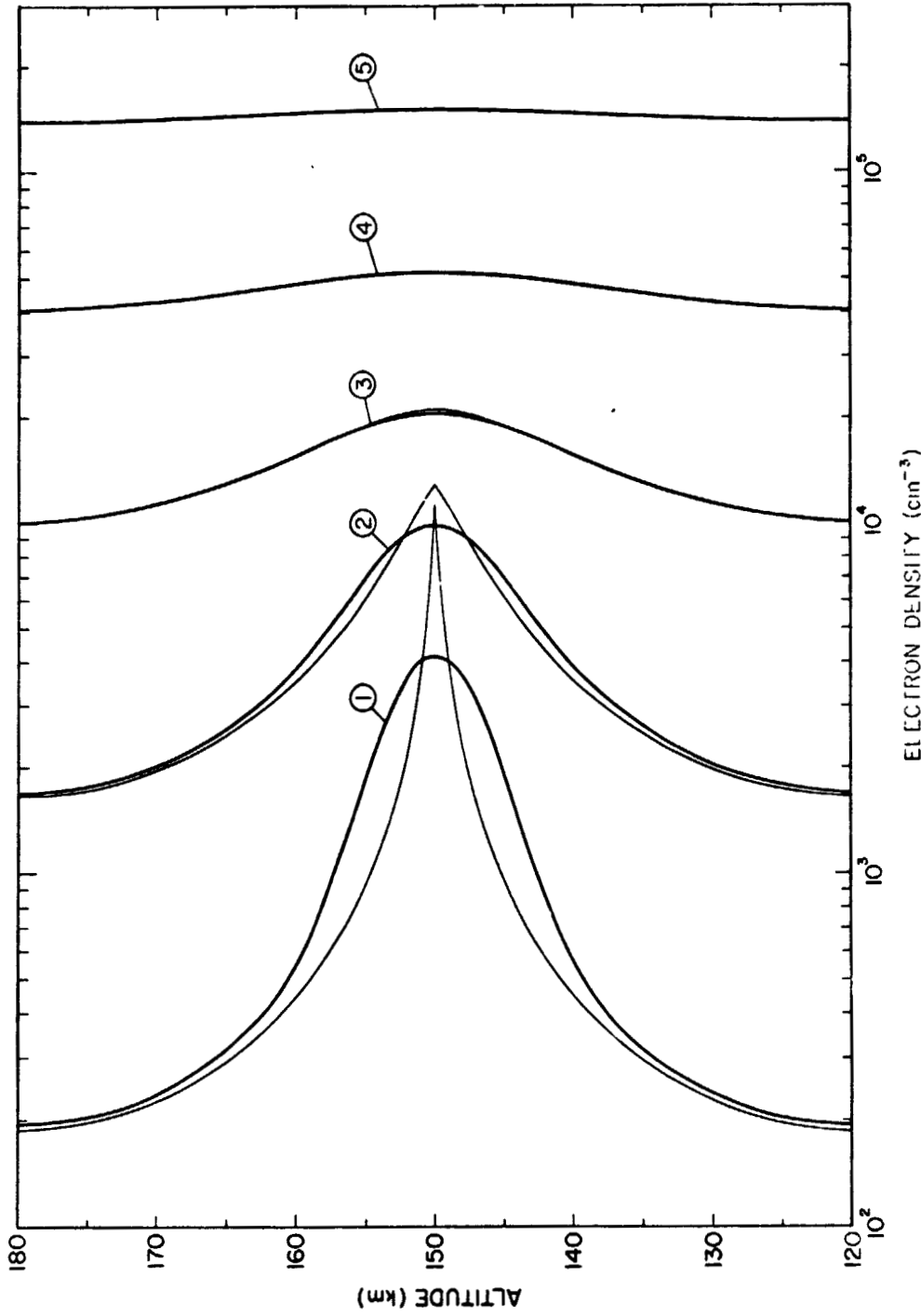
Figure 3.2 Simulations of the intermediate layer with the vertical ion drift given by $w = 20 \sin[\pi(150-z)/30]$ msec^{-1} for altitude z in km, with the recombination coefficient 1.9×10^{-7} cm^3 sec^{-1}, for production rates of (1) 0.4, (2) 4.0, (3) 40, and (4) 4000 cm^{-3} sec^{-1}. The thin line is the solution neglecting diffusion; the thick line is the complete solution with a diffusion coefficient of 2.10^8 cm^2 sec^{-1}.
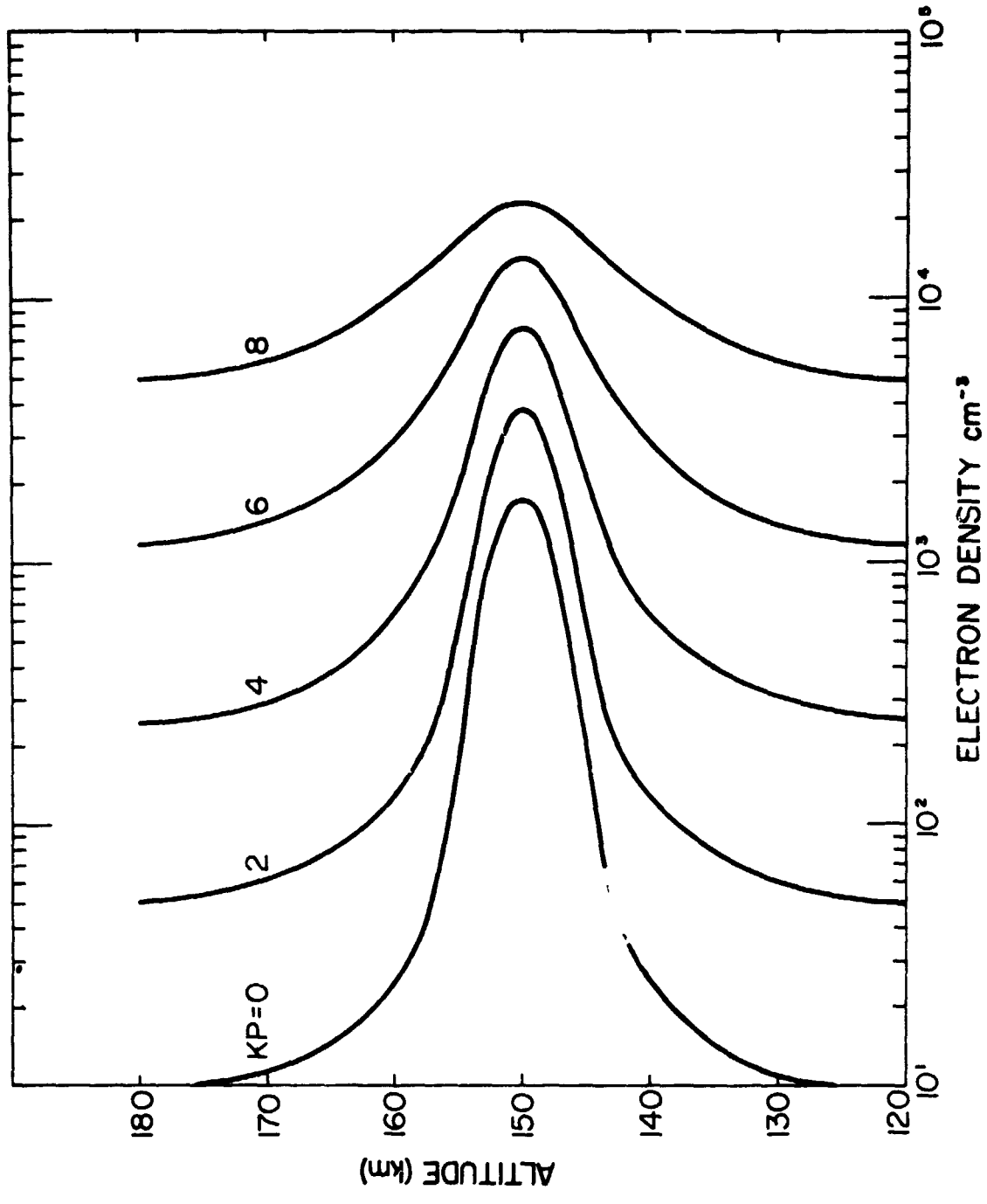
Figure 3.3 Calculated intermediate layer for ionization rates deduced from K_p invoking equation (2.4).
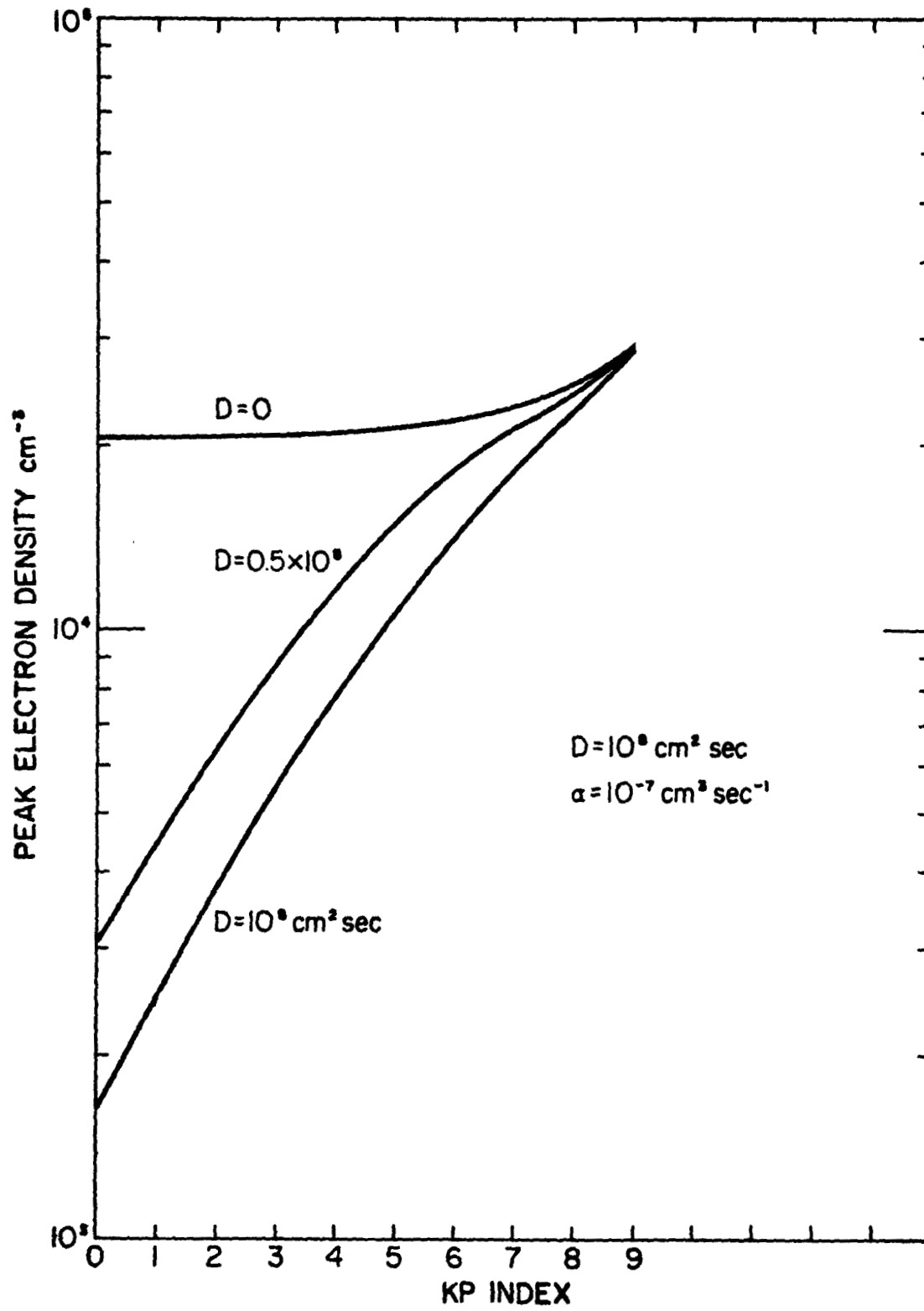
Figure 3.4 Variation in the peak electron density of the intermediate
layer for various K_p values.
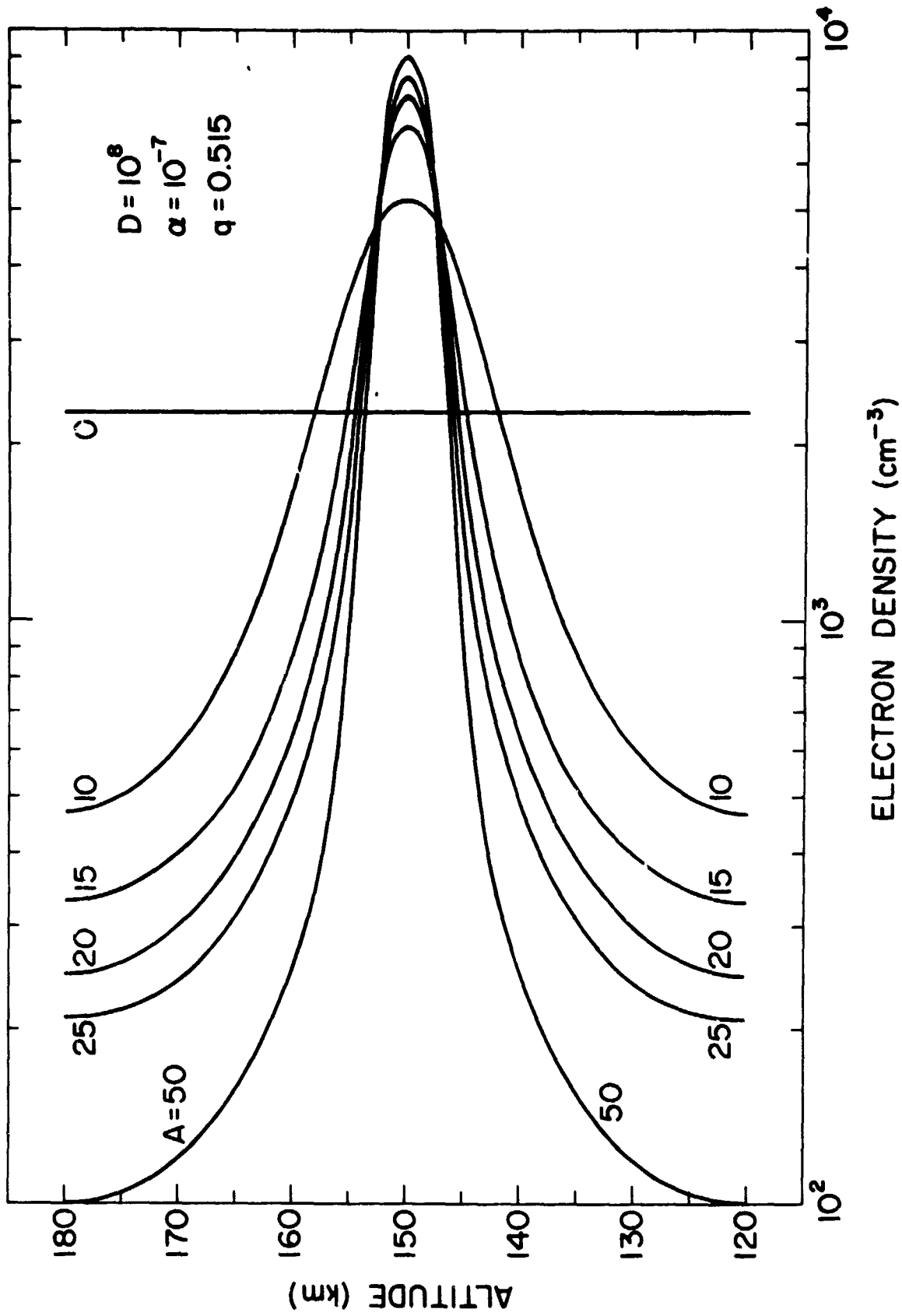
Figure 3.5 Sensitivity of the continuity equation (3.7) to vertical ion wind variations in amplitude.

3.3 *Winds Derived from Electron-Density Profiles*

The electron-density profiles of the intermediate E-region layer may be used to deduce information of ion and therefore neutral winds. For this purpose the continuity equation is employed using the deduced ionization rates calculated for the upper and lower part of layer (equation 2.3). Referring to the continuity equation (3.7) and taking the lower integration limit z_1 to be the altitude where $w = \frac{dN}{dz} = 0$ and rearranging, becomes

$$w(z) = \frac{1}{N(z)} \int_{z_1}^{z} (q - \alpha N^2)dz + D \left(\frac{dN}{dz}\right)_z \qquad (3.9)$$

where q is evaluated as in Section 2.1. This expression gives the vertical ion wind velocity in a readily available form as a function of production, recombination, diffusion, and electron density. The program used to calculate the average ionization rate, $\bar{q}$, and the vertical ion wind is presented in Appendix IV. The program requires electron densities every 0.5 kilometers. The recombination (Section 3.2.2) and diffusion coefficient are taken to be variable.

3.3.1 *Winds calculated for various disturbed conditions.* Solving equation (3.9) for the intermediate layers (Figure 2.1) measured during K_p values of 0+, 1, 2+, and 3+ yields the associated wind patterns of Figure 3.6. The sinusoidal wind pattern is apparent. No strong correlations exist; however, some justification can be made for a positive correlation of the wind root-mean-squared-amplitude verses K_p. No reasonable hypothesis for this dependence is evident.
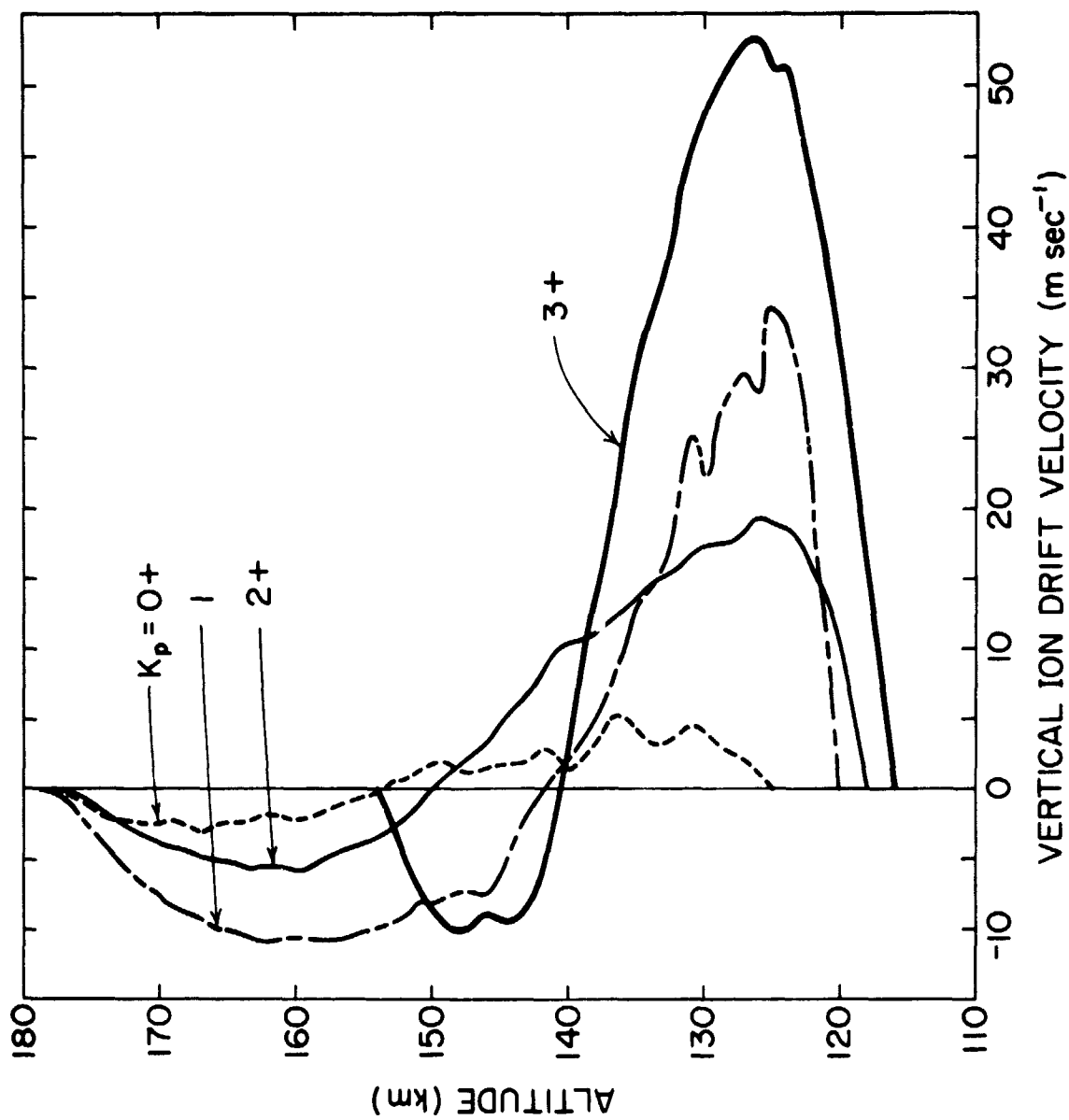
Figure 3.6 Vertical ion wind velocity calculated from electron-density profiles for K_p values of 0+, 1, 2+ and 3+.

The lower amplitude deduced for the upper ion wind has not been fully evaluated. Assuming the approximations made are indicative of this region, the straightforward conclusion is made that the velocity of the upper wind system is slower than the lower. A high correlation exists between the ratio of the upper and lower amplitudes.

The profile for K_p = 8 is not shown because of the large amplitude variation. During high values of K_p, the ionization rate is not believed to be uniform as for lower values. Consequently, erratic behavior is apparent in the electron-density profile for this case. The further incentive for not including large wind amplitudes is due to their inherent lower sensitivity to electron-density profiles as indicated in Section 3.2.3.

3.3.2 *Winds calculated from a nighttime series of profiles.* On February 22, 1968, five rockets were launched at 1.5 hour intervals beginning at 0009 EST. The electron-density results (Figure 3.1) clearly show the intermediate layer descending at approximately 1.5 km per minute. The winds derived from these profiles are shown in Figure 3.7. The assymetry of the ion wind profiles changes immediately as the layer begins to descend suggesting that the relative wind velocity reverses.

The descending layer can be associated with a tidal wind fluctuation. The apparent vertical wavelength (about 50 km) and nodel descent rate imply a wave period of about 14 hours. This is not too different from the parameters of the (2,4)-mode of the solar semidiurnal tides, the vertical wavelength being around 50 km and the period being 12 hours. This conclusion has likewise been reached by *Fujitaka and Tohmatsu* [1973]. A
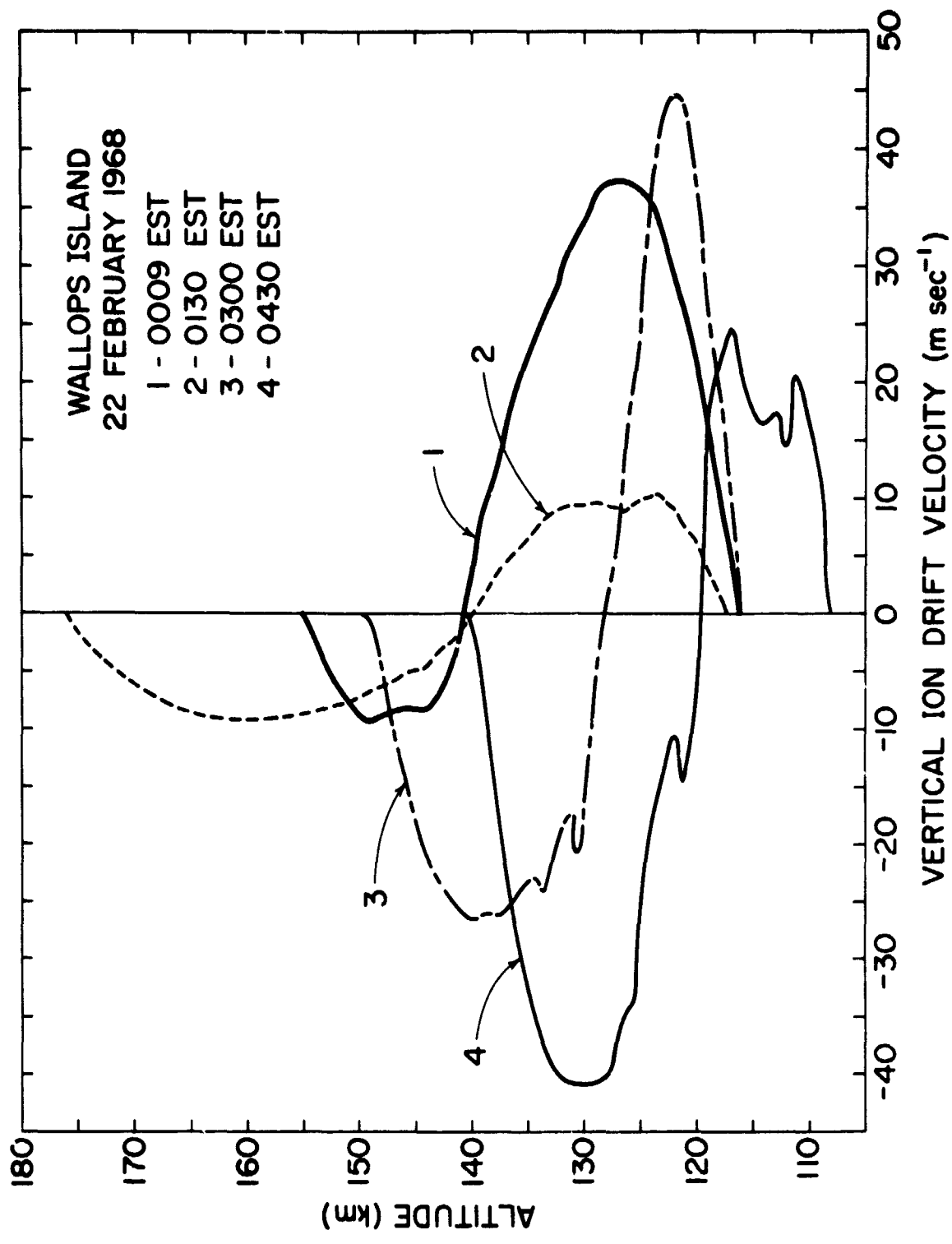
Figure 3.7 Vertical ion wind velocity calculated from electron-density profiles for K_p values of 0+, 1, 2+ and 3+.

theoretical prediction of an enhanced (2,4)-solar semidiurnal tide above 100 km has been put forth by *Lindzen and Hong* [1974].

The erratic behavior of the K_p = 8 electron-density profile and the 0602 early morning profile are used to derive the wind system shown in Figures 3.8 and 3.9. Both profiles are substantially outside of the limits of the original assumptions requiring that further justification be made. The erratic behavior of the K_p = 8 profile leads to the erratic derived wind system of Figure 3.8 if a dynamical explanation of wind shears is assumed. Irregular ionization is also a possible candidate due to erratic spectrum and pitch angle variations. The low (0602) profile needs to be re-evaluated for the appropriate recombinations coefficients associated with the lower E region. The rapid shear illustrated in the figure suggests an unnatural wind system and therefore additional forcing functions (i.e. electric fields) must be likewise investigated.
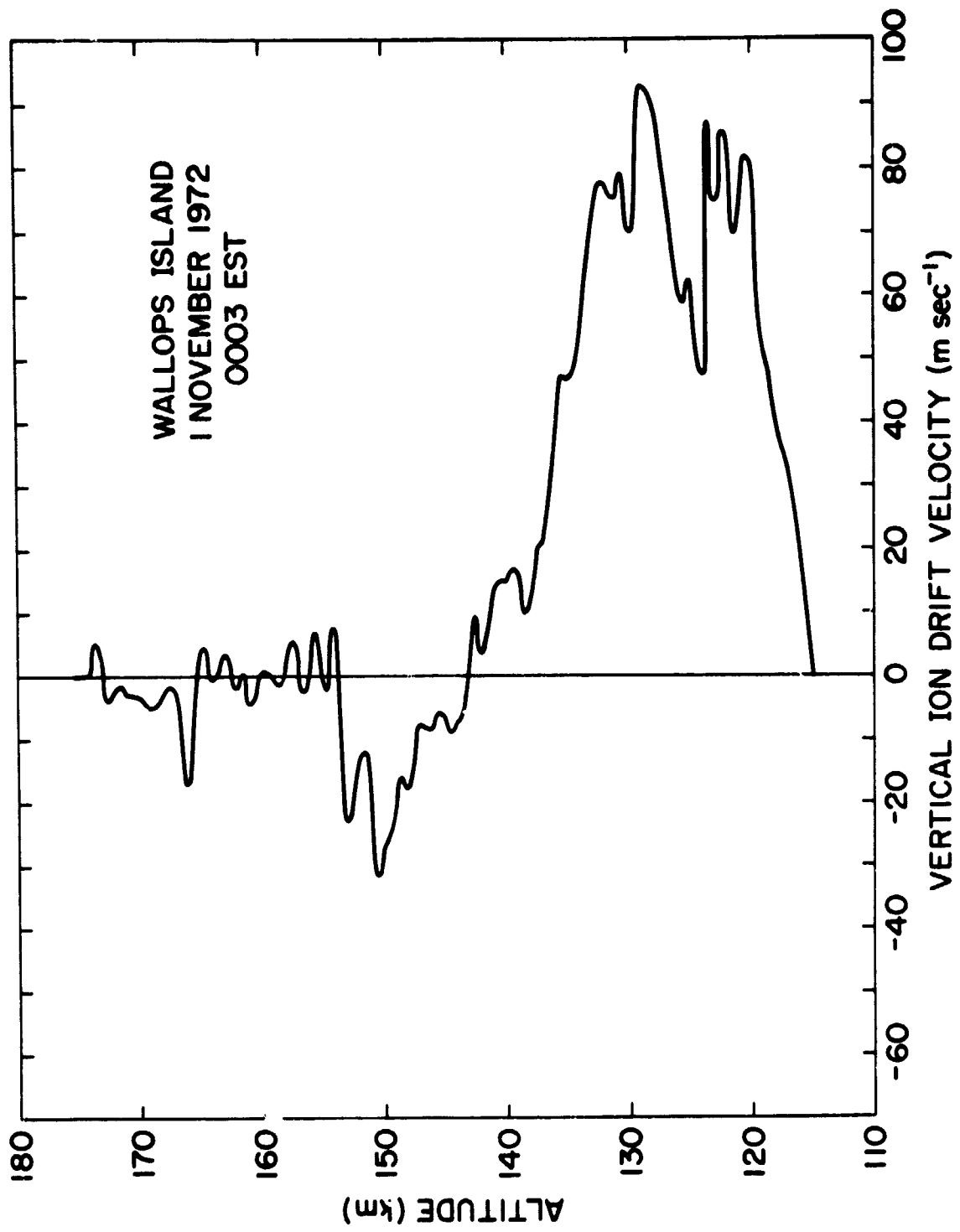
Figure 3.8   Anomalous vertical ion wind velocity calculated from a $K_p = 8$ electron-density profile.
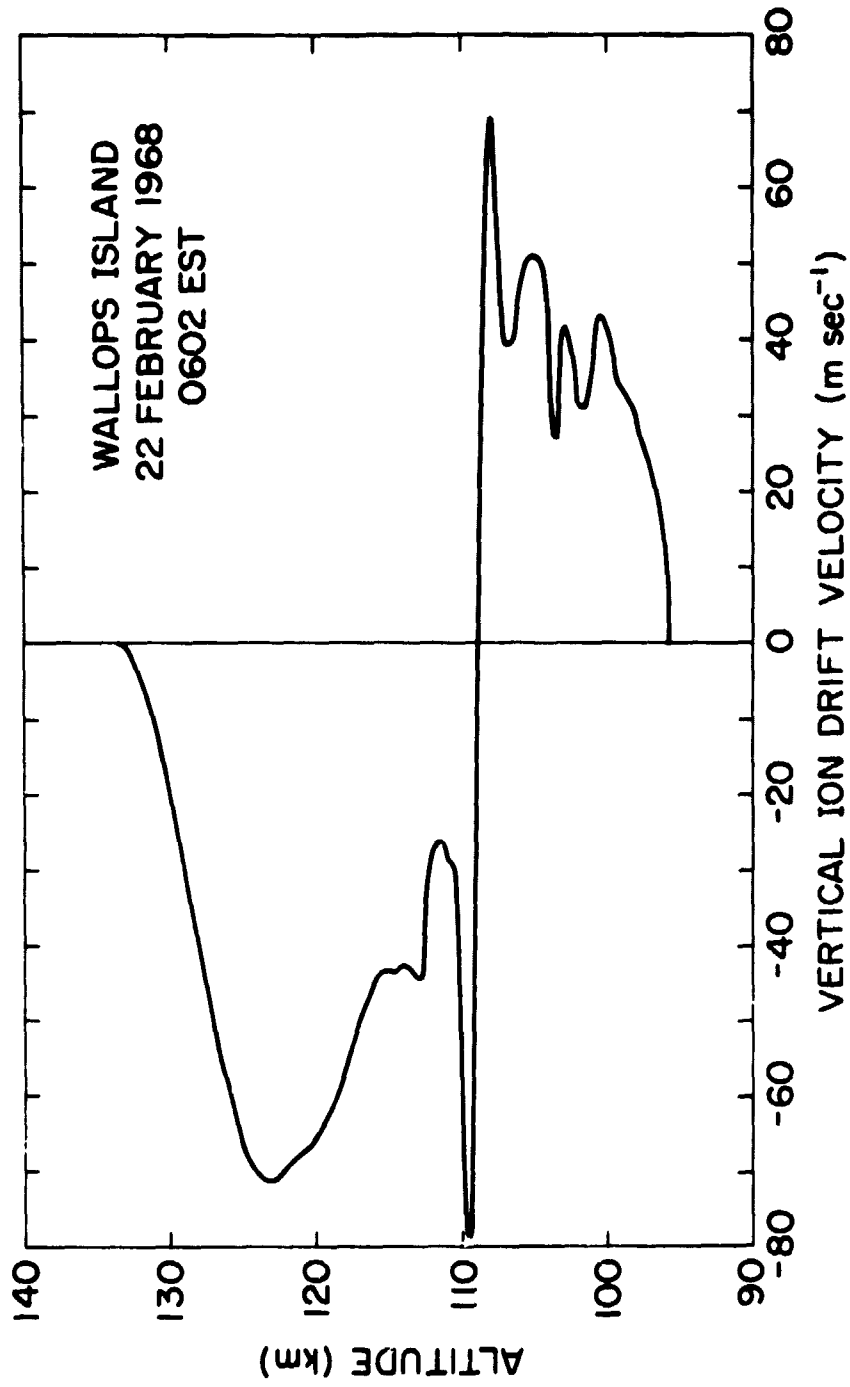
Figure 3.9 Anomalous vertical ion wind velocity calculated from an early morning (0602 EST) measurement.

4. THEORY OF SOLID-STATE PARTICLE DETECTORS

4.1 *Quantitative Theoretical Consideration*

Energetic charged particles propagating within a solid lose their kinetic energy through lattice interactions. These interactions may be approximately thought of as similar to ionization of a gas in a Geiger counter except that the gas is in a condensed form, a solid. In a gas, the decaying energetic particle produces electron-ion pairs which are subsequently swept out by an electric field. Accordingly, they increase their energy, yield multiplying secondaries, and together contribute to a current pulse.

The correct treatment for a crystal lattice, since there are interaction fields, is to formulate a many-body wave-function of the Hartree-Fock type, and then to apply an energetic particle wave as a perturbation in the Quantum Mechanical description. For interactions which are associated with particle detection it suffices that the "condensed gas" model applies utilizing Fermi-Dirac statistics. Here, the allowed energy states (called an energy band for a series of adjacent states) depend on the nature and spatial configuration of the molecules. The probability that a particular energy state (level) will be filled is given by the Fermi equation and is a function of energy, temperature, and impurity concentration. For a semiconductor crystal the energy states (from the Hartree-Fock equation) fall into two primary bands (valence and conduction) separated by a forbidden energy band gap. Energetic particles, impinging on the detector, supply energy to the lattice electrons lifting them from the nonmobile filled valence bands into the essentially empty conduction band.

Applying a gradient potential within the material, an electron-hole current is established. The hole current is the name for the process of sequential exchange of valence electrons between adjacent lattice sites.

The energy lost in ion-electron pair formation in a gas is approximately 35 eV whereas for silicon and germanium hole-electron formation is 3.5 eV and 2.9 eV, respectively. The actual band gaps for silicon and germanium are 1.1 eV and 0.67 eV. The differential energy discrepancy between the band gap and average pair generation energy is reconciled by coupling of electrons into lattice vibrations. This is analogous to the pair production within a gas where surplus energy is taken up in excitation and dissociation processes.

Various other crystalline solids have been used successfully. Diamond and cadmium sulfide have bee· used at room temperatures while halides of silver and thallium are suitable at low temperatures where their ionic conductivity is minimal. Typical charge separation energy for these solid dielectrics is 10 eV. Material impurities contribute to nonuniform collection of electron-holes pairs and, consequently, limit the use of solid dielectrics. This inhomogeneity is called "trapping" since the electrons or holes may be attached to high charge (polarization) centers. Semiconductors are less sensitive to "trapping" because electrons and holes have longer lifetimes and greater mobilities.

4.2 *Comparison of Particle Detectors*

4.2.1 *Advantages and disadvantages of a solid-state detector.* The principle advantages of solid-state particle detectors over gaseous devices are summarized as follows:

(a) Better statistics and resolution result since many more charge carriers are released for a particular incident energetic particle.

(b) Very short deadtimes on the order of a few nanoseconds are possible because of the small collection distances and large carrier mobilities. The collected charge is independent of the location of the ionization event.

(c) Increased experimental certainty is possible. Problems associated with the gas purity and time stability are eliminated as negligible contributions.

(d) Detectors are rugged, compact, and suited for easy mounting.

(e) Lower bias (about 100 volts); requires no elaborate corona-breakdown shielding precautions.

(f) Better control is possible of detector sensitive depth, area and geometry.

(g) Lower energy particles can be detected. Furthermore, the separation charge energy is independent of the incident particle type (electrons, protons, α particles, and heavier ions) which results in a linear function of initial energy.

(h) High stopping efficiencies of particles within a small region are possible. The total absorption peak efficiency is approximately 0.7 times the geometrical efficiency.

A solid-state detector suitable for rocket payload applications is shown in Figure 4.1. Two primary problems with solid-state detectors are channeling of energetic particles between crystal planes, and the relatively weak signals requiring extremely sensitive electronics.
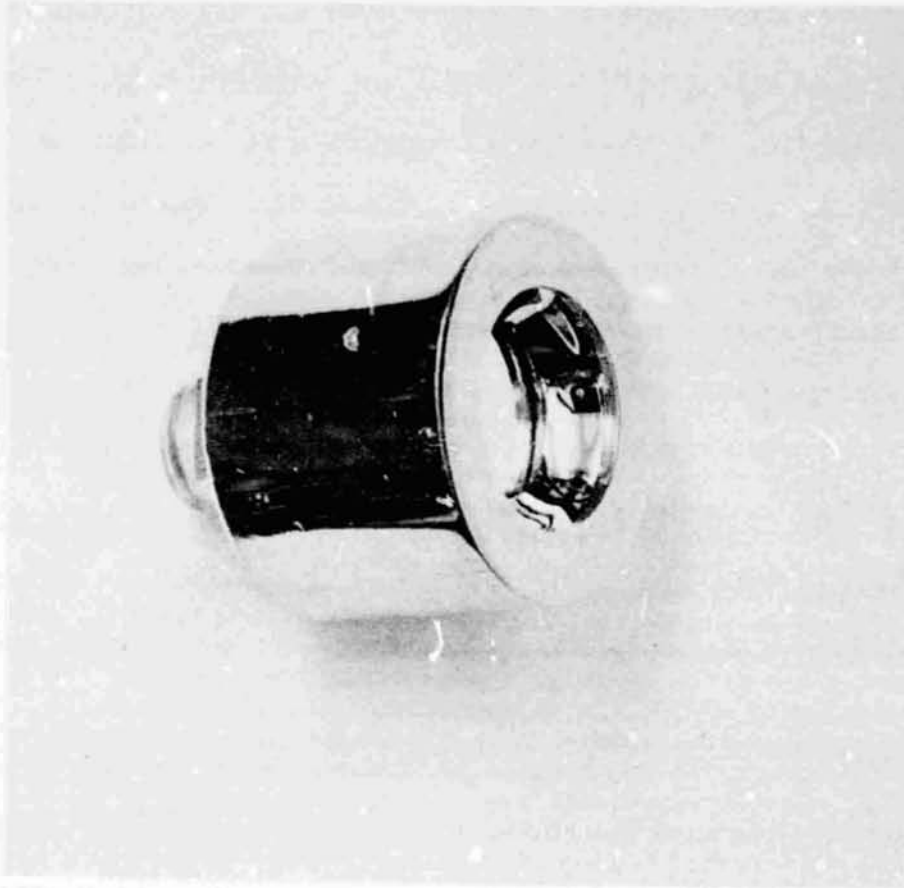
Figure 4.1 Ortec ruggedized surface barrier detector. The sensitive area is 50 mm^2, depletion depth of 100 μm operating at a reversed bias of 120 volts and a noise width of 6 keV at 25°C. The flat, mirror, surface on the right is the sensitive material.

These factors are discussed in later sections. The energy range of the solid-state detector is compared in Figure 4.2 with other detection schemes. Some characteristics of the other principal rocket-borne particle detectors are summarized below.

4.2.2 *Channeltron particle detectors.* The channel multiplier is the most attractive instrument for overall low energy coverage as indicated in Figure 4.2. The geometrical construction of the linear and helix channel multiplier are displayed in Figure 4.3. Figure 4.4.shows a curved channeltron interfaced to an electric-field scanning energy analyzer (black section) and collimator. Operationally, energetic particles impinging upon the inside surface of the channeltron tube opening collide with the resistive wall creating secondaries which are subsequently made to accelerate axially along the tube by an applied electric field. Further multiplication arises as the accelerated secondaries collide with the walls initiating tertiaries, etc. Typical gains are of 10^9 in linear and 10^8 in curved channeltrons.

Complications in the application of channel multipliers are 1) the gain is pressure sensitive due to the ionization of the neutral residual gas (ionic feedback), 2) necessity to vacuum seal the tube to prevent outgassing, 3) high voltages required to induce the electric field, and 4) early saturation begins at 10^5 pps because of field distortion and space charge effects. The chief reason for implementing a curved or spiral channeltron is to reduce ionic feedback. Further reference can be made to the following publications by *Adams and Manley* [1966], *Reed et al.* [1969], and *Sacerlotzky and Belanger* [1972].

PARTICLE DETECTOR ENERGY COMPARISON

ENERGY (Kev)

10^{-2} 10^{-1} 1 10 10^2 10^3 10^4 10^5

ELECTRONS

Geiger

Ionization Chamber

Scintillator

Channeltron

Cooled Type III Semiconductor

Cooled Type I or II Semiconductor

Semiconductor Type I or II

PROTONS

Semiconductor Type I or II

Cooled Type I or II Semiconductor

Cooled Type III Semiconductor

Channeltron

Scintillator

Ionization Chamber

Geiger
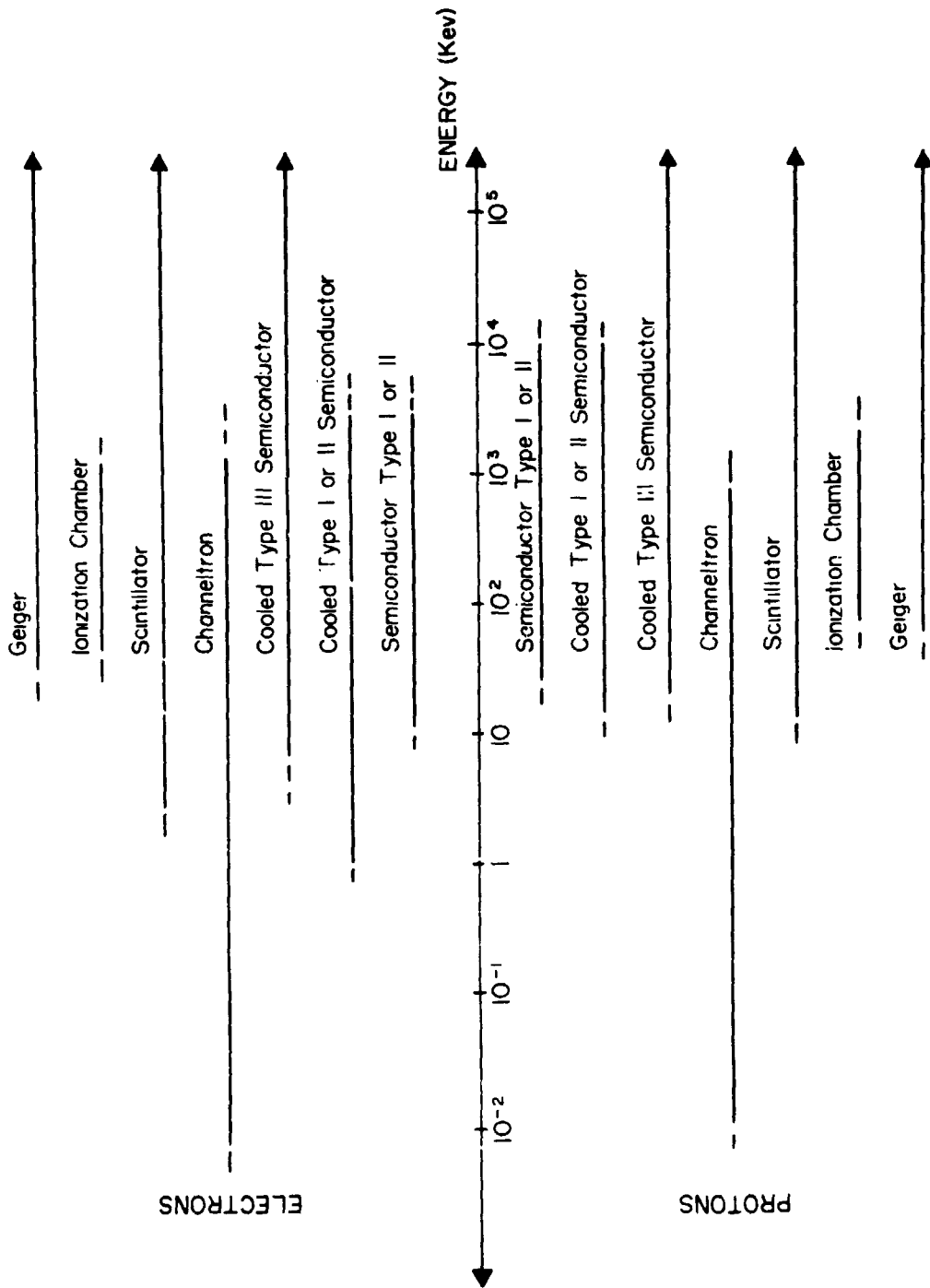
Figure 4.2   Sensitive energy range for various rocket-borne particle detection schemes. The energy comparison is made for electrons in the top half and for protons in the lower half.
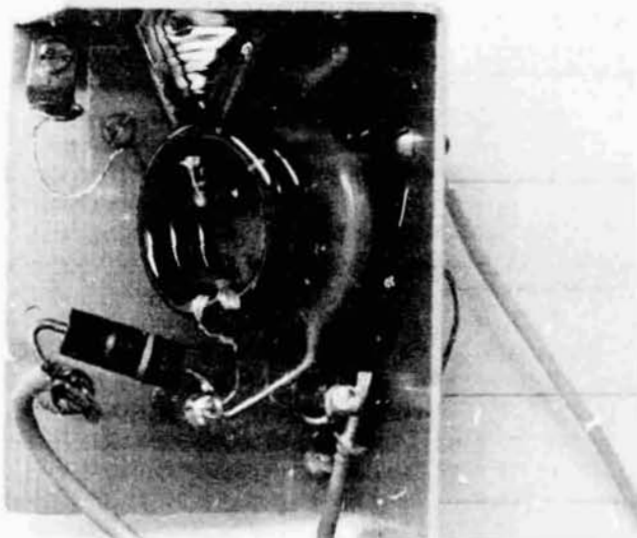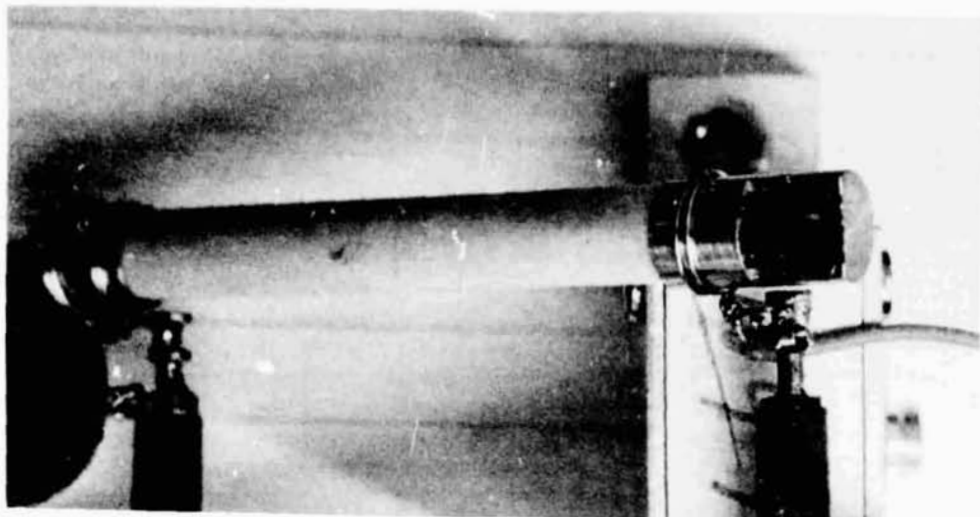
Figure 4.3 The linear channeltron in the top photo was used for cali-
bration of the solid-state detector discussed in Chapter 6.
Particles passing through the grid collide with the walls
and experience an applied axial electric field causing fur-
ther collisions and multiplication. The bottom photo illus-
trates a rocket-borne helical channeltron used to reduce
pressure sensitivity and overall dimension. The horizontal
lines are 0.86 cm apart.
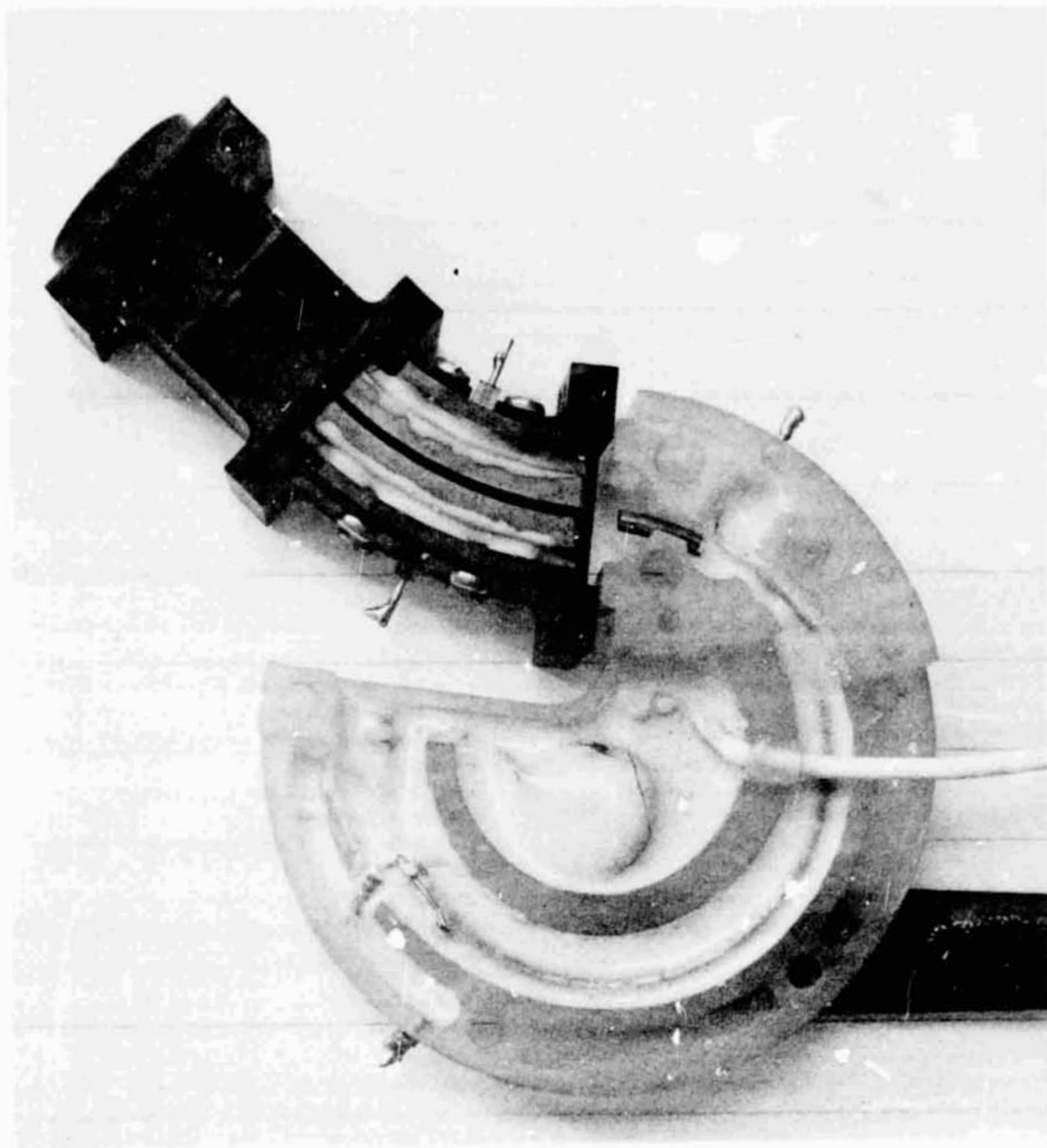
Figure 4.4   The curved channeltron, coated in epoxy, is attached to an
electric field scanning electrode used for spectrum determina-
tion. The entrance and collimator section procede the electric
field analyzer and provide the proper particle angular pattern.
Properly calibrated and used in conjunction with a so.i.-state
detector, complete, accurate and high resolution particle cover-
age is obtained.

4.2.3 *Scintillator particle detectors.* Energetic particles
colliding into a suitable solid or liquid material decay exciting elec-
trons which in turn release photons (scintillations). The light is
detected in a photomultiplier which is calibrated to give the proper
particle energy. Primary advantages of the scintillator are its sim-
plicity, large sensitive volume, and complete spectrum readout capa-
bility in a counting interval unlike that of a sweep magnetic spectro-
meter. The scintillator is applicable to energies down to approximately
2 keV; however, the main drawback is that there is poor energy resolu-
tion. The scintillator response to monoenergetic electrons is essen-
tially a gaussian peak whose width varies inversely with the square
root of photocathode and multiplication electrons in the photomultiplier.

4.2.4 *Gaseous ionization detectors.* The gas detector is classi-
fied into three modes of operation: ionization, proportional, and
Geiger operation. Figure 4.5 is a closeup view through the window of a
Geiger counter used to detect X-rays and energetic electrons. Counting
data are shown in Figure 2.4, for this unit. The collection scheme is
based on the principle of the ionization of a gas by a charged particle
whereby the ions are accelerated in an electric field yielding a current
pulse. If no secondaries are formed (low electric field) the output
pulse is simply the very small charge released by the decaying particle
and is proportional to its initial energy. When used in an integrating
mode this is an ionization chamber. The proportional counter utilizes
the multiplication of secondaries by applying a higher electric field
strength. Increasing the field still further gives complete breakdown
of the gas in the chamber and is termed the "Geiger region". Although
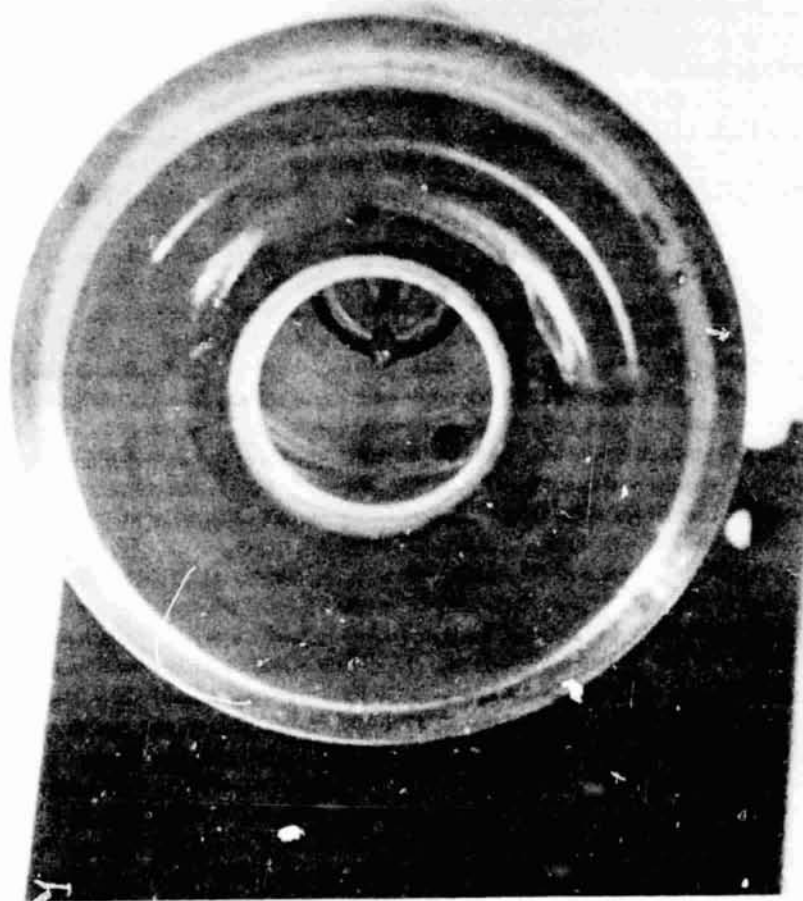
Figure 4.5 Displayed is a proportional counter chamber.
Energetic particles pass through the window to
ionize the enclosed gas. The applied electric
field accelerates the ionized charge causing
further ionizations and increased current flow.

a simple experiment, the gas detectors suffer because of 1) gas purity, 2) position sensitiveness with respect to where the ionization track takes place within the gas, and 3) associated deadtimes due to slow ion mobilities.

Detection schemes which have been employed to a minor extent are photographic film, spark chambers, spacecraft charging [*DeForest*, 1972] and tracks left in plastic, glass, or micasheets. A review of the various detection methods may be found by *O'Kelley* [1962].

4.3 *Diode Geometry and Construction of Solid-State Detectors*

Signals introduced by an energetic particle are usually very small $(10^{-15}$ coulomb) requiring every precaution to insure maximum signal-to-noise ratio. The reverse current flow with the applied electric field appears as noise at the output. It is minimized by increasing the effective resistivity. One of the most attractive procedures to accomplish this is the p-n semiconductor diode junction in which large electric fields can coexist with low reverse leakage currents. A qualitative analysis will be given in Section 4.4 of diode behavior. Other techniques used to increase resistivity are the implantation of gold impurities at low temperatures [*Davis*, 1958] and high temperature imperfections introduced by temporarily heating crystals to 1000°C. Two principal problems associated with these methods are induced "trapping" centers and necessity for low temperature hardware, which make them unsuitable for space applications.

Figure 4.6 illustrates the basic geometry of three types of semiconductor detectors; the diffused (type I), surface barrier (type II), and the lithium drift (type III). The type I sensitive surface consists
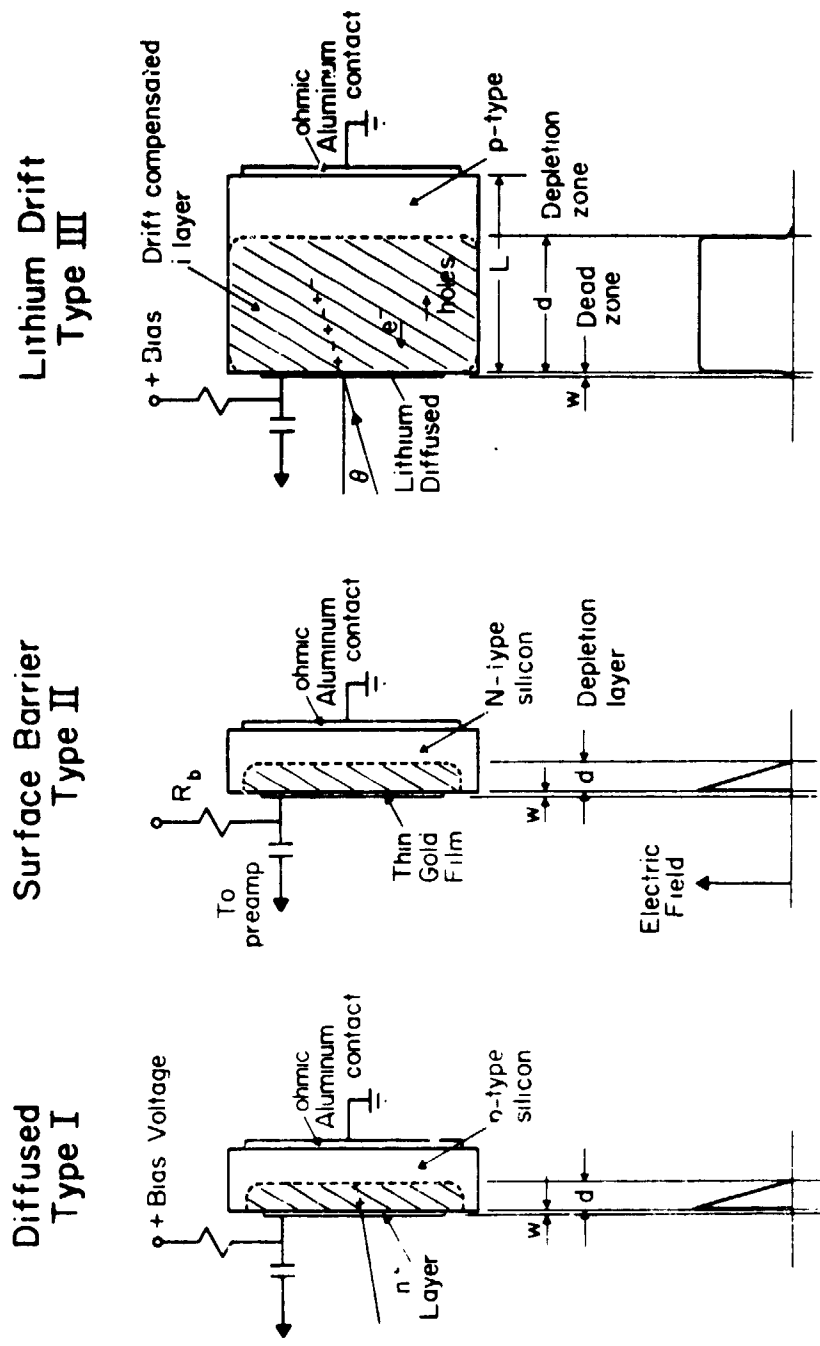
Figure 4.6 Three types of solid-state particle detectors are represented showing their respective geometry and electric field strengths. For totally depleted detectors, the depletion region depth is equal to the total detector length L.

of a thin highly doped n^+ donor impurity while the type II case is a metallic surface e.g. gold in contact with the n material. Two qualifications placed on the diode are that 1) it must be fabricated such that the depletion region extends over a range somewhat larger than the incident particle decay path if energy spectrum information is desired and; 2) energy lost in the thin surface region (dead zone) before entering the depletion region is optimized to its smallest reasonable value since .t does not contribute to the output signal. In the depletion region an electric field exists resulting from the redistribution (diffusive process) between adjacent materials of the unequal number density of conducting band electrons and free holes (maximum entropy occupancy of energy and space states).

For large energies requiring wide depletion regions the Lithium ion drift (type III) technique was introduced by *Pell* [1960]. Layers approximately 15 mm long are possible with nearly intrinsic resistivity at low bias voltages of 100 V. Firstly, this method, like normal junction fabrication, allows diffusion of donor (lithium) atoms into the crystal by passing a high concentration of donor atoms at elevated temperatures over the surface of a low-resistive p-type crystal. A junction is formed at the point where the concentration of ⁿ acceptors equals that of n donors. Secondly, to spread the depletion width Pell applied a reverse bias to the junction at contiued elevated temperatures causing lithium ions to drift into the p-type base under the action of the electric field. The charge-compensating effect of the Lithium donor movement in the electric field offsets the acceptor impurities to give a uniform region, the i layer, of intrinsic resistive mate⁻ l.

4.4 *Qualitative Considerations of Particle Impingement in Type I and II Diodes*

To properly interpret the retrieved data from a solid-state detector it is of fundamental importance that discussion be made of the basic theory of operation and the sensitivity of the detector to external conditions. This section is intended to develop an intermediate working language of the detector operation with emphasis on the pertinent factors involved in the rocket-borne design of Chapter 5. Advanced and detailed treatments are in the publications by *Deme* [1971], *Bertolini and Coche* [1968], and *Taylor* [1963].

4.4.1 *Energy deposition in solid-state detectors.* Figure 4.7 shows $\frac{dE}{dx}$ relationships for electrons replotted from *Stermheimer* [1959] and for protons and alpha from [*Williamson et al.,* 1962]. Channeling of ions between crystal planes can cause deviations from the data. The energy loss is primarily due to Coulomb interaction of the incident charged particle with excitations of the absorber electrons. The functional dependence has been deduced by *Livingston and Bethe* [1937] to be

$$\frac{dE}{dx} = - \frac{4\pi e^4 z^2 ZN}{mv^2} \, ln \; \frac{2mv^2}{I} \quad [erg/cm] \qquad (4.1)$$

where E is the kinetic energy of the incident ion, x is the particle track, e is the unit charge, z is the charge of the particle, and Z is the atomic number of the absorber material, N is the absorber density (cm^{-3}), m is the electron mass, v is the particle velocity and I is the average ionization potential of the absorber.

Letting M be the mass of the particle, (4.1) becomes

$$\frac{dE}{dx} \propto \frac{z^2}{v^2} \left[ln\, v^2 + const \right] \propto \frac{z^2 M}{E} \left[ln\, \frac{E}{M} + const \right] \qquad (4.2)$$

Therefore

$$E\, \frac{dE}{dx} \propto Mz^2 \left[ln\, \frac{E}{M} + const \right] \simeq Mz^2\, (const) \qquad (4.3)$$

Accordingly, equation (4.3) shows that particle identification is possible if simultaneous measurements are made of $\frac{dE}{dx}$ (Figure 4.7) and total energy E. Their product may be formed in a multiplying circuit yielding discrimination of $z^2 m$. A working arrangement employed is to have to detectors, a thin totally depleted detector of length dx directly above an absorbing detector for final energy measurement.

The range in silicon, R, is found by integrating the specific energy loss, equation (4.1)

$$R = \int_{E_o} \frac{1}{\frac{dE}{dx}}\, dE = \frac{mM}{4\,e^4 z^2 zN} \int_o^{v_o} \frac{v^3 dv}{ln\left[\frac{2mv^2}{I}\right]} \qquad (4.4)$$

where E_o and v_o are the initial energy and velocity of the particle. The range in silicon for electrons, protons, and alpha particles is plotted in Figure 4.8 from data by *Williamson et al.* [1966].

4.4.2 *Charge signal generated in a solid-state detector.* The shape of the electric field depends on the diode type and composition.
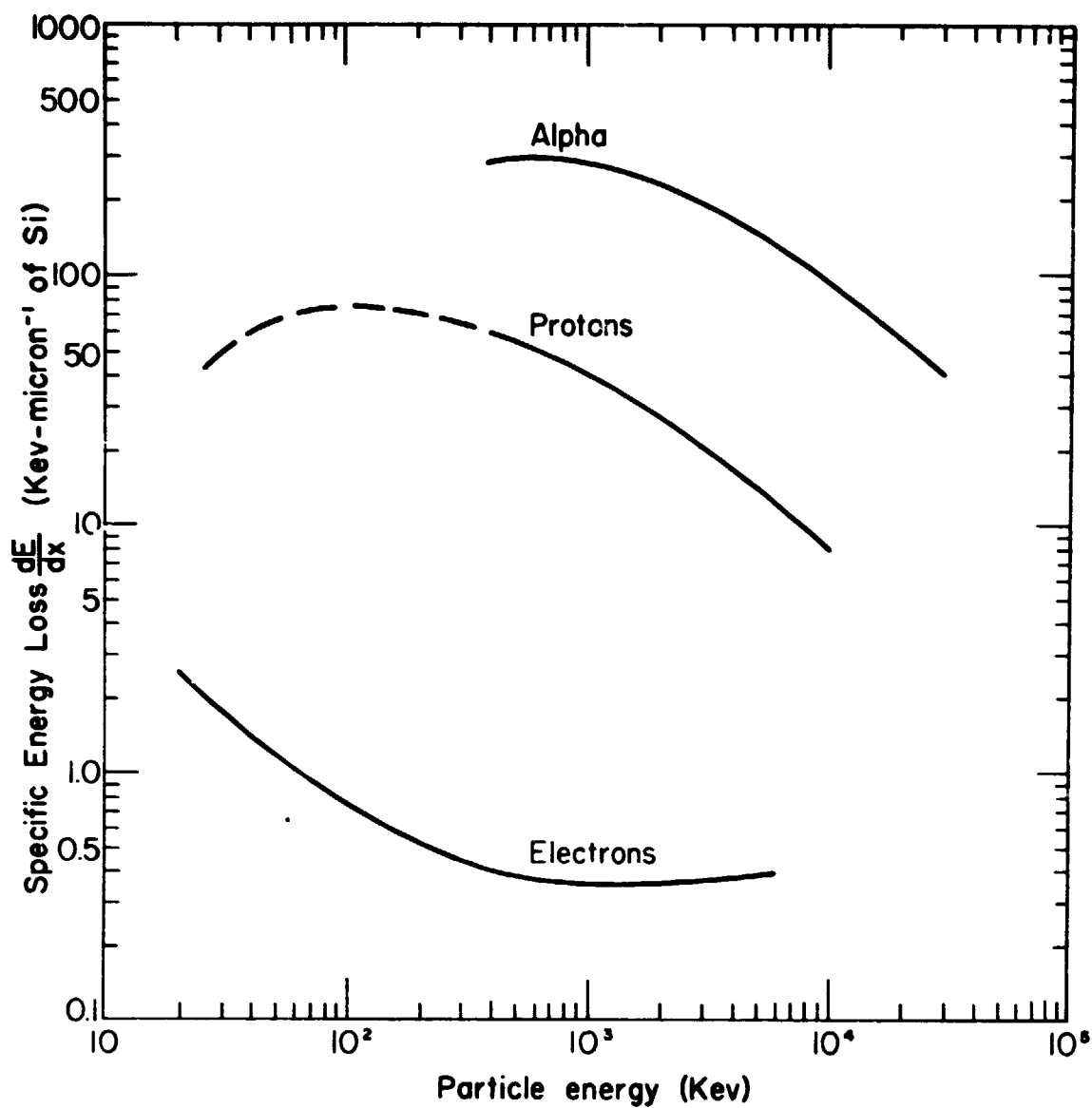
Figure 4.7 Specific energy loss for electrons, protons, and alpha
particles in silicon. (Data replotted from *Stermheimer*
[1959] and *Williamson et al.* [1962]).

C-2
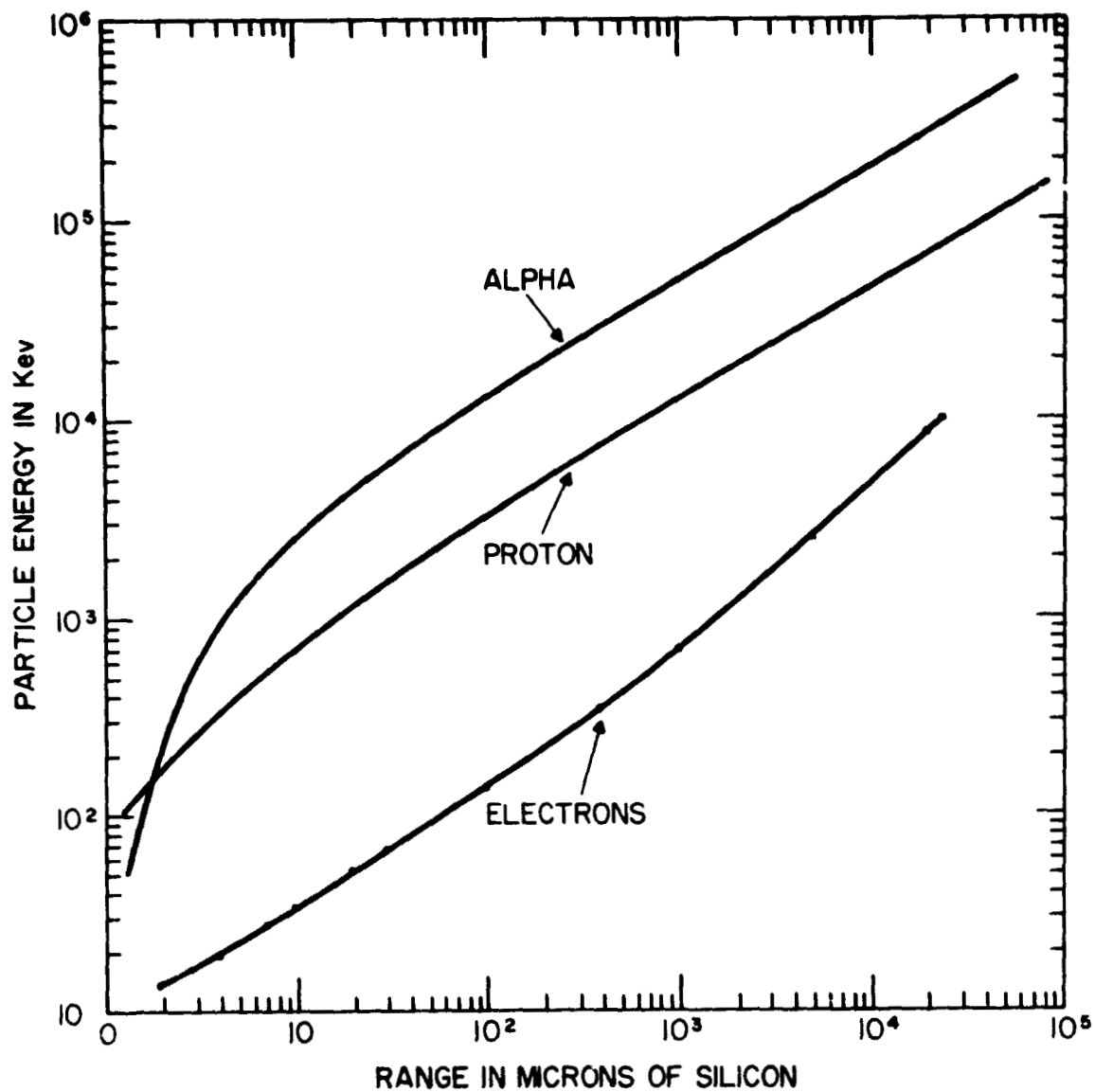
Figure 4.8 Range-energy curves for electrons, protons, and alpha particles in silicon. (Data replotted from *Williamson et al.* [1966]).

Using diffused and surface barrier detectors, the electric fields are nearly linear as shown in Figure 4.6.

$$\epsilon = \pm \frac{2V_T}{L^2} (L-x) + \frac{V-V_T}{L} u (V-V_T) \qquad (4.5)$$

where V_T is the voltage required to totally deplete ($L=d$) the detector.

Given information on the electric field (equation 4.5), $\frac{dE}{dx}$ energy loss (Figure 4.7) and mobilities, $u(\epsilon,t)$ (Figure 4.9) it is possible to calculate the charge transit time which together with the "plasma time" specify the output charge signal $Q(t)$.

To develop this relationship necessitates the use of a fundamental theorem first enunciated by *Ramo* [1939]. The theorem states that the induced charge ΔQ derived from a carrier charge q' transit in a region ΔX (normal component) between two parallel plane electrodes separated by a distance L is:

$$\Delta Q = q' \frac{\Delta X}{L}$$

Now for charges generated along a track of length R, the above theorem suggests that the charge produced in each segment ΔX can be summed to yield the total induced charge $Q(t)$. Since two carriers are present, holes and electrons, the total charge $Q(t)$ is composed of two parts; hence,

$$Q(t) = Q_p(t) + Q_n(t)$$
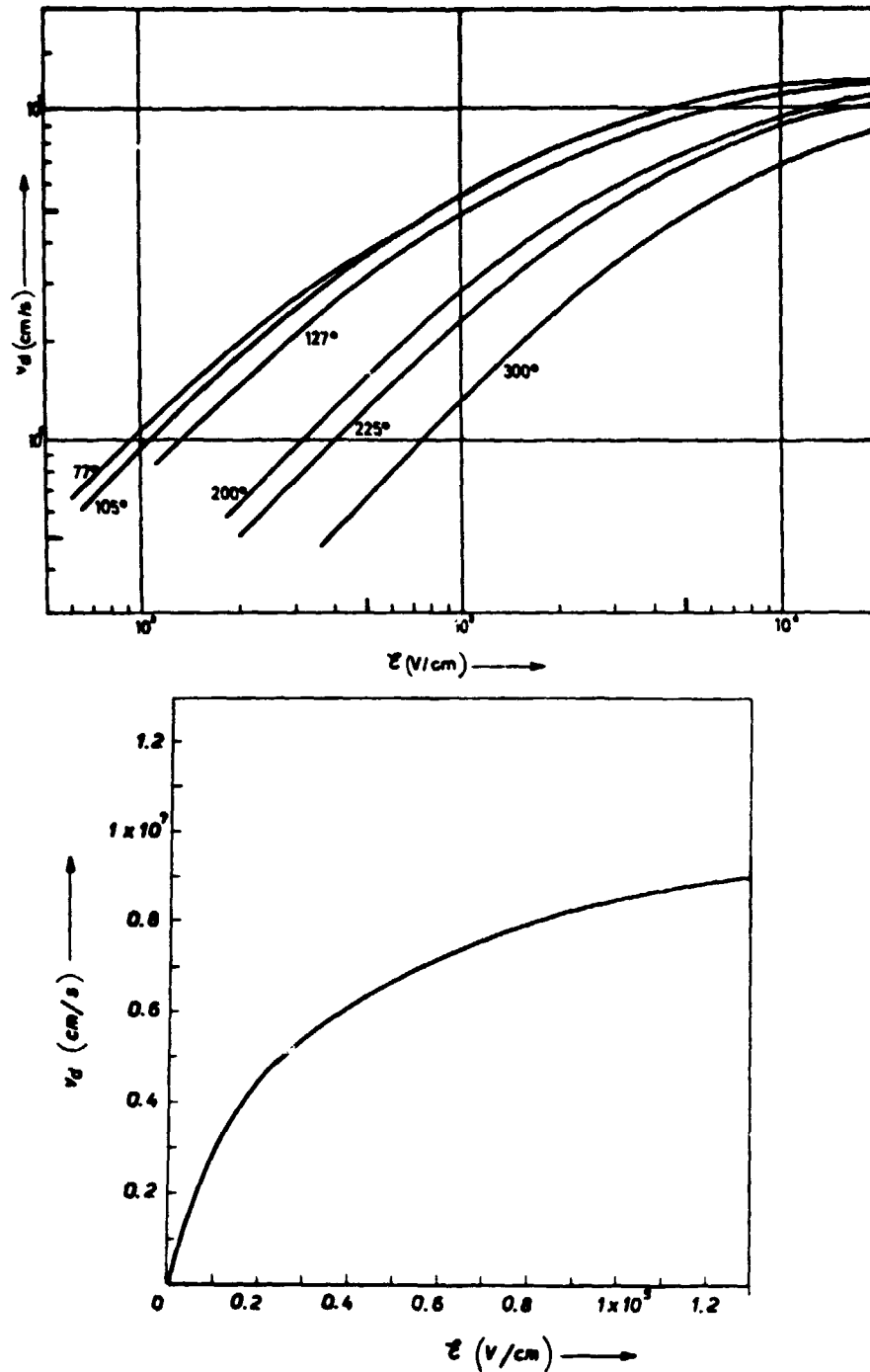
Figure 4.9 The upper and lower figures indicate the drift velocity in silicon for electrons and holes, respectively. The temperatures in the upper figure are in Kelvin and the lower profile is at room temperature. The upper figure is by *Tauch*, [1958] and the lower figure by *Dodge, et al.*, [1964].

Now summing, as indicated above, gives

$$Q_p(t) = \sum_i q_i' \frac{X_i(t) - X_{oi}}{L}$$

where X_{oi} is the location where the ith ionized charge is generated, X_i is the position in which the charge moves away from X_{oi} and

$$q_i' = \frac{q}{E_c} \left[\frac{dE}{dX_o} \right]_i \Delta X_i$$

where q is the charge unit (1.6 x 10^{-19} coulomb) and E_c is the average energy required for ionization of a hole-electron pair. Hence in the limit,

$$Q_p(t) = \int_o^R \frac{q}{E_c} \left[\frac{dE}{dXo} \right] \frac{x(t) - X_o}{L} dX_o \qquad (4.6)$$

Finally, $X(t)$ may be obtained from Figure 4.9 by solving the differential equation

$$V_d = \frac{dx}{dt} = \mu_o [\epsilon(x)] \epsilon(x)$$

with initial condition $X(o) = L$.

Similar expressions hold for Q_n using electron associated mobilities, a minus sign for the negative charge and the $X(t)$ initial condition $\frac{dx}{dt} = 0$ at $x = 0$. The two charge components have been calculated by *Quaranta et al.* [1965] and are reproduced in Figure 4.10 as a function
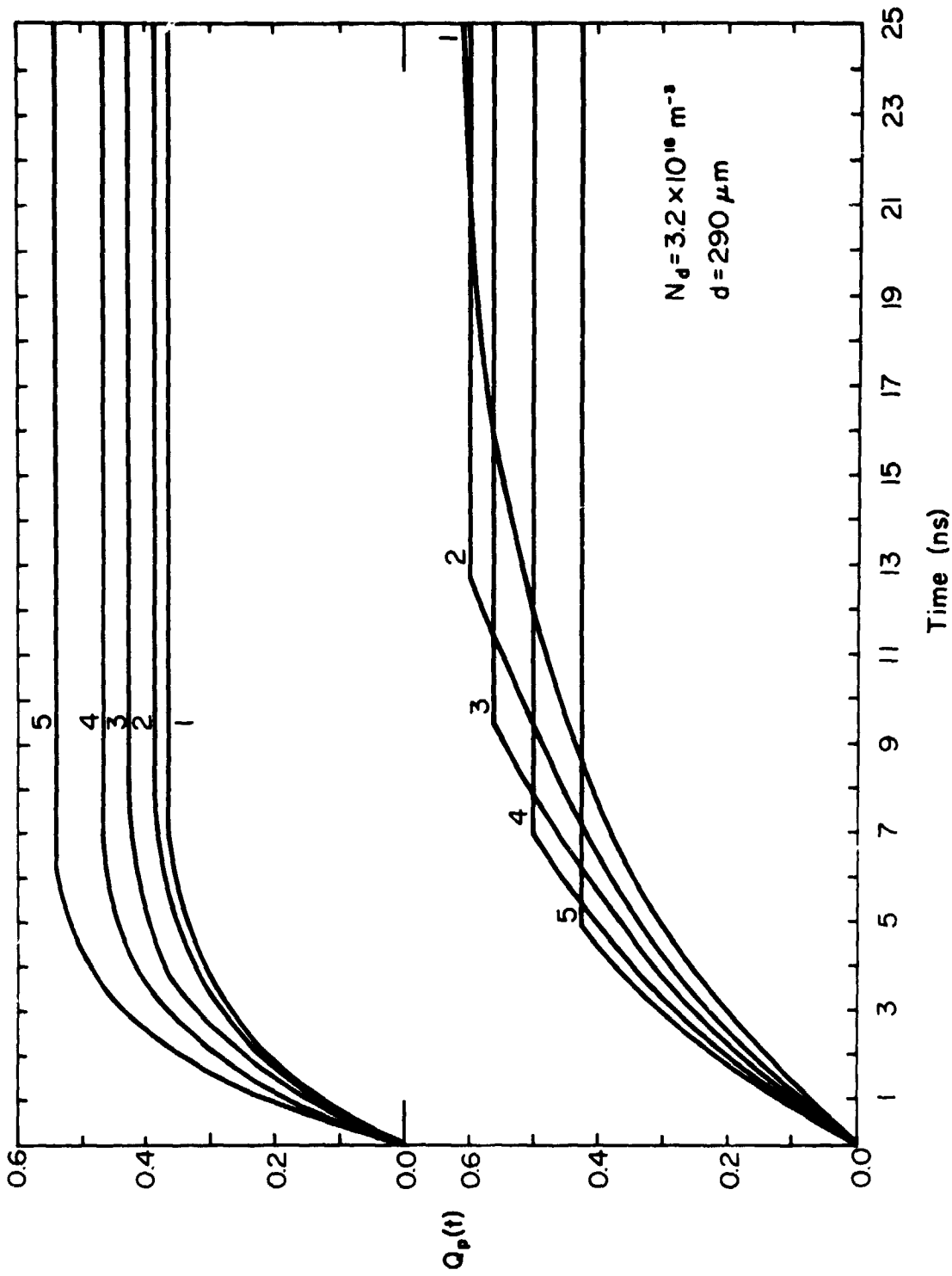
Figure 4.10 The upper and lower figures indicate the charge pulse waveforms in a surface barrier detector for electrons and holes, respectively. (Data replotted from *Quaranta et al.* [1965]).

of time for a type II detector. The calculations were made using α-particles with donor concentration (N_d) equal to 3.2 x 10^{18} m^{-3} and L = 290 μm at a 200 volt bias.

The numbering of curves can indicate either various incident energies or angles of incidence. Curve numbers 1, 2, 3, 4, and 5 are associated with energies 25, 24.7, 23.8, 22.5, and 20.6 MeV, respectively for perpendicular radiation or impact angles of 0°, 15°, 35°, and 45°, respectively for 25 MeV radiation.

4.4.3 *Dead zone region.* Two principal factors influence the above results; the dead zone layer and the collection efficiency. First, the effective dead zone may be determined as follows. By assuming that the dead zone is a slab contained within the gold or n^+ (p^+) surface, [*Ewing*, 1962] different travel distances are expected through the dead zone depending on the particular angle of incidence [*Williams and Webb*, 1962].

If the slab (window) thickness is w (Figure 4.6) then the maximum energy deposited (MED) is proportional to the initial particle energy minus that which is lost in the window; hence

$$MED = E_o - w \frac{dE_o}{dx}$$

By varying the angle of incidence θ, it becomes

$$MED = E_o - \frac{w}{\cos\theta} \frac{dE_o}{dx} \tag{4.7}$$

where θ is measured from the normal (Figure 4.6).

The differential energy for angles compared to the perpendicular then becomes

$$\Delta E = w \; \frac{dE_o}{dx} \left[\frac{1}{\cos\theta} - 1 \right] \qquad (4.8)$$

Therefore, by illuminating a collimated monoenergetic beam of particles upon the surface, the value of $w \; \frac{dE_o}{dx}$ can be found by measuring the angular dependence (a slope) of the peak pulse height since it is proportional to *MED*.

Ray and Barnett [1969] utilizing this technique have determined an energy loss of 2.59 keV for a 10 keV proton beam incident upon a $40\mu\text{gm cm}^{-2}$ gold surface barrier detector.

4.4.4 *Collection efficiency*. The second loss mechanism is attributed to the fact that not all of the liberated charge from an ionization source is capable of continued motion in the electric field across the depletion region for some recombines. The collection efficiency, η, is defined to be equal to Q_c, the collected charge, divided by Q_L, th charge liberated within the depletion region. An upper limit to the charge collection time may be established if the depletion width L and the appropriate carrier velocity (Figure 4.9) are known. The recombination is essentially of three mechanisms: 1) recombination via excitations; 2) direct radiative recombination [*Chynoweth and McKay*, 1956]; and 3) recombination centers "trapping" [*Shockley and Read*, 1952].

An analytical form for collection efficiency for particles with range distances short compared to depletion depth L is given by *Miller et al.* [1962] as

$$\eta = \left(1 + \frac{d}{2\mu_i \tau_i \varepsilon_m}\right)^{-1} \tag{4.9}$$

where μ_i and τ_i are the hole or electron mobility and lifetime, respectively, and ε_m is the maximum electric field. From this, one deduces that, first, the distance, "trapping length", $\varepsilon\mu\tau$, should be long compared to d and, second, that "trapping" losses are independent of applied bias.

Since "trapping" is a nonuniform process, a distortion effect is introduced yielding poor resolution and the so-called "multiple peaking" [*Miller et al.*, 1962] which is the occurrence of two adjacent energy peaks observed from a monoenergetic beam. Additionally, multiple peaking can be produced by charge multiplication caused by carrier injection at the device contacts. Figure 4.11 illustrates this multiple peaking behavior for the detector displayed in Figure 4.1. Both photographs are taken from the multichannel pulse height analyzer for 60 keV energetic electrons with the electronics described in Chapter 5. The lower photograph is the logarithm of the top linear plot. The peak to the far left is the noise.

In summary, the depletion region electric field is, on the average, linear in type I and II detectors (Figure 4.6); however, because of fabrication inhomogeneities, perturbations exist causing the ionized carriers to traverse a somewhat larger path and, consequently, have less chance of survival for a fixed lifetime, τ. The fractional loss of carriers by trapping is given by *Shockley and Read* [1952] to be

$$\frac{\delta n}{n} = -\frac{t_p}{\tau} \tag{4.10}$$

where τ is the recombination lifetime and t_p is the plasma time.
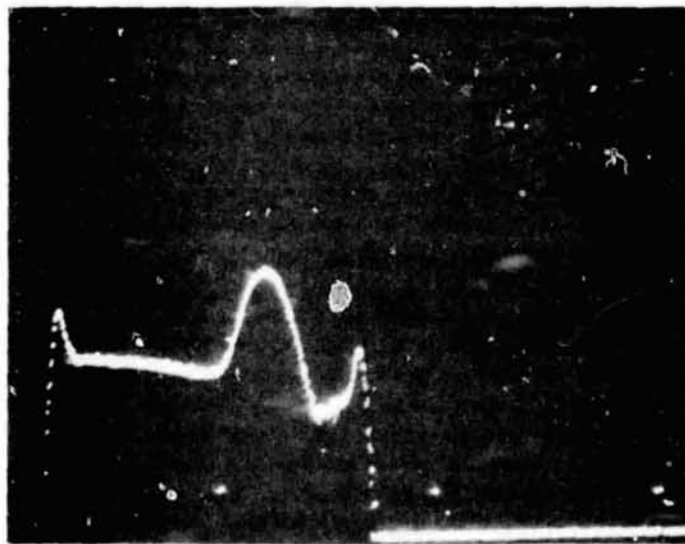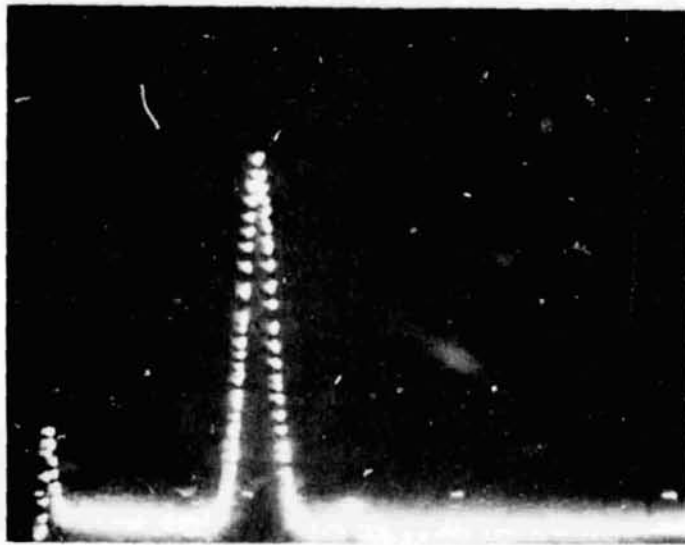
Figure 4.11   The upper and lower figures are a linear and log
plot, respectively, of the solid-state detector
output analyzed on a 400-channel pulse height
analyzer. The multiple peaking effect is observed
at the right, the high peak represents the 60 keV
incident electrons and the far left peak is the
noise buildup.

4.4.5 *Plasma time and rise time.* The plasma time is defined to be the period that the particle track is held together by its own electro-static forces. If the electric field is sufficiently low, it is unable to fully penetrate the high density plasma track. Hence, the charge collection time is lengthened.

Tore and Seibt [1967] have resolved the following functional relationship for t_p in a coaxial detector.

$$t_p = \frac{qn_c r_t}{\mu \varepsilon \varepsilon_o^2} - \frac{r_y}{\mu} \qquad (4.11)$$

where

q is the electronic charge $(1.6 \times 10^{-19}$ coulomb$)$

ε is the relative dielectric constant (12 for silicon)

ε_o is the vacuum dielectric constant $(\varepsilon_o = 8.85 \; 10^{-12} \; Fm^{-1})$

r_t is the radius of the original track

r_y is the radius over which the track charge is distributed by unit transit time

Meyer and Langmar [1965] have resolved the following experimental relationship for α-particles in a surface barrier detector.

$$t_p = \frac{a}{\varepsilon_o^2 t^2} \qquad (4.12)$$

where $a = 1.9 \times 10^{-2} \pm 15\%$ V^2 sec cm^{-2} and $\varepsilon = 300$ V cm^{-1}.

The time required for the collected charge to go from 0.1 to 0.9 of its maximum value is called the rise time, t_r. Figure 4.12
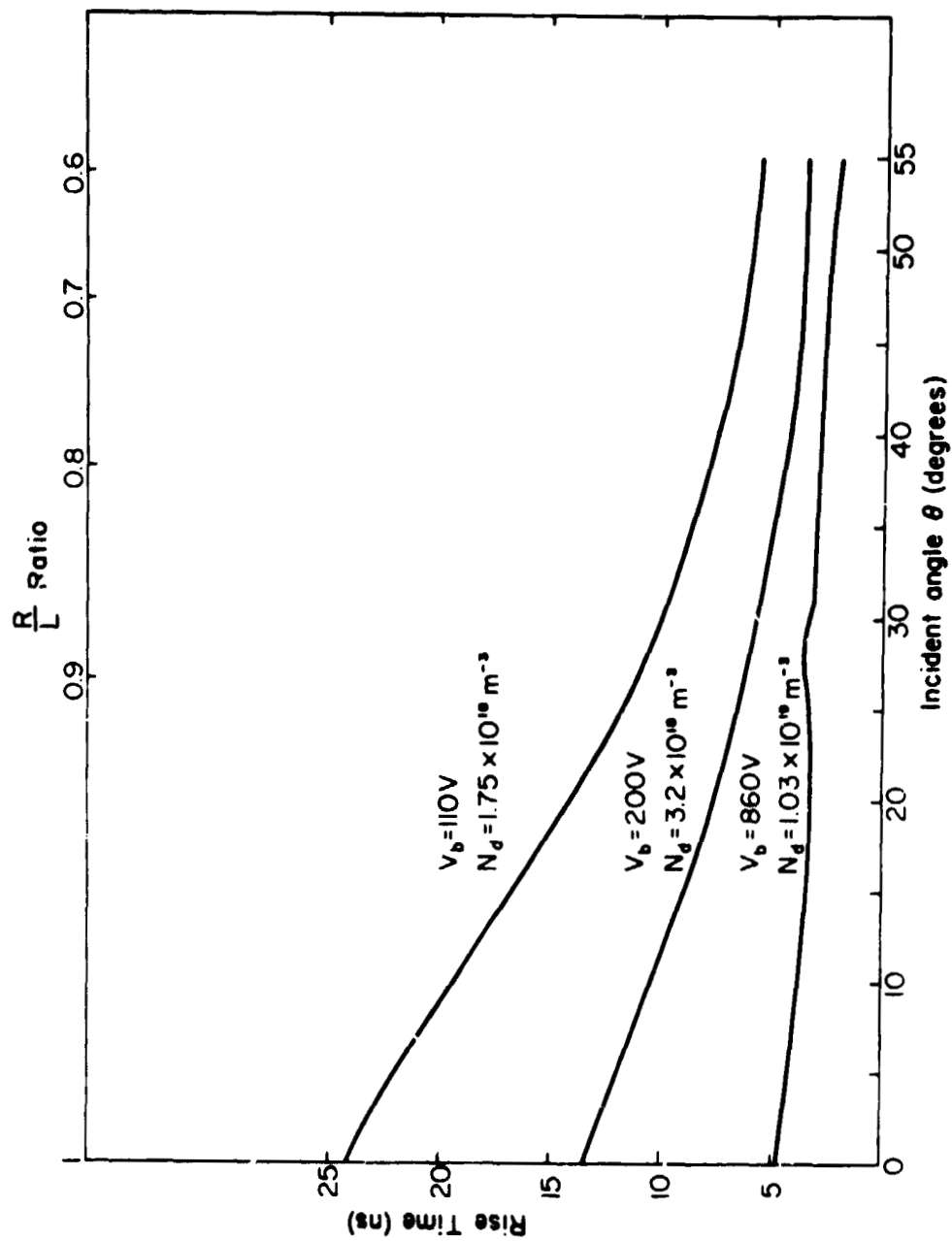
Figure 4.12   Illustrated is the charge pu...   isetime T_r as a function of either R/X_O ratio or impact angle, θ, for various impurity concentrations N_d in a surface barrier detector. (Replotted from *Quaranta et al.* [1965]).

[*Quaranta et al.*, 1965] compares rise time as a function of impact angle θ or $\frac{R}{L}$ ratio for differing impurity concentrations N_d, in a surface barrier detector. An intuitive understanding for why the rise time falls rapidly for increasing angles or small $\frac{R}{L}$ ratios is that the ionization is deposited closer to the boundaries of the depletion region. Since there is less distance to traverse ($R \sin\theta$ for nonperpendicular radiation) the collection time would be less giving a faster rise time. More fundamentally, the rise time is composed of three components in a time field yielding

$$t_R = \left[t_r^{\;2} + t_p^{\;2} + t_d^{\;2} \right]^{1/2} \tag{4.13}$$

where t_r = rise time of the charge pulse due to transit time only.

t_p = plasma time.

t_d = rise time associated with capacitance and resistance of the detector equivalent circuit.

4.4.6 *Channeling.* Crystallographic symmetry with respect to the incoming radiation, causes differing quantum efficiencies of ionization resulting in a nonuniform $\frac{dE}{dx}$ deposition rate. The most symmetrical cut of a crystal is normal to the axis of the crystal growth, the [111] direction, thus giving the highest percentage of channeling. *Gibson* [1966] has transmitted 4.9 MeV protons through 35 μmSi crystal at directions parallel to the [111], [110], and "no symmetry" directions (Figure 4.13). *Dearnaley* [1964] has determined that wafers should be cut at 10 to 20 degrees from the [111] plane in order to minimize symmetry (channeling).
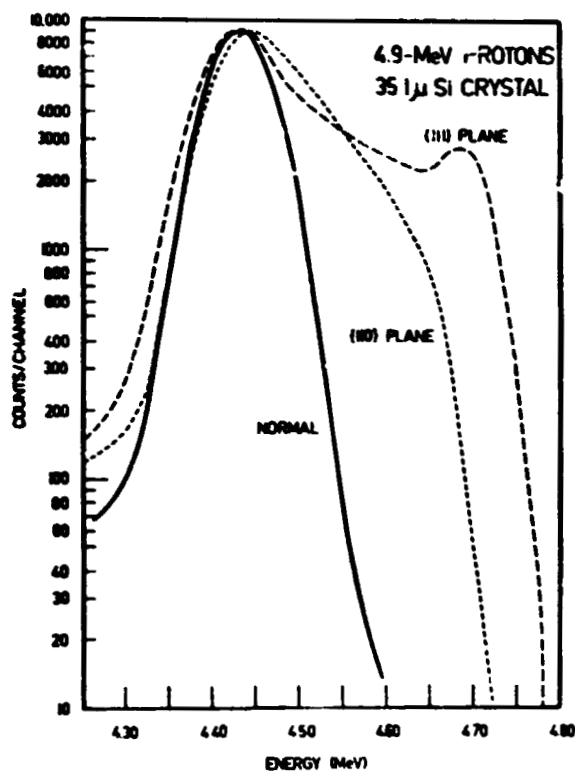
Figure 4.13 Channeling is an important factor in the orientation of a detector crystal and particle calibrations for wide angle applications. The above curves show the strong dependence on the relative angle of incident radiation. Data taken from *Gibson* [1966].

4.4.7 *Detector equivalent circuit*. The output charge generated in the depletion region is modified by the surrounding conductors, contact points and internal electrical semiconductor properties, i.e. polarization. Simplifying, the equivalent circuit may be thought of as containing four impedance components associated with the four distinct regions of the detector; the depletion region, undepleted semiconductor region, contact points, and the external connectors and shielding. A more rigorous treatment may be made employing transmission line equations, especially for the high frequency case. Each section, because it is capable of charge storage across a potential, constitutes a capacitance along with the ohmic loss. Figure 4.14 illustrates the equivalent circuit where C_o and C_s are evaluated in the same way as that of a plane parallel capacitor.

$$C_p = \frac{\varepsilon \varepsilon_o A}{L} \quad \text{the depletion layer capacitance}$$

$$R_s = \rho \frac{D-L}{A} \quad \text{undepleted zone resistance} \quad (4.14)$$

$$C_s = \frac{\rho \varepsilon \varepsilon_o}{R_s} \quad \text{undepleted zone capacitance}$$

where ρ is the semiconductor resistivity. The depletion region resistance is negligibly small for a reverse biased diode. The impedance, Z (contact point), can considerably influence the pulse and shows considerable distortion at lower temperatures. The connectors are primarily capacitive in nature. Techniques developed to measure circuit parameters are
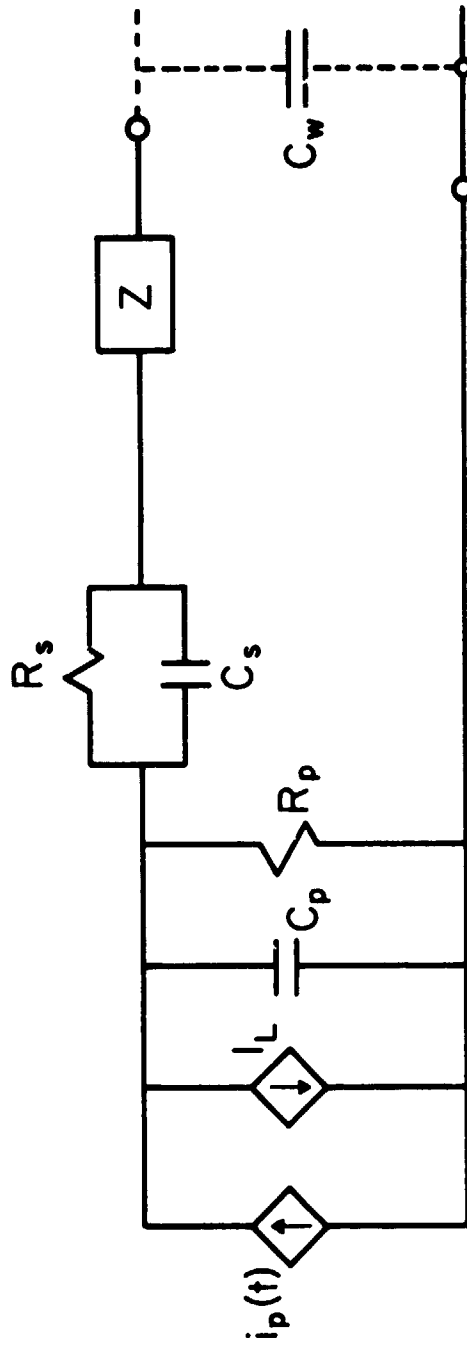
Figure 4.14 Detector equivalent circuit, $i_p(t)$ is the current introduced by an energetic particle, I_L is the leakage current, C_P and R_P are the parallel capacitance and resistance of the depletion region, C_S and R_S are the series capacitance and resistance of the semiconductor material, Z is the contact point impedance and C_W is the wire and connector capacitance.

discussed by *Quaranta et al.* [1966] and *Quaranta* [1969]. A nomogram is reproduced in Figure 4.15 to facilitate understanding of depletion region thickness, capacitance, resistivity, and impurity concentrations with applied bias. Figure 4.16 illustrates the contribution of electrons (a) and holes (b) to the final current pulse for a 400 μm thick surface barrier detector using 6000 Ω cm *n*-type silicon [*Quaranta et al.*, 1967].

Figure 4.17 is a typical output current pulse from a surface barrier detector for three bias voltages (90, 150, and 250 volts) with amplification utilizing a 3 ns rise time amplifier.

4.4.8 *Sensitivity of detector operation to external factors.* External effects of interest include 1) radiation damage, 2) light sensitivity, 3) temperature, 4) humidity and contaminants, 5) pressure changes, 6) mechanical shock, and 7) magnetic fields.

Radiation, if extreme, is harmful to detectors since nuclear modification results and crystal structure is perturbed by movement of atoms into intersitital positions. In rocket-borne detectors ionospheric radiation conditions are moderate and short; operation periods result in negligible degradation. Year long satellite programs through the radiation belts record only minor performance loss because of radiation damage.

Light quanta with energies greater than the forbidden band gap of silicon are capable of exciting charge carriers and thereby increase the reverse current of the diode and ultimately the noise. Figure 4.18 shows the noise introduced by a light source on the detector near the breakdown region. Surface barrier detectors are the most sensitive to light because of the thin gold layer; the thicker the layer the less light
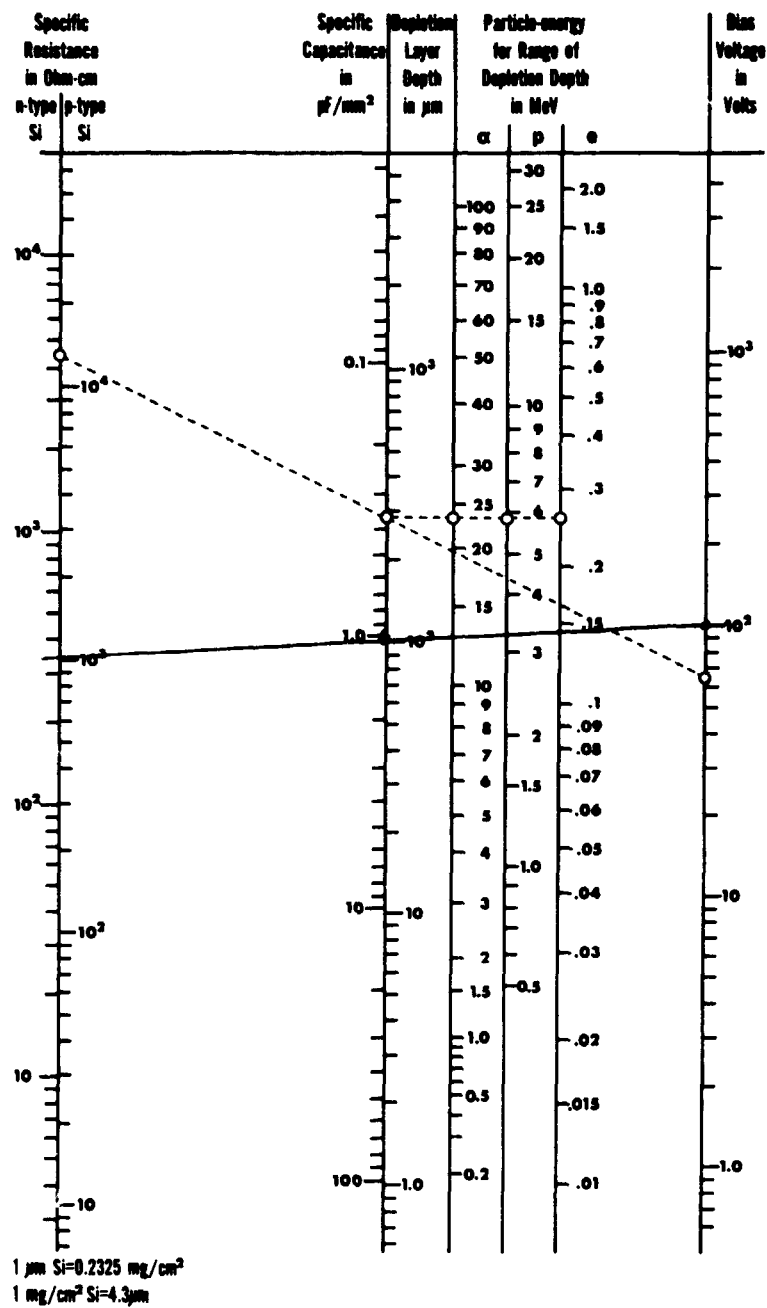
Figure 4.15 Solid-state detector nomogram for silicon. The solid line represents the detector displayed in Figure 4.1. Data taken from Ortec instruction manual.

TIME (ns)
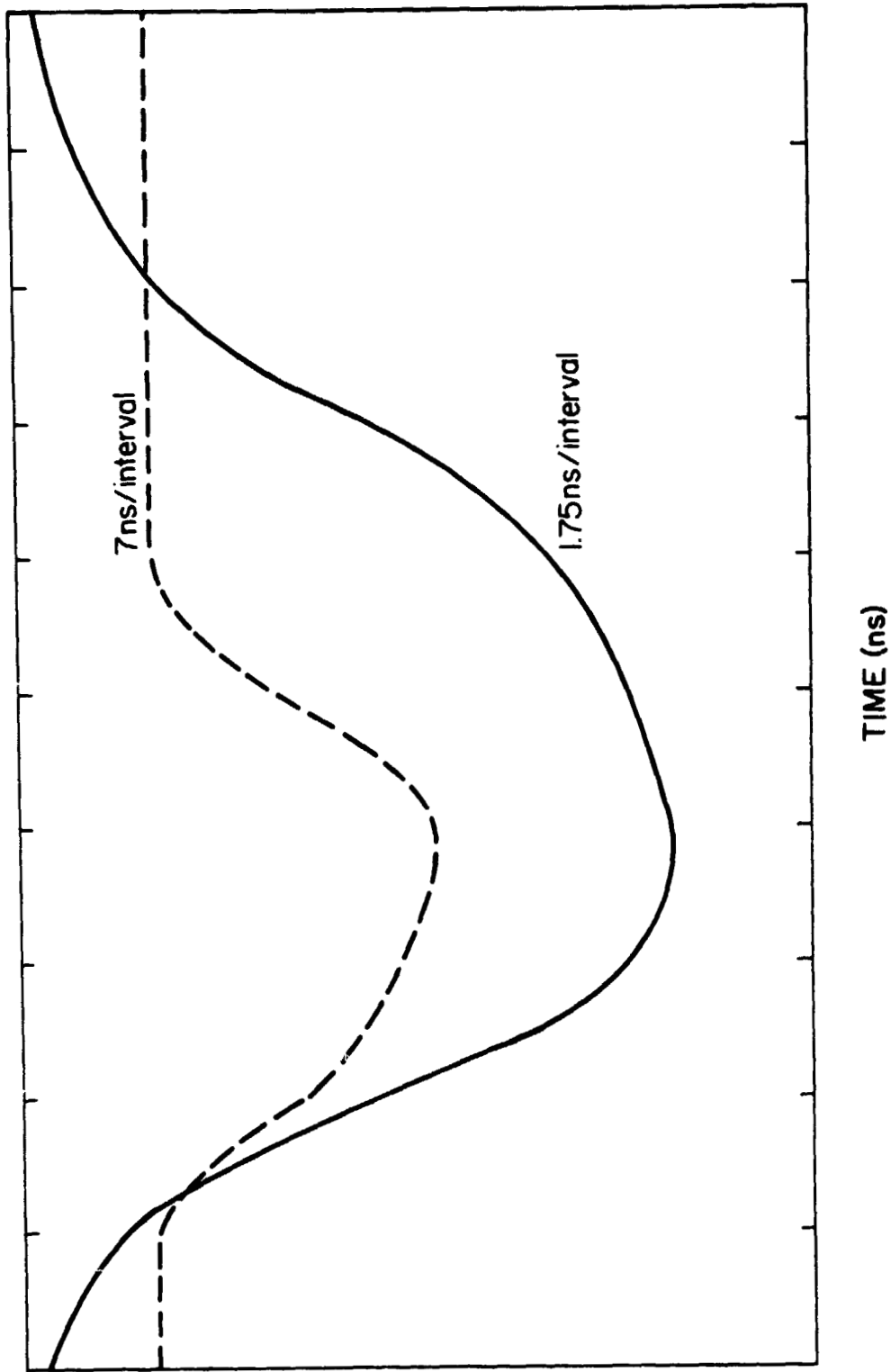
Figure 4.16 Current pulses due to electrons (upper) and holes (lower) in a 400 μm thick surface barrier totally depleted detector. Horizontal sensitivity is 1.75 ns/main division lower. Vertical sensitivity is the same. Data replotted from *Quaranta et al.* [1967].
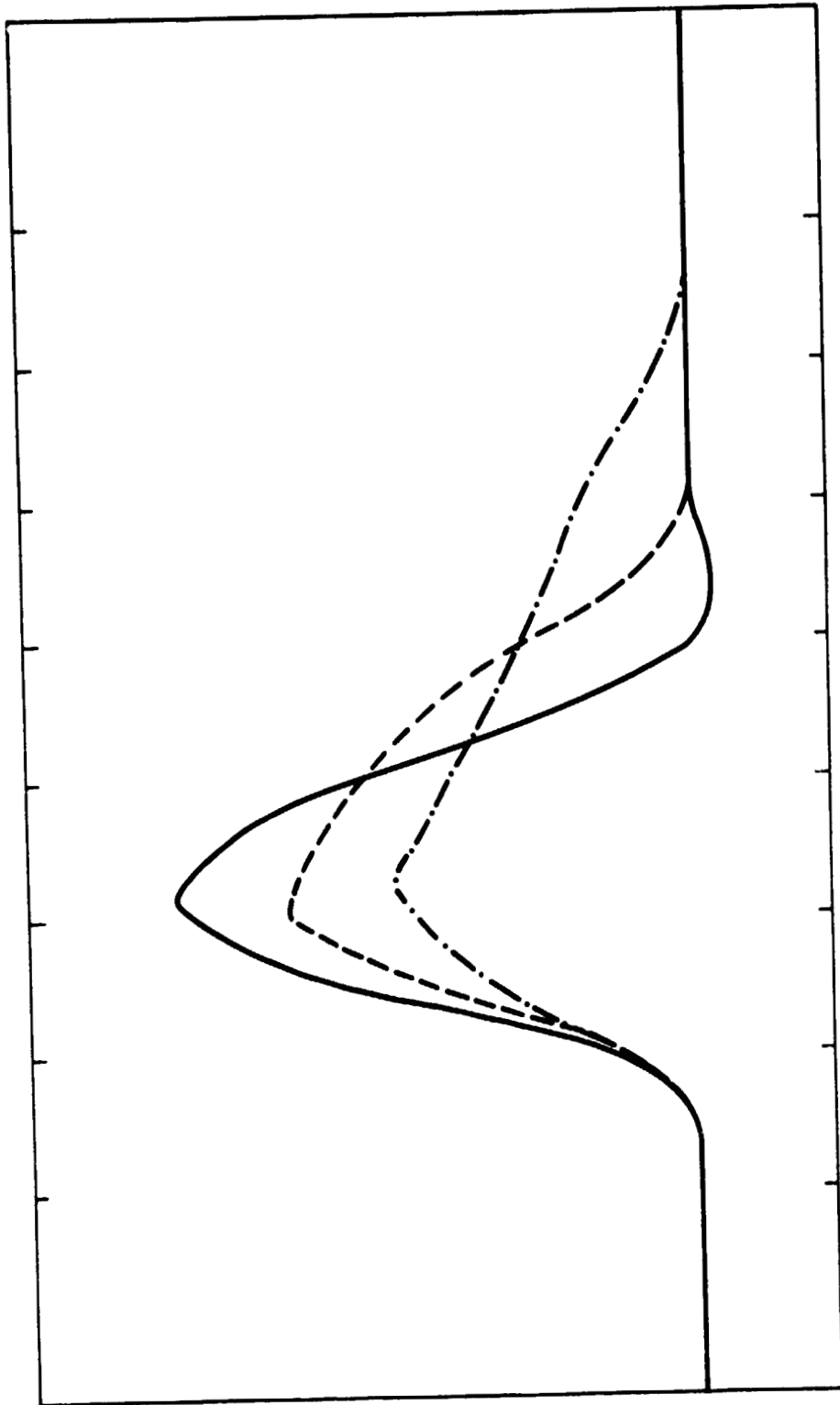
TIME (4ns/interval)

Figure 4.17 Current pulse from a surface barrier detector for bias voltage of 90, 150, and 250 volts. Data replotted from *Quaranta et al.* [1967]. Horizontal sensitivity is 4 ns/main division.
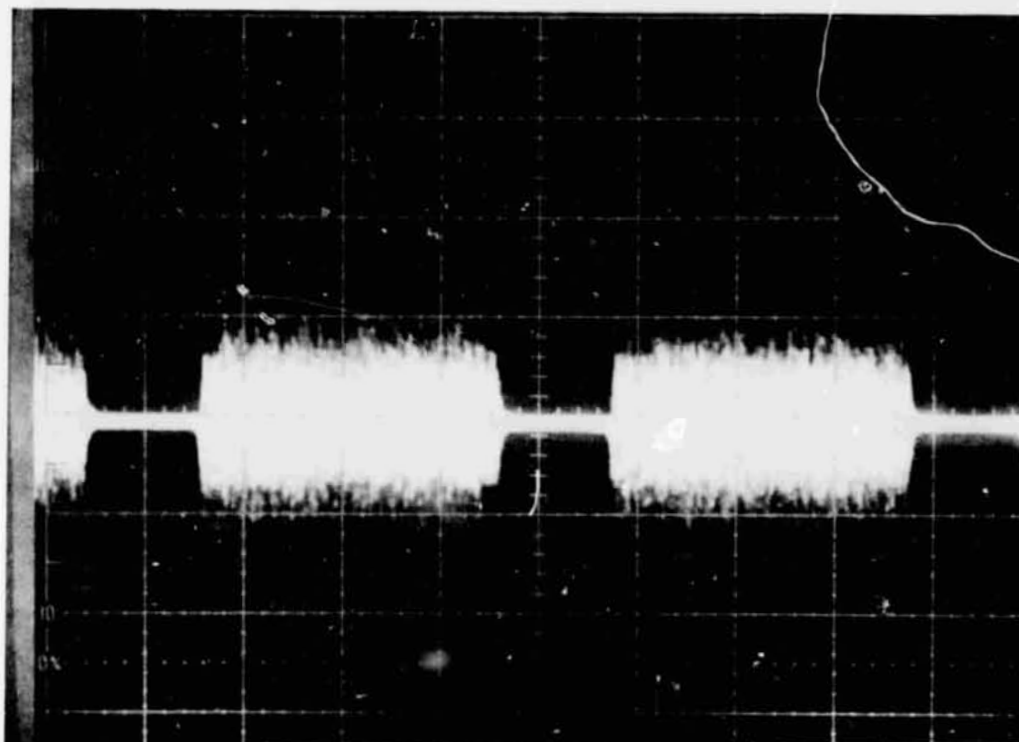
Figure 4.18 Preamplifier output illustrating the breakdown phenomenon
resulting from a bright light source (eg. the sun). The
vertical scale is 0.1 volts/division and the horizontal
is 2 msec/division.

sensitive. Special coatings can be placed over the gold to reduce light passage. Greater bias voltages can also be applied to a detector in the dark. Figure 4.19 is a plot of noise verses light intensity for the detector shown in Figure 4.1.

Temperature effects will be discussed in Chapter 5 in greater detail. The noise is gaussian and varies as the expotential of the inverse of temperature.

Humidity and vapors of organic solvents are able to react with the silicon (e.g. silicon hydride) or gold surface producing harmful effects. Silicon detectors should be stored with some drying agent in a sealed air-tight container. When detectors are pumped down in vacuum systems, mercury diffusion pumps should be avoided since mercury reacts with gold.

Surface leakage currents can be a dominant noise source as compared to space-charge generated currents in the presence of water vapor or other contaminants. Figure 4.20 shows the marked effects of dry oxygen and wet nitrogen on the surface leakage current of a diffused n^+p junction [Buck, 1961]. Accumulation of moisture and/or ionizable impurities near the surface can break down the intense electric field region in micro-plasma. If a detector is stored over a period of time or is exposed to a contaminant the bias voltage should be raised slowly allowing the contaminants to drift out of the field region. Figure 4.21 illustrates the intermittent behavior of microplasma breakdown. The bottom trace is the preamp output showing saturation of the signal over most of the trace. The top trace is the postamplifier output again showing similar behavior.
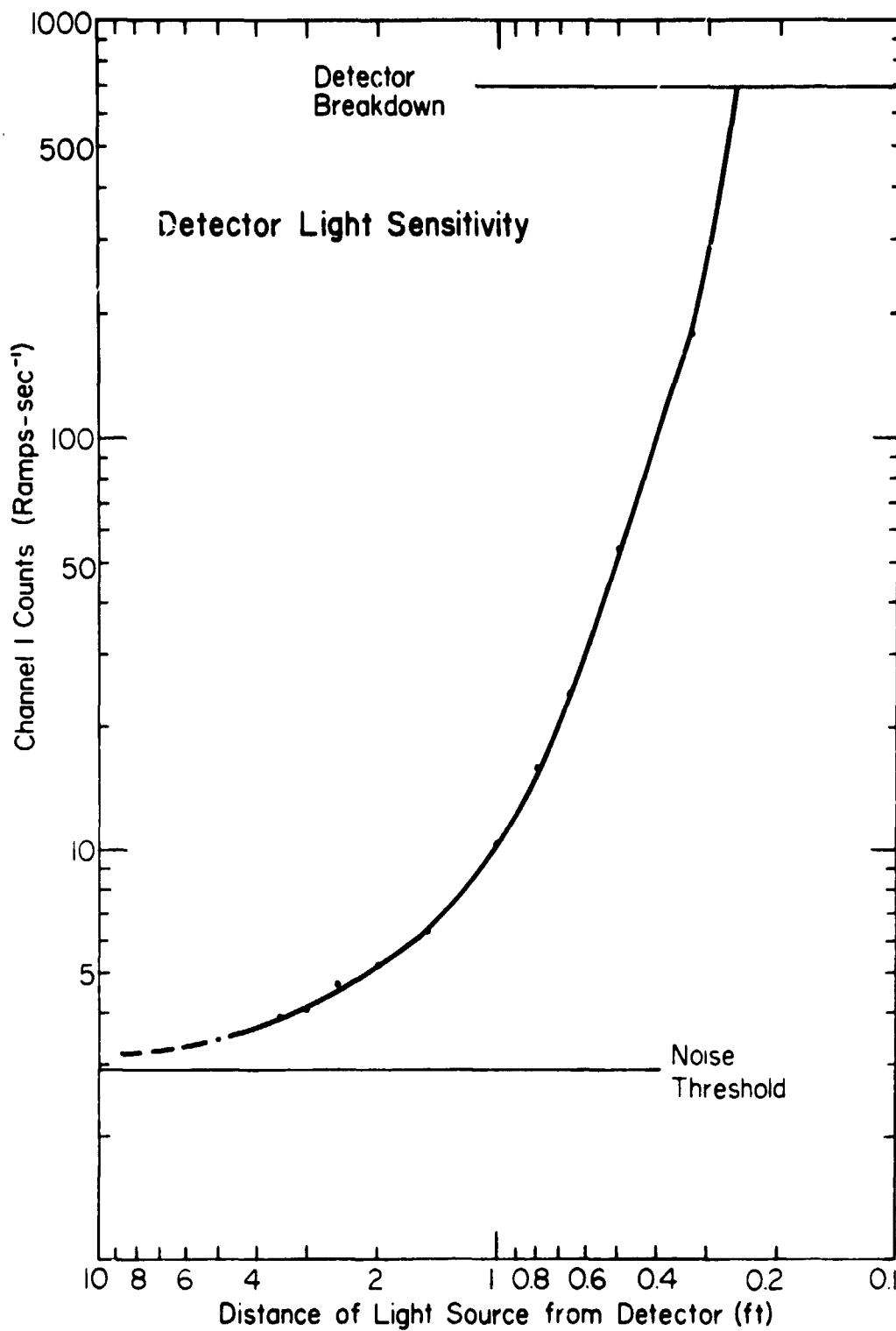
Figure 4.19 Noise counts recorded in the first channel of the voltage discriminator described in Chapter 5 for an 80-watt light-bulb source.
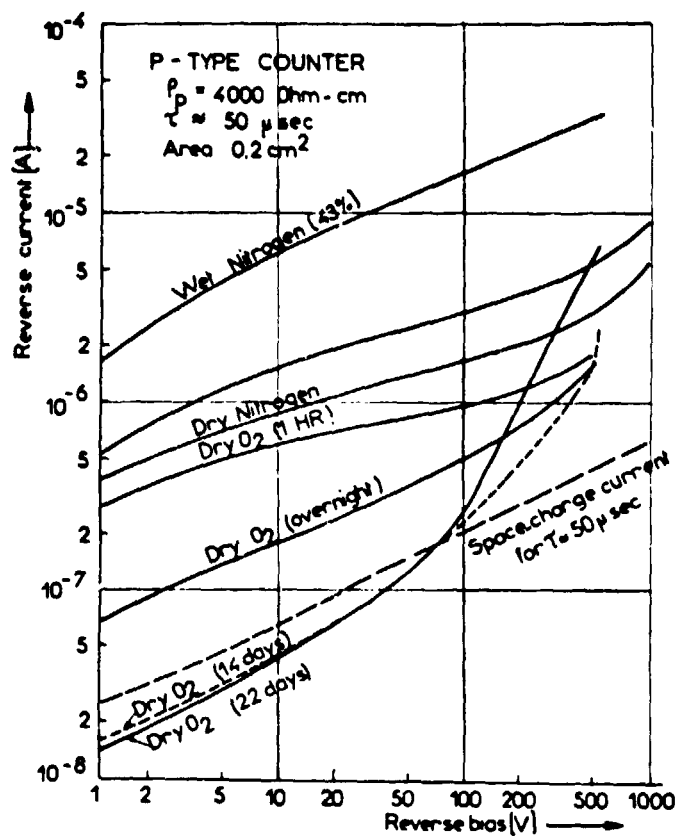
Figure 4.20   Reverse current versus reversed bias voltage showing the strong dependence upon the external air environment.   Data taken by *Buck* [1961].
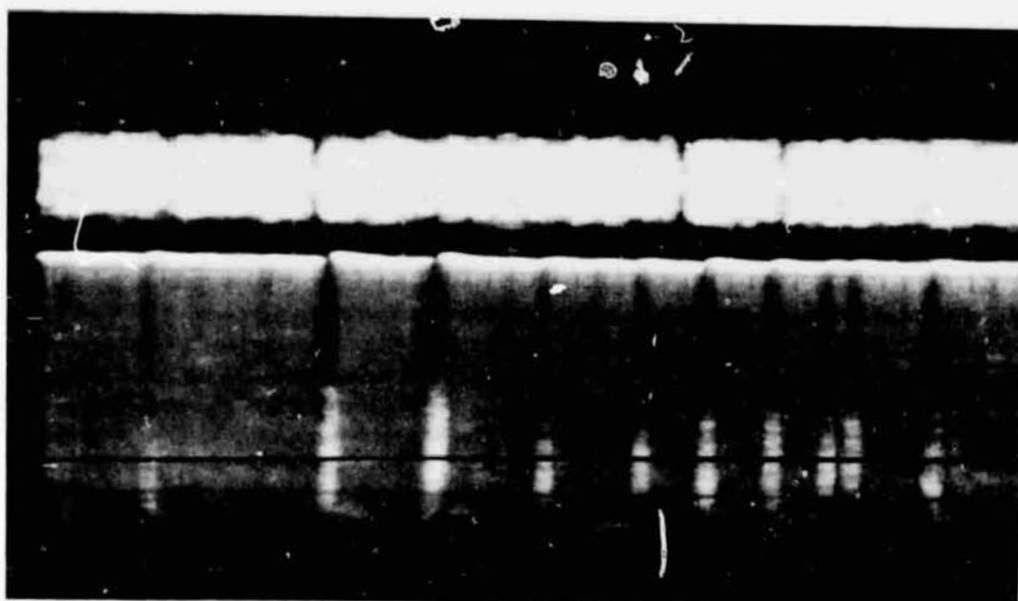
Figure 4.21 Microplasma breakdown is shown in the alternate trace of
the preamp output (top trace is at two volts/box) and
postamplifier output (bottom trace at 5 volts/box).
During short time intervals the detector is seen to recover
from saturation noise to its normal operation.

Mechanically the detectors are quite rugged and show insignificant pressure dependence. Their mechanical stability is similar to transistors.

The solid-state detector is independent of magnetic fields of several thousand gauss because of the intense electric field strength distributed over the very small depletion region.

5. DESIGN OF A SOLID-STATE PARTICLE DETECTOR

The approach will be taken, as in the actual design, of first setting down some of the essential rules and design philosophy for an overall low noise system moving then into the working block diagram of the detection process. A simplifying FORTRAN computer program (NOISE) may be employed at this point to aid in the design for a particular detector, preamp, filter, and postamp operation. After establishing the desired parameters, a description will be given of the chosen design. Finally, some attention will be given to future improvement.

5.1 *Noise Generation and Reduction in Semiconductor Detectors*

An outstanding problem in low energy particle detection is the reduction of noise. Not only does minimizing noise enhance the low energy threshold of the detector but it increases the overall resolving power for all energies.

5.1.1 *Thermal, shot, and leakage noise.* Referring to the detector equivalent circuit of Figure 4.14. there are essentially three generators of noise: the thermal noise of the resistors R_p and R_s, shot noise (also called space charge noise) and noise associated with the leakage current I_L. The resistance, R_p, is usually very large and its thermal noise contribution can be neglected for the following reason.

From basic statistical arguments, the mean squared noise voltage is given by the relation

$$\overline{v_N^2} = 4kT\ R\ \Delta f \tag{5.i}$$

where k is the Boltzmann constant, T is the absolute temperature, R the resistance, and Δf the frequency range over which the measurement is made. Now, applying Kirchoff's voltage law to a resistor (with equivalent series noise generator) shunted across a capacitance, C, the value of $\overline{v^2}_{NR}$ across the parallel combination is given by

$$\overline{v^2}_{NR} = \frac{4\ K\ T\ R\ \Delta F}{1\ +\ (\omega RC)^2} \tag{5.2}$$

and the total mean square thermal noise is obtained by integrating equation (5.2) over all frequency intervals.

$$v^2_N = \int_0^\infty \frac{4\ K\ T\ R\ d\ f}{1\ +\ (2\pi\ f\ R\ C)^2} = \frac{KT}{C} \tag{5.3}$$

Equation (5.2) clearly shows that as R increases $\overline{v^2}_N$ decreases providing C is not too small.

The series resistance R_S is likewise shunted across a capacitance and the noise, $\overline{v^2}_N$, is usually negligible even though R_S is much smaller than R_p. The reason why the $\overline{v^2}_N$ is comparable or larger than the $\overline{v^2}_N$ for the parallel branch is that the series capacitance is much smaller.

Several components contribute to the leakage current. First, leakage around the periphery of the detector in the high electric field region produces an increased level of low frequency noise. Imposing a guard-ring and suitable epoxy around the edges will considerably reduce this leakage. No adequate model has been developed to explain this source.

The second major contributor to the leakage current is shot noise derived from random fluctuations in the number of charged carriers emitted

.from a surface. By applying statistical mechanics again, the functional dependence is obtained

$$\overline{I_S{}^2} = 2I_L \, q \, \Delta f \tag{5.4}$$

where I_L is the detector leakage current and Δf is the frequency interval in which the measurements are made.

By similar analysis as made for equation (5.2) employing Kirchoffs voltage law the $v^2{}_{NS}$ across the parallel combination of the noisy current source and equivalent capacitance is

$$\overline{v^2{}_{NS}} = \frac{2q \, I_L \, f}{(\omega C_{eqv})^2} \tag{5.5}$$

and the total mean square thermal noise is obtained by integrating equation (5.5) over the appropriate frequency intervals.

$$\overline{v^2{}_{NS}} = \frac{1}{2\pi^2} \int_{F_1}^{F_2} \frac{I_L \, df}{C^2{}_{eqv} \, f} = \frac{q \, I_L}{2\pi^2 \, C^2{}_{eqv}} \, ln \, \frac{F_2}{F_1} \tag{5.6}$$

Figure 5.1 gives the noisy equivalent circuit. Figure 4.19 shows the leakage contributions of shot noise and peripheral leakage due to contaminants.

5.1.2 *Detector bias regulation*. Over the life of the detector the leakage current is expected to vary and thus precautionary measures should be made to regulate the applied bias voltage. Figure 5.2 is a
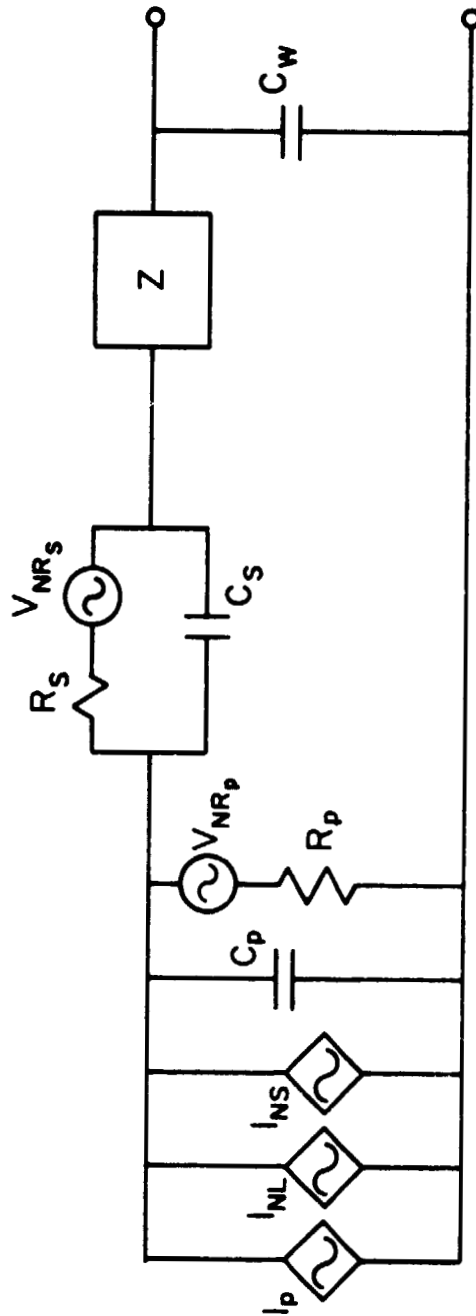
Figure 5.1 Solid-state noise equivalent circuit. The current sources I_p, I_{NL}, and I_{NS} represent the current introduced by an energetic particle, by the leakage noise and by the shot noise, respectively. V_{NRS} and V_{NRp} represent the noise introduced by the resistors R_p and R_s.
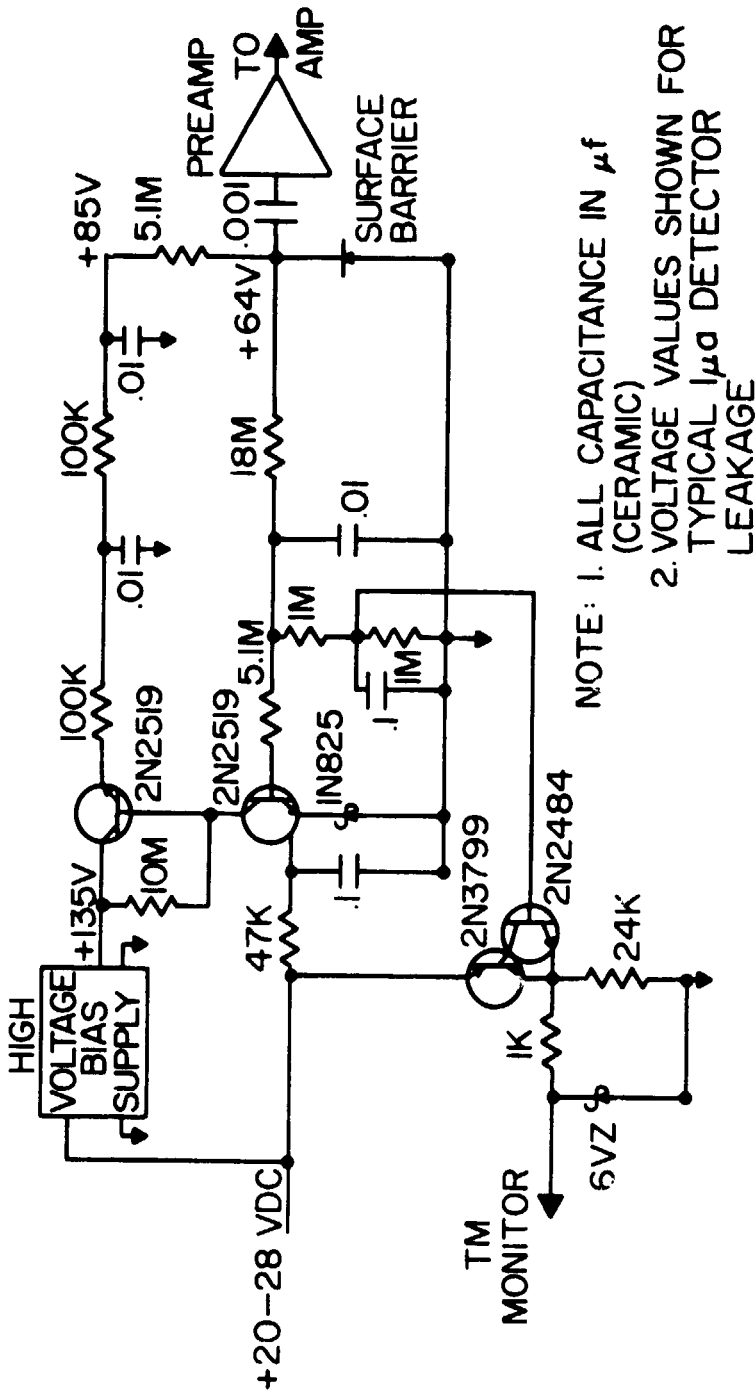
Figure 5.2 Circuit diagram employed to regulate the bias current for a surface barrier detector. Factors known to significantly change the current are temperature, radiation, and long-range storage. Proper bias insures correct preamp matching and minimizes noise (Circuit taken from *Bakke et al.* [1969]).

detailed circuit diagram employed by *Bakke et al.* [1969] to regulate a surface barrier detector and would be an excellent improvement over the present system, to be described later.

The depletion region width (and therefore capacitance) is directly related to the applied bias (equation 4.16) and consequently to the thermal noise. Figure 5.3 is a plot of noise versus applied bias voltage for the Ortec detector displayed in Figure 4.1

To measure the bias voltage accurately, an extremely high input impedance meter must be employed since the detector resistance is approximately 5×10^8 ohms. The circuit (Figure 5.4) uses an operational amplifier with an input resistor of 2×10^{10} ohms.

5.1.3 *Mathematical treatment of noise and its temperature varia-tion.* The most significant factor in reducing noise is to lower the temperature. To facilitate a fundamental understanding of the arguments involved, an investigation will be made of the spectrum characteristics of noise.

Since noise in a material originates from the unequal balance of random mutually-exclusive charge-carrier events, the guassian distribution applies. It is expressed in mathematical form as

$$P(E)dE = \frac{1}{\sqrt{2\pi}\sigma} \exp\left[- \frac{(E-\mu)^2}{2\sigma^2} \right] dE \tag{5.7}$$

where $P(E)$ is the probability that in an energy interval E to $E + dE$ there exists $\frac{N_i}{N_o}$ charge movements across the band gap E_g, N_i is the charge movements in the ith interval and N_o is the maximum charge movements made
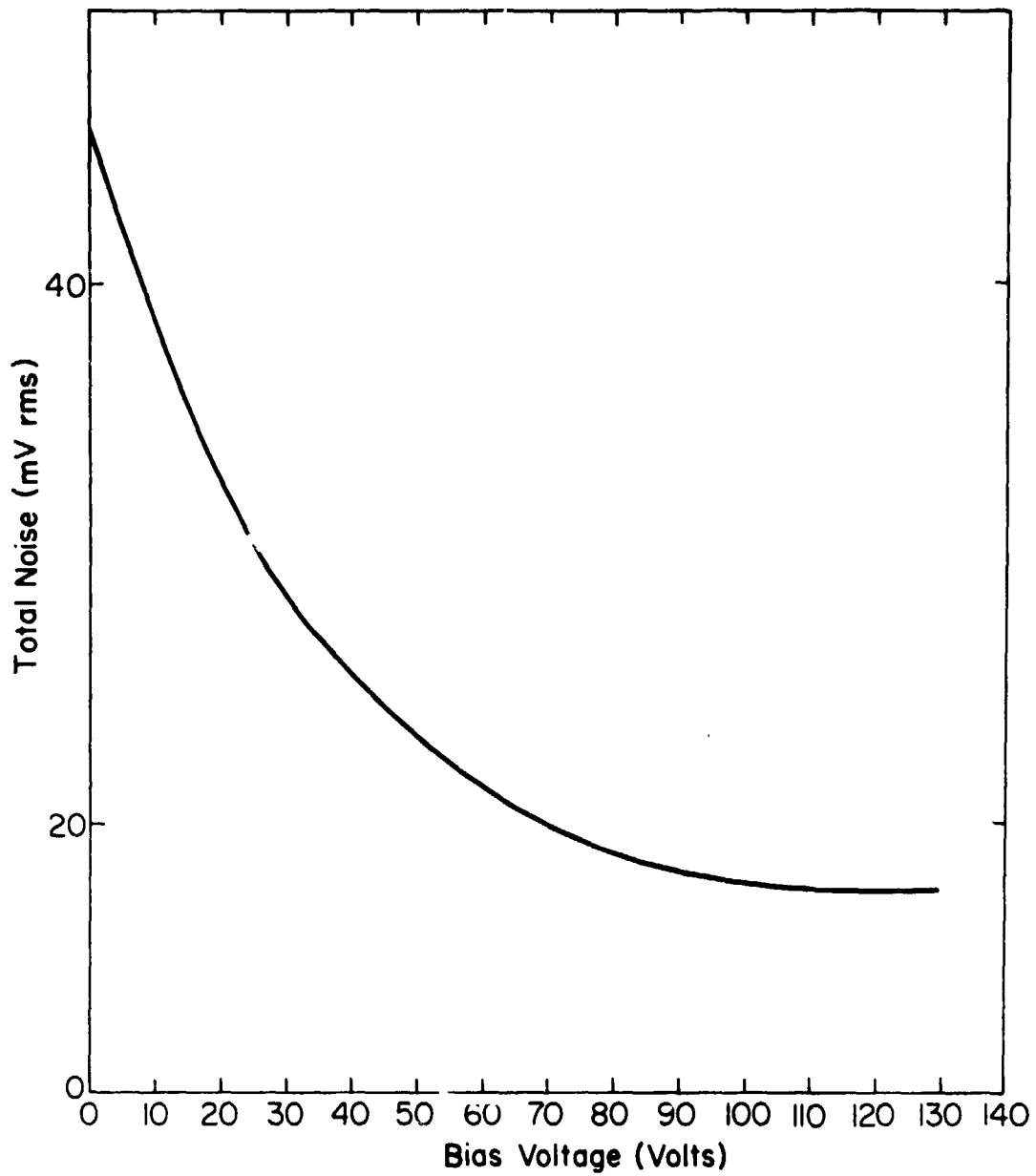
Figure 5.3 Surface barrier detector total noise versus bias
voltage. Designed bias is 130 volts.
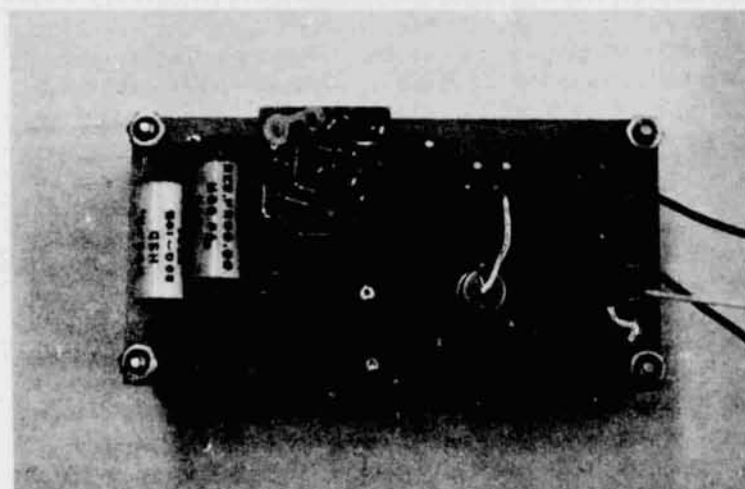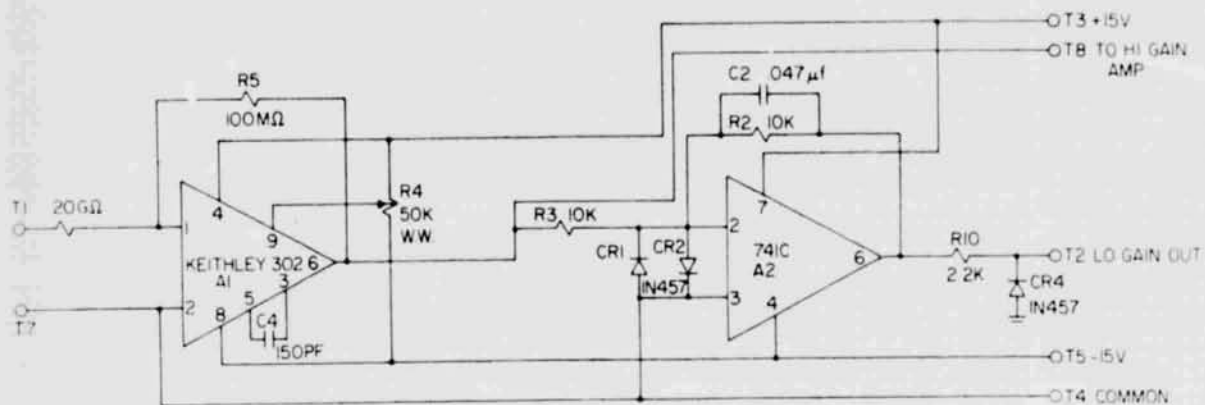
Figure 5.4   Shown is the high input impedance circuit used to measure
the bias voltage across the detector diode.

in the interval, σ is the standard deviation, and μ is the offset of the gaussian peak due to unequal probabilities of generating (g) and recombination (r) of charge carriers. The distribution is depicted in Figure 5.5 along with the defining parameters and may be compared to the actual distribution taken from the detector utilizing a pulse height analyzer.

The essential statistical expressions for μ and σ are given by

$$\mu = (g-r)N\,E_g$$

$$\sigma = 2\sqrt{Ngr}\,E_g$$

(5.8)

Here E_g is the mean energy required to generate one electron hole pair. For pure noise, i.e. random noise, $g = r$ and therefore $\mu = 0$ and

$$\sigma = E_g\sqrt{N_T} = E_g\,\frac{Q_N}{q}$$

(5.9)

where q is the elementary charge unit 1.6×10^{-19} coulomb and Q_N is equivalent noise generated at the amplifier input. The second equality intuitively comes from the fact that the number of carries which jump the energy gap E_g (a capacitance, C_d) have a dependence on energy equal to $Q^2{}_N/2C_d$. The next two important relationships for σ follows directly from their defining properties.

$$\sigma = \frac{E_g}{q}\,C_{eqv}v_{rms} = \frac{FWHM}{2.35}$$

(5.10)
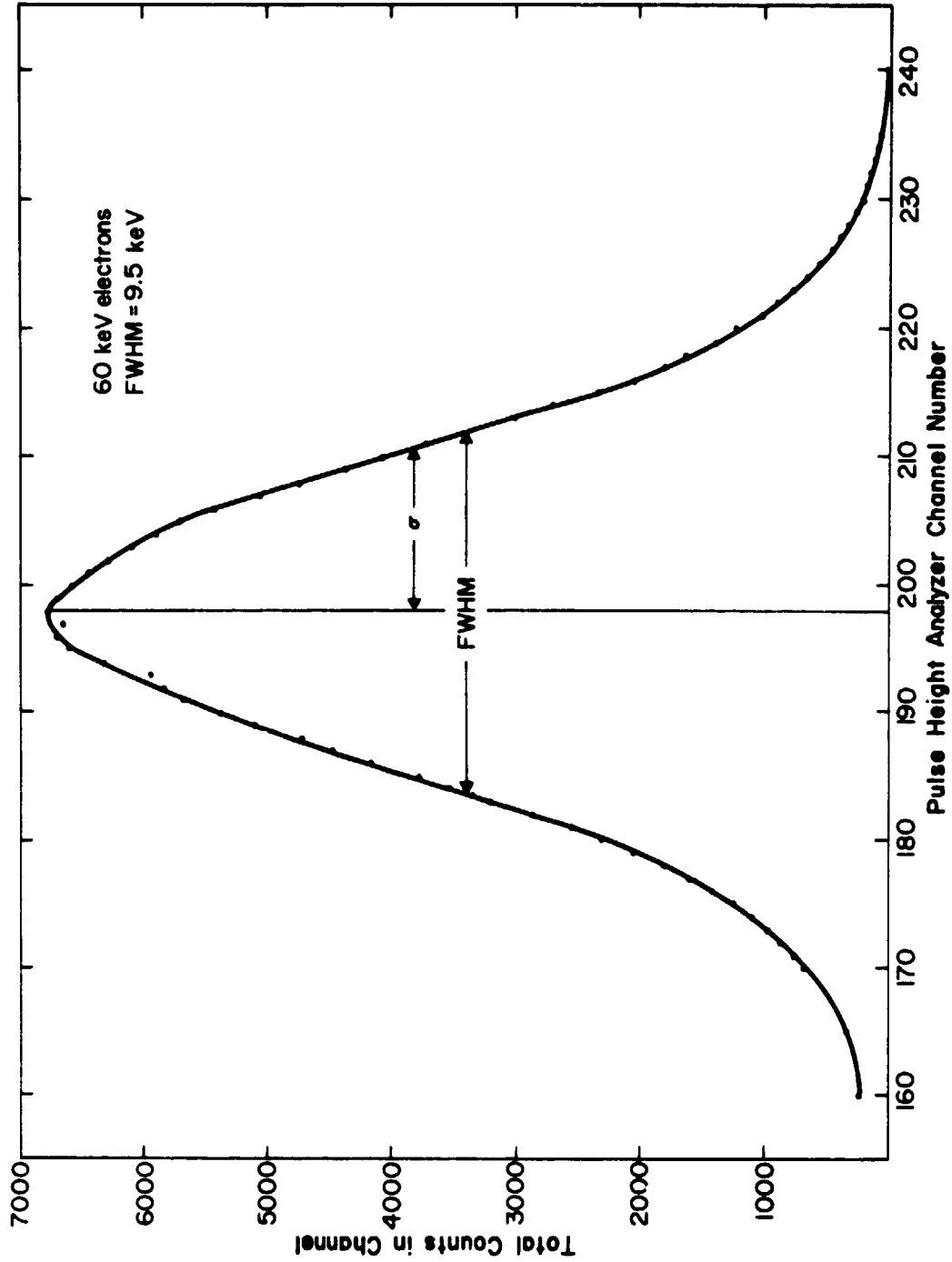
Figure 5.5   Experimentally-derived distribution for 60 keV electrons obtained from a
pulse height analyzer. Each channel represents an interval of 0.317 keV
giving a FWHM of 95 keV.   In this case μ is channel 198 representing 60 keV
and σ = FWMH/2.35 = 4.05 keV.

$$G_v = \frac{\sqrt{v^2_{NO}}}{\sqrt{v^2_{NI}}} = \frac{\sqrt{v^2_{NO}}}{5.2 \times 10^{-16}} \, C_{eqv} = \frac{v_{sig}}{\frac{C_1}{C_1 + C_{eqv}} \, v_{ger}} \simeq \frac{v_{sig} \, C_{eqv}}{v_{ger}} \qquad (5.12)$$

Solving for v^2_{NO} one obtains approximately 19 mV which agrees close with 19.5 mV measured. The small error is due to incomplete specification of the complex input impedance.

Now the first channel discriminator is set near the tail of the gaussian distribution and therefore σ is of considerable importance, especially since $\sigma = f(T)$. To start with, the probability of an event occurring greater than some threshold energy, E_T, of the detector must be determined. The result is obtained by integrating over $P(E)dE$ distribution from E_T to ∞ or

$$P(> E_T) = \frac{1}{\sigma \sqrt{2\pi}} \int_{E_T}^{\infty} e^{-1/2 \left(\frac{v-m}{\sigma} \right)^2} dv$$

or

$$P(> E_T) = 1 - \frac{1}{\sigma \sqrt{2\pi}} \int_{-\infty}^{E_T} e^{-1/2 \left(\frac{E-\mu}{\sigma} \right)^2} dE \qquad (5.14)$$

$$\equiv 0.5 - \Phi \left(\frac{E-\mu}{\sigma} \right)$$

where

$$\Phi \left(\frac{E_T-\mu}{\sigma} \right) \qquad \Phi(z) = \frac{1}{\sqrt{2\pi}} \int_{-\infty}^{z} e^{-z^2/2} \, dz \; erf \left(\frac{z}{\sqrt{2}} \right)$$

The integral values for the $\phi(z)$ are tabulated and found in any mathematical handbook. For the designed detector, the threshold energy was set at 11.6 keV hence $z = 11.6/3.6 = 3.23$ yielding from the tables $\phi(3.23) = 0.99936$ or $P(> E_T) = 6.4 \times 10^{-4}$. Therefore, the total number of counts from equation (5.9) is 9.4×10^6 requiring the number of counts greater than E_T to be $N_T = 6000$ counts per second. This agrees with the experimental results displayed in Figure 5.6 for a temperature of 30°C.

To deduce theoretically the $\sqrt{v^2}_N$ vs. channel one count rate, equations (5.9), (5.10), and (5.14) must be used. For a change in the root mean squared voltage, there is a corresponding linear charge in the standard deviation (equation 5.10). The number of counts for energies greater than E_T, $N(\ E_T)$, is thus given by

$$N(> E_T) = P(> E_T)N_T = \left[1 - erf\left(\frac{E_T}{\sqrt{2\sigma}} \right) \right] \left(\frac{\sigma}{E_g} \right)^2 \qquad (5.15)$$

Substituting for σ from equation (5.9) and (5.12) gives

$$N(> E_T) = \left[1 - erf\left(\frac{E_T\ q\ G}{2E_g C_{eqv}\sqrt{v^2}_{ON}} \right) \right] \left[\frac{C_{eqv}\sqrt{v^2}_{ON}}{qG} \right]^2 \qquad (5.16)$$

Now using $v_{rms} = 14$ mV, equation (5.16) gives a count rate of 60 counts per second which agrees beautifully with the experimental curve.

The temperature dependent curve of Figure 5.6 is likewise related to the number of counts above E_T by equation (5.15); however, σ is now a function of temperature. The particular functional form will be
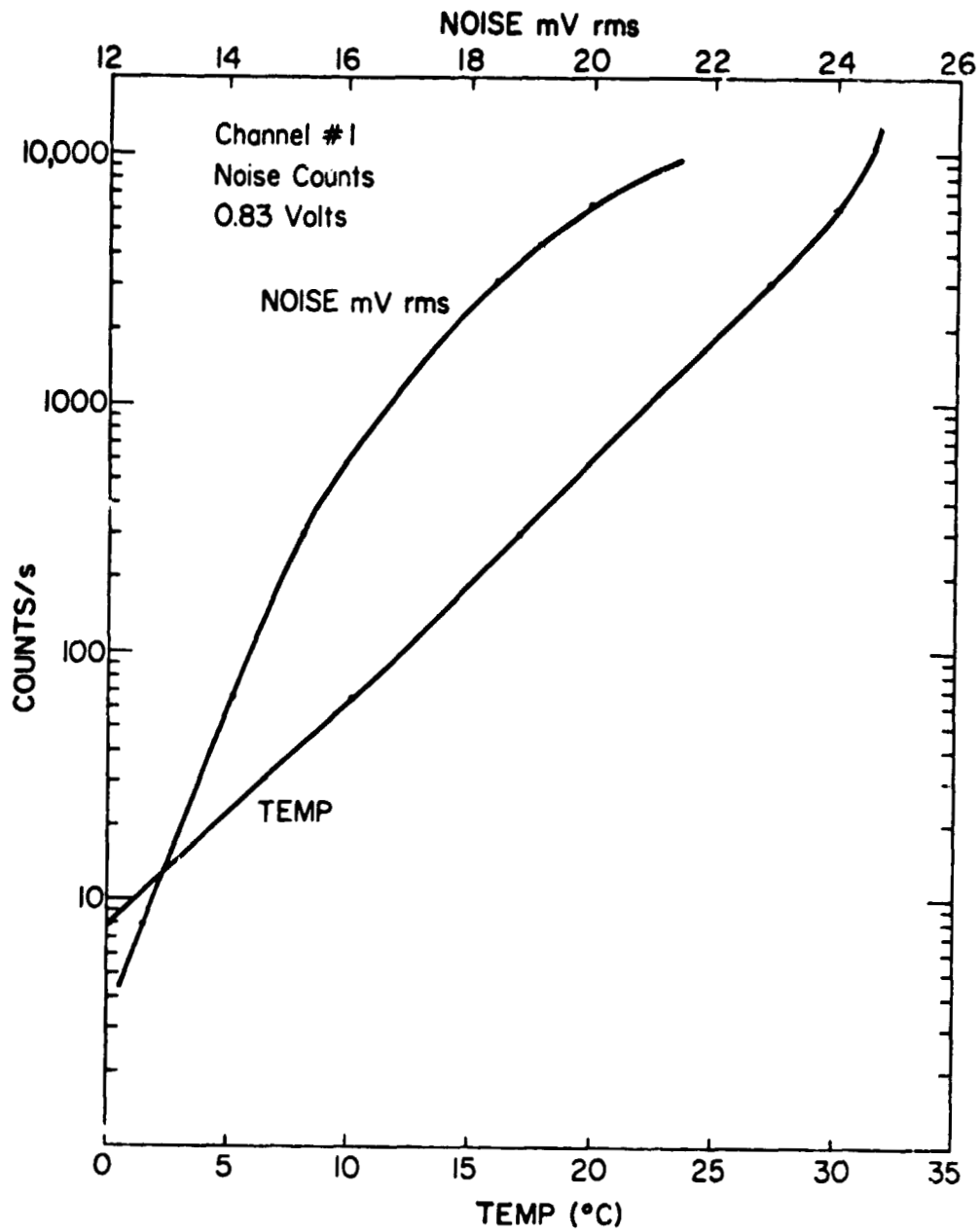
Figure 5.6 Total noise counts recorded above the lowest channel threshold voltage, 0.83 volts for various temperatures and root mean square voltages.

investigated after a study is made of the preamplifier noise contribution. From Figure 5.6 it is apparent that $\sigma(T)$ must be some function which is less sensitive to T than the linear dependence of equation (5.10). Referrin, to equations (5.18), (5.9), and (5.15) the general temperature dependence of the channel counts above a threshold energy can be formulated.

5.2 *Preamplifier Noise and Detector Postamplifier Interface*

5.2.1 *System amplification philosophy.* A complete block diagram of the detection and amplifying circuits is represented in Figure 5.7. The current introduced into the preamp from an energetic particle is integrated in the first stage by applying capacitive feedback. The resulting charge pulse is shaped and amplified in succeeding stages. The preamplifier is a double differentiation and double integration pulse shaping network with a low noise high input impedance field effect transistor employed in the first stage. Postamplification is made for final pulse height discrimination. The Norton equivalent circuit is substituted for the detector.

Experiments show that the Norton admittance is primarily capacitive in nature where upon simple analysis yields the first stage output. By making a Thevenin equivalent to the left of the first stage and assuming the coupling capacitance and resistive feedback are chosen to have minor influence on the output, the basic relation for operational amplifiers applies; namely

$$E = - \frac{1}{R_T C_S} \int E_T \, dt \qquad\qquad (5.17)$$

Particle Amplification Stages
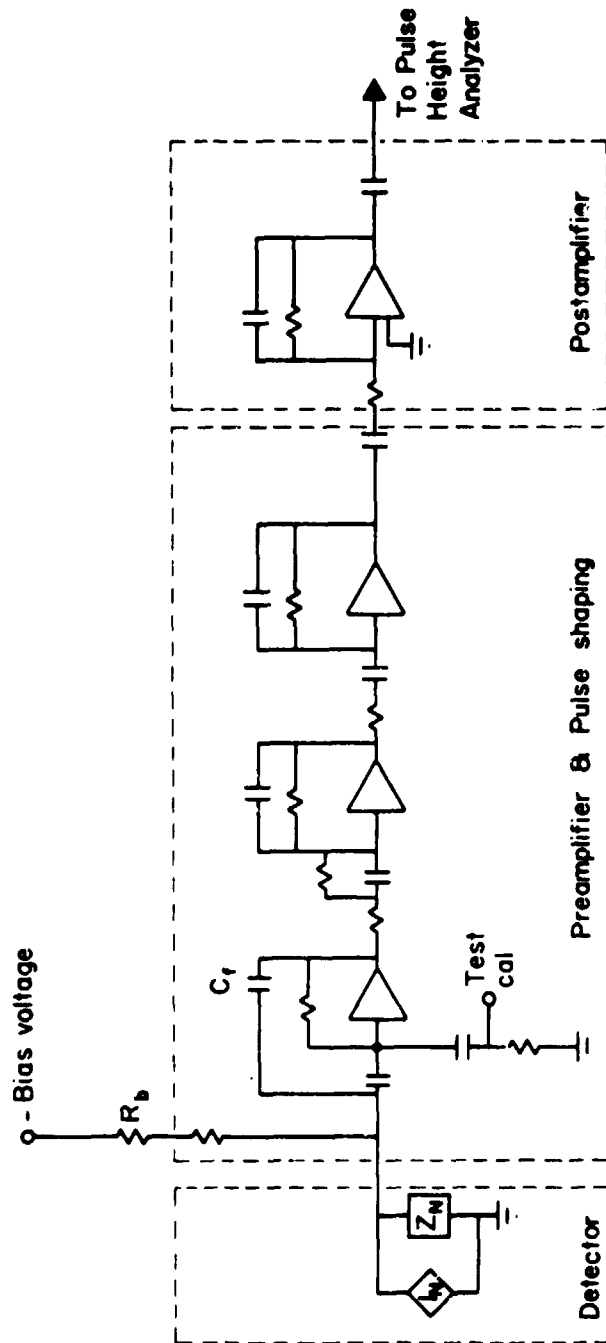
Figure 5.7 Basic amplification system. The detector is represented by the Norton equivalent impedance and current source. The final three amplifiers are used for gain and pulse shaping using triple integration and double differentiation circuits.

where E_T and R_T are the Thevenin equivalents, given by

$$E_T = \frac{\dfrac{R_B}{V_B} + I_N(t)}{\dfrac{1}{R_B} + j\omega C} \qquad\qquad R_T = \frac{R_B \dfrac{1}{j\omega C}_{eqv}}{R_B + \dfrac{1}{j\omega C}}$$

This can be reduced to the following relation

$$E_o = -\frac{1}{C_f}\int I(t)\,dt = -\frac{Q}{C_f} \qquad\qquad (5.18)$$

The collected charge produces a voltage signal of magnitude Q/C_f. This is independent of the detector capacitance and thus applied bias giving improved overall stability. The available signal energy supplied from the detector is $Q^2/2C_N$ requiring C_N to be minimized for increased signal-to-noise ratio.

5.2.2 *Equivalent preamplifier noise generator.* The field effect transistor (FET) used as the first stage of the preamplifier was chosen for its inherent low noise performance, simplicity, ruggedness, and ability for substantially reducing noise upon cooling. Later improvements would have the FET mounted adjacent to the detector and both cooled, for example by dry ice. On an energy basis the sensitivity could be improved by a factor of two. The present design utilizes a detector designed specifically for rocket-borne applications by Nucleometrics and is pictured in Figure 5.8 and in schematic form in Figure 5.9. Table 5.1 list the preamplifier specification.

The proper interface of the detector with the preamplifier requires optimization of the preamplifiers sensitivity, time constants, and input
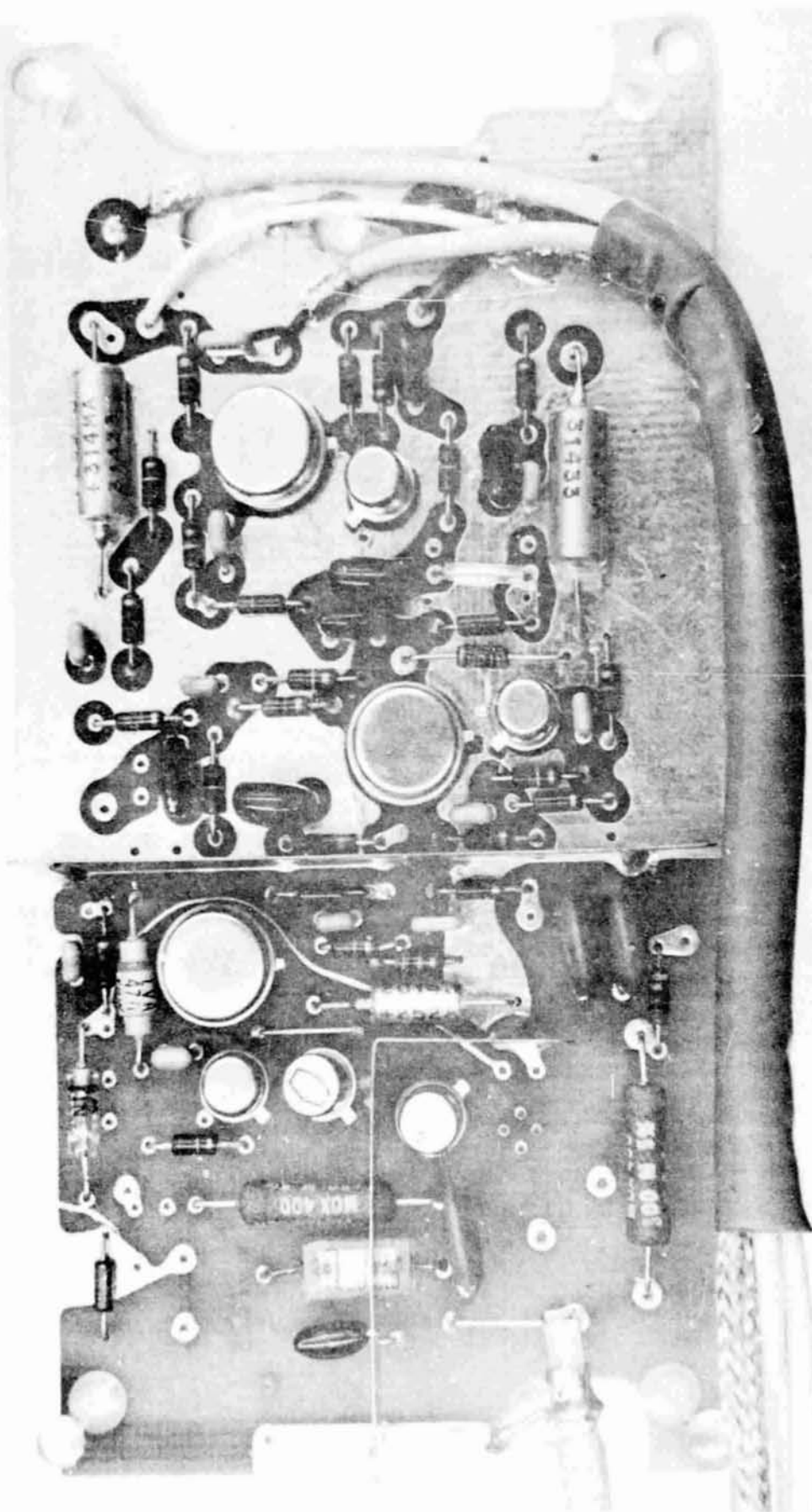
Figure 5.8 Preamplifier assembly and electronics developed by Nucleometrics and specifically designed for detector pictured in Figure 4.1.
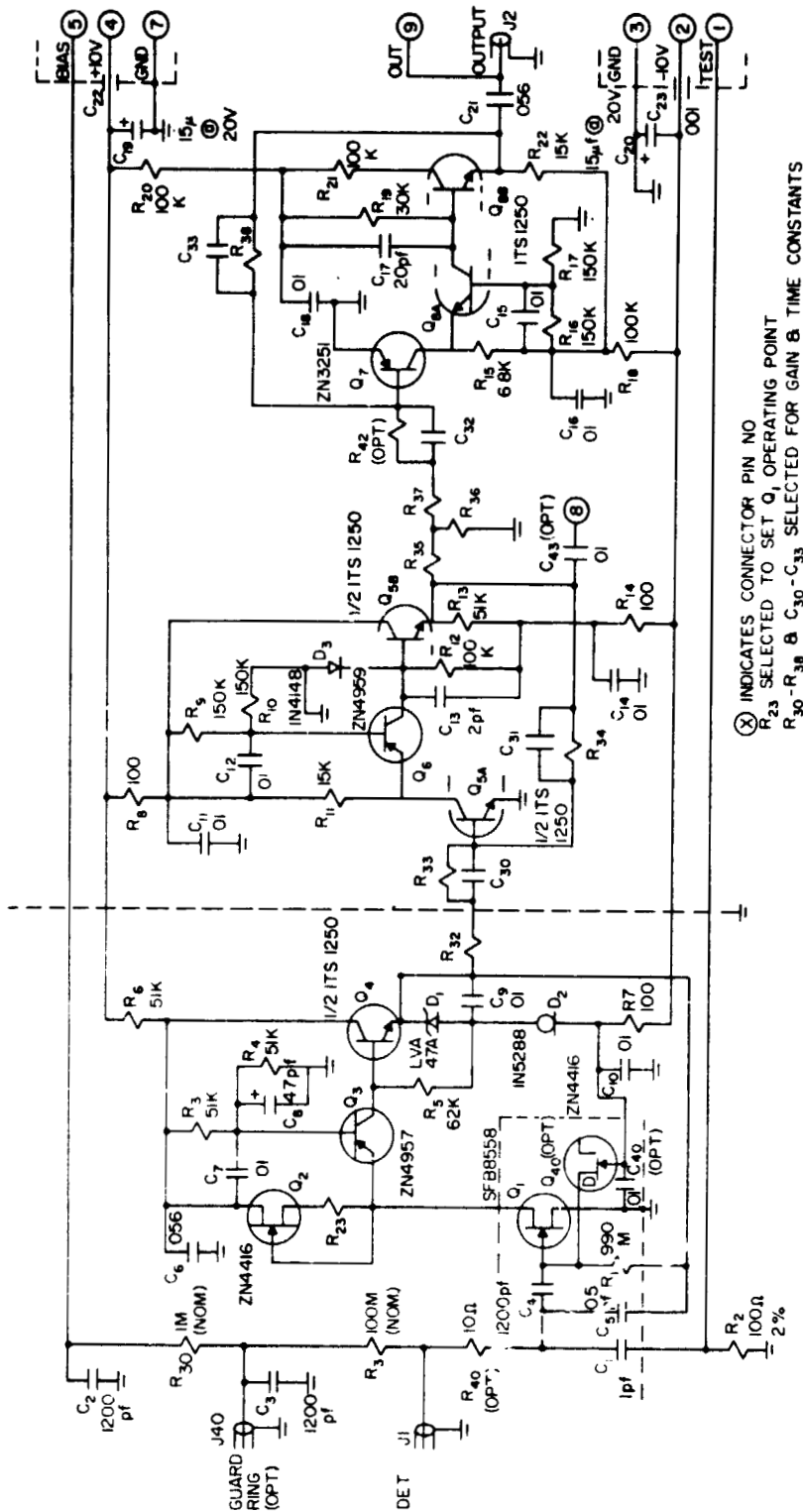
Figure 5.9 Preamplifier circuit diagram showing the pulse shaping and amplification stages.

Table 5.1

Charge Sensitive Amplifier

Specifications

Sensitivity: 22 to 110 v/pC

Time constant: 0.5 to 2 micro-sec

Load resistor: 100 meg ohm

Dynamic input capacitance: 5000 pf

Temperature stability -40°c to +60°c: ±1%

Gain variation with supply voltages: 1%/v

Dynamic output impedance: <20 ohm

Integral linearity to 5.0 v output: ±0.2%

to 2.5 v output: ±0.05%

Overload recover x 10 : 30 micro-sec

x 100 : 50 micro-sec

x 1000: 100 micro-sec

For 40 pf input capacitance: Noise: <5 keV FWHM (Silicon)

Rise time: <20 nano-sec

With 100 meg ohm load resistor: Noise: <2 keV FWHM (Silicon)

Power required: Positive: +9 to +12 v, 8 ma

Negative: -9 to -12 v, 2 ma

Detector bias: 250 v (max)

Input/output polarity: Detector input: negative

Test pulse input: negative

Amplifier input: positive

Dimensions: 4.375 x 2.375 x 0.820 in

Weight: <6 oz.

Connectors: Input/output (each): Microdot S-93 screw receptacle

Power/Test/Bias: Cannon DEM-9P

Environment: Appropriate for use in Nike Apache rocket payloads.

impedance. A rigorous analysis requires the aid of computer program routines and will be discussed in Section 5.2.4. Briefly, the mean equivalent input noise charge, Q_N, characterizing the preamplifier detector is the aggregate noise of the component systems. The two primary types of noise sources have been introduced in previous sections and are represented by equations (5.1), (5.2), and (5.5). The total noise is then the sum of the energy contributions of each of the parts being related to the voltages as V^2_N. The total noise is consequently the square root of the sum of the squares of the individual V^2_N, hence

$$Q_N = C_{eqv} \left[\frac{4kT \ R_{eqv}}{\tau} + \frac{4kT \ \tau}{R_B C^2_{eqv}} + \frac{2q(I_L + I_g)\tau}{C^2_{eqv}} + A_f \right]^{1/2} \qquad (5.18)$$

Furthermore, by making the reasonable approximation that the flicker noise and the R_B noise are minor the following simplifications result at a temperature of 273°K.

$$Q_N = 15 \times 10^{-21} \frac{R_{eqv} \ C_{eqv}}{\tau} + 3.2 \times 10^{-19}(I_g + I_L) \qquad (5.19)$$

The optimum time constant, τ_{opt}, for minimizing the noise is obtained by differentiating equation (5.19) with respect to τ and setting the derivative to zero. The equivalent input noise for optimum time constant is thus

$$\tau_{opt} = 0.22 C_{eqv} \frac{\sqrt{R_{eqv}}}{I_g + I_L} \qquad (5.20)$$

Again it is apparent that decreasing the input capacitance and leakage current is desirable along with increasing the transconductance, g, since $R_{eqv} \simeq 0.7/g$ [Bilger, 1966] for a FET. The optimum input noise level is consequently

$$Q^2_{N\ opt} = 1.3 \times 10^{-19}\ C_{eqv}\ R_{eqv}(I_g + I_L) \qquad (5.21)$$

The particular equivalent noise input for the preamplifier for various input capacitance and time constants 0.5, 1.0, and 2.0 μsec are shown in Figure 5.10. The electronics noise contribution can be expressed in charge units since this is what the amplifier is designed to measure. Either the units are expressed in equivalent electron charge (coulombs) or in terms of their spread in a gaussian distribution associated with the probability that a monoenergetic particle will produce carriers. The latter method uses the full spectral width at half the maximum (FWHM) of the distribution. The output noise can alternatively be recorded as a root mean square voltage or current and is related to the equivalent charge by equations (5.9) and (5.10). Since E_g is a function of the material used the FWHM must also be associated with a material e.g., FWHM (silicon).

Two methods employed to experimentally measure the FWHM are by direct measurement of the spectral width from a multichannel pulse height analyzer or indirectly using the root mean square voltmeter method. The latter method is based on applying a generator voltage pulse of amplitude V_{gen} through an injection capacitor C, to the

NOISE IN KeV FWHM (SILICON)
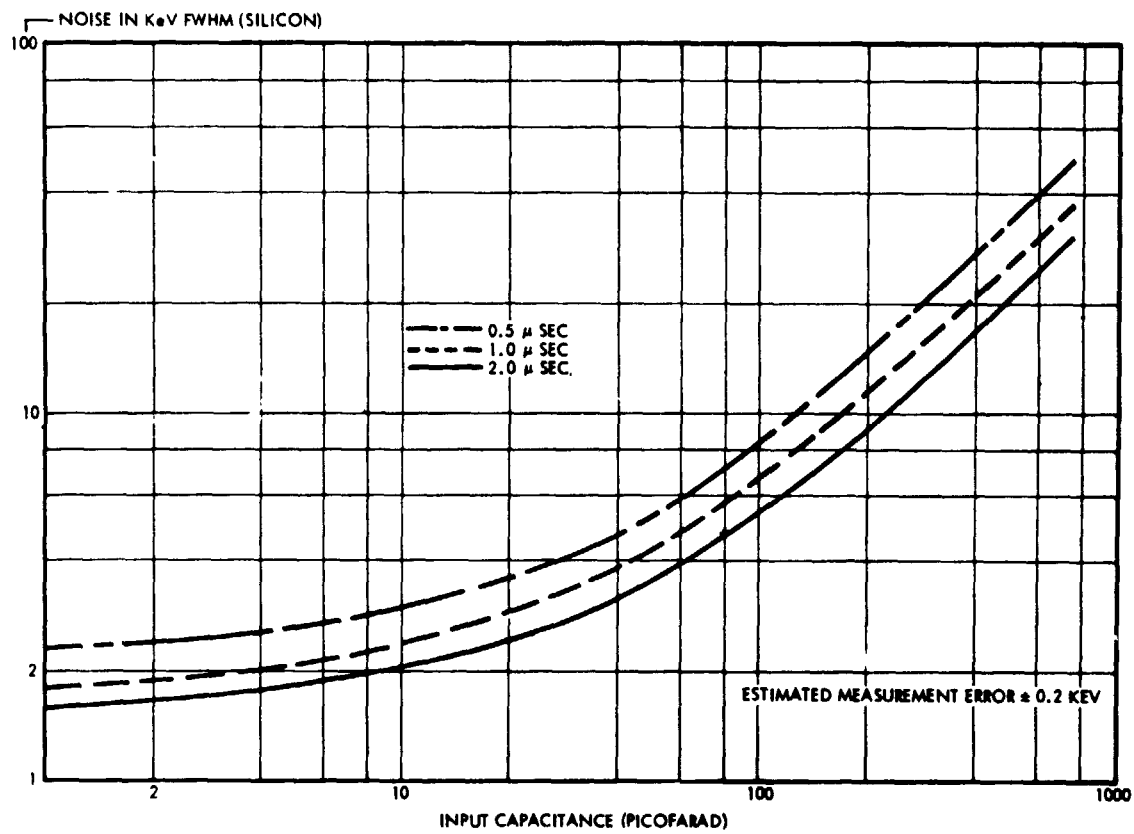
Figure 5.10 Amplifier noise versus input capacitance for preamplifier
time constants of 0.5, 1.0, and 2.0 μsec. From Nucleometrics
specification sheet.

detector preamp input. The signal input charge to the FET is the series combination of C_1 and C_{eqv}

$$Q_{sig} = \frac{V_{gen} \, C_1 \, C_{eqv}}{C_{eqv} + C_1} \tag{5.21}$$

and if C, is chosen small with respect to C_{eqv} the above equation becomes

$$Q_{sig} = C_1 \, V_{gen}$$

If Q_N is the equivalent noise charge at the amplifier input required to produce V_{rms} noise voltage at the output than for an overall calibration gain G_c the following expression is valid

$$G_c \propto \frac{v_{rms}}{Q_N} \, \frac{V_{sig}}{Q_{sig}}$$

and the final result obtained is

$$Q_N = \frac{Q_{sig} \, v_{rms}}{V_{sig}} + \frac{V_{gen} \, C \, v_{rms}}{V_{sig}} \tag{5.22}$$

Referring to the schematic diagram of Figure 5.9, the time constants are governed by C_{30}, C_{31}, C_{32}, C_{33}, and R_{33}. Table 5.2 gives the suggested values for selected time constants of 0.5, 1, and 2 msec.

For the Ortec ruggedized surface barrier partially depleted detector (Figure 4.1) the capacitance is 52 pf, the noise is 5 keV FWHM and reverse current 0.23 μamps. The R_{eqv} of the detector preamplifier is approximately equal to or less than 10^{-3} ohms. Substituting these parameters into equation (5.20) yields a design time constant of 0.5 μsec.

Table 5.2

Amplifier time constant adjustment.

Time Constant (μsec)	C_{30}	C_{31}	C_{32}	C_{33}	R_{33}
0.5	100	3.0	100	3.0	5.1 Meg
1	200	6.0	200	6.0	2.4 Meg
2	390	13	390	13	1.3 Meg

The gain resistors

R_{32}	R_{34}	R_{35}	R_{37}	P_{38}
5.1	150	5.1	0	150

5.2.3 *Pulse shaping network*

The step response to a positive 10 mV test calibration pulse produces the output response shown in Figure 5.11 for a sweep rate of 0.5 msec per cm and vertical sensitivity of 0.2V cm. The v_{rms} output noise v is measured to be 0.19 volts yielding an equivalent input noise of 5×10^{-16} coulombs by application of equation (5.22). For comparison purposes, a 10 keV particle loses approximately 3.5 eV per released charge carrier (as previously discussed) contributing a total charge of 4.7×10^{-16} coulombs, comparable with the noise as anticipated.

The approximation made in equation (5.18) that the bandwidth is Δw is about $1/\tau$ where τ is the time constant of the shaping circuits can be more fundamentally formulated in terms of the system frequency response. Proceeding with equation (5.17) with the stipulation that the flicker noise component is of minor significance the translated equality becomes

$$\overline{v^2_{NT}} = \frac{\Delta w}{2\pi C^2_{eqv}} \left[a + \frac{b}{w^2} \right] \tag{5.23}$$

where

$$a = 4kT \, \frac{0.7}{gm} \, C^2_{eqv}$$

and

$$b = \frac{4kT}{R_b} + 2q(I_g + I_L)$$
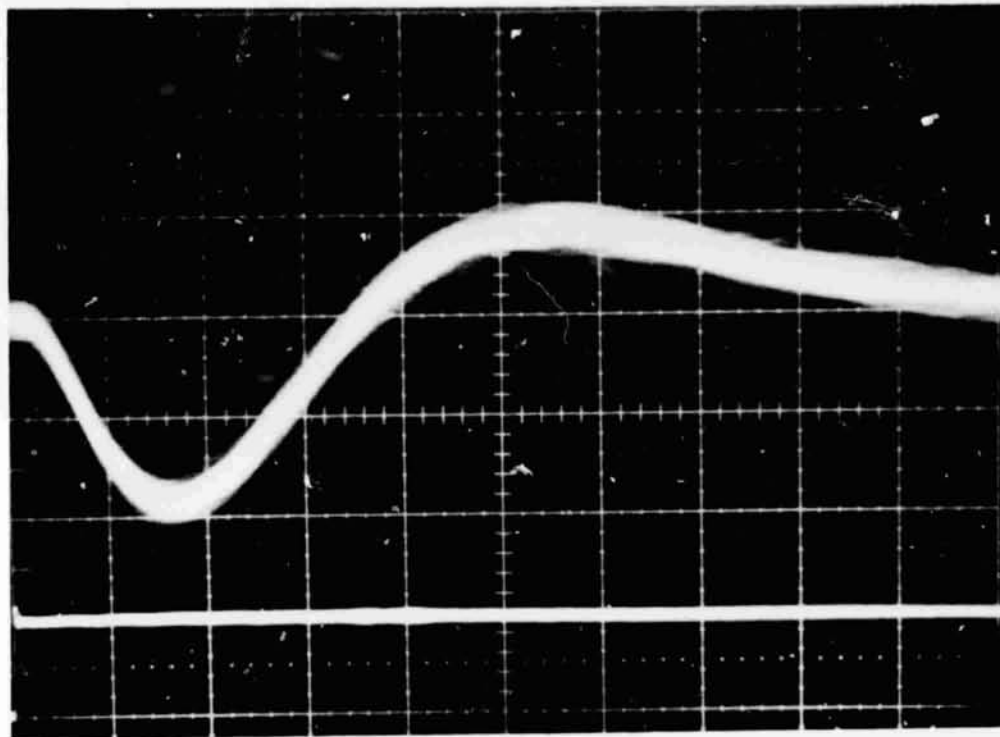
Figure 5.11 Preamplifier step response (top trace) for a positive
10 mV test calibrate input pulse (bottom trace). The
horizontal sweep rate is 0.5 μsec per main division
and the vertical sensitivity is 0.2 volts per main
division.

To obtain the overall spectral noise characteristics an integration must be performed over all frequency intervals Δw of the product of the noise contribution times the attenuation index, $f(w)/F(o)$, for the frequency w where $f(w)$ is the frequency response of the system and $F(o)$ is the normalization factor equal to the maximum value of $f(w)$ or equivalently the maximum amplitude of the system step response (Figure 5.10).

$$Q_{NT} = \left[\frac{q}{2\pi F^2(o)} \int_0^\infty \left(a + \frac{b}{w^2} \right) f^2(w) \; dw \right]^{1/2} \qquad (5.24)$$

Listed in Table 5.3 [*Tsukuda*, 1964] are the significant pulse shaping networks and their associated parameters. The optimum equ valent noise charge, (ENC), is the Q_{NT} divided by the unit charge 1.6×10^{-19} coulomb. Here it is seen that the delay line clipping (DL) networks perform better than the RC types; however, to construct filters possessing variable time constants, as is mandatory in delay line clipping, is not a simple undertaking. Improvements here could reduce noise by as much as 40% and future designs should incorporate the delay line clipping methods as they become available.

For the system designed, a RC filter was chosen using double differentiation and double integration stages. Referring to the schematic Figure 5.9 the first and second differentiation is governed by R_{32}, C_{30}, and R_{35}, R_{36}, R_{37}, C_{32}, and the first and second integration by R_{34}, C_{31} and R_{38}, C_{33}, respectively. The input pole zero cancellation by R_{42}, C_{32}.

The frequency response $f(w)$, is obtained from basic circuit analysis although very tedious in procedure for a complete analysis (NOISE

Table 5.3

Optimum signal to noise ratio obtainable with different pulse shaping networks. Data compiled by *Tsukuda* [1964].

Pulse shaping network		Frequency response of the filter $f^2(\omega)$	ENC opt	$T_{int\cdot opt}$	$\lambda_{opt} = \dfrac{T_{diff}}{T_{int}}$	Pulse shape
Differentiator	Integrator					
(DL)²	RC or operational	$\dfrac{\sin^4 \omega T_D}{(1+\omega^2 T^2_{int})}$	$1.075\,\sqrt[8]{ab}$	$T_{diff\cdot opt} = 1.7\sqrt{ab}$	$\lambda \to 0$	
DL	RC	$\dfrac{\sin^2 \omega T_D}{(1+\omega^2 T^2_{int})}$	$1.098\,\sqrt[4]{ab}$	$1.29\sqrt{\dfrac{a}{b}}$	1.036	
DL	(RC)²	$\dfrac{\sin^2 \omega T_D}{(1+\omega^2 T^2_{int})}$	$1.107\,\sqrt[4]{ab}$	$0.53\sqrt{\dfrac{a}{b}}$	2.623	
RC	(RC)²	$\dfrac{\omega^2 T^2_{diff}}{(1+\omega^2 T^2_{diff})(1+\omega^2 T^2_{int})^2}$	$1.215\,\sqrt[4]{ab}$	$0.57\sqrt{\dfrac{a}{b}}$	1.06	
RC	RC	$\dfrac{\omega^2 T^2_{diff}}{(1+\omega^2 T^2_{diff})(1+\omega^2 T^2_{int})}$	$1.355\,\sqrt[4]{ab}$	$\sqrt{\dfrac{a}{b}}$	1	
(RC)²	RC	$\dfrac{\omega^4 T^4_{diff}}{(1+\omega^2 T^2_{diff})^2(1+\omega^2 T^2_{int})}$	$1.406\,\sqrt[6]{ab}$	$1.4\sqrt{\dfrac{a}{b}}$	1.38	

Note DL = delay line clipping, (DL)² = double delay line clipping.

computer solution, Section 5.2.4) the primary response may be made referring to the simplified circuit illustrated in Figure 5.7. Transforming into the Laplace transform space, the output response is quite simply the system transfer function, $H(s)$, multiplied by the input excitation.

$$V_o(S) = H(s) \ V_i(s) \tag{5.25}$$

The frequency response is obtained from the complex Fourier transform space which may be obtained by substitution of jw for s in equation (5.25).

The magnitude, $|H(jw)| = H(\omega)$, is the corresponding frequency response and the angle θ of the complex point $H(jw)$ is the phase change of the output to the input excitation

The step $(V_i = \frac{1}{s})$ response of the preamplifier is shown in Figure 5.10 and may be used to graphically evaluate $H(w) = |jw \ V_o \ (jw)|$ where $V_o(s)$ is determined from the Laplace transform definition.

$$V_o(jw) = V_o(s) = \int_0^\infty \upsilon_o(t) \ e^{-st} \ dt \tag{5.26}$$

To gain an understanding of the functional dependence of the frequency response an analytical expression may be obtained utilizing the simplified circuit of Figure 5.7. Here the transfer function is the product of the transfer function of each of the similar pulse shaping networks. For an operational amplifier with feedback, Z_f, and input, Z_i,

impedance the gain and thus the single transfer function is given by $-z_f/z_i$ and the two stage complex transfer function is the product $z_{f1}z_{f2}/z_{i1}z_{i2}$

$$H(s) = \frac{s^2 R_{1f} C_{i1} R_{2f} C_{i2}}{(1 + S\tau_{f1}) (1 + S\tau_{f2}) (1 + S\tau_{i1}) (1 + S\tau_{i2})} \tag{5.27}$$

where $\tau_{f1} = 1/(R_{1f} C_{1f})$ is the time constant of the first stage feedback, etc. For stability reasons the two feedback and input time constants are made identical giving a frequency response of

$$H(\omega) = \frac{\omega^2 R_f^2 C_i^2}{(1 + \omega^2 \tau_f^2) (1 + \omega^2 \tau_i^2)} \tag{5.28}$$

This is comparable with the $(RC)^2 - (RC)^2$ shaping network suggested from Table 5.2. The frequency response is plotted in Figure 5.12. Substituting equations (5.18) into (5.24) and evaluating, the equivalent noise charge may be acquired. As before, differentiation of Q_{NT} with respect to the time constants and setting the expression to zero will give a minimum $Q_{NT\text{opt}}$ for the optimal time constants, τ_i and τ_f. Further addition of integration stages improves performance with the theoretical limit as $n \to \infty$ of a signal-to-noise ratio of 1.12 as compared to 1.00 for the cusp response filter. Emphasis is thus made to utilize the post-amplification stage as an additional integrator to enhance overall noise performance. The step response of the postamplifier is illustrated in Figure 5.13 for a 0.1 volt, 1 μsec, negative going pulse. The rise time observed is 0.45 μsec as compared to the 0.5 microsecond rise time of
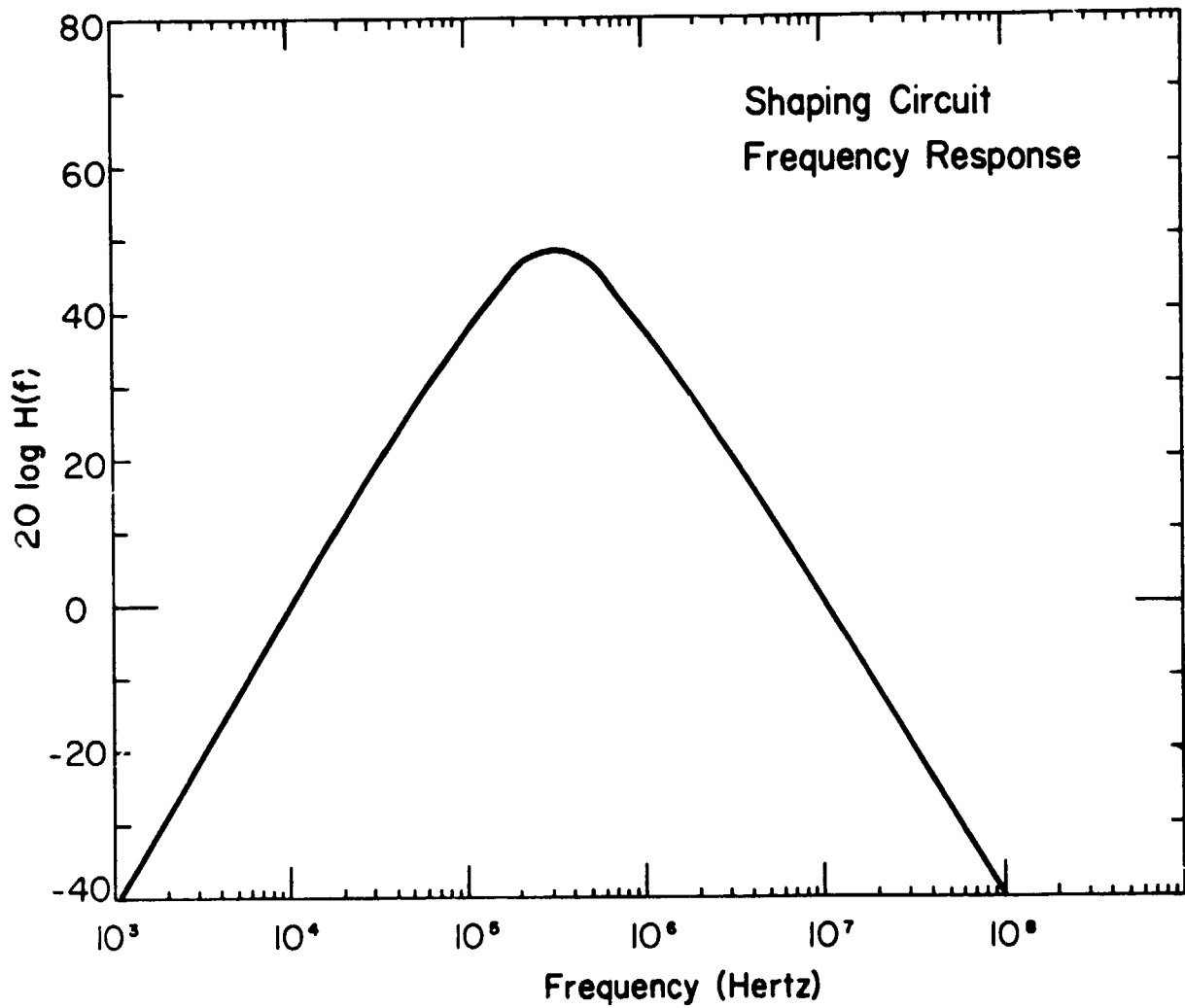
Figure 5.12   Typical frequency response for a double integration double differentiation pulse shaping network representive of equation (5.28).
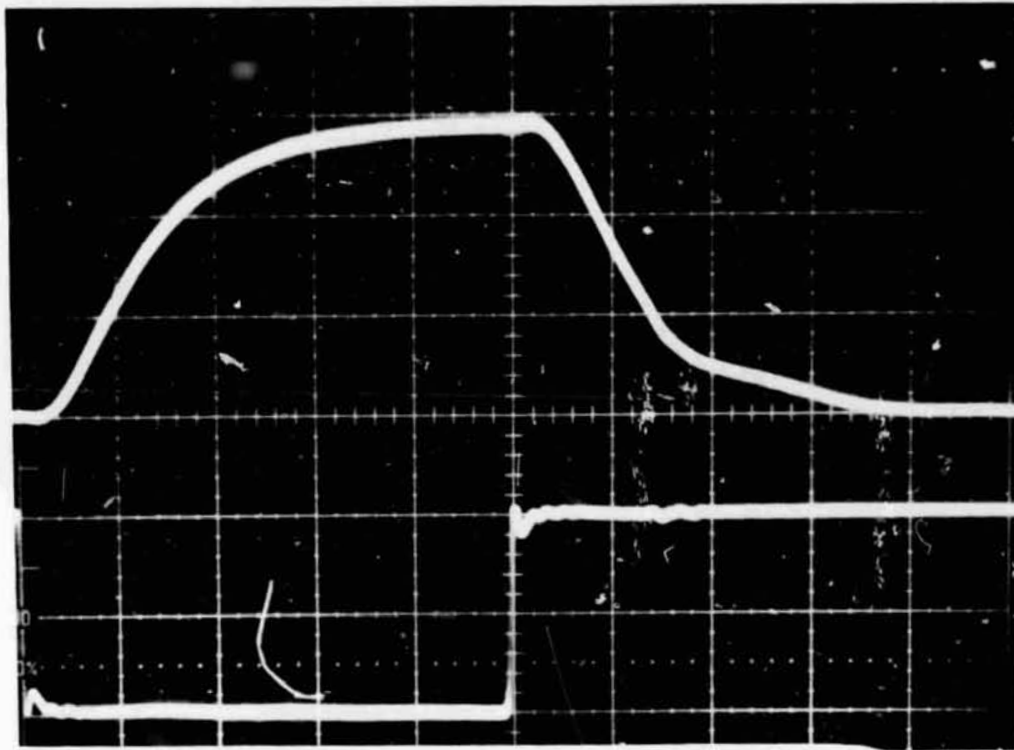
Figure 5.13 Postamplifier step response (top trace) for a negative 0.1 volt input pulse (bottom trace). The horizontal sweep rate is 0.2 μsec per main division and vertical sensitivity is 1 volt per main division.

the preamplifier. Future optimization is possible by employing capacitive feedback in an integration mode.

The final item of interest is the functional time dependence of the output signal. Tiis is resolved immediately since the transfer function, $f(s)$, is already available in equation (5.27). For a step input the output signal is

$$v_o(t) = \mathcal{L}^{-1} \{H(s)\ V_i(s)\} = \mathcal{L}^{-1} \left\{ \frac{S(R_{1f}\ C_1)^2}{(1+S\tau_f)^2(1+S\tau_1)^2} \right\} \qquad (5.29)$$

evaluation of this equation using the method of partial fractions leads to a time dependence of

$$v_o = A\ e^{-t/\tau_f} + B\ e^{-t/\tau_i} + Cte^{-t/\tau_f} + Dte^{-t/\tau_i} \qquad (5.30)$$

where A, B, C, and D are functions of the circuit passive elements. This equation expresses the observed output response depicted in Figure 5.9.

5.2.4 *NOISE computer program*. To facilitate a comprehensiv evaluation of a sensor-amplifier shaping-circuit electronic system a description of a general noise analysis program developed by *Motchenbacher and Fitcher* [1973] is here investigated with particular emphasis on the solid-state detector design. Quick, accurate, low cost and low noise design is obtained along with a better understanding of the processes involved. The program is able to simulate the amplifier network by either individual component interconnections or by overall amplifier response curves. The six available outputs are listed in Table 5.4.

Table 5.4

Available outputs in computer program NOISE.

1. Total equivalent input noise over a band.

2. Input network frequency response.

3. Input noise at any one frequency.

4. Input noise versus frequency.

5. Total noise at the output.

6. Total system gain response.

The source model for the solid-state detector applicable to the computer program is represented in the first section of Figure 5.14 and the particular element values are listed in Table 5.5.

The first stage amplifier model (Figure 5.14, Table 5.5) called NOSMOD represents the most crucial gain stage. The noise spectrum of E_N and I_N can be approximated by the piecewise linear relationship shown in Figure 5.16.

The final model (Figure 5.15), AMPLGN, is the main amplifier and pulse shaping networks. Any arrangement of the curves shown in Figure 5.16 is valid to represent the particular pulse shaping frequency response. For example, N8 is the rate-of-rise in 6 dB/octave steps of the response curve. For N8 = 2 the rise is 12 dB/octave, etc. The end points for each segment must also be specified. The derived frequency response curve is illustrated in Figure 5.12 and provides typical input to AMLLGN for analysis permitting one of the parameters to vary in equation (5.27) thereby recovering the most optimum configuration. Further references should be made to *Motchenbacher and Fitcher* [1973] for a generalized treatment of noise systems.

5.3 *Pulse Voltage Discrimination and Counting Circuits*

The design approach for interfacing the solid-state detector-preamplifier output pulse with the telemetry is based on a conventional Geiger counter system design in addition to a pulse height discriminator circuit. The system, as designed, was intended to be kept as elementary as possible fulfilling the experiment requirements. The two primary requirements referred to in Chapter 2 are to ascertain the particle flux and energy spectrum of energetic electrons so that particle ionization
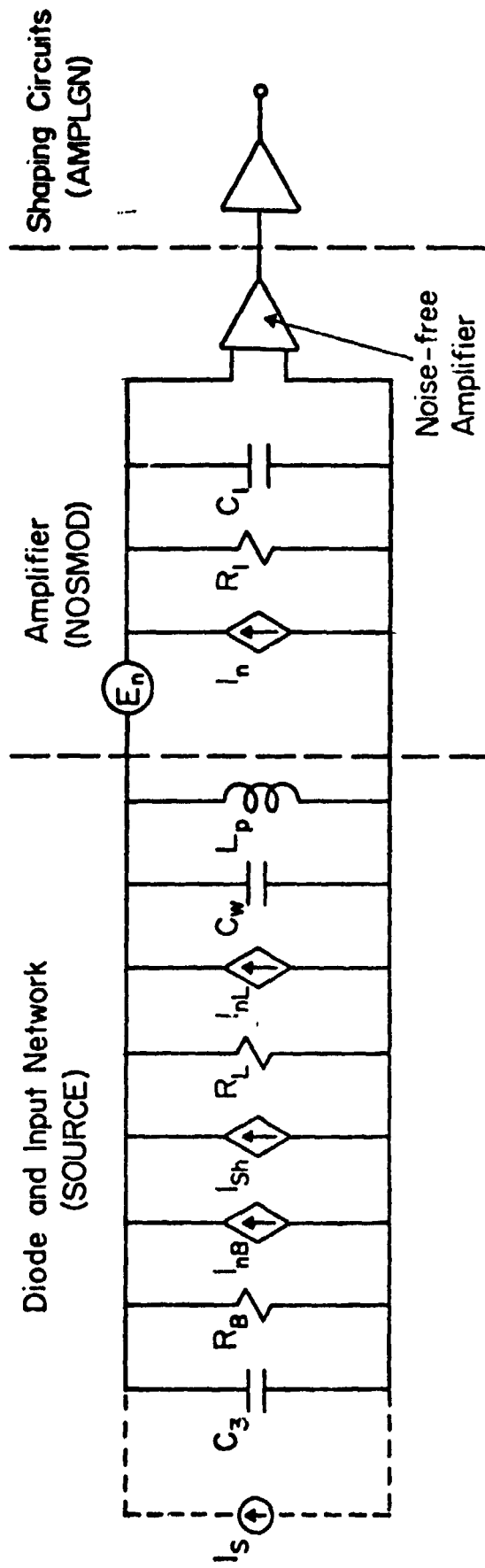
Figure 5.14 Equivalent circuit model of semiconductor detector used for input into computer program NOISE.

Table 5.5

Symbol equivalents used in computer program NOISE.

R_I = $R1$ = amplifier input resistance

R_B = $R2$ = real part of sensor leakage resistance

R_L = $R3$ = load resistance

C_I = $C1$ = amplifier input capacitance

C_S = $C2$ = cell capacitance

C_W = $C3$ = wiring capacitance

L_P = $L1$ = shunt inductance

F_L = $F6$ = $1/f$ excess-noise corner

I_{dc} = $I2$ = sensor leakage current

I_{nB} and I_{nl} = $(4k\ T\Delta f/R)^{1/2}$ = thermal noise of R_B and R_L

I_{sh} = $(2q\ I_{dc}\ \Delta f)^{1/2}$ = shot noise of cell current

E_n and I_n = E and I = amplifier equivalent noise mechanisms

NOSMOD

6 dB/octave

Noise E_n or I_n

F_1 or F_3 F_2 or F_4

3 dB/octave

Log frequency

AMPLGN

S5

S4   F5

Gain in dB

FO   S3

NB

frequency →

N9
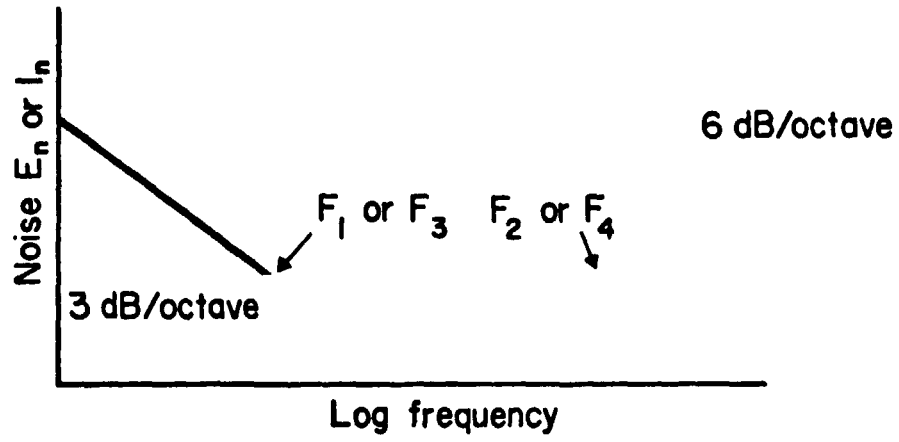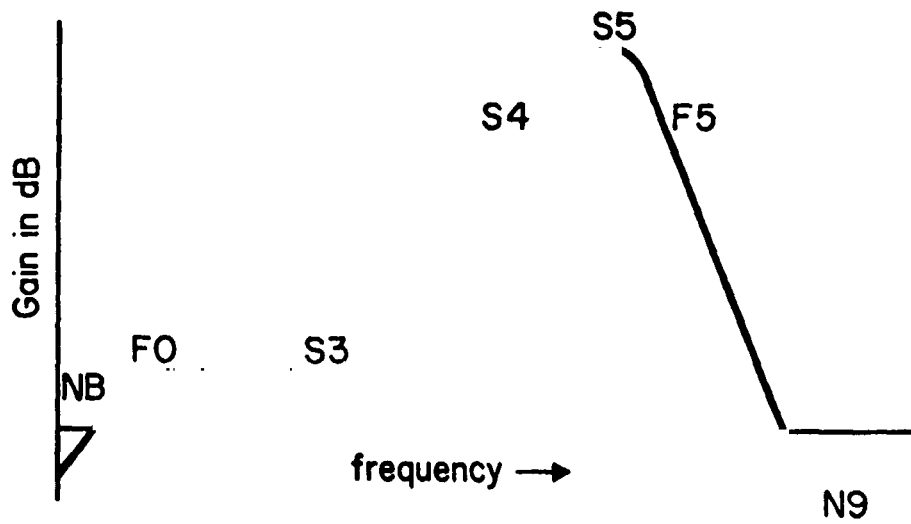
Figure 5.15 Frequency response models for use in subprograms NOSMOD and AMPLGN.
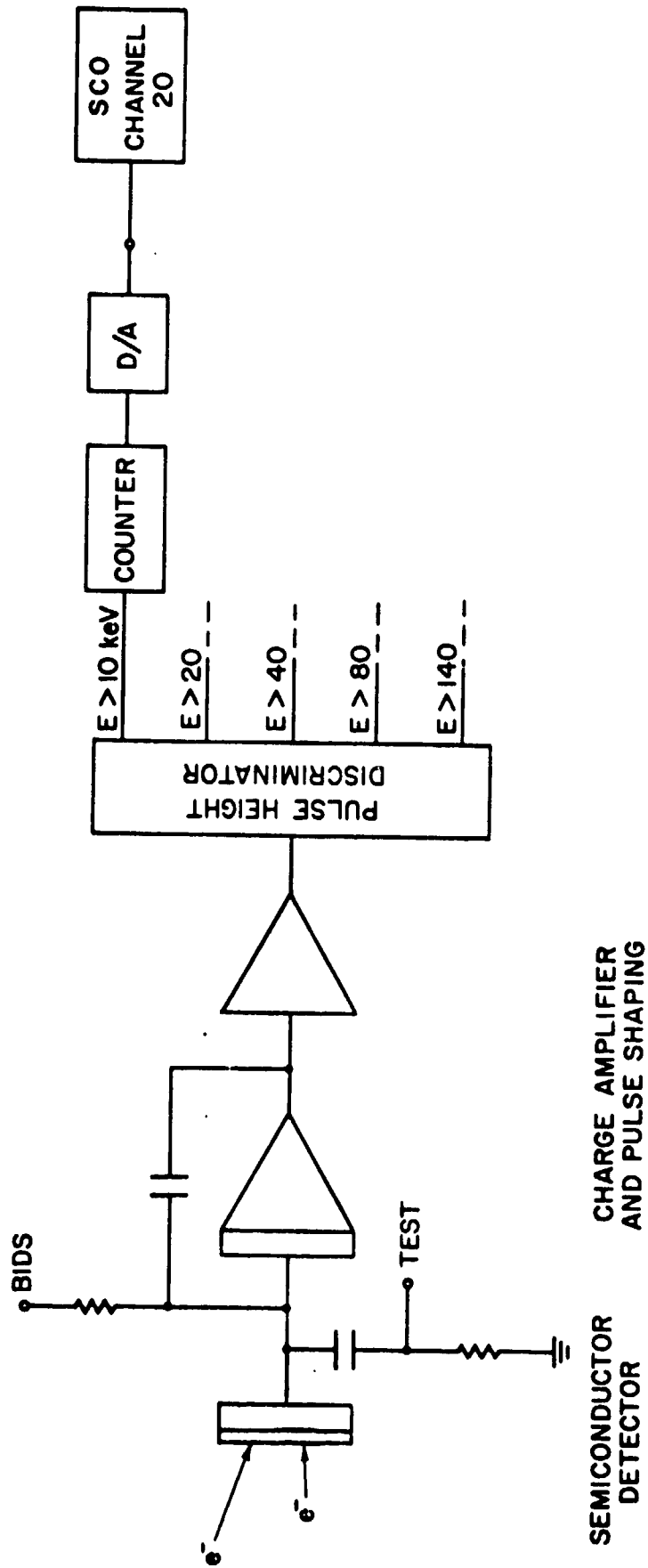
Figure 5.16 System representation of the solid-state particle detector experiment. The particle produces a charge within the detector, whereupon it is amplified and pulse height discriminated. Each pulse within the discriminator range triggers a digital 4 bit counter and is then converted into analog form for telemetry transfer.

rates could be established. To most simply accomplish these investigations a six channel energy analyzer circuit was decided upon since previous indications [*Potemra*, 1973] suggested that the spectrum followed a monotonically decreasing count rate verses increasing energy. More elaborate procedures for data manipulation and reduction are available options to the system as familiarity, feasibility, and scientific objectives dictate.

Further concern of the design includes; 1) shock and vibration protection, 2) shielding from interferring payload equipment and high power radar, 3) ease of replacing and checking units, 4) operation under low pressures, 5) temperature insensitivity, and 6) noise immunity.

A description will be given of the method and hardware implemented to apply the above design approach. To properly aid in understanding this material an effort is made to include an ample number of photos; illustration, and oscilliscope displays.

First, the electronics will be examined as to system operation, noise immunity, design, construction, and future improvements.

Secondly, the mechanical construction will be discussed in Section 5.4 and reference should be made here as to component location.

5.3.1 *Counting circuits operation*. The fundamental operation of the solid-state energetic particle experiment is system represented in Figure 5.16. Incident particles impinging on the semiconductor detector create electron hole pairs proportional to the particle energy. A specially designed charge preamp described in Section 5.2 senses this current pulse and amplifies it acccrdingly. The signal is height discriminated, restoring the particle energy information for subsequent particle count and data transmission.

The pulse height circuit uses six series-connected voltage comparators as a window discriminator. Each signal is then shaped and accumulated in a self-resetting 16-count 4-bit binary counter. This information is then converted to analog form for interface with telemetry VCO.

5.3.2 *Noise immunity*. One of the most challenging problems encountered in the design is elimination of unwanted spurious pickup. The three primary noise sources are interferences from the high voltage power supply (30 V to 300 V converter), ground loop modulation, and power lead pickup. The final consequence of noise exhibited in the circuit is extraneous pulse counts, thereby reducing overall sensitivity and accuracy.

Power supply noise can most simply be reduced by using decoupling capacitors. A 0.1 µf disk ceramic capacitor is mandatory for RF frequency bypassing and a large electrolytic capacitor for transient suppression. Further, noise suppression is obtained by bypassing each IC with a 0.01 µf disk ceramic capacitor placed as near as possible to the IC. Direct radiation pickup from power supply wiring is reduced by separating signal and power supply wires and enclosing the power supply in a grounded metal shield.

Ground loops result from the finite resistance of conductors and consequently may experience a voltage difference. Possible mechanism capable of generating voltage fluctuations are mutual capacitance between all bodies, static potentials, changing magnetic flux linkages, piezelectric effects, and varying reference plane currents. To minimize current loops a ground plane should be used on each circuit board and all system grounds tied to a single ground point. For the sensor, preamplifier

and electronics the shielding technique should be used as illustrated to Figure 5.17.

5.3.3 *Counting circuits design*. The detector and associated circuits are arranged in the payload on two decks, as shown in Figure 5.18. These decks are interfaced through a pin connector to the main payload wiring channel, shown in Figure 5.18, for data transfer and low voltage (+30V and -30V) battery power sources.

The upper deck (Figure 5.19) consist of the solid-state detector, charge preamplifier, high voltage power supply and voltage dividing network. The power converter chops the 30 Volt dc battery pack power at a frequency of 5 kHz and steps up the voltage to 300 VDC. The numbers in the right-hand vertical box designate the pin connector number. TP1 and TP2 refer to bias power converter test point and the calibrate test point of the preamplifier, respectively.

The postamplifier design was placed on the lower deck for space and power compatibility reasons. Future designs should include the postamplifier near to the preamplifier. Also, separation should be made of the power converter and regulator on the reverse side of the metal deck from the detector and amplifier electronics.

The lower deck (Figure 5.20) contains three stacked circuit boards. The lowest circuit board is used for the power supplies and for the counting circuits because the regulators can use the metal deck as a heat sink. Three supplies were required; a + 5 Volt for the IC logic, a ± 15 V supply for the operational amplifiers and the digital-to-analog converters and a + 15 V reference supply for the voltage discriminators. The power supply board also contains the postamplifier circuit. The postamplifier
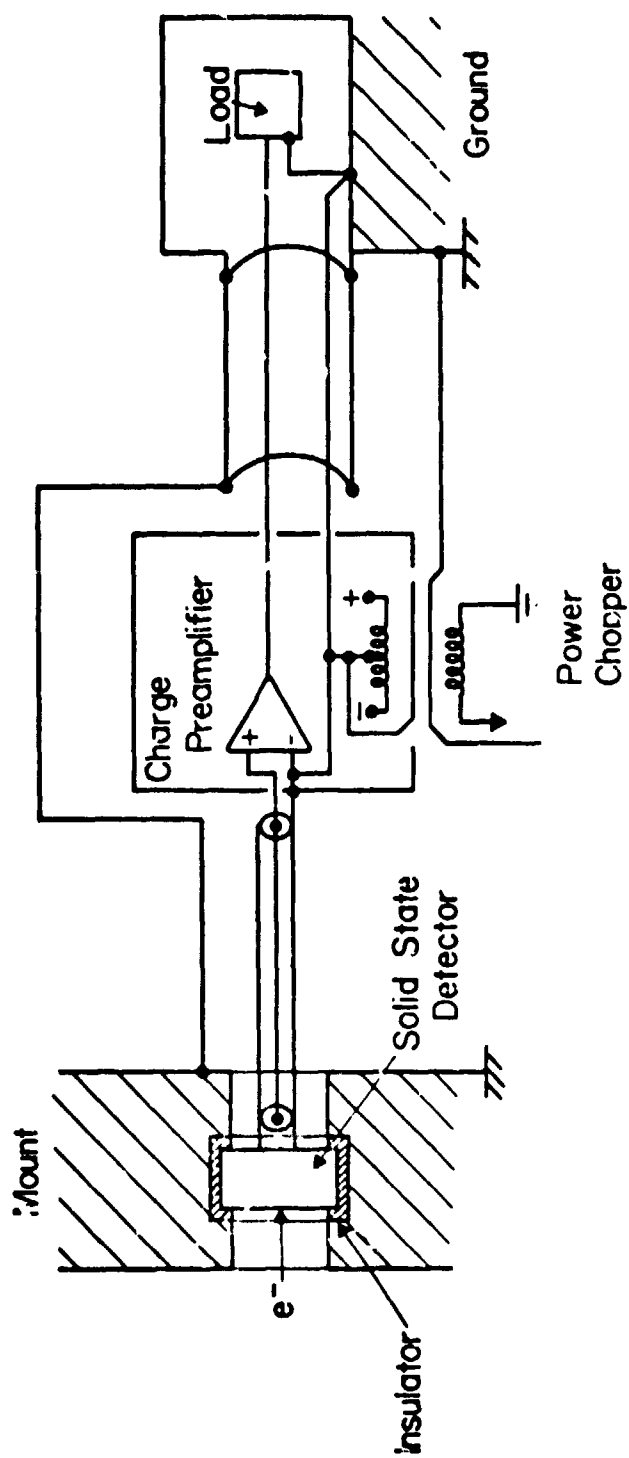
Figure 5.17 System layout and shielding procedure to minimize ground loops and interfering radiation.
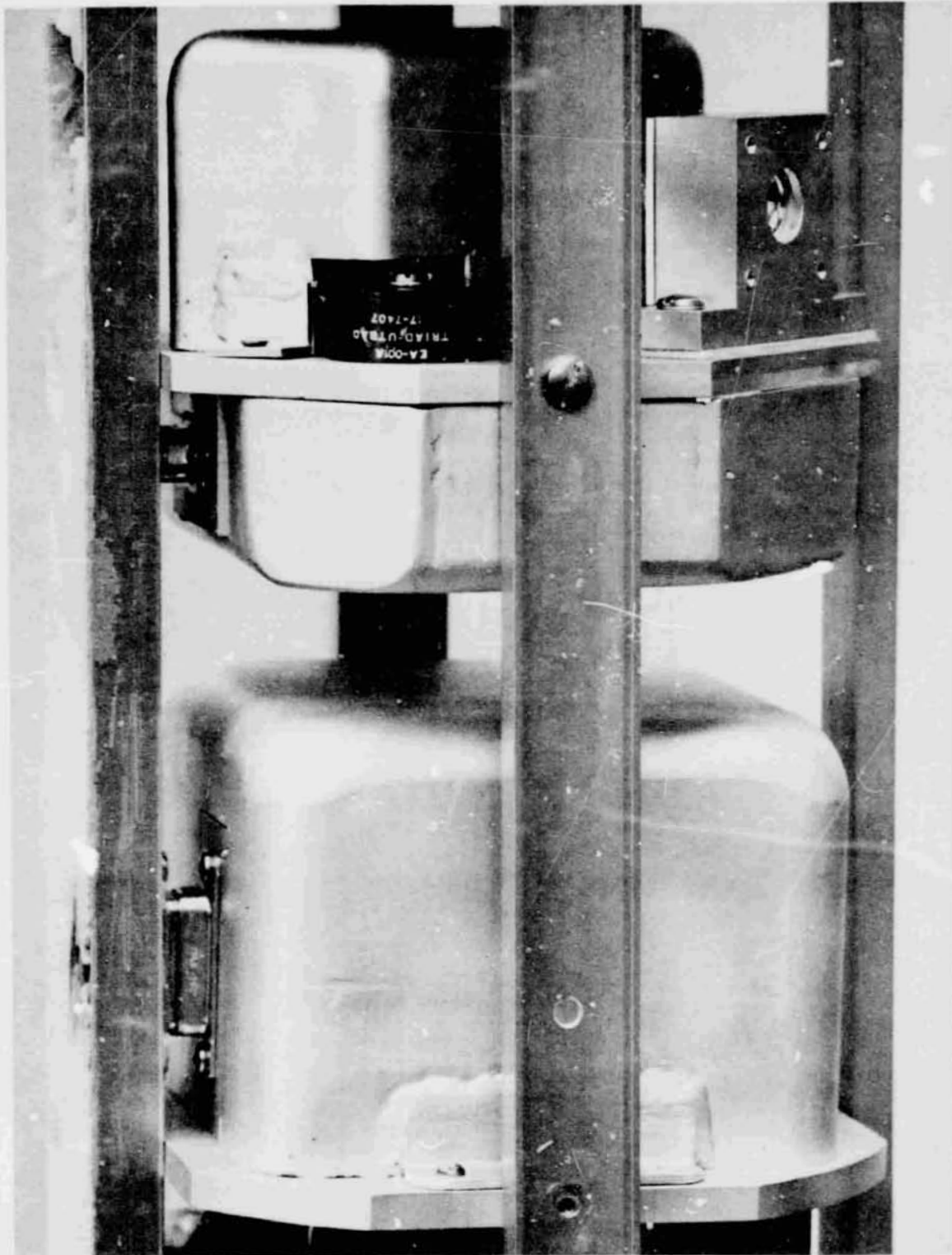
Figure 5.18   The arrangement of the energetic electron spectrometer in the payload of a Nike Apache rocket. The upper deck contains the detector, preamplifier and high voltage supply complementing the lower deck counting electronics and low voltage power supplies. Both decks are interfaced through pin connectors to the main wiring channel shown on the extreme left.
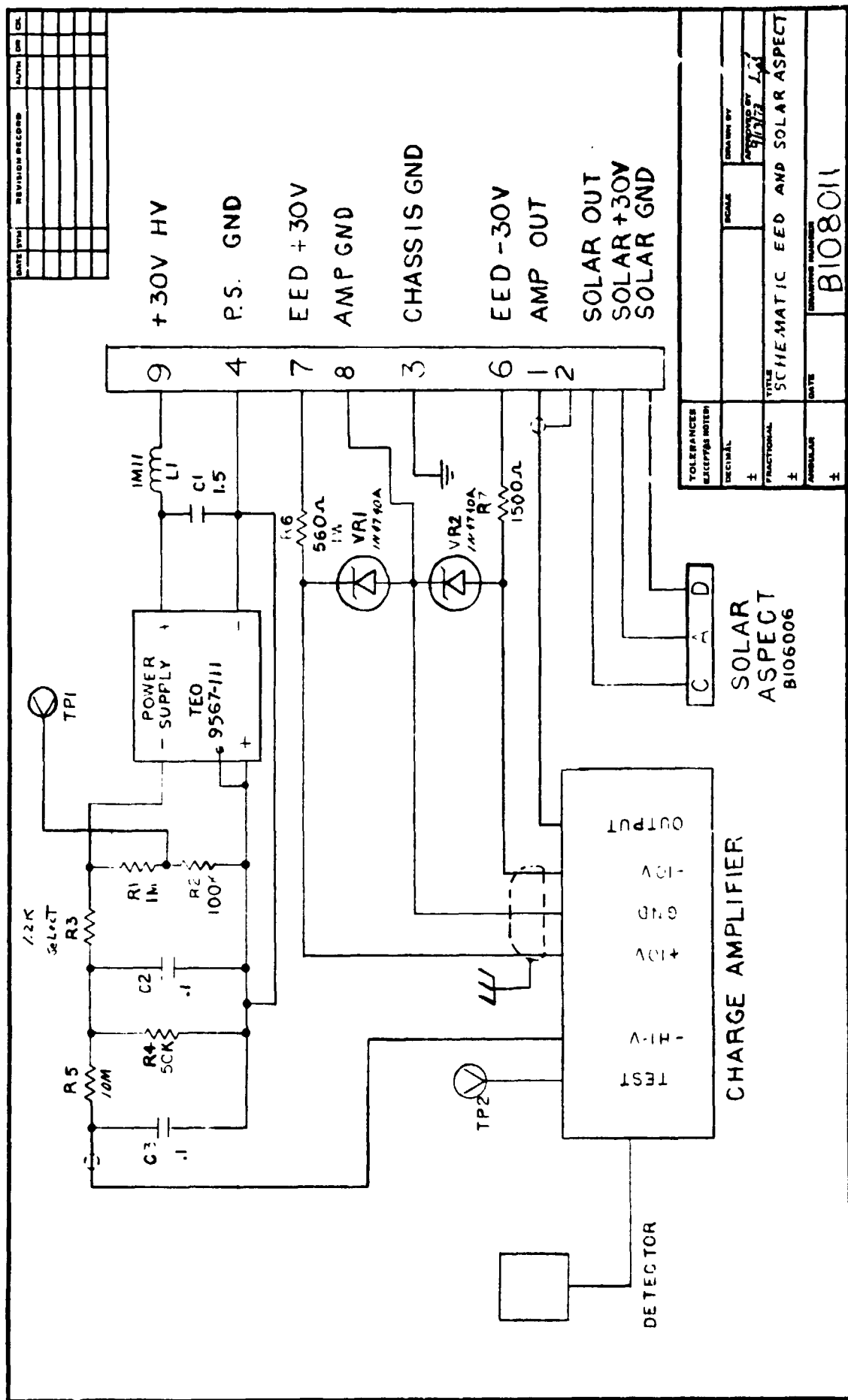
Figure 5.19 Schematic representation for components on the upper deck. The high voltage power supply output (about 300 V) is resistively divided to approximately 125 volts for detector bias.
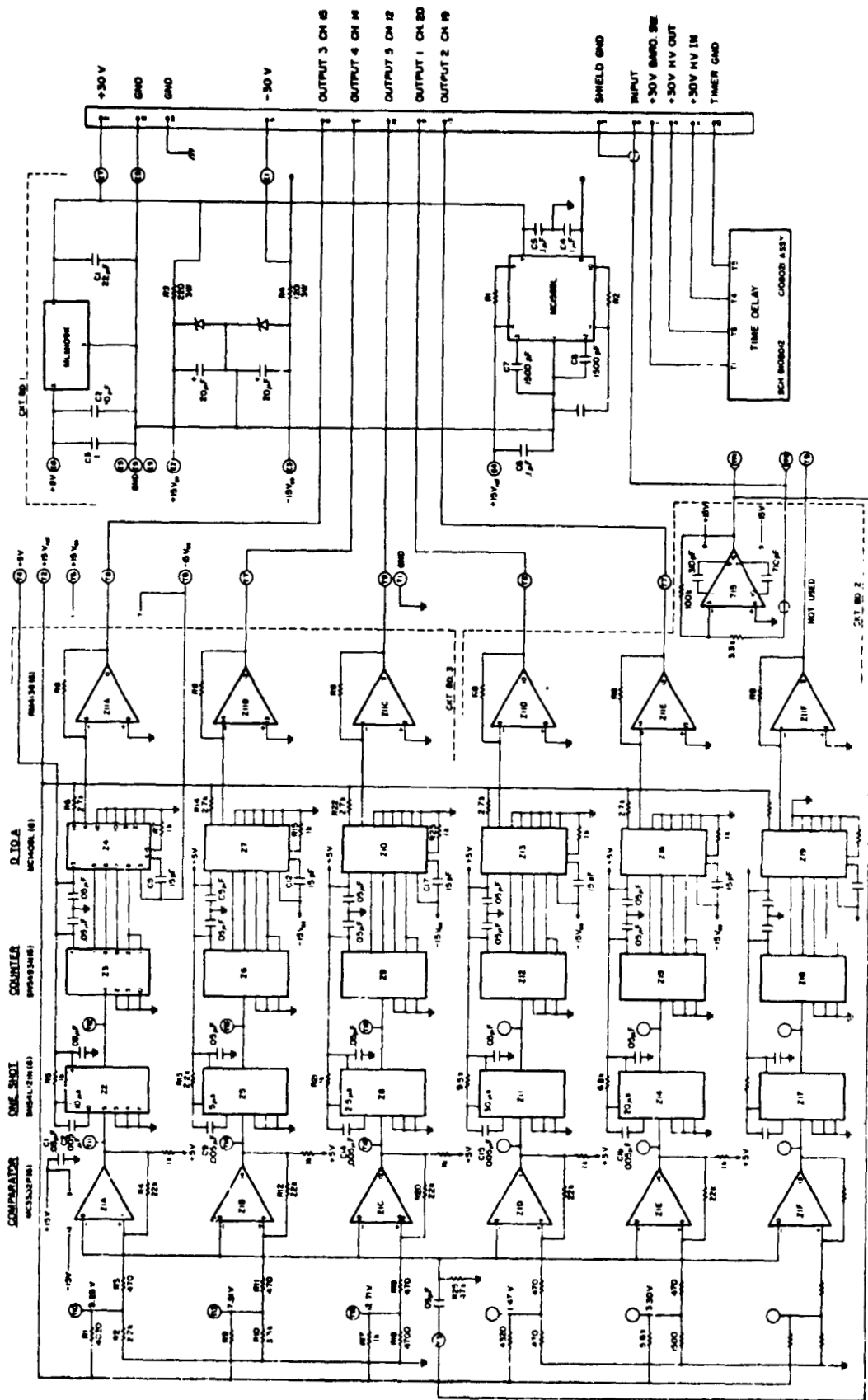
Figure 5.20 Circuit diagram of six channel pulse height analyzer electronics. The input pulse is height discriminated, shaped, counted, and converted into analog form for telemetry transfer.

employs a Fairchild µA715 operational amplifier, used in the inverting
mode. The RC feedback was used for pulse integration in addition to
pulse gain. Gain response was measured to be linear to 14.5 Volts before
saturation was reached. Two compensation capacitors were used to pre-
vent oscillations, to modify the time constant and to increase stability.
The basic circuit parameters are discussed in reference materials.

The upper two circuit boards are identical, each containing three
complete channels of counting circuits. Further circuit boards may be
easily added for increasing the total number of pulse height measure-
ments. The input pulse to the pulse height analyzer circuits is essen-
tially the inverse of the preamplifier pulse displayed in Figure 5.11.
Some modification within the negative portion of the postamplifier output
occurs (Figure 5.21) due to coupling from the ADC, and shaping circuits.
This coupling is associated with instabilities in the negative portion
of the transfer function. However, it is not of concern since the pulse
height is not affected. No amendable solution was found which did not
modify the original pulse.

For voltage discrimination a st. 'd array of voltage comparators
were employed. Each comparator was re. renced at a different voltage
from a resistive voltage divider network. To save space, a quad com-
parator integration circuit was used on each counting circuit board.
Hysteresis was added to reduce the sensitivity of the transition region
to approximately 3 mV. The typical output from a comparator is illus-
trated in the top trace of Figure 5.22 for the input pulse in the bottom
trace. The comparator output is observed to be delayed approximately
12 µsec from input pulse trigger.
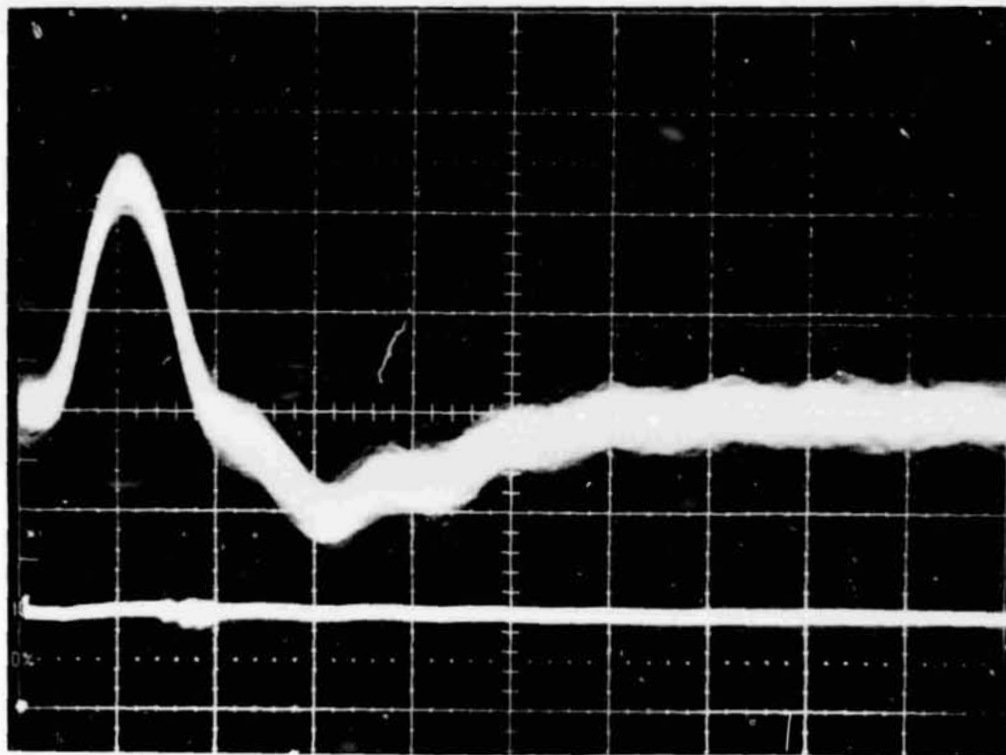
Figure 5.21 Output signal (upper trace) from the postamplifier for a 10 mV test calibrate signal (lower trace) supplied to the preamplifier. The horizontal sweep rate is at one microsecond per main division. The oscillations apparent in the negative portion of the pulse are the result of coupling from the ADC and shaping circuits.
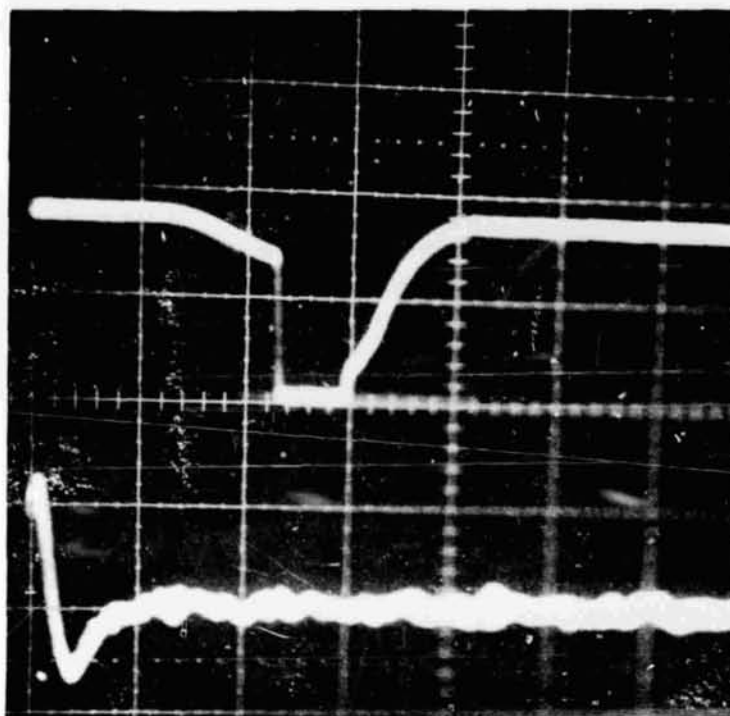
Figure 5.22 Output from the voltage discriminator (upper trace) for
            the input signal displayed in the lower trace. The hori-
            zontal sweep rate is 5 µsec per main division.

The next stage is used for triggering and predetermining the dead-times specified for each channel. When a negative-going signal is received from the comparator the one-shot locks on for a set time and is not affected by subsequent pulses during the dead-time period. This eliminates effects from multiple triggering as well as defining the pulse shape, and drives the succeeding counter stage. The value of dead-time chosen is determined from the data capability of the telemetry bandwidth when saturation begins. For IRIG telemetry channel 20, approximately 2×10^3 counts per second can be transferred accurately. Since the counts are grouped into ramps of 16 counts, the maximum resolving power is $16 \times 2 \times 10^3$ or approximately 3.2×10^4 counts per second. This dictates a dead-time of $(3.2 \times 10^4)^{-1}$ seconds = 30 μsec.

For counting rates approaching 3.2×10^4 statistical analysis predicts the correction factor for particles which are within the built-in dead-time. Figure 5.23 illustrates this behavior. The formulas may be referenced in statistical handbooks. The correction factor for a dead-time, τ_d, actual count rate of N_{act} and observed counting rate of N_{obs}

$$C.F. = \frac{N_{obs}}{N_{act}} = \frac{1}{1 + \tau_d N_{act}} \qquad (5.31)$$

Because of the nature of the particle spectrum, higher energy channels are not expected to saturate; therefore, reducing the need for longer dead-times for the smaller bandwidth channels. The dead-times are also staggered to reduce simultaneous surges in the ADC and counters
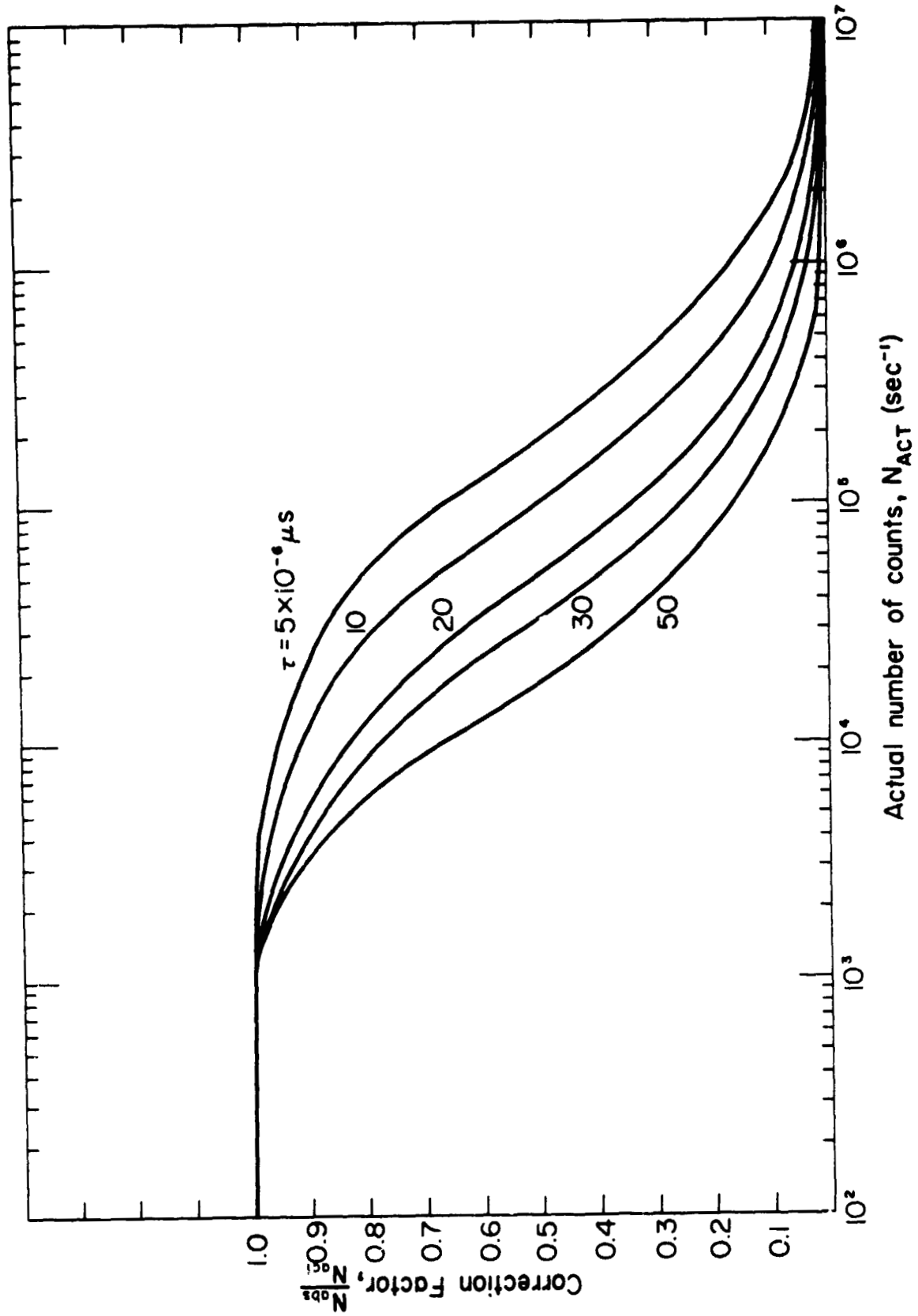
Figure 5.23 Graph showing the limiting counts registered from the electronics for a random count rate.

causing distortion effects eluded to in Figure 5.21. Figure 5.24 illustrates the dead-times associated with the four high count channels. The sweep rate is 5 μsec per main division where the top trace is the highest count channel.

The shaped pulses are next counted in a 4-bit binary counter and paralleled across to the ADC. For high counting rates an improvement can be made to enhance the counting capability 16 times by employing an 8-bit (or at least greater than 4-bit) binary counter and resolving only the most significant four bits to the ADC. Each ramp is therefore representative of 256 counts giving an overall count rate for channel 20 of $2 K X 256 = 5.12 \times 10^5 \sec^{-1}$.

The binary count received from the counter is transformed into an equivalent analog representation by use of a MC1508L-8 ADC and a quad operational amplifier. The operational amplifier is necessary to convert the current signal from the ADC to a voltage signal of sufficient magnitude for interface with telemetry voltage controlled oscillators (VCO). Typical output from the electronics for a random input flux is displayed in Figure 5.25. The circuit board layout is pictured in Figure 5.26 for the power supply board and counting electronics.

5.3.4 *Future improvements of counting circuits*. The present design, although satisfactory, has two limitations:

1) Each spectrum interval requires one IRIG telemetry
   channel (consequently the total number of channels
   available to the detector experiment is limited).
   Additionally inefficient use is made of telemetry
   space. Fine structure may also play an important
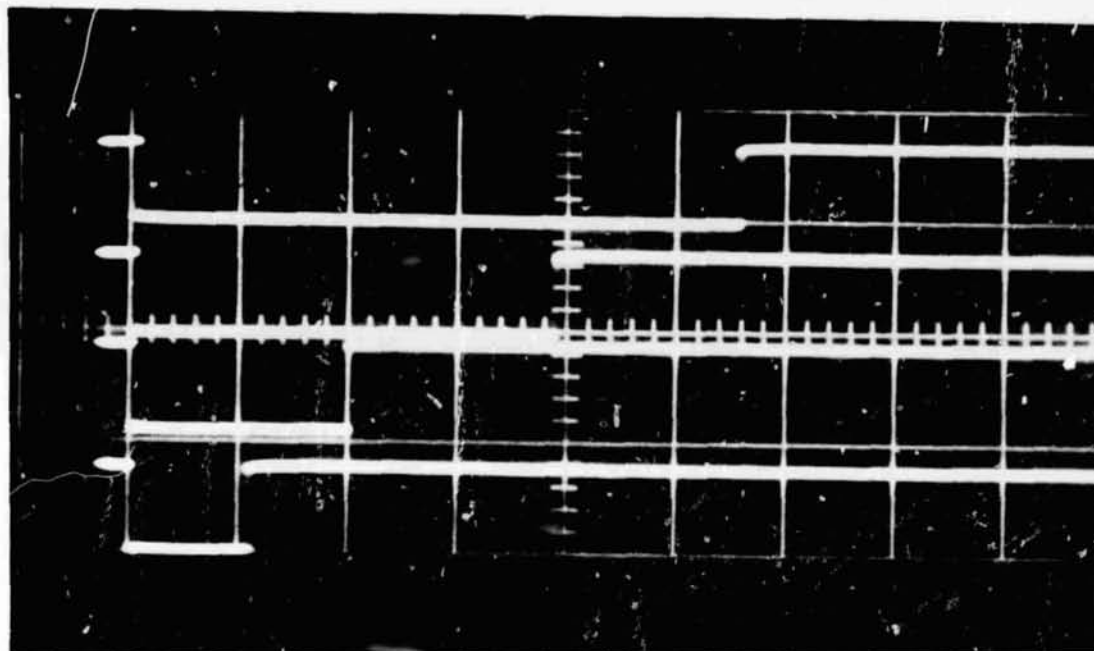
Figure 5.24   The above four pulses show the staggering utilized in
the pulse shaping circuits. The upper pulse corresponds
to the high count rate channel and is set for the maxi-
mum bandwidth for IRIG channel 20. Horizontal sweep
rate is 5 μsec per main division.
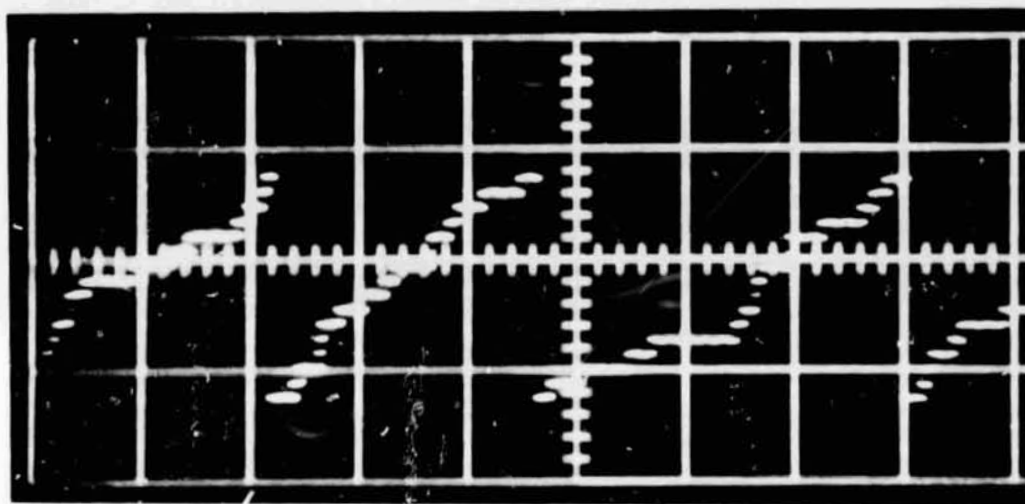
Figure 5.25 Output signal supplied to telemetry for the high count
rate channel. Each ramp represents 16 counts. The
counts shown here are the result of noise pulses greater
than the channel threshold. The horizontal sweep rate is
10 m sec/ Box yielding a count rate of approximately
55 counts per second. The temperature is 10°C and the
rms noise is 14.2 mV.
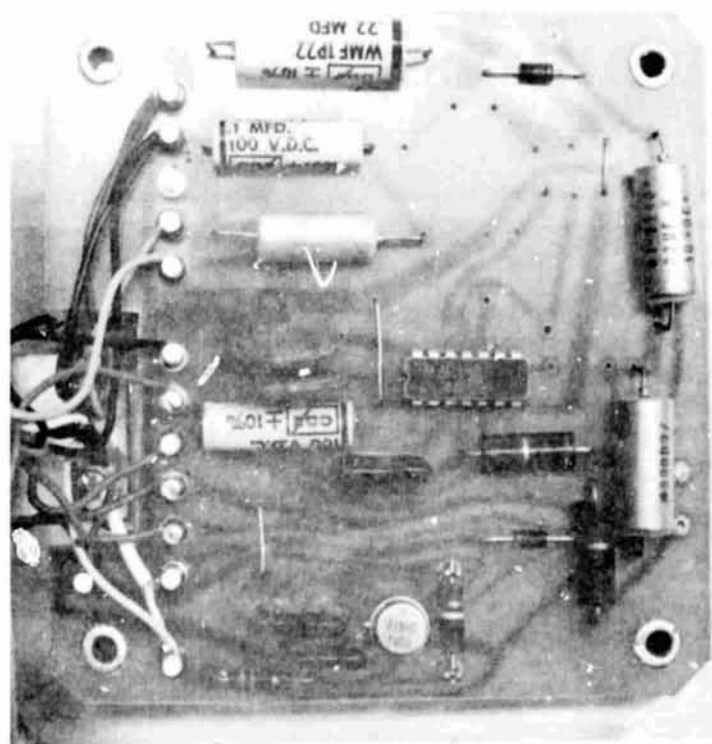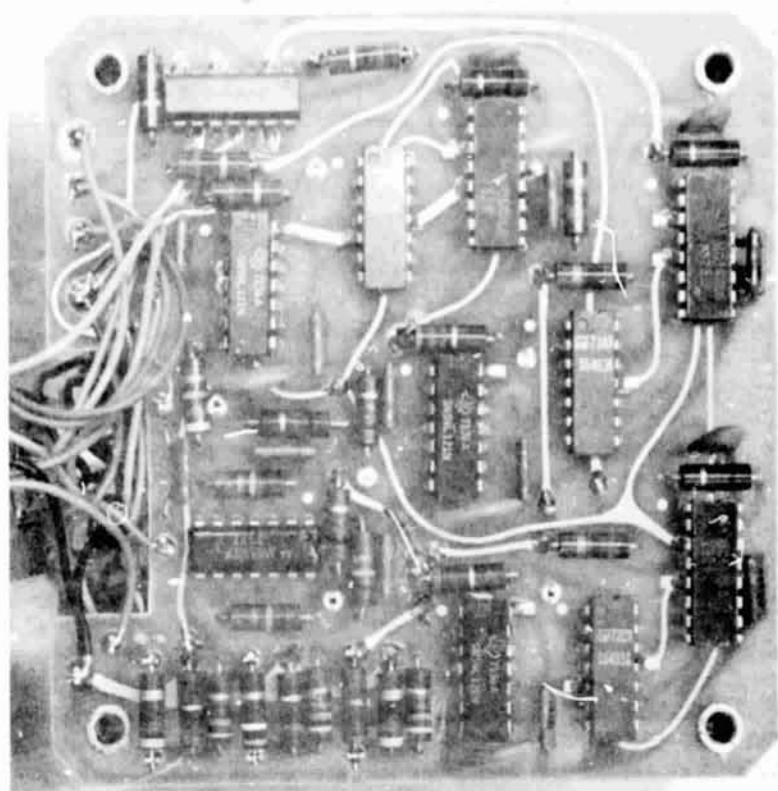
Figure 5.26   Electronics package counting circuit board (upper picture)
and power supply board (lower picture).

role in determination of ionization rates requiring

a detailed spectrum and ample channels.

2) Pitch angle data reduction is a quite complicated

procedure with the present data format.

These problems are eliminated in an advanced design outlined in Figure 5.27 which is capable of 64 spectrum channel coverage. All of this information can be integrated on one IRIG channel of an FM tele- metry system. The provision is additionally made to have the counted data synchronized with the aspect magnetometer for simple pitch angle analysis.

The principle of operation is similar to the system described in Section 5.3.1 with the following important changes and additions. The input pulse supplied from the postamplifier is tracked and made to lock on to the peak of the pulse. An analog-to-digital converter reads the steady-state peak amplitude and resets the peak detector. The digi- tal equivalent of the measured peak can then be transferred to a PCM telemetry network, if available. However, telemetry space can be signi- ficantly reduced if spectrum is internally analyzed. To accomplish this, the 6-bit binary signal is converted into one of 64 bins corresponding to the magnitude of the binary word. Each pulse transferred to a bin is individually counted. The first and second most significant group of 4 bits is then converted into two analog voltages, respectively. The two analog signals comprise a two digit hexadecimal number resulting in 128 analog output signals. These 128 signals are multiplexed at a rate of 2000 samples per second, the bandwidth for IRIG channel 20. Each counter is reset sequentially in step to give a counting period and

Figure 5.27 Advanced design for telemetry transfer of particle information. Each pulse from the postamplifier is height-analyzed and counted in such a manner for compact utilization of an IRIG channel.

scan period of 128 divided by 2000 = 63 msec. The rocket spin rate is
approximately 5 rps or 200 msec giving approximately three counter scans
per rocket rotation. To improve the position sampling the multiplexing
rate must be increased (i.e. use two IRIG channels), the spectrum infor-
mation reduced or, to simply reduce the counting period. If the period
is halved the position information is doubled, etc. The divider network
is easily adopted to this operation. The basic reasoning in the latter
approach is that not every particle penetrating the detector need be
counted but only periodic samples during each revolution. The final
output would therefore have three position measurements per second over
a reduced scanning interval. For spectrum scans of 32 energy channels,
there would hirty positions measurements per second for pitch angle
information and 32 spectrum scans per second all of which could be
transferred as IRIG channel 20.

The pulse-height analyzer circuit is a non-inverting peak detector
based on a voltage-following principle. Referring to the circu. dia-
gram (Figure 5.20) diodes D1 and D2 are used for transient protection
and for compensating nonlinearities introduced by D3. Capacitors C1 and
C2 are used to compensate the loop for fast tracking applications in
which overshoot is present. The response speed is also dependent on
C_H, the holding or storage capacitor. Since speed is important and
storage is only needed for a few microseconds, C_H is correspondingly low.
Reset of C_H to zero voltage is initiated by the FET saturating after a
predetermined time interval governed by one shot 1. The second one shot
is set slightly less than the first one shot so that the ADC can read
the stored voltage.

The binary to decimal converter is fabricated as a complete unit integrated circuit. The counters and AC are operated in the same manner as discussed in Section 5.3.4. The multiplexer is again a standard off the shelf item and must be capable of sequentially reading twice the number of spectrum channel. The clock is a crystal controlled oscillator with an attached counter for dividing down the clock rate so the accumulators can be reset.

5.4 *Mechanical Layout of Detector System*

The mechanical design required integration of the various components in such a way that (1) electrical interference was minimized, (2) flexibility of replacing units and easy subsystems checkout could be made, (3) that precautionary measures exist to resist shock and vibration and (4) that temperature and pressure charges are insignificant.

For a versatile design, the conclusion is reached that the system should be constructed on two decks; the upper deck to contain the amplifier and detector stages and the lower deck to contain the counting and height discrimination electronics. The option for interchanging electronics packages could then be made as design improved or scientific objectives dictated. Both packages communicate by use of pin connectors to the main rocket wire tray as previously discussed. The upper and lower decks are pictured in Figures 5.28 and 5.29

To guard against vibration, shock, and pressure each compartment is encapsulated. The foam used, Eccofoam FP, is airtight to maintain operation during sudden pressure changes. Furthermore, the foam in its solidified state rigidly bonds all the individual components to prevent vibrational fatigue and absorb shock impulses.
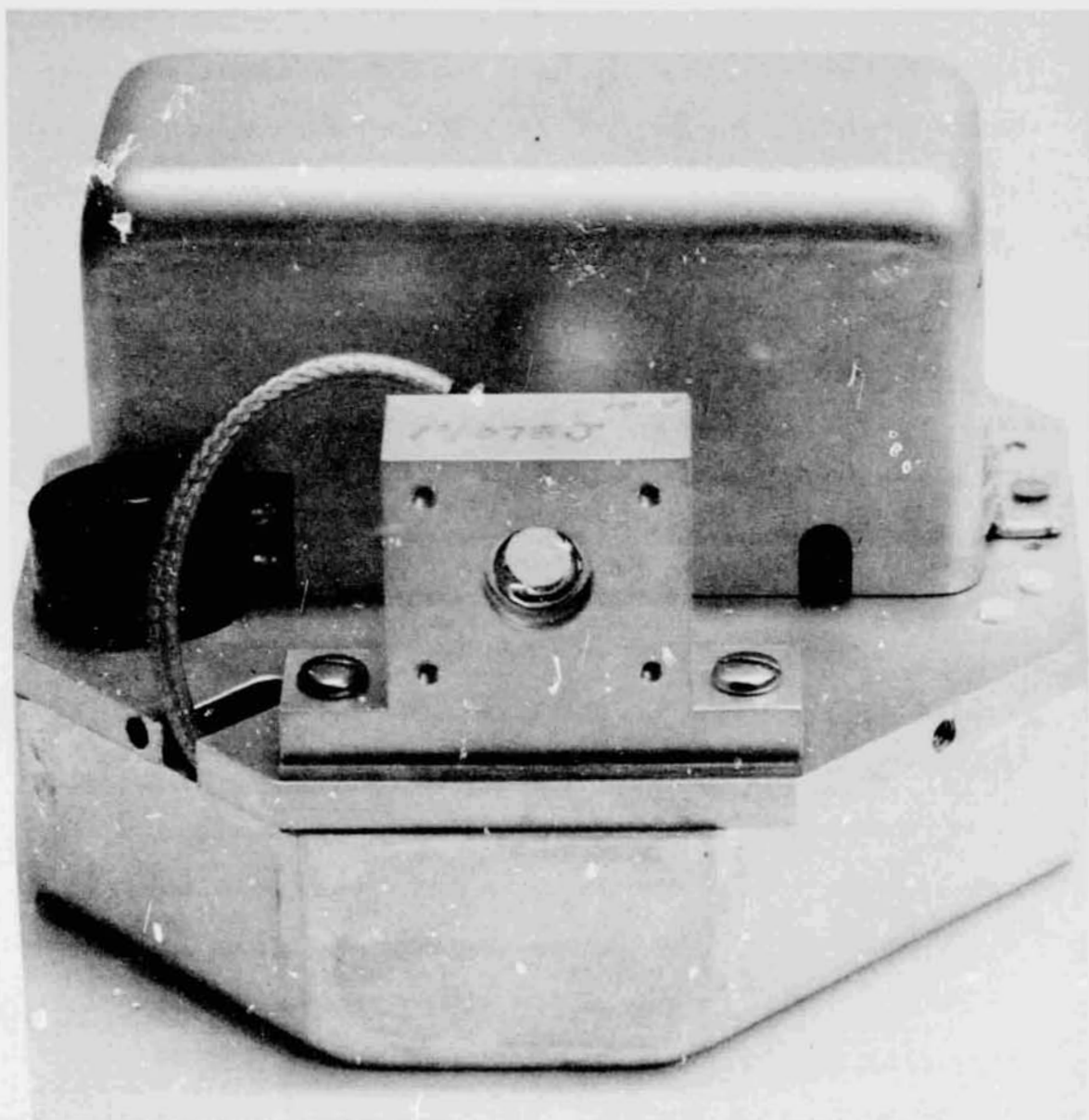
Figure 5.28 Upper deck of the energetic spectrometer. The bias power supply is located in the can behind the detector mount. The preamplifier and pulse shaping elec.ronics are located beneath the platform.
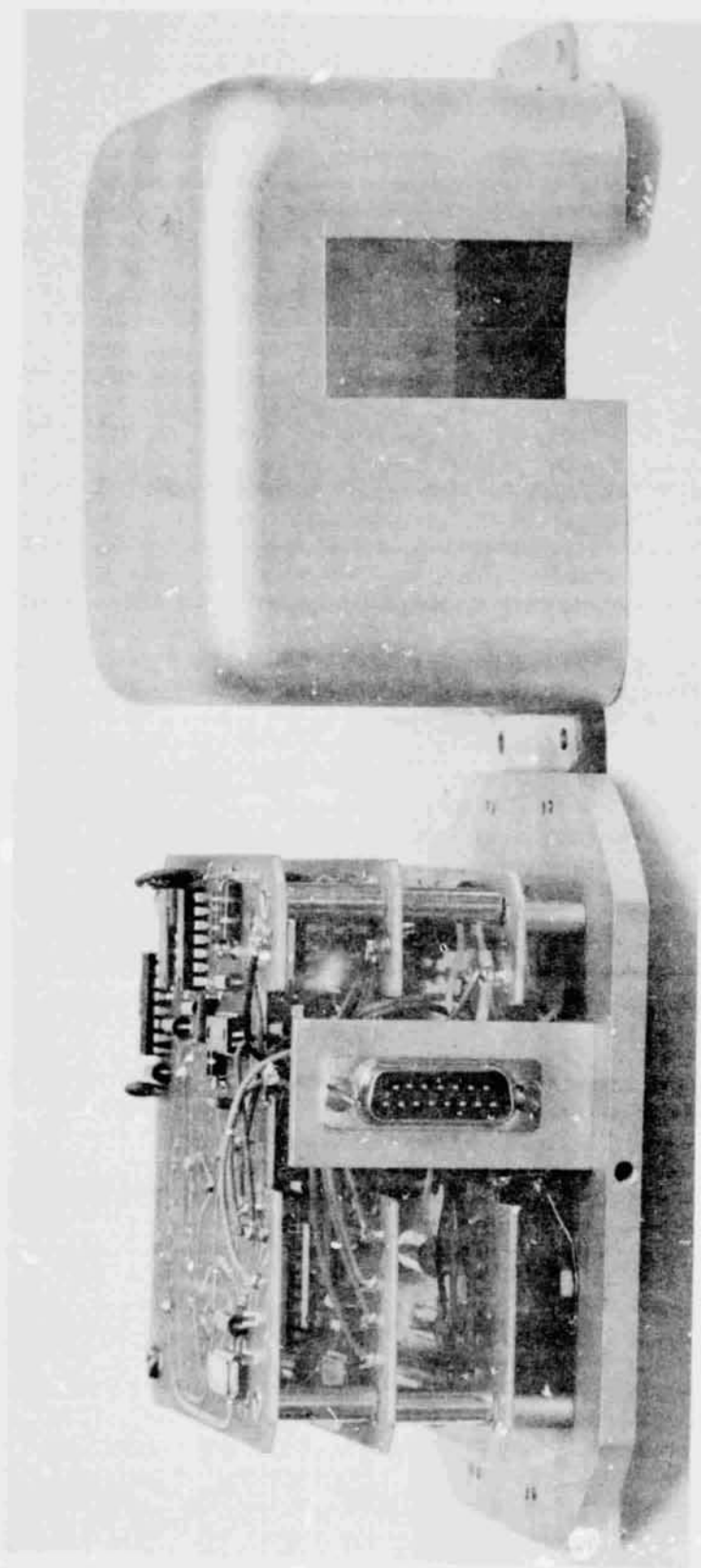
Figure 5.29 Lower deck of the energetic electron spectrometer. The two upper printed circuit boards contain the pulse height analyzer and counting electronics. The lower board contains the power supply and postamplifier circuits.

To protect the payload and, most importantly, the sensitive surface of the detector during initial flight two doors are situated on the rocket shell. At an altitude of approximately 40 km the doors are ejected, exposing the detector. Figure 5.30 illustrates the location of the detector relative to the door opening. The detector mount is shown in Figure 5.31.

To further increase the resolving power and directional capabilities of the detector future improvements should include provision for cooling the detector and adoption for collimator tubes. The low energy threshold and resolving power could be halved, to about 6 keV, if the detector were to be cooled by dry ice. The basic problem here is not the difficulty of cooling the detector but more so the application of a seal to prevent condensation, a harmful contaminant, to the detector surface. A possible solution for sealing is to mount the detector in an evacuated cylinder, having the same diameter as the detector. Immediately after door ejection the front corner of the detector could be removed by solenoid action. The chamber is thermally insulated from the mounting platform while thermal contact is made with a dry ice reservoir surrounding the perifery of the cylinder.

Various collimator systems have been devised. Basically, apertures should be positioned as shown in Figure 4.3 to reduce scattering off the walls. Brass has been used to construct these apertures because of the greater likelihood of particle absorption. Further adaptions include magnets of approximately 1000 gauss to discriminate between protons and electron particle content.
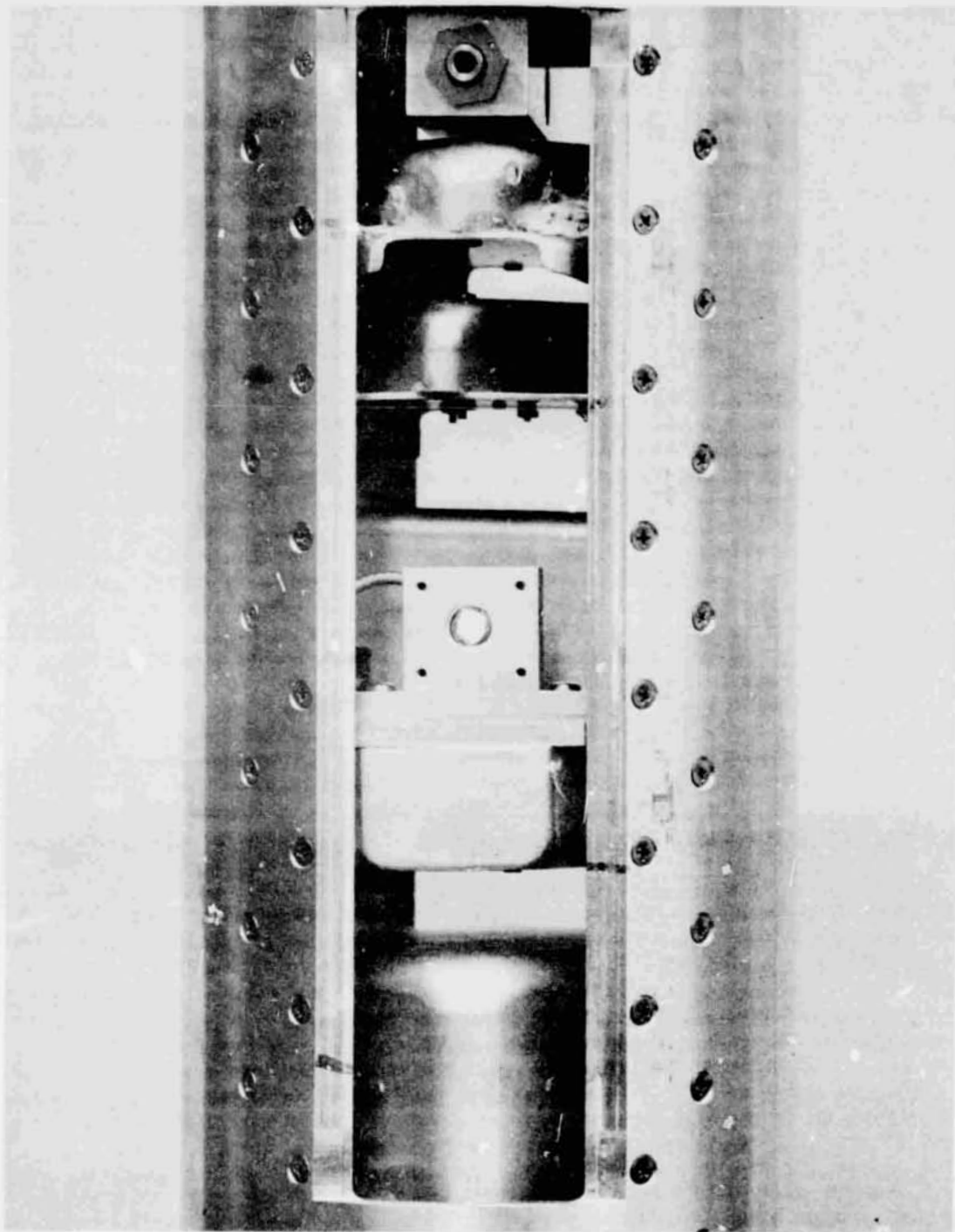
Figure 5.30   Position of the energetic electron spectrometer relative to the rocket shell door.   Door ejection is made at approximately 40 km.
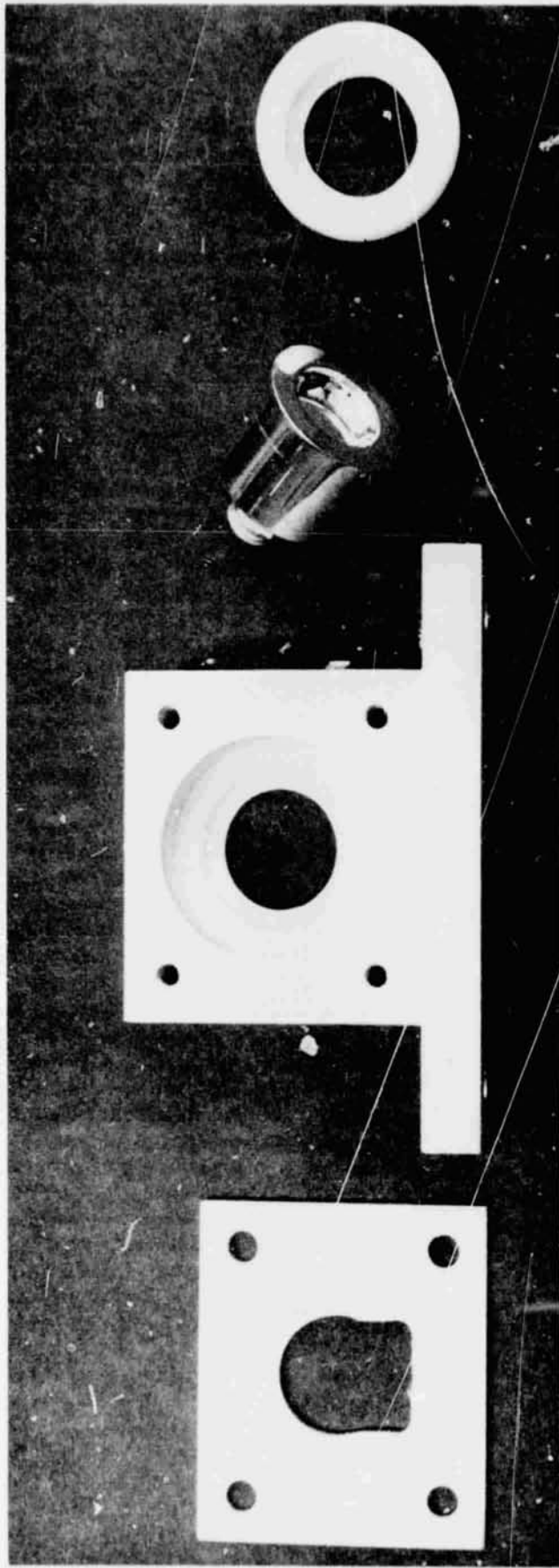
Figure 5.31 Mounting hardward for the solid-state detector. The teflon ring is used for electrical and thermal insulation.

where C_{eqv} is the total equivalent capacitance referred to the input and v_{rms} is the equivalent noise, $\sqrt{v^2_{NT}}$, generator referred to the input. *FWHM* is the full width at half the maximum of the distribution. The final relationship for σ will be derived later; however, it is advantageous to state it now as

$$\sigma = E_g \frac{C_1 \sqrt{v^2_{NO}} \, V_{ger}}{q \, V_{sig}} \tag{5.11}$$

where $\sqrt{v^2_{NO}}$ is the rms output noise, C_1 is the series capacitance through which a calibrated signal V_{ger} is applied (Figure 5.9) to the preamplifier input producing an output signal, V_{sig}.

For the designed amplifier the *FWHM* was measured to be (Figure 5.5) 8.4 keV *FWHM* (silicon) at a temperature of 30°C. The output rms noise, $\sqrt{v^2_{ON}}$ of the preamplifier at this temperature is 20 mV rms. The calibration gain, V_{sig}/V_{ger}, was measured to be 34.5 (Figure 5.11) and C_1, is, from the schematic (Figure 5.9), 1 pf. This information leads to the conclusions from the above equations that, 1) the standard deviation is 3.6, from equation (5.10) or from equation (5.11); 2) the number of movement events is $9.4 \times 10^6 \ \text{sec}^{-1}$ from equation (5.9); and 3) $C_{eqv}v_{rms}$ is equal to Q_N which is 5.2×10^{-16} coulombs.

From conclusion three and Figures 5.11 and 4.15 for $\tau = 0.5$ sec, C_{eqv} is 90 pf yielding $v_{rms} = 5.8 \times 10^{-6}$ volts and thus the overall amplifier voltage gain is 3500. This can be cross-checked by observing that the calibrated signal is voltage divided down through C_1 and C_{eqv}, hence:

6. CALIBRATION OF THE SOLID-STATE DETECTOR

The calibration procedure involves consideration of the detector
sensitivity to various kinds of particles with respect to the energy
and to the particular direction at which the particles enter the semi-
conductor. The primary theoretical discussions for the above variation
have been dealt with in Chapter 4. The purpose of this chapter is to
verify this material with experimental results and obtain the direct
relationship between the input excitation and the output response with-
out reference to the system physical makeup. The first section is
concerned with the directional properties of the detector and how the
modeled angular dependence calculation agrees with the experimentally
determined dependence. The second section develops methods for energy
calibrations using radioactive conversion electron sources with known
energy emissions. The final section presents calibration results
obtained from an electron and proton accelerator.

6.1 *Detector Geometrical Factor and Angular Resolution*

One of the most important calibration measurements is to ascertain
the angular response of the detector to incident particles. Experimental
results indicate that the angular pattern is significantly different from
the theoretical calculations for electron energies greater than 20 keV.
The associated reason for this discrepancy is reconciled due to scatter-
ing of the higher energy particles off of the collimator walls.

The geometrical factor is a useful quantity which relates the counting
rate of a detector to the flux, assumed isotropic, to which it is exposed.
Thus

$$\text{G.F.} \equiv \frac{N}{\Phi} \qquad\qquad (6.1)$$

where N is the detector counting rate and Φ is the number of particles per square centimeter per second per steradian. Figure 6.1 illustrates the detector geometry with the detector mounted in the rocket payload. Assuming that all electrons colliding into the wall are absorbed, an analytical expression may be derived for the geometrical factor.

Projection of the circular aperture of the collimator on the plane of the detector circular area for a particular angle θ displaces the circles centers by $t \tan \theta$ as shown in the lower diagram of Figure 6.1. For $\theta < \theta_{crit}$ there is no vignetting whereby the exposed sensitive area is $\pi r^2 \cos\theta$, the effective area of a disk viewed from the angle θ. If $\theta > \theta_{crit}$ the exposed area is $A \cos\theta$ where A is the intersection of the two circles illustrated in Figure 6.1 by the section lining. To determine A the following relationships are valid

$$\text{Sector } \alpha + \text{Sector } \beta = \text{Triangle } \alpha\beta + 1/2 \, A$$

where

$$\text{Sector } \alpha = \frac{\pi R^2 \alpha}{2\pi} = \frac{R^2 \alpha}{2}$$

$$\text{Sector } \beta = \frac{R^2 \beta}{2}$$

$$\text{Triangle } \alpha\beta = 1/2 \, R^2 \cos\alpha \, \sin\alpha + 1/2 \, r^2 \cos\beta \, \sin\beta$$

Solving for A gives

$$A = R^2 \left(\alpha - \frac{\sin^2 \alpha}{2}\right) + r^2 \left(\beta - \frac{\sin^2 \beta}{2}\right) \qquad (6.2)$$

using the law of cosines yields α and β as

θ_{MAX}

θ_{CRIT}

.300" — .500"

.083"

.031"

.125"

.239"

$R \equiv .250"$

$r \equiv .150"$

$t \equiv .239"$

$(a - a \cos \phi)$

$Area = 2a^2 (\phi - \sin \phi \cos \phi)$
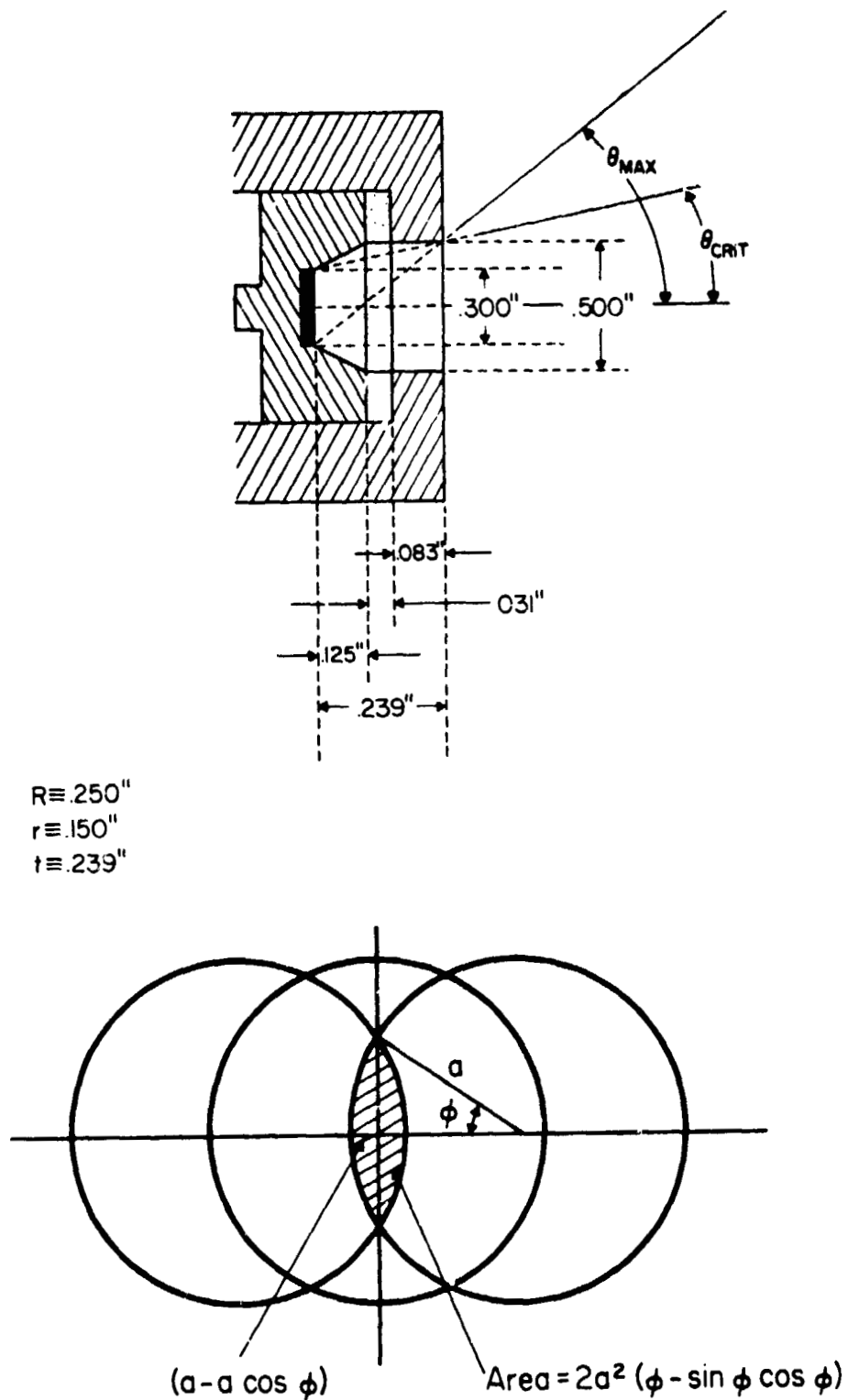
Figure 6.1   The upper figure illustrates the collimator geometry and
mounting hardware for the solid-state detector. The
lower figure shows the construction for calculation of
the geometrical factor.

$$\cos\theta = \frac{R^2 - r + t^2\tan^2\theta}{2Rt\ \tan\ \theta}$$

$$\cos\beta = \frac{-(R^2 - r^2) + t^2\tan^2\theta}{2Rt\ \tan\ \theta}$$

(6.3)

The geometrical factor in ster^{-1} is related to the effective area, A, by

$$\text{G.F.} = \frac{\int A\ \cos\theta\ d\Omega}{A_o}$$

(6.4)

since the number of particles counted is the integral of the flux over each element of solid angle $d\Omega = 2\pi\ \sin\theta\ d\theta$ weighted by the effective area A. In keeping with equation 6.1 the division by A_o is required to account for the flux, Φ, when the vignetting is zero. For $\theta < \theta_{crit}$

$$\int_o^{\theta_{crit}} A\ \cos\theta\ d\Omega = \int_o^{\theta} \pi\ r^2\ \cos\theta\ 2\pi\ \sin\theta\ d\theta = \pi^2 r^2\ \sin^2\theta_{crit}$$

(6.5)

and for $\theta > \theta_{crit}$ the appropriate expression is

$$\int_{\theta_{crit}}^{\theta_{max}} A\ \cos\theta\ d\Omega = 2\pi\int_{\theta}^{\theta} d\theta\ \sin\theta\ \left\{ R^2(\alpha - \frac{\sin 2\alpha}{2}) + r^2(\beta - \frac{\sin 2\beta}{2}) \right\} \cos\theta$$

(6.6)

Solving the last integral numerically and substitution for the appropriate parameters into equation (6.4) results in the determination of the geometrical factor. For the case presented in Figure 6.1 the geometrical factor is 1.49 ster^{-1}.

The angular dependence of the detector is calculated from the normalized effective area A. Figure 6.2 illustrates this angular dependence for two collimator geometries. The curve for the beam width of 64 degrees represents the geometry of Figure 6.1. Also shown is the experimentally measured curve (BW = 82 degrees) using 1.5 keV electrons. The results
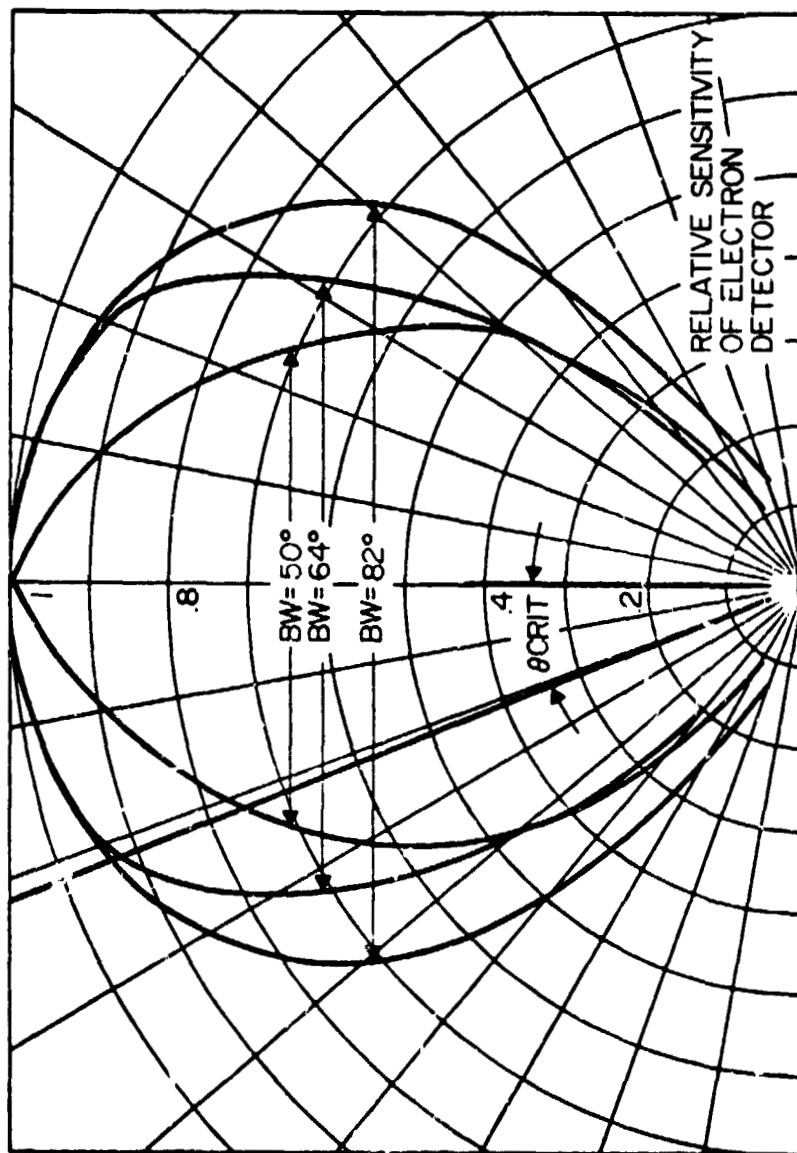
Figure 6.2 Angular patterns showing the relative sensitivity of the electron detector. The BW of 64° represents the geometry of Figure 6.1. The pattern of beam-width of 82° was measured experimentally for high energy particles where scattering was prominent.

clearly illustrate the increased sensitivity due to scattering of high energy particles off the walls.

The experimental apparatus used in making the first measurement is portrayed in Figure 6.3. A radioactive source (Cobalt 57) coated by nylon is used to excite electrons. The electron source is shielded except for an opening having a diameter of 3 mm. The vacuum chamber is necessary to keep the electrons from being scattered and absorbed in the ambient air. The conversion electron source is directed at the solid-state detector and rotated about the detector on a radius of 13 cm. The detector is connected to counting circuits external to the system. The beam width deduced in this manner is 82 degrees. The discrepancy between this value and the calculated value of 64 degrees is discussed later in this section.

Subsequently the facilities of the Goddard Space Flight Center were utilized. The description of the electron accelerator system is discussed in Section 6.3.1. For discussion here it is sufficient to note that pulse height analyzer spectrums were made for various angles, θ, of a controllable electron beam. The pulse height spectrum obtained for 20 and 40 keV electrons is shown in Figure 6.4. The 20 keV spectrum to the left is resultant of θ equal to 0, 20, 30, 40, 50, and 60 degrees. The theoretical cutoff angle is 42 degrees suggesting that scattering off the walls is the only viable explanation for the 40 keV particle counting at angles of 50 and 60 degrees. At 20 keV the theoretical cutoff is observed. To better qualify this wall scattering energy dependence, the experimental results are plotted in Figure 6.5. Suppression of wall scattering effects may be accomplished by inserting baffles into the collimator section, as illustrated in Figure 4.4.
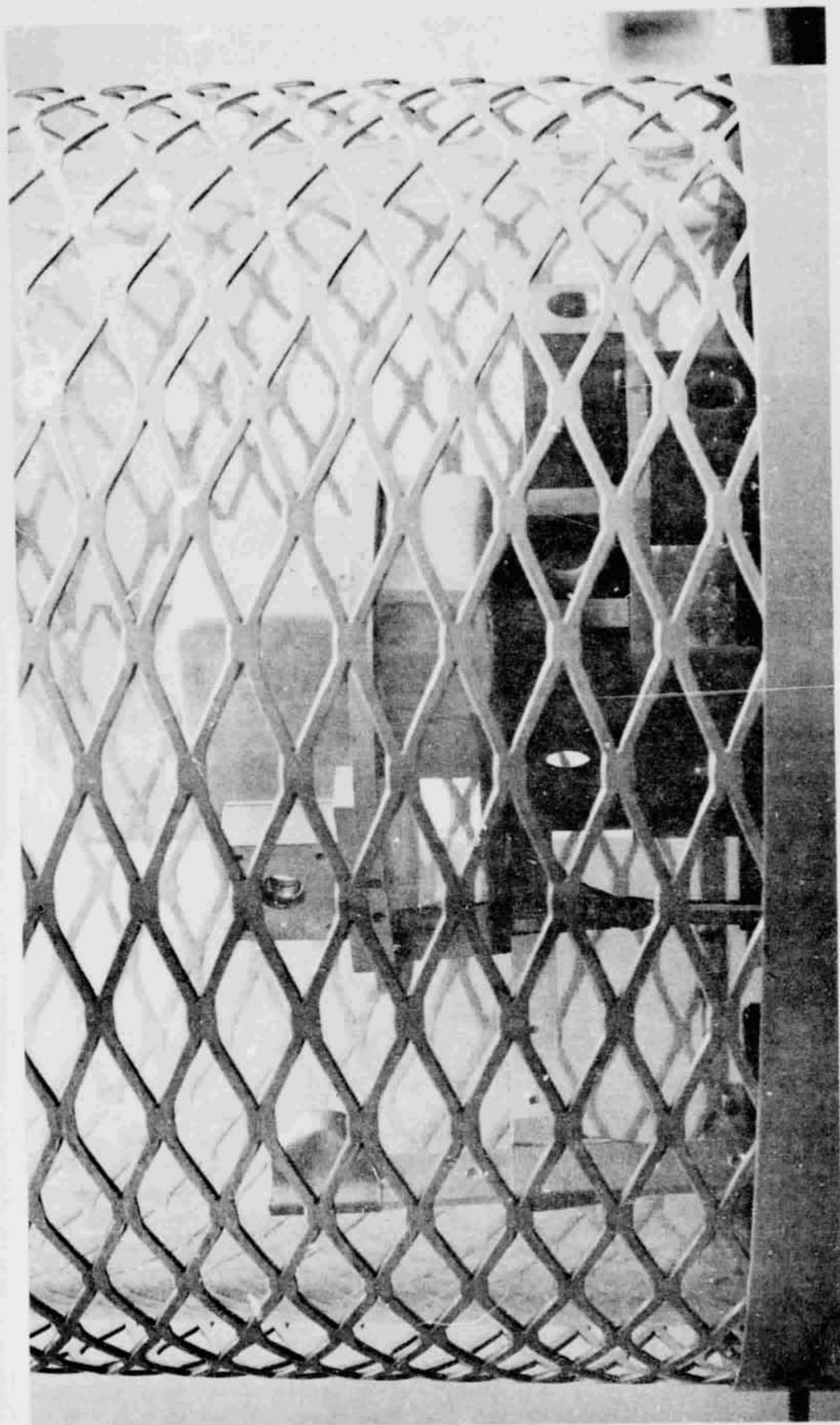
Figure 6.3 A radioactive particle source was made to rotate about the sensitive surface of the solid-state detector and in a vacuum chamber to reduce scattering. Angular patterns could then be made as shown in Figure 6.2.

C-3
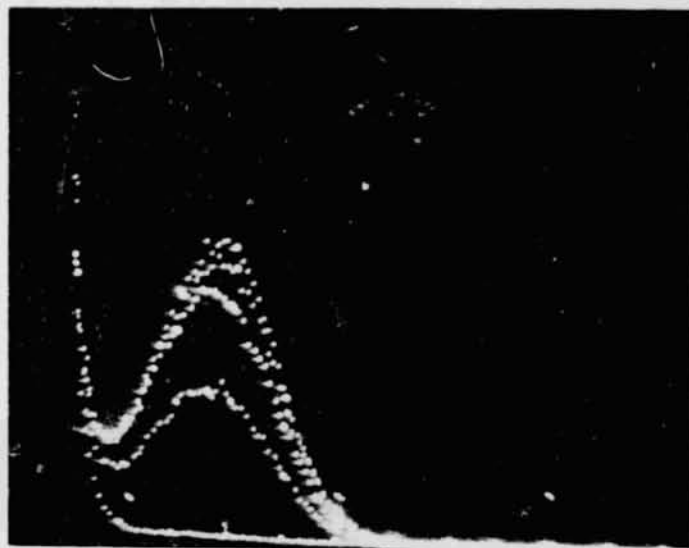
Figure 6.4   Pulse height spectrum obtained for 20 and 40 keV electrons
using the instrumentation of the GSFC. The 20 keV spectrums
(top photo) are for particles with angles of 0, 20, 30, 40
and 50 degrees and the 40 keV spectrums for 0, 20, 30, 40, 50
and 60 degrees.
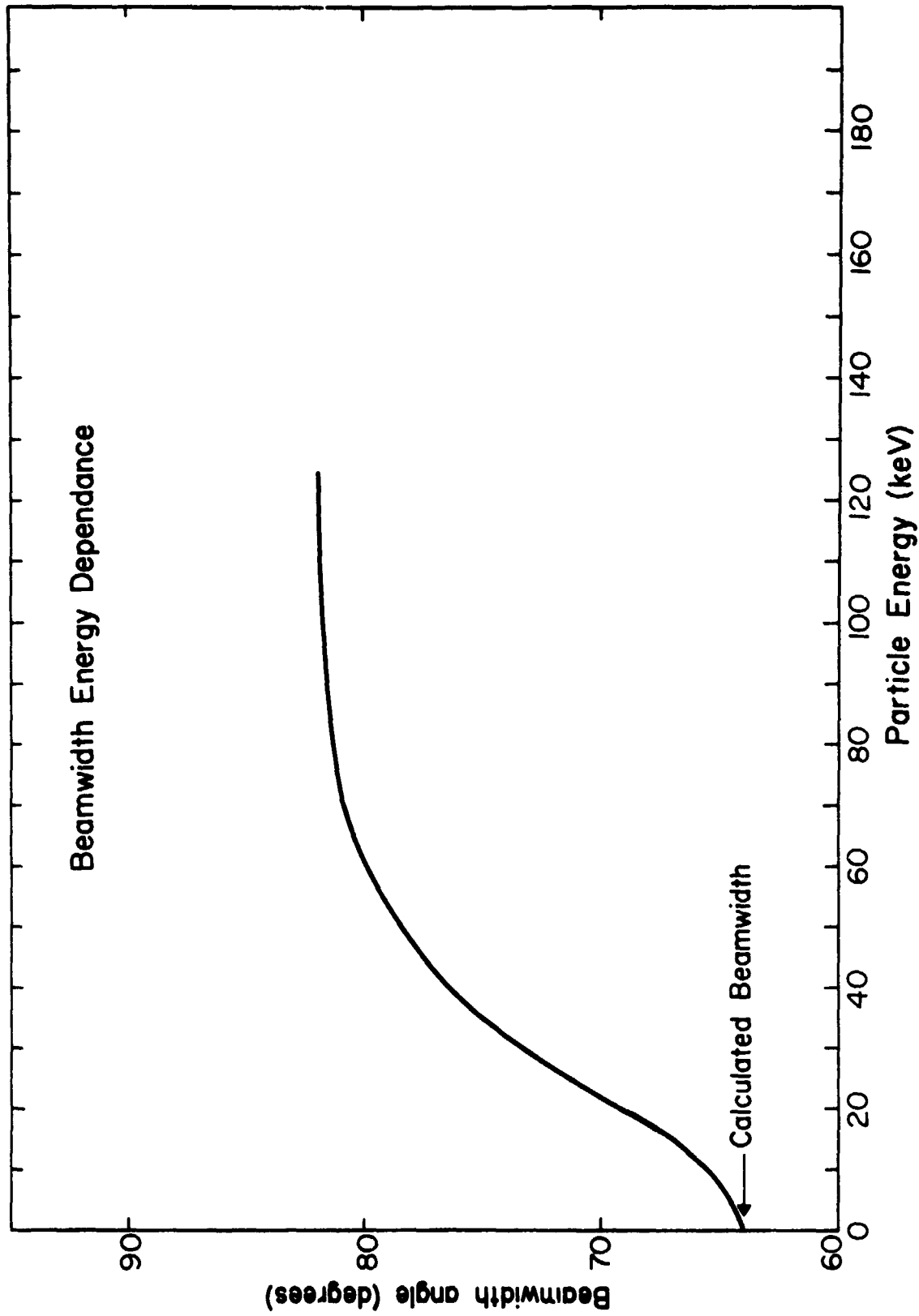
Figure 6.5 Experimental results were used to obtain this relationship of beamwidth variation with energy. These results show that scattering off the walls is significant.

6.2 *Conversion Electron Sources*

One simple method which can be used to calibrate the output voltage signal is to introduce a radioactive source of known energy and measure the resultant averaged pulse height or even better yet the analyzed spectrum. The radioactive source employed uses Cobalt-57 in contact with a mylar surface. Gamma radiation interacts with the mylar and releases energetic electrons of nearly identical energy (minus approximately 5 to 6 keV, lost in overcoming the work function). For Cobalt-57 the gamma energies are 122 and 137 keV producing electrons of 116 and 130 keV, respectively. The output pulse for this case is portrayed in Figure 6.6. The two top peaks can be associated with the above-mentioned decay energies.

Assuming that the dead zone region absorbs 2 to 3 keV and the detector is linear, the calibration curve shown in Figure 6.15 is suggested. The method is capable of resolving energies within 9%.

The error may be halved by employing a pulse height analyzer which averages over a time interval to give a most probable peak. Figure 6.7 shows the double peak produced by Cobalt-57. Again, the calibration curve is derivable from this information, assuming linear behavior.

6.3 *Facilities Employed to Obtain Final Spectrum and Energy Information*

6.3.1 *Electron and proton accelerator system.* Final calibrations were made using an electron-proton accelerator at the Goddard Space Flight Center in Maryland. The accelerator features a high voltage DC power supply and is designed to produce electrons or protons at controlled particle intensities with energy variable from thermal to 160 keV. The generated beam is directed to a vacuum chamber shown in Figure 6.8 in which calibration experiments are performed. The positioning of the
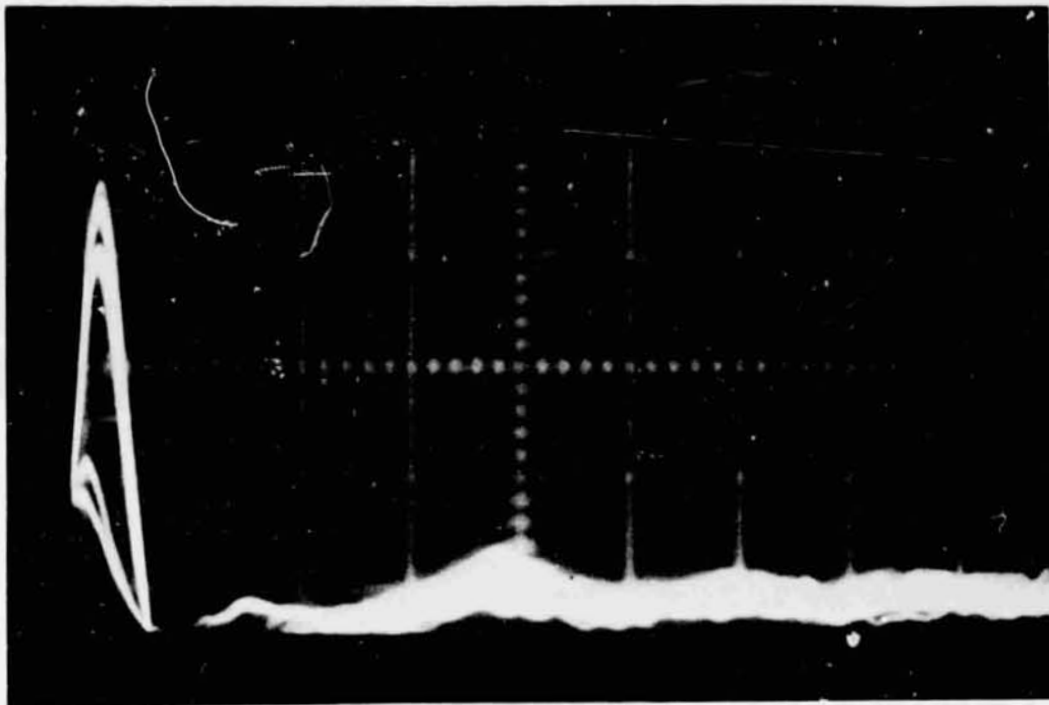
Figure 6.6 Output pulse from a Cobalt - 57 radio active source. The two pulse heights correspond to the decay energies of 116 and 130 keV electrons. A quick calibration measurement can therefore be made.
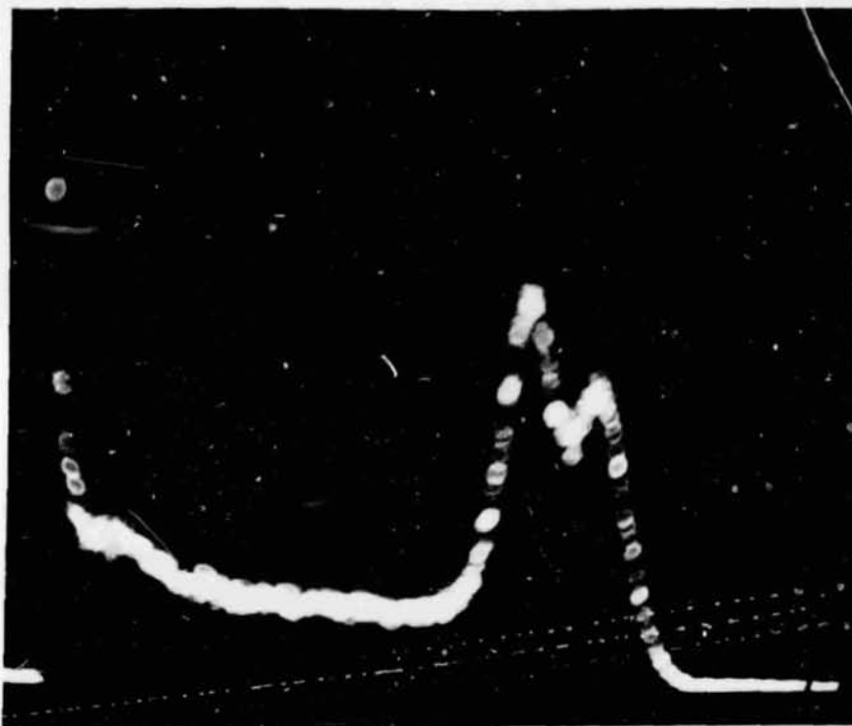
Figure 6.7 Employing a pulse height analyzer to the output produced
by a Cobalt source a double peak is produced corresponding
to energies of 116 and 130 keV. A calibration curve can
thereby be produced.
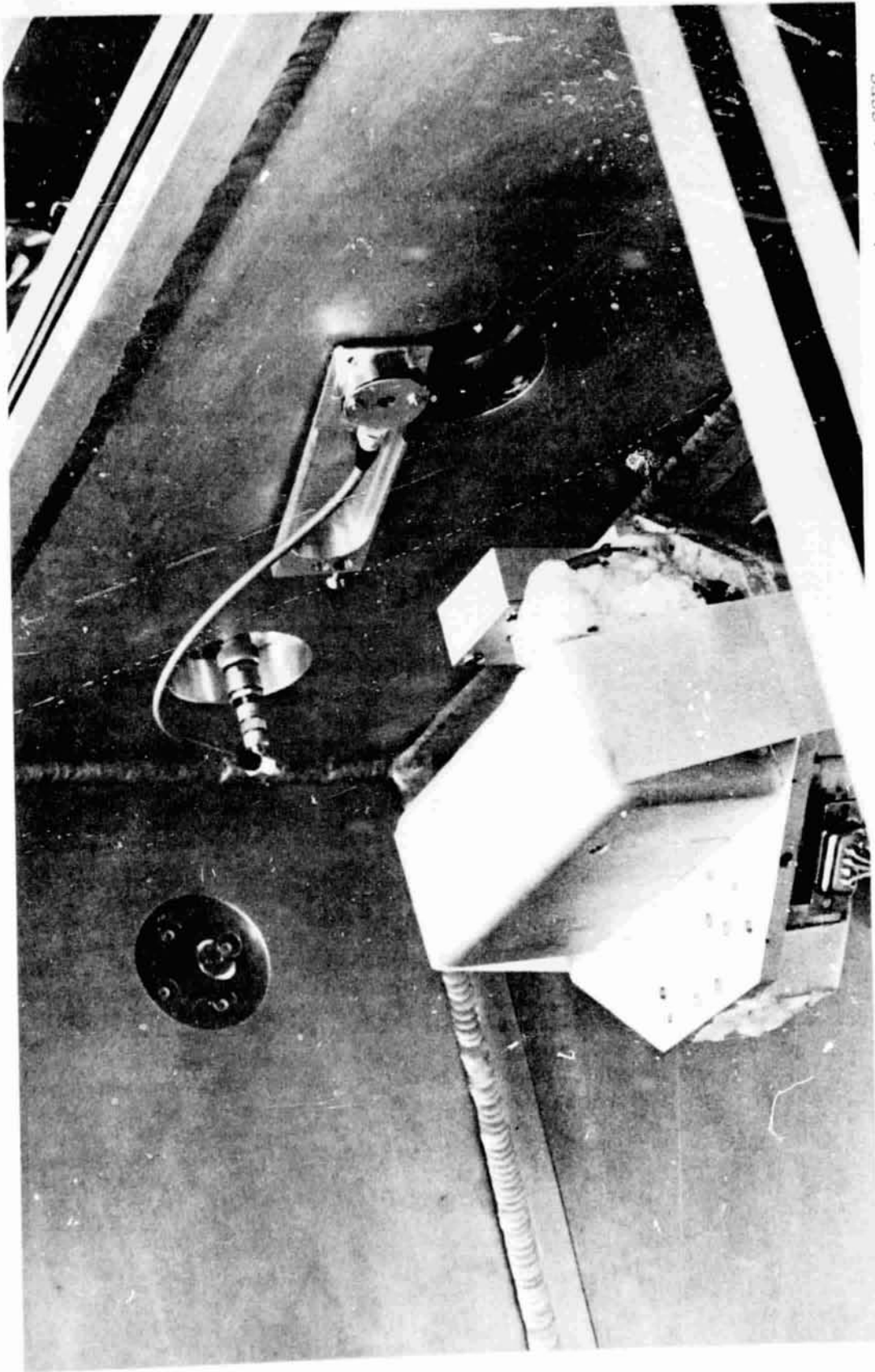
Figure 6.8 Vacuum chamber and position of spectrometer used for calibration experiments at GSFC. The positioning of the detector is in line of the beam and located directly above the rotation axis of the attached platform.

detector is in line of the beam and located directly above the rotation axis of the attached platform. The monitor is positioned adjacent to the extreme part and may be rotated in front of the beam for comparison purposes. All necessary electrical connections are fed through vacuum seals to monitors outside the vacuum chamber.

Figure 6.9 displays the electronics used for calibration. Signals from the monitor detector (solid state or channeltron) are preamplified at the exterior feedthrough of the vacuum chamber and transferred to the main amplifier shaping electronics located on the top of the moveable rack. The monitor pulses are then counted and averaged over a five second interval period (monitor counter is under top shelf). The solid-state monitor is responsive to electron energies down to 20 keV. For energies less than this a linear channeltron shown in Figure 4.3 is used. The background counts (ionic feedback) due to the residual gas contributes 160 counts per second.

The preamplified signal from the detector being calibrated is similarly fed through the vacuum chamber wall to the counting circuits and to a unity gain inverting amplifier located on the top shelf. Signals from each channel are connected to a counter and paper-tape punch located beneath the monitor counter. The inverted preamp signal was joined to an HP noise voltmeter (next to counter), oscilliscope, and pulse height analyzer (comprising the foreground electronics rack). Signals to the pulse height analyzer are fed into the peak detector and converted into digital form (fourth panel from top). The digital representation is stored in a 4000 channel memory (third panel from top) and interfaced with the oscilliscope via the display control panel. Provisions are additionally
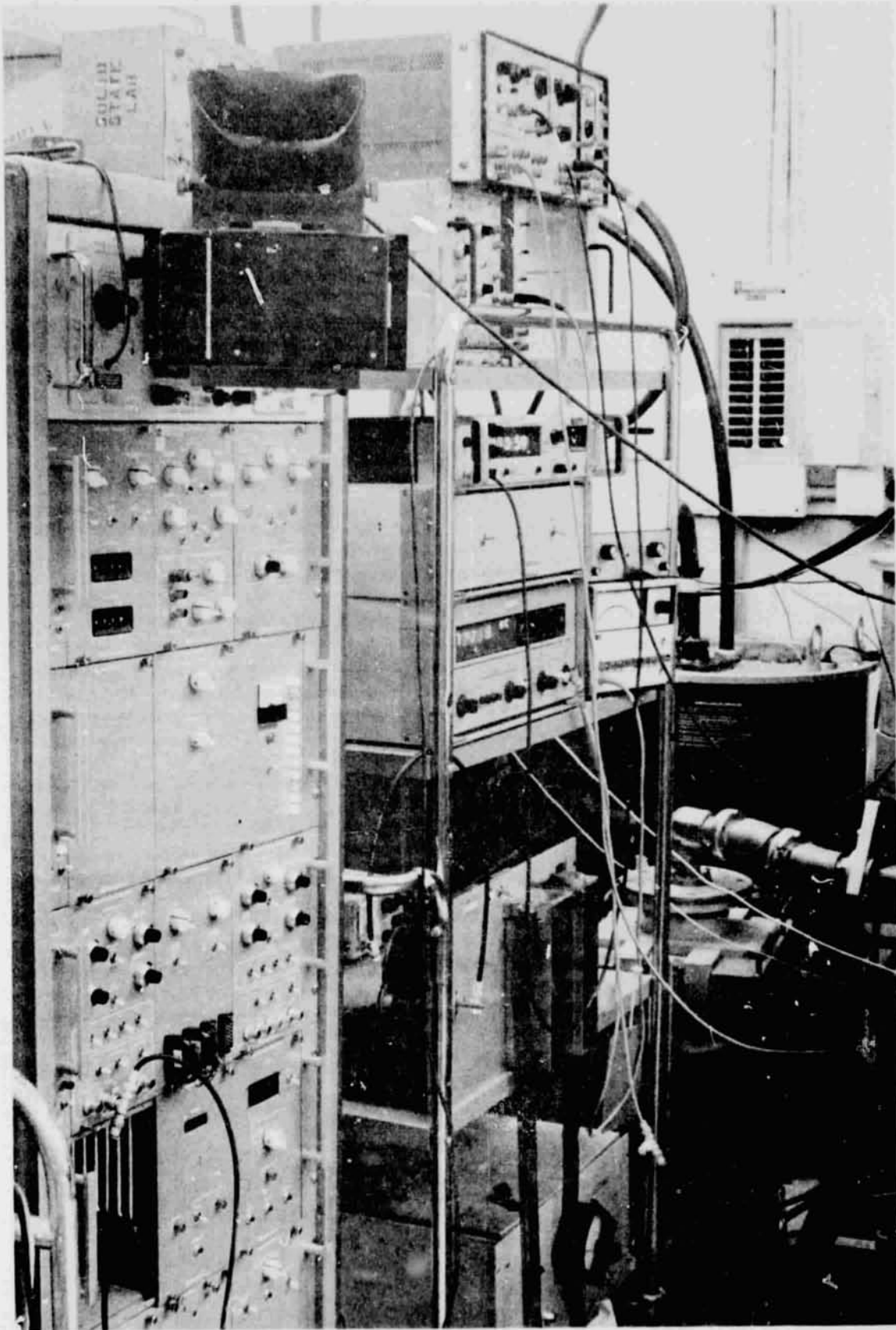
Figure 6.9 Displayed is the electronics used for calibration at GSFC.

made for digital printout of channel contents (lowest panel) and polaruid

photographs of displayed information. The instrument placed on top of

the PHA is a standardized signal for checking the performance of the

monitor.

6.3.2 *Channel passband calibration.* The data retrieved from the

detector counting circuits are dependent upon the efficiency of each

channel to discriminate and pass voltage pulses. The foundation of

the problem rest in the distortion of a constant pulse height due to

superposition of random noise fluctuations. Analytically this can be

represented by the gaussian distribution (equation 5.7) translated such

that μ represents the energy of the initial incident particle. The

probability, $P(E)$, that the final output pulse will be in an energy

interval dE is again

$$P(E)\ dE = \frac{1}{2\pi\ \sigma}\ \exp[-(E-\mu)^2/2\sigma^2] \tag{6.7}$$

Now, since the voltage comparators are sensitive to voltages greater

than a set threshold value, the passed counts will be all those pulses

whose probability is greater than E_T. This is the integral of equation

(6.7) from E_T to infinity. Representation of this is expressed analytically

in equation (5.15), and experimentally derived by measuring channel counts

for incident particle beams every 2 keV (Figure 6.10).

The major concern is that variation in σ resulting from variation

in temperature, changes the measured efficiency of counting. Figure 6.11

shows this sensitivity. Accurate determination of the channel efficiency

curves can be made if the temperature, rms noise voltage, or channel one

noise count rate is monitored and knowledge is available on the dependence.
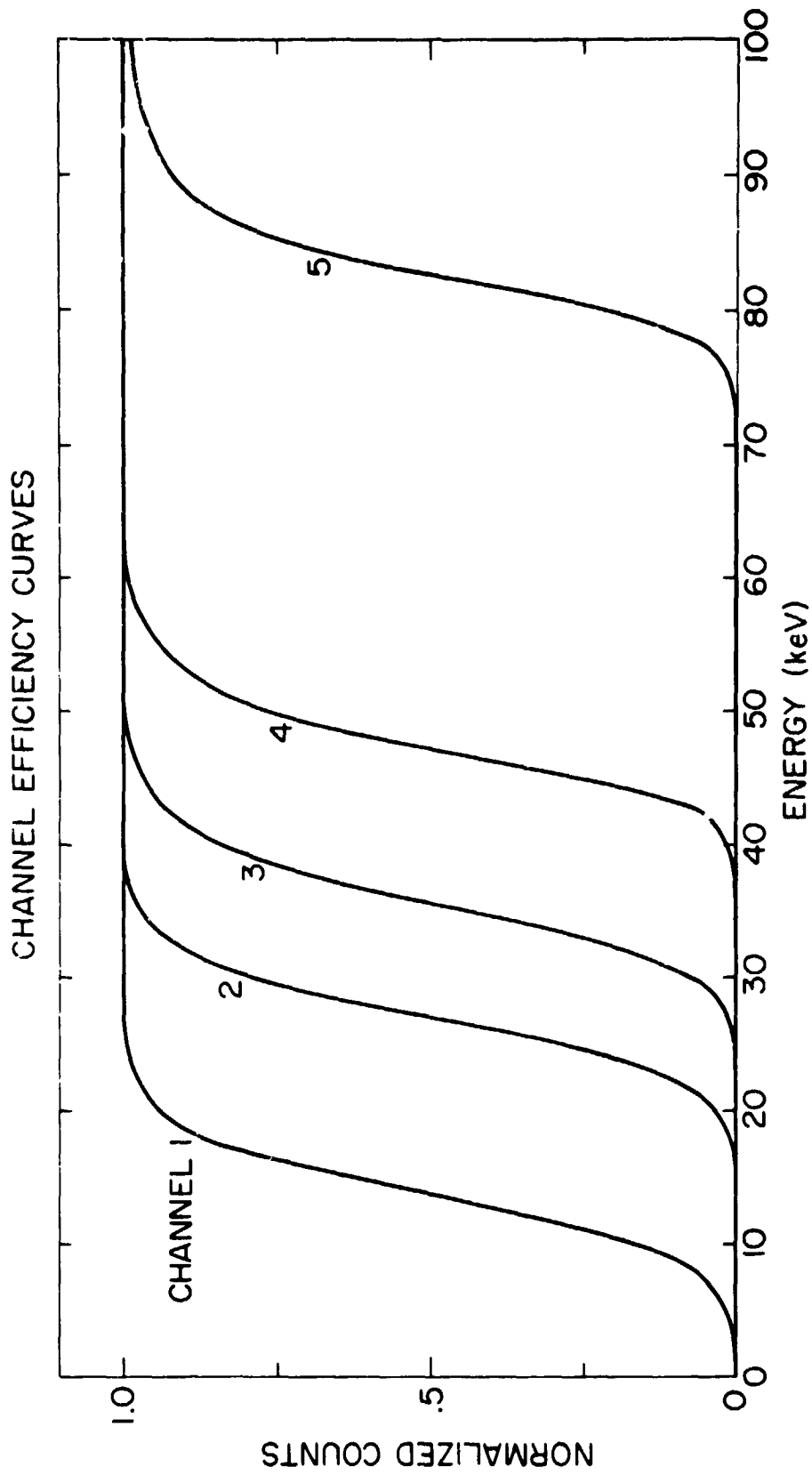
Figure 6.10 Experimentally derived channel efficiency count curves which are comparable to the derived formulation of equation (5.15). These results were made at GSFC.
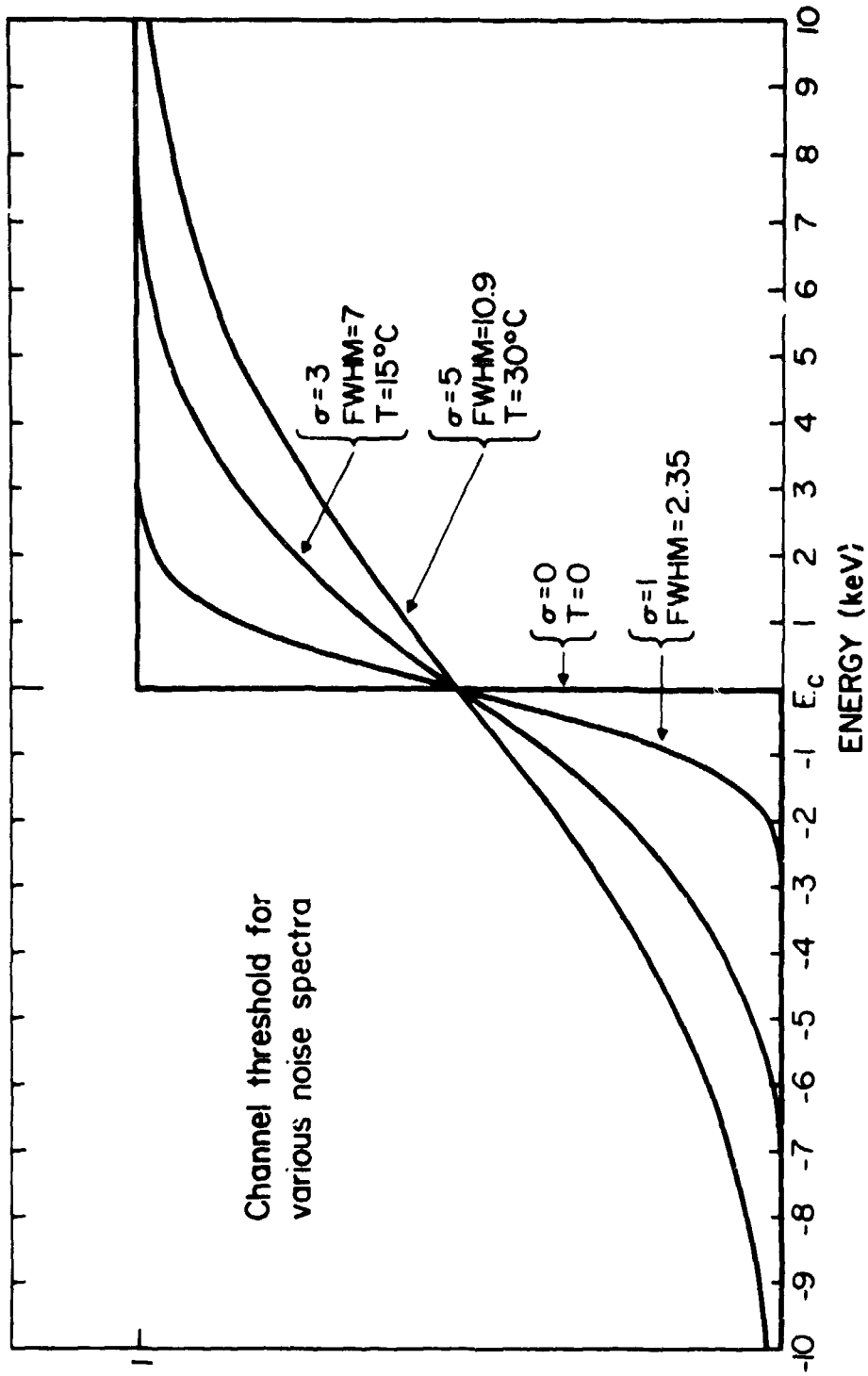
Figure 6.11 Theoretical temperature ̄ation of channel efficiency curves. Equation (5.15) was used for the calculation. ̄ ults clearly indicate that temperature is an important consideration for prope. ̄ of an effective threshold energy.

The actual method employed is to record the noise count rate before rocket launch and during descent when the rocket is out of the particle region and interpolate between these. For most cases the noise change is small and affords only a secondary correction.

The next important consideration is the effective cutoff threshold defined as the energy where half the maximum number of particles are passed per energy interval. Clearly for a continuous energy spectrum the effective energy threshold is in the center of the efficiency curve. In general, the spectrum is not constant over the threshold region and the effective threshold energy is determined by the product of the efficiency curve, $C(E)$, and particle spectrum $P(E)$.

$$\left\{ \begin{array}{l} \text{\# particles per energy} \\ \quad \text{interval } dE \text{ passed by} \\ \quad \text{the discriminator} \end{array} \right\} = C(E) \; P(E) \; dE \qquad (6.8)$$

Now assuming the spectrum to be a power law of the form E^{-x} where x is a positive constant and the efficiency curve is linear over the transition range, $C(E) = \frac{1}{2\sigma} (E-E_1)$, equation (6.8) becomes equal to

$$\frac{1}{2\sigma} E^{-x} \; (E-E_1) \qquad (6.9)$$

where σ is the noise standard deviation and is approximately the energy span between E_1 and E_2. The parameters are further illustrated in Figure 6.12.

E_8 is the energy where the slope of the product curve is zero and may be obtained by differentiating equation (6.9)

$$E_8 = \frac{x \; E_1}{x-1} \qquad (6.10)$$
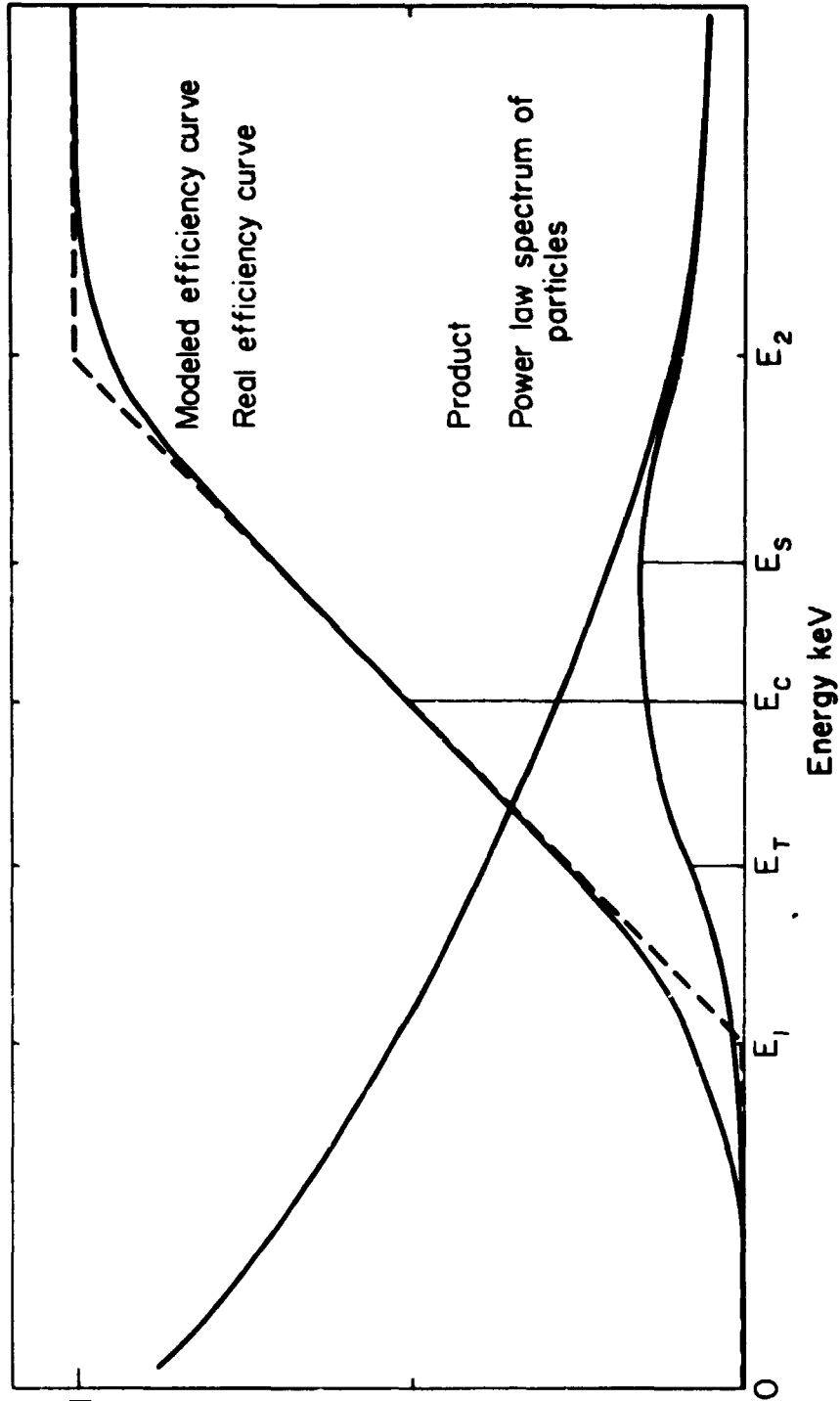
Figure 6.12 The particle spectrum appreciably varies over the threshold region. The effective threshold energy, E_T, can deviate from the center. Shown is the power law spectrum, efficiency curve and product curve from which the formulation given in the report enables E_T to be derived.

E_T is the effective energy threshold of the channel and is defined to be half of the value of the product curve at E_s for $X > \frac{E_2}{E_2-E_1}$, or at E_2 for $X \geq \frac{E_2}{E_2-E_1}$, hence

$$E_T^{-x} (E_T-E_1) = 1/2 (E_x-E_1)E_s^{-x} \qquad (6.11)$$

The equation is solved for E_T. Given $E_1 = 20$, $E_2 = 30$, and $x = 1$ the value of the product function at E_T is half the value at E_2 or

$$E_T^{-1} (E_T-20) = 1/2 \; 30^{-1}(30-20) = 1/6 \qquad (6.12)$$

giving $E_T = 24$ keV. Since the center energy, E_c, equals 25 keV the correction is 1 keV at $x = 1$. For $x = 2$ the correction is 2.1 keV.

The spectrum is actually unknown to begin with, requiring that the value of x be determined. For initial analysis the threshold, E_T, for each channel, is taken to be the center energy, E_c. The x of the spectrum is then derived and used to compute the new E_T. Relaxation in this manner converges to the proper x in about two itterations.

Another important consideration is the linearity of the detector to different flux intensities. One of the predominant problems is the pile-up of output pulses, which simply means the superposition of two or more coincident particles giving an erroneous energy count. Each pulse is stretched to approximately 5 μsec duration. The probability then that a second pulse distorts the first in a random generation in a one second interval is 1 divided by 10^{+5} sec = 10^{-5}. This occurs because any succeeding particle within plus or minus 5 μsec appreciably distorts the origi-

nal pulse. Allowing three pulses to originate within a one second inter-
val gives a probability of 2 times 10^{-5} for the last two pulses to land
on the first and 10^{-5} for the third to land on the second totaling 3×10^{-5}.
Continuing in this manner for four pulses reveals $(3 + 2 + 1)10^{-5} = 6 \times 10^{-5}$
chances of distorting and so forth. For N pulses

$$P = (1 + 2 + 3 + \ldots + N - 1)10^{-5} \qquad (6.13)$$

where P is the probability that at least one of the N pulses is coinci-
dent. By equating the opposite terms of the series, the above equation
reduces to

$$P = \frac{(N-1)N}{2} 10^{-5} \approx \frac{N^2}{2} 10^{-5} \qquad (6.14)$$

For $P = 1/2$ the number of particles need only be 320 for at least one
of the N pulses to be distorted half of the time.

Figure 6.13 illustrates the detector linearity for channels one
through four at 70 keV and channels one through three at 20 keV. The
center energies of the thresholds are 12 keV, 18 keV, 26 keV, and 55 keV
for channels one through five, respectively. Channel 1 shows the noise
contribution of 65 ramps per second added to the monitor counts. Also,
the count rate of channel one is observed to decrease at high rates
because of the built-in deadtime of 25 μsec. The experimental data
indicate that the instrument is extremely linear.

6.3.3 *Pulse height analyzer calibration.* Two methods were employed
to obtain pulse height measurements from the accelerator electrons. The
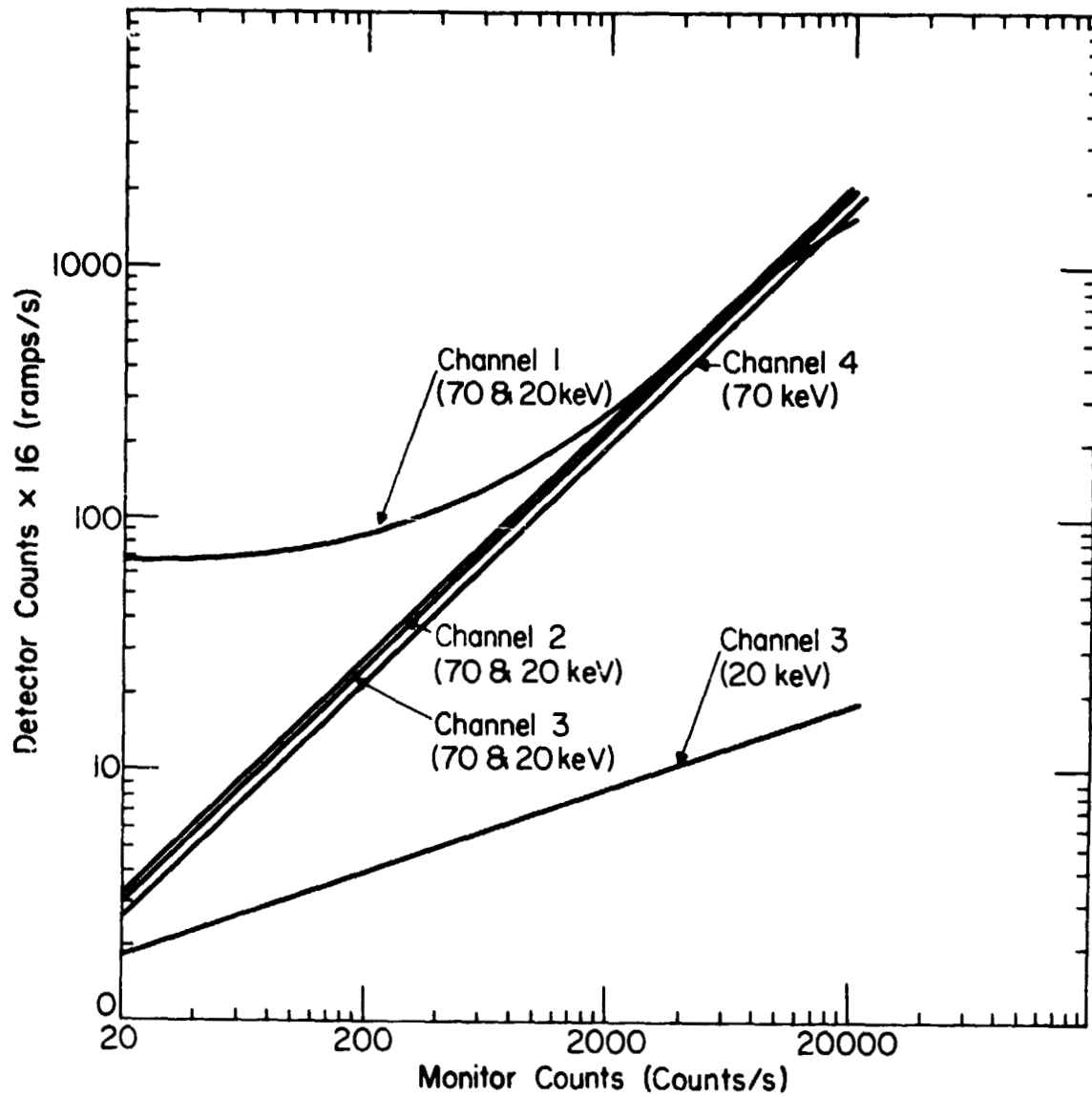
Figure 6.13   Illustrated is the detector linearity curves (experimentally
derived) for channels one through four at 70 keV and channels
are through three at 20 keV. Channel 1 shows the noise contri-
bution of 65 ramps per second added to the monitor counts.

first method is the simplest and requires only the measurement of an oscilloscope photograph output pulse. The second method used the integration of many pulses into pulse height channels. The channel counts can be displayed giving the spectrum of the pulses. The peak of the spectrum is the desired electron energy.

The first method is directly accomplished by placing a line centrally through the zero line of the noise and another parallel to the first through the maximum intensity point of the peak. The difference between the lines is the voltage calibration desired for the known electron energy. Figure 6.14 is a reproduction of recorded wave shapes for various energetic electrons. The final calibration curve relating the voltage peak associated with a particular energetic electron is shown in Figure 6.15.

The second method requires the use of a pulse height analyzer. A sequence of height spectrums are made for particular particle energy inputs. Three such spectrums are illustrated in Figure 6.16 for input energies of 20, 30, and 40 keV electrons. Again, results can be used to determine the final calibration curve for the output voltage peak verses incident radiation.

6.3.4 *Sensitivity of the detector to protons.* Protons are attenuated to a large degree because of their inherent mass difference and quantum interaction efficiency. The dead zone region consequently reduces the proton energy approximately 10 keV before contribution is made to the current pulse. For calculations of the proton range, $\frac{dE}{dx}$ and depletion equivalent energy depth for silicon reference should be made to Figures 4.7, 4.8 and 4.15, respectively.

190
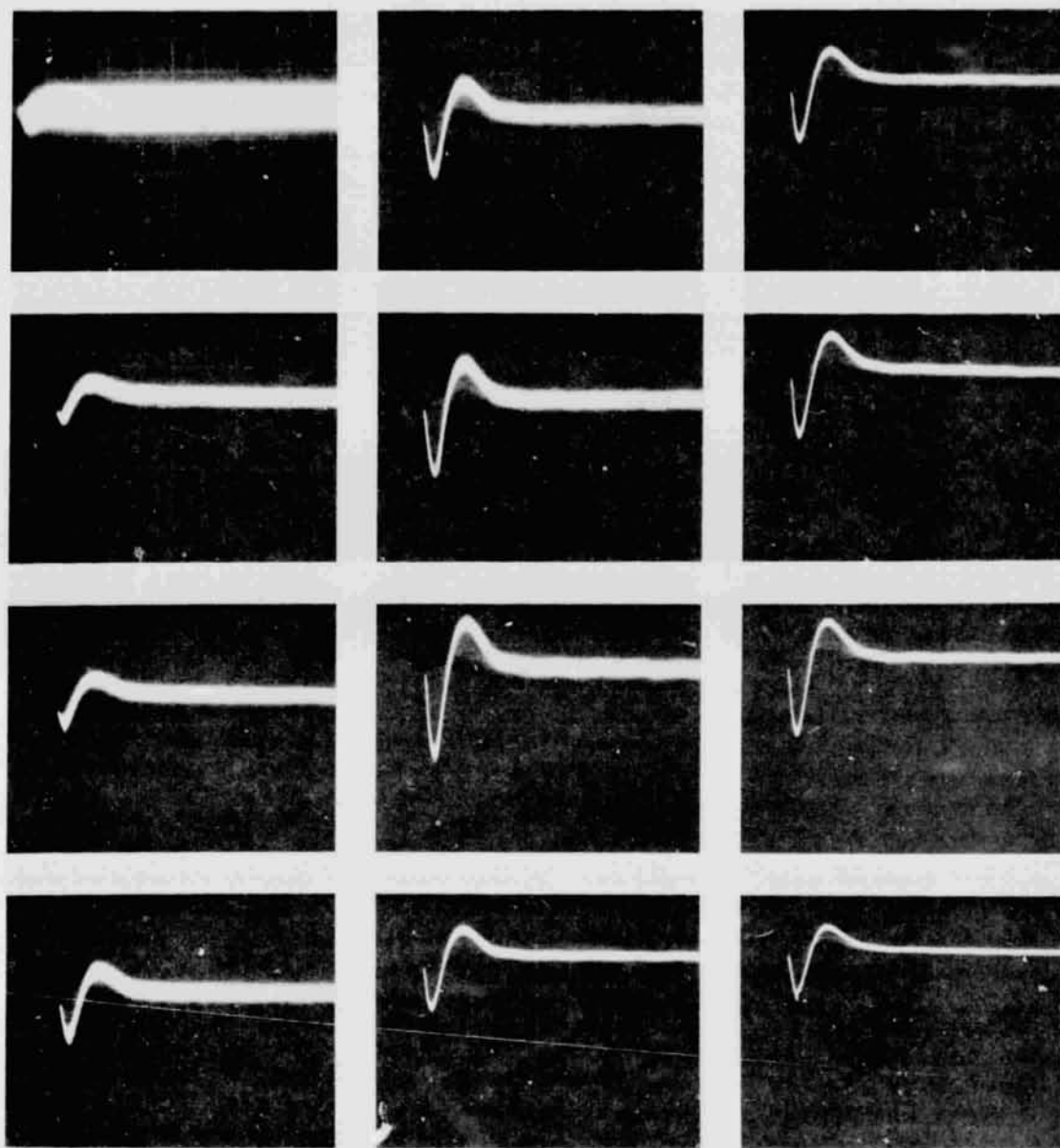
Figure 6.14 Output pulses from the preamplifier for various monoenergetic beams of electrons incident on the detector. The height of the pulse provides excellent calibration over the entire energy range of interest. The upper left hand record shows the noise (vertical scale of 50 mV/Box). Directly beneath and adjacent is shown the waveforms for 15, 20, 30, 40, 50 and 60 keV (vertical scale of 100 mV/Box). The next four correspond to energies of 70, 80, 90 and 100 keV (vertical scale of 200 mV/Box). Finally, saturation is shown in the lower right hand signal for a 150 keV electron (vertical scale of 500 mV/Box).
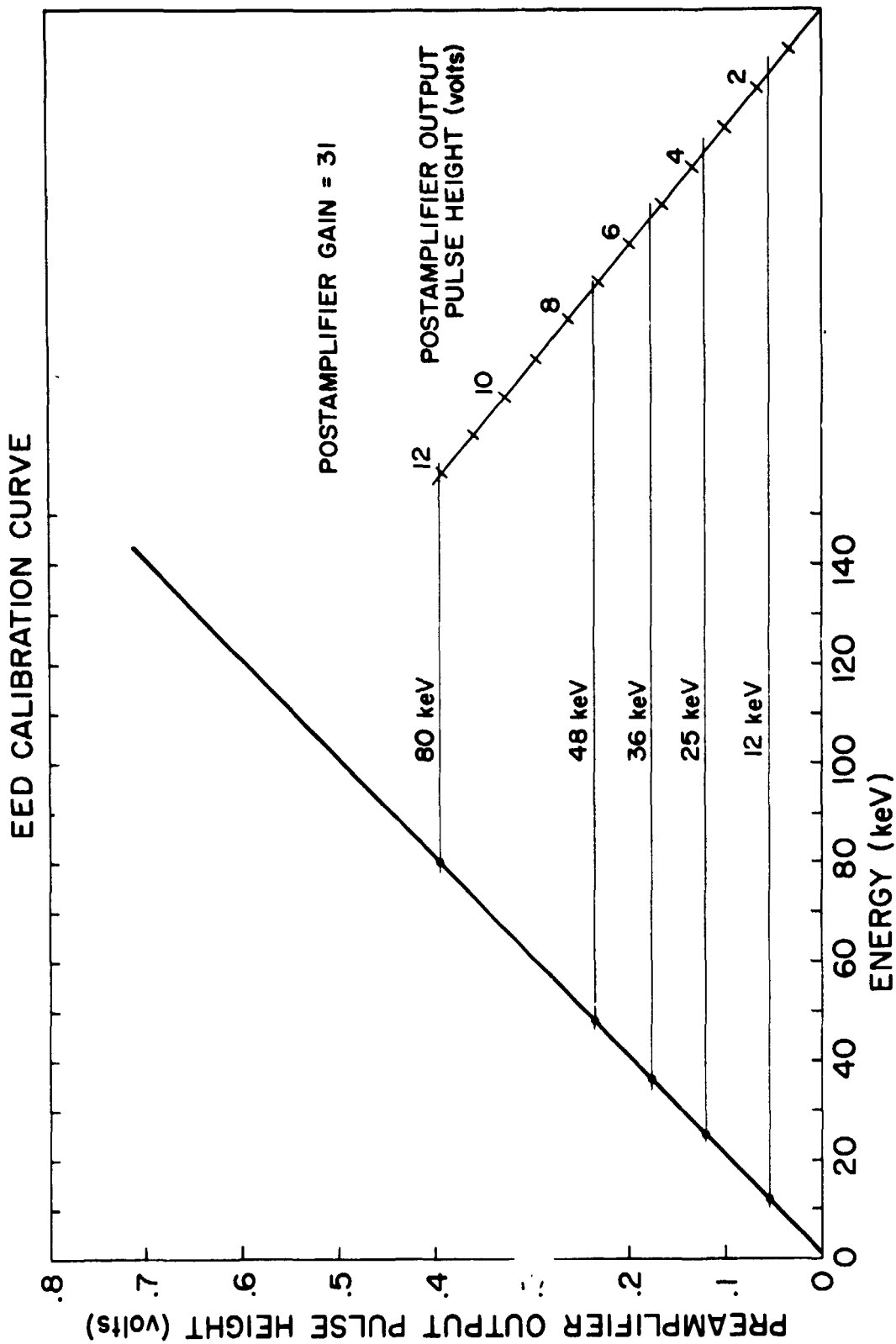
Figure 6.15 Final calibration curve for energetic electrons relating the preamplifier and postamplifier peak output pulse with the incident particle energy.
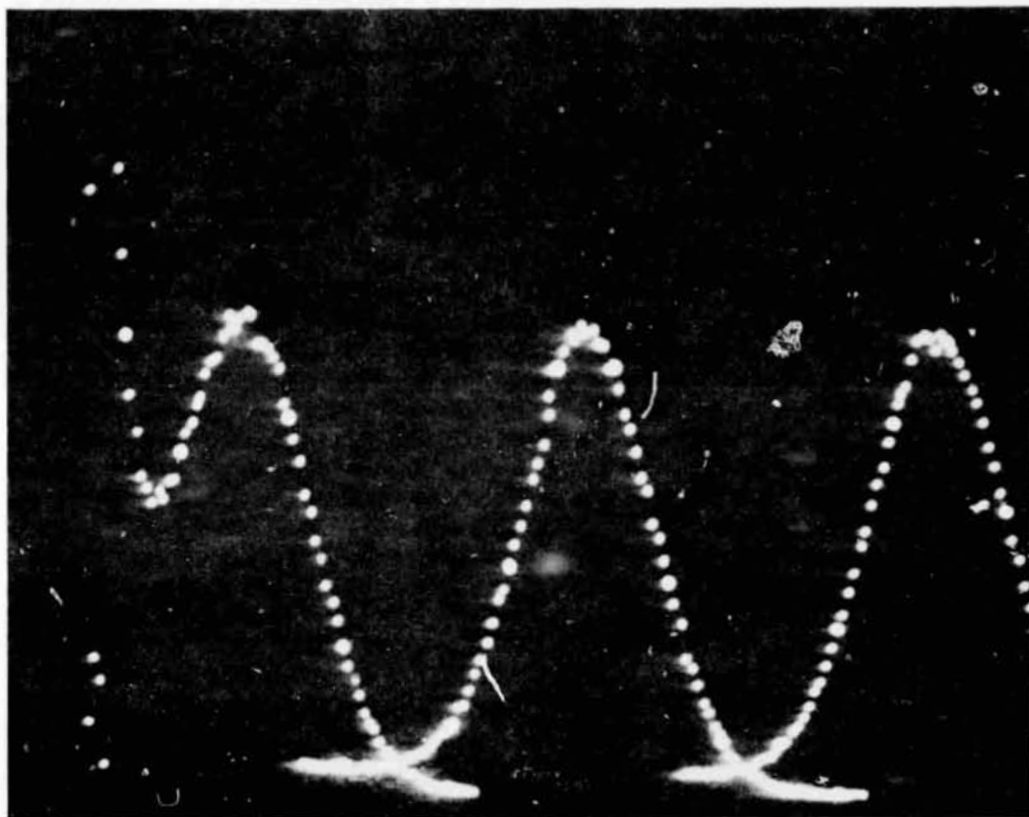
Figure 6.16 Pulse height analyzer spectrums for 20, 40 and 60 keV
electrons. The pulse at the left is due to noise
buildup.

7. CONCLUSION

Energetic electrons play a significant role in the upper E-region ionization as shown by direct particle measurements and other indirect indicators. Analysis of electron-density profiles in the upper E region near midnight at Wallops Island indicate that the ionization rate is very strongly correlated with geomagnetic activity. No additional source of ionization from scattered solar UV radiation is needed to account for the ionization rates at Wallops Island. In fact, the present data indicate that an upper limit for ionization sources other than energetic electrons is 10^{-1} cm^{-3} sec^{-1} in the upper E region near midnight. The pitch angle distribution of particles and the linear particle count rate with altitude suggest that there is a strong concentration of particles near and somewhat greater than 90 degrees. This accounts for increased ionization in the upper E region give a particular energy spectrum since particles are not able to penetrate as low in altitude. The spectrums are related by power laws with exponent approximately between 1 and 4.

The intermediate layer, observed at night, is explained in terms of ionization redistribution caused from horizontal neutral winds. These winds induce a converging vertical ion drift which builds up ionization at the wind shear (reversal) interface. Using a typical wind pattern the continuity equation is solved numerically yielding the modeled layer. The layer, using appropriate production, recombination and diffusion coefficients, is in good agreement with observed measurements. This analysis provides an explanation for why the intermediate layer is more

noticeable during quiet geomagnetic conditions than under disturbed conditions. A wind sensitivity analysis shows that small values of vertical ion drift (about 10 m s^{-1}) are sufficient to give rise to a marked intermediate layer. Applying the continuity equation, given a particular electron-density profile, an averaged production rate can be deduced independent of diffusion and of the particular wind system configuration. The continuity equation may likewise be solved to determine the winds given the intermediate electron-density layer, recombination, and production variation. The wind system is observed to descend approximately 1.5 km minute^{-1} during the night and can be associated with the tidal winds of the (2, 4)-mode of the solar semidiurnal tides.

The design of a rocket-borne solid-state particle spectrometer was undertaken to further enhance the information on the role of energetic electrons in the midlatitude ionosphere. The theory, design, calibration and operation of this experiment are described in detail. The experiment has successfully been flown on four Nike Apache flights, one on 18 April 1974, and three on 29-30 June 1974, providing plentiful particle data. Some of the preliminary results of 18 April 1974 are illustrated in Figures 2.5 and 2.6. Complete analysis of the above flights will be referred to a later report, suffice it to say that flight chart records indicate similar behavior to that anticipated in the developed theory of Chapters 2 and 3.

Future analysis will investigate the ionization relationship in midlatitudes to the anisotropic pitch angle distribution and particle spectrums. A unified theory needs to be developed relating the satellite observations with rocket altitude data and atmospheric interactions. Furthermore, the interaction responsible for perturbing the radiation

belts and continually replenished then with trapped particles needs

to be established. Questions relating to geographic variation can be

assimulated as better interpretations of satellite data are made to

cohere with an ionization model. This material must be supplemented

with further rocket investigations to verify the completeness of the

developed theories.

APPENDIX I

COMPUTER PROGRAM USED TO CALCULATE IONIZATION RATES

FROM PARTICLE FLUX AND SPECTRUM INFORMATION

The program used to compute electron ionization altitude profiles

of Figure 2.12 was based upon the methods enunicated by *Wulff and*

Gledhill [1973]. The pitch angle distribution, employed in this develop-

ment, is assumed to be isotropic over the downward hemisphere. Although

this approximation is not necessarily valid the resulting attenuation

curves are extremely helpful in determining overall sensitivity of

profiles to spectrum and interaction coefficients. This program was, in

the main, developed by *Monro* [1974]. The height profiles are

calculated for exponential spectrums with exponents of 1.0 thru 7 in

half interval steps. The relevant ionization of each major constituent

(O^+, O_2^+, N_2^+, N^+) is printed verses the altitude. The input data from

Table 1 of *Wulff and Gledhill* [1973] is read into array A(20). The

number densities are read into AN(4, 20).

```
C       PRODUCTION RATES FROM ENERGETIC ELECTRONS
        DIMENSION A(20),HT(26),AN(4,20),Z(20),Q(5)
        CONA=LOGF(10.)
        READ 1,N,M
1       FORMAT(2I5)
        READ 2,(A(I),I=1,M)
2       FORMAT(10F8.0)
        READ 2,(HT(I),I=1,N)
        DO 3 I=1,4,1
        READ 2,(AN(I,J),J=1,N)
        DO 3 J=1,N,1
3       AN(I,J)=EXPF(AN(I,J)*CONA)
        READ 4,(Z(I),I=1,N)
4       FOPMAT(8E10.0)
        READ 2,EOMIN,EOMAX,DEO
        EO=EOMIN
13      PRINT 15,EO
15      FORMAT(2X,4HEO =,F5.1/)
        PRINT 16
```

```
16    FORMAT(4X,6HHEIGHT,7X,3HQO+,8X,4HQO2+,8X,
      14HQN2+,9X,3HQN+,8X,4HUTOT)
      DO 12 I=1,N,1
      Q(5)=0.
      EN=1.0
10    RP=4.17E-6*EN**1.74
      ZRP=Z(I)/RP*1.064
      IF(ZRP-1.2)5,5,6
5     J=1
      P=.1
9     IF(ZRP-P)7,7,8
8     J=J+1
      P=P+.1
      GO TO 9
7     AFT=A(J+1)+(P-ZRP)/.1*(A(J)-A(J+1))
      AZR=AFT*EN*1.E3/RP
      R=EN/EO
      FH=AZR*AN(4,I)*100./FXPF(R)/35./EO/1.E3
      Q(5)=Q(5)+FH
6     EN=EN+.1
      IF(EN-20.)10,10,11
11    IF(Q(5)-1.E-12)20,20,21
20    DO 22 J=1,5,1
22    Q(J)=0.
      GO TO 12
21    BK=1.+1.15*(AN(2,I)+AN(1,I)/2.)/AN(3,I)
      Q(1)=(.29*AN(2,I)+AN(1,I)/2.)*1.15/AN(3,I)*Q(5)/BK
      Q(2)=1.15*.71*AN(2,I)/AN(3,I)/RK*Q(5)
      Q(3)=.81*(Q(5)-Q(1)-Q(2))
      Q(4)=.19*(Q(5)-Q(1)-Q(2))
12    PRINT 17,HT(I),(Q(J),J=1,5)
17    FORMAT(2X,F7.2,2X,5E12.3)
      EO=EO+DEO
      IF(EO-EOMAX)18,18,14
18    PRINT 19
19    FORMAT(1H0/////)
      GO TO 13
14    CALL EXIT
      END
```

APPENDIX II

SOLUTION OF TIME-INDEPENDENT CONTINUITY EQUATION WITHOUT DIFFUSION

Two methods of solution were persued; 1) an analytical representation and 2) a numerical computer algorithm. The appropriate continuity equation to be solved is

$$N \frac{d\omega}{dz} + \omega \frac{dN}{dz} = q - \alpha N^2 \qquad (A2.1)$$

where ω is the vertical ion wind taken to be sinusoidal (equation 3.8) and q and α are the production and recombination coefficients assumed to be constant for the analytical representation. The equation, in general, is nonlinear with variable coefficients.

Analytical solution. Equation (A2.1) is classified as a form of the Riccati equation given as

$$\frac{dy}{dz} + Q(z)y + R(z)y^2 = P(z) \qquad (A2.2)$$

For the special case of $q = 0$ the substitution of $y = \frac{1}{v}$ transforms the equation into a first order linear equation which can be directly solved.

The nonlinear first order equation (A2.2) can be transformed into a second order linear differential equation

$$R \frac{d^2u}{dz^2} - (R' - QR) \frac{du}{dz} - PR^2u = 0 \qquad (A2.3)$$

where y is given by

$$y = \frac{1}{Ru} \frac{du}{dz} \qquad (A2.4)$$

For the case of interest α and q are constant and dw/dz is given by

$$\frac{\partial}{\partial z} w = \frac{\partial}{\partial z} (20 \sin\frac{z}{30} \pi) = \frac{2}{3} \pi \cos\frac{\pi}{30} z \qquad (A2.5)$$

proceeds as follows. The appropriate R, Q, and P are

$$R = \frac{\alpha}{w} = \frac{\alpha}{20} \csc\frac{z}{30} \pi$$

$$Q = \frac{1}{w} \frac{\partial w}{\partial z} = \frac{\pi}{30} \operatorname{ctn} \frac{z}{30} \pi \qquad (A2.6)$$

$$P = \frac{q}{w} = \frac{q}{20} \csc \frac{z}{30} \pi$$

Making these substitutions into equation (A2.3) and rearranging gives

$$\left[D^2 + \frac{\pi}{30} (\operatorname{ctn} \frac{z}{30} \pi + \operatorname{ctn} \frac{z}{30} \pi) D - \frac{q\alpha}{400 \sin^2 \frac{z}{30} \pi} \right] u = 0$$

where D is the differential operator.

Now letting $X = \frac{\cos\pi z}{30}$, the reduced equation is formulated as

$$\left[D^2 + aD - \frac{b}{X(1-X^2)} \right] u = 0 \qquad (A2.7)$$

where

$$a = \frac{\pi^2}{450} \text{ and } b = \frac{q\alpha}{400}$$

Equation (A2.7) is a linear second order differential equation. The state space $\bar{\bar{A}}$ matrix is given as

$$\bar{\bar{A}} = \left| \begin{array}{cc} 0 & 1 \\ -\dfrac{b}{X(1 - X^2)} & a \end{array} \right| \qquad (A2.8)$$

which is applicable to standard analysis methods. Also equation (A2.7) may be solved using the WKB method of solution.

Numerical Solution. The equation (A2.1) was found to be quite sensitive requiring every precaution to insure stability. A predictor-corrector method of the Euler-Romberg type was found to operate satisfactorily. Further reference to the theory of this method is found in *McCalla* [1967]. The program used to solve the continuity equation, employing this technique, is provided on the following pages.

```
C        FORTRAN PROGRAM FOR EULER-ROMBERG METHOD
1        DIMENSION X(100), Y(100), T(20)
2        COMMON LIMIT
3        PI=3.14159265
4        LIMIT=1
C        INPUT INITIAL VALUES, STEP SIZE, CONVERGENCE TERM,
5        READ (5,100) X(1), Y(1), H, EPS, LMAX, NC
C        COMPUTE NUMERICAL SOLUTION VALUE FOR EACH STEP N
C        COMPUTE VALUES BY EULER METHOD
6        N=1
7        GO TO 5
8      3 LIMIT =1
9        X(N+1)=X(N)+H
10       Y(N+1)=T(1)
11       N=N+1
12     5 T(1)=Y(N)+H*FCT(X(N),Y(N))
13       IF (LIMIT) 9,3,8
14     8 L=1
15    10 XC=X(N)
16       YC=Y(N)
17       LIM=2**L
18       DO 15 J=1, LIM
19       F=FCT (XC,YC)
20       IF (LIMIT) 14,3,14
21    14 XC=XC+H/FLOAT(LIM)
22    15 YC=YC+(H/FLOAT(LIM))*F
23       T(L+1)=YC
C        COMPUTE EULER ROMBERG TABLE VALUES T(K)
24       M=1
25       K=L
26    20 T(K)=(2.**M*T(K+1)-T(K))/(2.**M-1.)
27       IF (K-1) 35,35,25
28    25 IF (ABS(T(K)-T(K-1))-EPS) 50,50,30
29    30 M=M+1
30       K=K-1
31       GO TO 20
32    35 IF (L-LMAX) 40,75,75
33    40 L=L+1
34       GO TO 10
35    50 X(N+1)=X(N)+H
36    55 Y(N+1)=T(K)
37       S=FCT(X(N),Y(N))
38       XS=X(N)*1.E-5+120.
39       W=SIN(PI/3.E+6*X(N))*20.
40       WRITE (6,110) XS,Y(N),S, W
41       N=N+1
42       IF(N-NC) 5,60,60
C        OUTPUT SOLUTION POINTS COMPUTED BY EULER ROMBERG
43    60 WRITE (6,105)
44       DO 65 N=1,NC
45       S=FCT(X(N),Y(N))
46       XS=X(N)*1.E-5+120.
```

```
47              W=SIN(PI/3.E+6*X(N))*20.
48              WRITE (6,110) XS,Y(N),S, W
49        65 CONTINUE
50           GO TO 99
   C      OUTPUT SOLUTION POINTS PRIOR TO CONVERGENCE FAILURE
51        75 WRITE (6,113)
52           N2=N
           WRITE (6,110) (X(N), Y(N), N=1,N2)
        99 STOP
       100 FORMAT (2F15.7, 2F10.2, 2I2)
       105 FORMAT(2X,5HHEIGHT/KM,8X,12HDENSITY/CM-3,3X,15HDERIVITIVE/CM-4,3X
           111HWIND/ M/SEC )
       110 FORMAT(1X, F10.5,7X,E12.4,5X,F10.5,5X,F10.4)
       113 FORMAT (20H FAILURE TO CONVERGE)
           END


           FUNCTION FCT(ARG1,ARG2)
           COMMON LIMIT
           PI=3.14159265
           W=SIN(PI/3.E+6*ARG1)*2000.
           IF (ABS(W).GT. 1.E-20) GO TO 5
           LIMIT=0
        3 FCT=0
           RETURN
        5 IF (ALOG(ABS(ARG2)).GT.30.) GO TO 3
           FCT=1./W*(4000.-1.E-7*ARG2**2-ARG2*2./3.E+3*PI*COS(PI/3.E+6*ARG1)
           RETURN
           END
```

APPENDIX III

COMPUTER PROGRAM USED TO SOLVE THE TIME-INDEPENDENT

CONTINUITY EQUATION WITH DIFFUSION

The steady-state continuity equation can be written as

$$\frac{d}{dz}(wN) = q - \alpha N^2 + \sin^2 I \frac{d}{dz}\left(D\frac{dN}{dz}\right) \qquad (A3.1)$$

where z is the altitude, w is the ion vertical wind velocity, N is the electron density, q is the ionization rate, α is the recombination coefficient, I is the dip angle and D is the plasma (or ambipolar) diffusion coefficient. The particular wind model employed for the converging ion wind is a sinusoid

$$w = 20 \sin \frac{\pi(150 - z)}{30} \qquad (A3.2)$$

For initial analysis D, q, and α were taken to be realistic constants appropriate to 150 kilometers.

The equation is very sensitive and prone towards instability if slight errors are encountered. Difference equation methods for solving the equation resulted in instability in every case tried, even for implanted damping factors.

An iterative integration method was employed which gave promising solutions; however, required much computer time for analysis. This method seems to be applicable to a much more generalized analysis and therefore outlined. Integration of equation (A3.1) from 0 to z yields a first order differential equation where $w = \frac{dN}{dz} = 0$ at $z = 0$, namely

$$\frac{dN}{dz} - \frac{w}{D} N + \frac{1}{D} \int_{o}^{z} (q - \alpha N^2) \, dz \qquad (A3.3)$$

Now, any first order equation has a solution of the form

$$N = e^{-\int_{o}^{z} P(z)dz} \int_{o}^{z} Q(z) \, e^{\int_{o}^{z} P(z)dz} \, dz \qquad (A3.4)$$

where $P(z)$ is $-\frac{w}{D}$ and $Q(z)$ is $-\frac{1}{D} \int_{o}^{z} (q - \alpha N^2)dz$.

The procedure is to assume an N distribution and thereby determine $Q(z)$ and then $N(z)$ by application of (A3.4). This value of $N(z)$ is again used to calculate a new $Q(z)$ and $N(z)$. Relaxation converges upon the desired profile if sufficient accuracy is taken.

The best method found for solving equation (A3.1) is to employ the fourth order Runge-Kutta method using 0.5 km steps. The procedure requires specification of an initial slope and magnitude as a starting boundary condition, however, the actual boundary conditions known are zero slope at the peak and valleys of the profile. To make these boundary conditions compatible with those demanded by the Runge-Kutta method a relaxation process was employed. The initial slope was set at zero and a zero diffusion value was initially picked as the starting value. The marching solution then diverged either positively or negatively. If positive the initial value was reduced and vice versa until the condition of zero slope was rendered at the peak and valley. Usually five to twelve iterations are required for the final solution to lie within the chosen limits. This procedure is reproduced on the following pages.

```
0001            IMPLICIT REAL*8 (A-H,O-Z)
0002            REAL*4 XG(600),YG(600),T(4),XINCH
0003            DIMENSION Y(300),V(300)
0004            COMMON Q,A,B,D,ALP,PI
0005            PI=3.14159265
0006            T(1)=0.
0007            T(2)=5.
0008            T(3)=120.
0009            T(4)=200.
0010            XG(1)=T(2)
0011            XG(2)=T(1)
0012            YG(1)=T(3)
0013            YG(2)=T(3)
0014            YG(600)=T(4)
0015            XINCH=10.
0016            A=2000.
0017            B=PI/3.E+6
0018            D=2.D+8
0019            ALP=1.9D-7
0020            L=1
0021            FK=10.
0022          5 J=1
0023            NC=300
0024            I=1
0025            PK=12
0026            ACT=0.999E-5/7.*PK+1.E-8
0027            Q=2.1E-02*DEXP(0.8*PK)
0028            Q=4.
0029            SS=DSQRT((A*B)**2+4.*ALP*Q)
0030            PN=(+A*B+SS)/(2.*ALP)
0031            TN=(-A*B+SS)/(2.*ALP)
0032            H=1.E+4
0033            V(1)=0
0034            YU=BN
0035            YB=DSQRT(Q/ALP)
0036            WRITE (6,3) Q, BN, TN,PK
0037          3 FORMAT (1X,3E15.5,F8.1)
0038          8 Y(1)=(YU+YB)/2.
0039            WRITE (6,9) Y(1),YU,YB,X,J
0040          9 FORMAT (1X,3E20.10,E15.5,I4)
0041         10 X=DFLOAT(I)*H+3.E+6-H
0042            Y1=Y(I)
0043            V1=V(I)
0044            P1=H*FCT(X,Y1,V1)
0045            X2=X+H/2.
0046            Y2=Y(I)+H/2.*V(I)
0047            V2=V(I)+P1/2.
0048            P2=H*FCT(X2,Y2,V2)
0049            X3=X+H/2.
0050            Y3=Y(I)+H/2.*V(I)+H/4.*P1
0051            V3=V(I)+P2/2.
0052            P3=H*FCT(X3,Y3,V3)
0053            X4=X+H
```

```
0054            Y4 =Y(I)+H*V(I)+H/2.*P2
0055            V4=V(I)+P3
0056            P4=H*FCT(X4,Y4,V4)
0057            Y(I+1)=Y(I)+H*V(I)+H/6.*(P1+P2+P3)
0058            V(I+1)=V(I)+1./6.*(P1+2.*P2+2.*P3+P4)
0059            IF (J) 42,21,11
0060         11 IF (V(I+1)) 14,14,12
0061         12 YU=Y(1)
0062            I=1
0063            GO TO 8
0064         14 IF (Y(I+1)) 18,18,16
0065         16 I=I+1
0066            IF (I-NC) 10,20,20
0067         18 YB=Y(1)
0068            I=1
0069            GO TO 8
0070         20 J=0
0071            SA=0
0072         21 I=I+1
0073            IF (I-NC) 10,23,23
0074         23 IF (DABS(V(300)).LT.ACT) GO TO 40
0075            IF (V(300)      ) 35,40,30
0076         30 YU=Y(1)
0077            I=1
0078            GO TO 8
0079         35 YB=Y(1)
0080            I=1
0081            GO TO 8
0082         40 J=-1
0083            WRITE (6,41)
0084         41 FORMAT (1H1,4X,6HHEIGHT,8X,7HDENSITY,9X,5HSLOPE)
0085            I=1
0086         42 SA=SA+H*Y(I)**2
0087            WRITE (6,15) X,Y(I),V(I),SA
0088         15 FORMAT (1X,3E15.5,5X,E15.5)
0089            XG(300+I)=DLOG10(Y(I))
0090            XG(301-I)=XG(300+I)
0091            YG(300+I)=120.+X*1.E-5
0092            YG(301-I)=180.-X*1.E-5
0093            I=I+1
0094            IF (I-NC) 10,50,50
0095         50 XG(600)=XG(599)
0096         60 STOP
0097            END
```

```
0001            FUNCTION FCT (Z,Y,V)
0002            IMPLICIT REAL*8 (A-H,O-Z)
0003            COMMON Q,L,B,D,ALP,PI
0004            GO TO 5
0005          3 FCT=0
0006            WRITE (6,12)
0007         12 FORMAT (1X,3HXXX)
0008            RETURN
0009          5 IF (DLOG(DABS(Y)).GT.30.) GO TO 3
0010            FCT= 1./D*(V*A*DSIN(B*Z)+Y*A*B*DCOS(B*Z)+ALP*Y**2-Q)
0011            RETURN
0012            END
```

APPENDIX IV

COMPUTER PROGRAM USED TO DERIVE WINDS FROM AN ELECTRON-DENSITY PROFILE

To calculate the winds, $w(z)$, from an electron-density profile,

$N(z)$, the derived equation (3.9) applies

$$w(z) = \frac{1}{N(z)} (z - z_1)\bar{q} - \int_z^z \alpha N(z) \left. \frac{dN}{dz} \right|_z \qquad (A4.1)$$

where the appropriate $\bar{q}$ is used for the lower and upper portion of the

profile. The average ionization $\bar{q}$ is first calculated in the program by

use of Simpson's rule.

$$\bar{q} = \frac{1}{z_2 - z_1} \int_{z_1}^{z_2} \alpha N^2 \, dz$$

The recombination coefficient α is taken to be variable as discussed

in Section 3.2.2.

```
        $JOB
   1         IMPLICIT REAL *8(A-H,O-Z)
   2         DIMENSION EN(200)
   3       1 Q=0
   4         QSS=0
   5         M=1
   6         K=1
   7         ALP=1.9E-7
   8         DO=2.E+8
   9         H=0.5 E+5
  10         S=C
  11         I=1
  12       5 READ (5,6) A,B,C,D,E,F
  13       6 FORMAT(6E10.2)
  14         IF (A) 9,9,7
  15       7 EN (I)=A
  16         EN(I+1)=B
  17         EN(I+2)=C
  18         EN(I+3)=D
  19         EN(I+4)=E
  20         EN(I+5)=F
  21         I=I+6
  22         GO TO 5
  23       9 Z1=B*1.E+5
  24         Z2=C*1.E+5
  25         Z3=D*1.E+5
  26         EN(I)=EN(I-1)
  27         EN(I+1)=EN(I-1)
  28         ZN1=B
  29         ZN2=C
  30         ZN3=D
  31         PK=E
  32         DZ=Z2-Z1
  33         WRITE (6,10) B,C,D
  34      10 FORMAT (1X,3F10.2)
  35         I=1
  36         ZN=B
  37      11 TE=(ZN-120.)*(1.4*PK+2.91)+355.
  38         ALP=4.5E-7*(300./TE)
  39         QS=ALP*H/DZ*(EN(I+1)**2+0.5*(EN(I)**2-EN(I+1)**2))+Q
  40      12 TE=(ZN-120.)*(1.4*PK+2.91)+355.
  41         ALP=4.5E-7*(300./TE)
  42         Q=ALP*H/DZ*(EN(I+1)**2+0.5*(EN(I)**2-EN(I+1)**2))+Q
  43         QSS=QS+QSS
  44         WRITE (6,106) ZN,Q,QSS,QS,QSM,K,I
  45     106 FORMAT (1X,5E15.5,2I4)
  46         ZN=ZN1+H*1.E-5*DFLOAT(I)
  47         I=I+1
  48         QS=ALP*H/(3.*DZ)*(EN(K)**2+4.*EN(K+1)**2+EN(K+2)**2)-QS
  49         K=K+1
  50         IF (ZN.GT.ZN2-H*1.E-5/2) GO TO 13
  51         GO TO 12
  52      13 GO TO (51,16), M
  53      51 M=2
  54         QB=Q
  55         DZ=Z3-Z2
  56         WRITE(6,14)QB
  57      14 FORMAT(1X,31HBOTTOM PROFILE PRODUCTION RATE=,F14.4)
  58         Q=0
  59         QSS=0
```

```
60       G0 T0 11
61    16 IF (ZN-ZN3) 12,20,20
62    20 QT=0
63       DZ=Z2-Z1
64       WRITE(6,21) QT
65    21 FORMAT(1X,28HT0P PR0FILE PR0DUCTI0N RATE=,F14,4)
66       I=1
67       Z=ZN1
68    25 TE=(Z-120,)*(1,4*PK+2,91)+355,
69       ALP=4,5E-7*(300,/TE)
70       PS=H*(QB-ALP*EN(I)**2)
71       IF (PS) 22,22,23
72    22 IF (EN(I+1),GT,EN(I)) G0 T0 26
73       G0 T0 27
74    23 IF (EN(I+1),GT,EN(I)) G0 T0 27
75       G0 T0 26
76    26 S=PS+S=H*0,5*0ABS((QB-ALP*EN(I+1)**2)-(QB-ALP*EN(I)**2))
77       G0 T0 29
78    27 S=PS+S+H*0,5*0ABS((QB-ALP*EN(I+1)**2)-(QB-ALP*EN(I)**2))
79    29 DER=DD*(((EN(I+1)-EN(I))/H+(EN(I+2)-EN(I+1))/H)/2,)
80       W     =1,/EN(I+1)*(S+DER)
81       W1    =1,/EN(I+1)*(S+0,5*DER)
82       W2    =S/EN(I+1)
83       WRITE(6,30)Z,EN(I+1),W     ,DER,S,QB,I,W1     ,W2,ALP
84    30 FORMAT(1X,F10,4,E15,4,F10,4,3E15,5,I4,2F11,4,E15,5)
85       Z=ZN1+H*DFL0AT(I)*1,E-5
86       I=I+1
87       ZN=Z
88       IF(ZN-ZN2)25,35,35
89    35 QB=Q
90       DZ=Z3-Z2
91       IF(ZN-ZN3) 25,40,40
92    40 G0 T0 1
93       END
```

REFERENCES

Adams, J. and B. W. Manley (1966), The mechanism of channel electron multiplication, *IEEE Trans. N c. Sci. NS 13* (3), 88-95.

Bakke, J. C., J. B. Reagan, R. D. Reed, W. L. Imhof, and J. D. Matthews (1969), A high-sensitivity particle spectrometer for the measurement of polar-cap-absorption events, *IEEE Trans. Nuc. Sci. NS 17,* (1), 91-96.

Berger, M. J., S. M. Seltzer, and K. Maeda (1970), Energy deposition by auroral electrons in the atmosphere, *J. Atmos. Terr. Phys. 32,* (6), 1015-1045.

Berkner, L. V. and S. L. Seaton ('940), Ionospheric changes associated with the magnetic storm of March 24, 1940, *Terr. Magn. Atmos. Elect. 45,* 393-418.

Bertolini, G. and A. Coch (1968), *Semiconductor Detectors,* John Wiley & Sons, Inc.

Bilger, R. H. (1966), Optimum energy resolution of semiconductor radiation detectors with preamplifiers using tubes, field-effect transistors and bipolar transistors, *Nucl. Instr. and Meth. 40,* 54-60.

Biondi, M. A. (1969), Atmospheric electron-ion and ion-ion recombination processes, *Can J. Chem. 47,* 1711-1722.

Buck, T. M. (1961), Surface effects on silicon particle detectors, Semiconductor nuclear particle detectors, *NAS-NRC-PUB. 876,* 111-120.

Cartwright, D. G. (1964), A 10-kilocycle per second Doppler observation of the intermediate layer of the nighttime ionosphere, *J. Geophys. Res. 69,* 4031-4035.

Chynoweth, A. G. and K. G. McKay (1956), Photon emission from avalanche breakdown in silicon, *Phys. Rev. 102* (2),   369-376.

Constantinides, E. and J. F. Bedinger (.), Observed redistribution of *E*-region ionization by neutral winds, *J. Atmos. Terr. Phys. 33*, (2),   461-472.

Dalgarno, A. (1964), Corpuscular radiation in the upper atmosphere, *Ann. Geophys. 20* 65-74.

Davis, W. D. (1958), Silicon crystal counters, *Jour. of Appl. Phys. 29*, (2),   231.

Dearnaley, G. (1964), The channeling of ions through silicon detectors, *IEEE Trans. Nucl. Sci. NS 11* (3),   249-253.

DeForest, S. E. (1972), Spacecraft charging at synchronous orbit, *J. Geophys. Res. 77* (4),   651-659.

Deme, S. (1971), *Semiconductor Detectors for Nuclear Radiation Measurement*, John Wiley & Sons, Inc.

Dodge, W. R., S. R. Domen, A. T. Hirshfeld, and D. D. Hoppes (1964), The anomaly in the response of semiconductor detectors, *IEEE Trans. Nucl. Sci. NS 11* (3),   238-243.

Evans, J. V. (1973), Millstone Hill Thompson scatter results for 1966 and 1967, *Planet Space Sci. 21*, 763-792.

Ewing, R. J. (1962), Response of silicon surface barrier detectors to hydrogen ions of energies 25 to 250 keV, *IRE Trans. Nucl. Sci. NS 9*, (3),   207-210.

Fritz, T. A. (1967), Spectral, spatial, and temporal variations observed from 10 to 100 k / with satellite Injun 3, Ph.D. thesis, University of Iowa, Iowa City.

Fritz, T. A. (1968), High latitude outer zone boundary region for ≳ 40-keV electrons during geomagnetically quiet periods, *J. Geophys. Res. 72* (23), 7245-7255.

Fujitake, K., T. Ogawa, and T. Tohmatsu (1971), A numerical computation of the ionization redistribution effect of the wind in the night-time ionosphere, *J. Atmos. Terr. Phys. 33,* 687-700.

Geller, M. A., L. G. Smith, and H. D. Voss (1975), Analysis of night-time *E*-region winds and ionization production, to appear in *Radio Science.*

Gibson, W. M. (1966), The role of particle channeling in detector systems, *IEEE Trans. Nucl. Sci. NS 13* (3), 162-175.

Gough, M. P. and H. L. Collin (1973), Energetic electron precipitation as a source of ionization in the nighttime *D*-region over the mid-latitude rocket range, South Uist, *J. Atmos. Terr. Phys. 35* (5), 835-850.

Hayakawa, S., T. Kato, T. Kohno, T. Murakami, F. Nagase, K. Nishimura, and Y. Tanaka (1973), Existence of geomagnetically trapped electrons at altitudes below the inner radiation belt, *J. Geophys. Res. 78* (13) 2341-2343.

Hill, R. W., R. J. Grader, F. D. Seward, and J. P. Stoering (1970), Soft particle flux above 130 km at midlatitude, *J. Geophys. Res. 75* (34), 7267-7271.

Hirao, K., N. Wakai, K. Sawada, T. Hikosaka, K. Yano, and K. Maeda (1965), Some evidences of the particle effects on the ionosphere at mid-latitudes, *Space Res. V,* 1058-1070.

Holmes, J. C., C. Y. Johnson, and J. M. Young (1965), Ionospheric chemistry, *Space Res. V*, North-Holland, 756-766.

Lindzen, R. S. and S. Hong (1974), Effects of mean winds and horizontal temperature gradients on solar and lunar semidiurnal tides in the atmosphere, *J. Atmos. Sci. 31*, 1421-1446.

Livingstone, S. and H. A. Bu ne (1937), Nuclear Physics, C. Nuclear Dynamics, Experimental, *Rev. Mod. Phys. 9*, 263.

MacLeod, M. A. (1966), Sporadic E theory, I. Collision-geomagnetic equilibrium, *J. Atmos. Sci. 23*, 96.

Maeda, K. (1965), Further study on possible effects of the dynomoelectric field on electrons trapped in the magnetosphere, *J. Geomag. Geoelec. 17*, 1.

McDiarmid, I. B., J. R. Burrows, E. E. Budzinski, and M. D. Wilson (1963), Some average properties of the outer radiation zone at 1000 km, *Can. J. Phys.,41*, 2064-2079.

Mechtly, E. A. and L. G. Smith (1970), Changes of lower ionosphere electron densities with solar zenith angle, *Radio Sci. 5*(7), 1407.

Meier, R. R. (1974), A numerical study of the nighttime E-region ionization profile, *EOS Trans. Amer. Geophys. Union 54* (4), 395.

Meyer, D. and H. J. Langmann (1965), Die Beweglichkeit "Heisser" elektronen und IHR einfluss AUF die anstiegszeit der impulse von halbleiterzählern aus n-silizium, *Nucl. Instr. and Meth. 34*, 77-87.

Miller, G. L., W. M. Gibson, and P. F. Donovan (1962), Semiconductor particle detectors, *Ann. Rev. of Nucl. Sci. 12*, 189.

Motchenbacher, C. D. and F. C. Fitcher (1973), *Low-Noise Electronics Design,* John Wiley & Sons.

O'Brien, B. J. (1962), Lifetimes of outer-zone electrons and their precipitation into the atmosphere, *J. Geophys. Res. 67* (10), 3687-3706.

O'Brien, B. J. and C. D. Laughlin (1963), Electron precipitation and the outer radiation zone, *Space Res. III,* 399-417.

O'Brien, B. J. (1964), High-latitude geophysical studies with satellite Injun 3.3; Precipitation of electrons into the atmosphere, *J. Geophys. Res. 69* (1), 13-43.

Ogawa, T. and T. Tohmatsu (1966), Photoelectric processes in the upper atmosphere, *Rep. Iono. and Space Res. (Japan) 20* (4), 595.

O'Kelley, G. D. (1962), *Detection and Measurement of Nuclear Radiation,* Washington, Subcommittee on Radio-chemistry, National Academy of Sciences-National Research Council; available from the Office of Technical Services, Department of Commerce.

Pell, E. M. (1960), Ion drift in an n-p junction, *J. App. Phys. 31* (2), 291.

Potemra, T. A. and T. J. Rosenberg (1973), VLF propagation disturbances and electron precipitation at mid-latitudes, *J. Geophys. Res. 78* (10), 1572-1580.

Potemra, T. A. and A. J. Zmuda (1970), Precipitating energetic electrons as an ionization source in the mid-latitude nighttime *D*-region, *J. Geophys. Res. 75*(34), 7161-7167.

Prasad, R. Y. and R. N. Singh (1972), Impact and bremsstrahlung photo-ionization due to precipitating electrons in the lower ionosphere, *Ann. Geophys. 28*(3), 593.

Quaranta, A. A., G. Casadei, M. Martini, G. Ottaviani, and G. Zanarini (1965), On the information available from the rise-time of the charge pulse supplied by semiconductor particle detectors, *Nucl. Instr. and Meth. 35,* 93-99.

Quaranta, A. A., M. Martini, G. Ottaviani (1969), The pulse shape and the timing problem in solid state detectors-A review paper, *IEEE Trans. Nucl. Sci. NS 16* (2),   35-61.

Ramo, S. (1939), Currents induced by electron motion, *Proc. IRE 27,* 584-585.

Ratcliffe, J. A. (1956), The formation of the ionospheric layers F-1 and F-2, *J. Atmos. Terr. Phys. 8,* 260-269.

Ray, J. A. and C. F. Barnett (1969), Detection of low energy heavy particles with silicon barrier detectors, *IEEE Trans. Nucl. Sci. NS 16* (1),   82-86.

Reed, R. D., E. G. Shelley, J. C. Bakke, T. C. Sanders, and J. C. McDaniel (1969), A low-energy channel-multiplier spectrometer for ATS-E, *IEEE Trans. Nucl. Sci. NS 16,* 359-370.

Rees, M. H. (1963), Auroral ionization and excitation by incident energetic electrons, *Planet Space Sci. 11,* 1209.

Sackerlotzky, O. H. and V. J. Belanger (1972), New ceramic electron multiplier, *IEEE Trans. Nucl. Sci. NS 19* (3),   63-70.

Shockley, W. and W. T. Read, Jr. (1952), Statistics of recombinations of holes and electrons, *Phys. Rev. 87* (5),   835-842.

Smith, L. G. (1969), *Small Rocket Instrumentation Techniques,* North-Holland, 1-15.

Smith, L. G. (1970), A sequence of rocket observations of nighttime sporadic-*E*, *J. Atmos. Terr. Phys. 32* (7), *7*, 1247-1257.

Smith, L. G., M. A. Geller and H. D. Voss (1974), Energetic electrons in the mid-latitude nighttime *E*-region, *J. Atmos. Terr. Phys.* (to appear).

Sternheimer, R. M. (1959), Range-energy relations for protons in Be, C, Al, Cu, Pb, and Air, *Phys. Rev. 115* (1),   137-142.

Swider, W., Jr. (1965), A study of the nighttime ionosphere and its reaction rates, *J. Geophys. Res. 70* (19),   4859-4873.

Tauc, J. (1959), Electron impact ionization in semiconductors, *J. Phys. Chem. Solids 8*, 219.

Taylor, J. M. (1963), *Semiconductor Particle Detectors*, Butterworths Inc.

Tove, P. A. and W. Seibt (1967), Plasma effects in semiconductor detectors, *Nucl. Instr. and Meth. 51*, 261-269.

Tsukuda, M. (1961), Pulse analyzing system for a gridden ionization chamber, *Nucl. Instr. Meth. 14*, 241-251.

Tuohy, I. R. and J. R. Harries (1973), Observation of electrons at mid-latitude during a magnetic storm, *J. Geophys. Res. 78* (34), 8381-8386.

Van Allen, J. A. and H. E. Tatel (1948), The cosmic-ray counting rate of a single Geiger counter from ground level to 161 kilometers altitude, *Phys. Rev. 73* (3),   245-251.

Wakai, N. and K. Sawada (1964), Rotational variation of the ionospheric *E*-region in a temperate latitude with geomagnetic disturbances, *J. Rad. Res. Labs. (Japan) 11*, 1.

Watts, J. M. and J. N. Brown (1954), Some results of sweep-frequency

   investigation in the low frequency band, *J. Geophys. Res. 59*, 71-86.

Williams, R. L. and P. P. Webb (1962), The window thickness of diffused

   junction detectors, *IRE Trans. Nucl. Sci. NS 9* (3),   160-166.

Williamson, C. and J. P. Boujot (1962), Range and rate of energy loss

   of charged particles of energy 0.5 to 150 meV, *Commissariat à*

   l'Energie Atomique-2189.

Wulff, A. and J. A. Gledhill (1974), Atmospheric ionization by precipi-

   tated electrons, *J. Atmos. Terr. Phys. 36* (1),   79-91.